Adaptive optics and remote focusing in biomedical microscopy



Jiahe Cui

Jesus College

Hilary Term 2022

A thesis submitted for the Degree of Doctor of Philosophy

at the University of Oxford

Abstract

Optical microscopy has been an indispensable tool for many biomedical applications. Compared to rapid developments in research labs striving for higher spatio-temporal resolution and information extraction efficacy, advances towards the clinic, especially those targeted at surgical applications, have been slow in comparison. Complex practicalities make the translation of cutting-edge technology much more challenging. Consequently, there is a constant need to address the limitations of conventional medical imaging devices using optical techniques and to develop new instrumentation that is task-oriented and capable of providing stabilised real-time high-resolution image guidance for improved surgical outcome. In particular, imaging in the human brain entails the most stringent requirements, for which label-free techniques would be most beneficial. Apart from the microscope design, optical aberrations also affect the image quality. Until now, the concept of adaptive optics (AO) has not been introduced to surgical microscopy, as it most noticeably benefits systems with higher theoretical resolution. For a high-resolution surgical microscope, AO would have many roles to play, making its integration a potentially rewarding and meaningful contribution.

This thesis concerns to date the focused development of a compact and contactless label-free neurosurgical microscope and the investigation of using AO methods to address practical needs in surgical scenarios. Specifically, a long-working-distance reflectance confocal microscope was designed and built with special considerations for compactness and portable transit. It provides cellular-level resolution over wide imaging fields of view (FOVs) and visualises individual cells even in normal brain tissue exhibiting minimal label-free image contrast. The elimination of direct tissue contact and fluorescence labelling also greatly reduces surgical risk and complexity. Closed-loop sensor-based AO and remote focusing was later implemented and characterised following the development of an open-source Python software, *SenAOReFoc*, which is now publicly available on GitHub `https://github.com/jiahecui/SenAOReFoc` for the wider community. It was designed with a user-friendly graphic user interface and modular functional units for easy integration into existing AO microscopes. The use of remote focusing for fast axial scanning avoids slow mechanical movements of the translation stage and simultaneously corrects for system aberrations at each refocusing depth. Both volumetric and depth-wise random access imaging functions have been enabled. To fulfil requirements for real-time display in clinical settings, some post-processing and image enhancement techniques are then demonstrated to remove image artefacts and improve image contrast with minimal computational effort. An extended range autofocusing technique that combines remote focusing with sequence-dependent learning using a bi-directional long short term memory network was developed to address possible respiratory and pulsing movements during surgery. A much larger system-aberration-free autofocusing range as compared to conventional methods was achieved in tissue both exposed to air and immersed in liquid. Network generality has been validated for different imaging FOVs and for specimens not seen during the network training process. Continuous tracking of axial sample motion has also been demonstrated under varying experimental conditions.

In the remainder of this thesis, a generalised AO method was proposed for high-numerical aperture aberration-free refocusing in refractive-index-mismatched media involving both stage translation and remote focusing. Two new sets of orthogonal modes were established using QR decomposition for either independent or balanced remote focusing and refractive index mismatch correction. Finally, first investigations of multi-conjugate AO in microscopy were carried out to correct for spatially-variant aberrations and increase the imaging FOV. For this purpose and to incorporate different imaging and AO modalities in the same system, a multi-purpose AO microscope was designed and developed beforehand.

Acknowledgements

I would like to take this opportunity to thank everyone who have provided me with invaluable guidance, support and encouragement during the course of my DPhil at Oxford. Primarily, I am most indebted to my supervisor Prof. Martin Booth, who has generously provided me with an ERC Research Studentship and the opportunity to be studying here at all. I would like to thank him for his patient advice, enthusiastic discussions, and especially the immense support, encouragement, and trust he has given me towards trying out new ideas and building new skill sets. I am also most grateful to Prof. Nigel Emptage from the Department of Pharmacology, for his generous support in providing lab space and resources, for writing various reference letters for me, and for his academic insight. I would also like to thank my Jesus College advisor, Prof. Steve Morris, for his advice, reassurance and encouragement towards my DPhil progress.

I would like to express my gratitude towards Dr. Karen Hampson and Dr. Raphaël Turcotte, who have provided me with guidance and support in all aspects of my research and for simply being there to help and chat whenever I was in a difficult situation. I am indebted to Dr. Patrick Salter for his enlightening discussions and invaluable advice towards career development. I am also thankful to Dr. Matthew Wincott for his help and expertise in software design, Dr. Jacopo Antonello for his research and mathematical rigour, and Dr. Jingyu Wang and Dr. Chao He for their continuous trust and encouragement. I would also like to thank Andrew Kirkpatrick for being such a supportive and helpful desk mate, as well as Carla Schmidt for providing biological samples, despite so many times I wasn't able to make them so useful as they possibly could be.

I am most grateful towards all members of the DOP group for their friendship, inspirations, and encouraging remarks over the years, as well as my friends at Jesus College for always being there for me, and Duncan Constable from the Department of Engineering Science Mechanical Workshop for helping me make so many bits and pieces for my research.

Finally, I most want to thank my parents and grandfather for their understanding during my time away from home, for their unconditional love, support and encouragement that has given me the solid basis of pursuing my research here, as well as their insights from being academic workers themselves; and dear Li for his tolerance, patience, and company over the years.

Contents

1 Introduction **1**
- 1.1 Optical microscopy in biomedical imaging . . . 3
  - 1.1.1 Confocal microscopy . . . 3
  - 1.1.2 Two-photon excitation microscopy . . . 5
  - 1.1.3 Optical coherence tomography . . . 7
- 1.2 Practical considerations for biomedical imaging . . . 8
  - 1.2.1 Influence of laser wavelength . . . 8
  - 1.2.2 Image contrast formation and enhancement . . . 11
  - 1.2.3 Power considerations . . . 12
  - 1.2.4 Choice of fluorophore . . . 13
- 1.3 Aberrations and adaptive optics . . . 15
- 1.4 Axial scanning techniques . . . 16
  - 1.4.1 Conventional axial scanning techniques . . . 16
  - 1.4.2 Remote focusing for fast aberration-free focus control . . . 17
- 1.5 Motivation and structure of thesis . . . 18

2 Image formation in optical microscopy **21**
- 2.1 Overview . . . 21
- 2.2 Diffraction theory . . . 21
- 2.3 Diffraction of a thin lens . . . 23
- 2.4 The amplitude point spread function . . . 27
- 2.5 Coherent and incoherent image formation . . . 30
- 2.6 Image formation in optical sectioning microscopes . . . 31
  - 2.6.1 The confocal microscope . . . 31
  - 2.6.2 The two-photon excitation microscope . . . 34

3 Aberrations and sensor-based adaptive optics **36**
- 3.1 Overview . . . 36
- 3.2 Aberrations in optical microscopy . . . 36
  - 3.2.1 Definition of phase aberrations . . . 37
  - 3.2.2 Source of phase aberrations . . . 37
  - 3.2.3 Zernike representation of phase aberrations . . . 39
  - 3.2.4 The Strehl ratio . . . 41
- 3.3 Direct wavefront sensing . . . 42
  - 3.3.1 The Shack-Hartmann wavefront sensor (SHWS) . . . 43

3.3.2 Centroiding of SH spot patterns . . . 45
3.3.3 Calculation of Zernike coefficients using slope values . . . 46
3.4 Sensor-based adaptive optics . . . 48
3.4.1 The electrostatic and electromagnetic deformable mirror . . . 48
3.4.2 Deformable mirror calibration . . . 49
3.4.3 Closed-loop adaptive optics control . . . 52
3.4.4 Correction of system aberrations . . . 54
3.5 Remote focusing using a deformable mirror . . . 54
3.5.1 Remote focusing calibration . . . 55
3.5.2 Real-time system-aberration-free remote focusing . . . 55
3.6 Multi-conjugate adaptive optics . . . 56
3.6.1 Limitations of pupil adaptive optics (PAO) . . . 56
3.6.2 Considerations for conjugate adaptive optics (CAO) . . . 57
3.6.3 Introduction of multi-conjugate adaptive optics (MCAO) . . . 58

4 A compact and contactless reflectance confocal microscope (CCRCM) for neurosurgery 60
4.1 Overview . . . 60
4.2 Current status of image-guided brain surgery . . . 61
4.3 Materials and methods . . . 63
4.3.1 Design concept . . . 63
4.3.2 System setup . . . 63
4.3.3 Zemax evaluation of system aberrations . . . 66
4.3.4 Reflectance imaging . . . 70
4.3.5 Sample preparation . . . 71
4.4 Experimental results . . . 71
4.4.1 *Ex vivo* imaging of fixed mouse brain . . . 71
4.4.2 *Ex vivo* imaging of frozen mouse calvaria . . . 73
4.4.3 Live tissue imaging of the rat hippocampus . . . 75
4.5 Discussion and conclusion . . . 77

5 SenAOReFoc: A closed-loop sensor-based adaptive optics and remote focusing control software 82
5.1 Overview . . . 82
5.2 Description of software functionalities . . . 84
5.3 GUI modular software functions . . . 85
5.3.1 SHWS initialisation and DM calibration unit . . . 85
5.3.2 Zernike aberration input unit . . . 87
5.3.3 AO control and data collection unit . . . 88
5.3.4 Miscellaneous control unit . . . 90
5.3.5 Remote focusing unit . . . 91
5.4 Discussion and conclusion . . . 93

6 Sensor-based adaptive optics and remote focusing in the CCRCM 95
6.1 Overview . . . 95
6.2 System setup and software control . . . 95

6.3 Characterisation of adaptive optics performance . . . 97
6.3.1 Calibration of deformable mirror and system aberration . . . 98
6.3.2 Evaluation of SHWS dynamic range . . . 98
6.3.3 Evaluation of Zernike mode coupling . . . 100
6.3.4 Correction of Zernike defocus . . . 100
6.3.5 Correction of multiple Zernike mode combinations . . . 102
6.4 Remote focusing in the CCRCM . . . 102
6.4.1 Remote focusing calibration results . . . 102
6.4.2 Remote focusing within frozen mouse calvaria . . . 106
6.5 Discussion and conclusion . . . 108

7 Post-processing and image enhancement techniques for real-time display 110
7.1 Overview . . . 110
7.2 Different imaging modes for clinical requirements . . . 111
7.3 Removal of image artefacts . . . 112
7.4 Calibration of spatial resolution . . . 114
7.5 Gamma correction for image contrast enhancement . . . 115
7.6 Discussion and conclusion . . . 118

8 Extended range aberration-free autofocusing via remote focusing and Bi-LSTM network prediction 120
8.1 Overview . . . 120
8.2 Status and limitations of existing autofocusing techniques . . . 121
8.3 Materials and methods . . . 123
8.3.1 Autofocusing workflow . . . 123
8.3.2 Evaluation of Zernike distribution curves . . . 126
8.3.3 Bi-LSTM network . . . 128
8.3.4 Sample preparation . . . 130
8.4 Network optimisation and experimental validation results . . . 131
8.4.1 Offline network optimisation results . . . 131
8.4.2 Characterisations for both air-exposed and water-immersed tissue . . . 134
8.4.3 Generalisation towards different size imaging FOVs and sample types . . . 135
8.4.4 Autofocusing in real time with continuous axial motion . . . 137
8.4.5 Autofocusing at target depths within live tissue immersed in liquid . . . 140
8.5 Discussion and conclusion . . . 140

9 A generalised adaptive optics method for high-NA aberration-free refocusing in refractive-index-mismatched media 144
9.1 Overview . . . 144
9.2 Background and motivation . . . 145
9.3 Representation of high-NA defocus Φ_d . . . 146
9.3.1 Zernike expansion of Φ_d . . . 148
9.3.2 Representation using a vector of Zernike coefficients . . . 149
9.4 Independent high-NA remote focusing in a homogeneous medium . . . 149
9.5 High-NA refocusing in stratified media with a single interface . . . 153
9.5.1 Effective numerical aperture . . . 153

9.5.2 Total phase contribution of RIM and high-NA defocus Φ_d 153
9.5.3 Independent remote focusing and RIM aberration correction 155
9.5.4 Minimal root-mean-square balancing for a desired focal depth 158
9.5.5 Balanced remote focusing and RIM aberration correction 160
9.6 High-NA refocusing in stratified media with multiple interfaces 162
9.6.1 Aberration-free refocusing through a cover glass 162
9.6.2 Generalisation towards multiple interfaces 166
9.7 Modified control matrix for adaptive device 168
9.8 Discussion and conclusion 169

10 Multi-conjugate adaptive optics in a multi-purpose adaptive optical microscope 172
10.1 Overview 172
10.2 Development of a multi-purpose adaptive optical microscope 173
10.2.1 System layout and modular functional units 173
10.2.2 Practical considerations for the system design 179
10.2.3 Demonstration of system imaging performance 181
10.3 Closed-loop multi-conjugate adaptive optics for microscopy 182
10.3.1 Closed-loop multi-conjugate adaptive optics control 182
10.3.2 Multi-conjugate adaptive optics in HeLa cells 184
10.4 Discussion and conclusion 187

11 Overall summary and outlook 189

A Zernike expansion of $\cos\beta$ and calculation of c_{2p} 192

Bibliography 194

Publications arising from this work 216

Chapter 1

Introduction

Optical microscopy has been at the core of biomedical imaging for decades, accelerating the understanding and fulfilling the diverse requirements of many research areas. Neuroscience is perhaps one of the fields that has benefited the most from technological advances in the ongoing pursuit to observe spatio-temporal dynamics of neuronal activity with synaptic resolution within large volumes [1, 2]. The interpretation of how neural circuits react to stimuli, process information, and lead to adaptive behaviour lies at the heart of all neuroscience research [3, 4]. From this arises two main topics of interest: high-temporal-resolution image acquisition methods to capture transient calcium signals, and high-spatial-resolution volumetric imaging methods to capture them simultaneously across a population of neurons [5, 6].

Optical microscopes have also been a fundamental tool for histological assessment. A wide range of fluorescent markers, imaging modalities, and analysis methods have been introduced to identify histopathological features with higher precision [7–10]. In particular, artificial intelligence (AI) has greatly accelerated the development of digital pathology in terms of providing computer-aided quantitative classification and diagnostics beyond the visual discernibility of experienced pathologists [11–13], as well as promoting accurate autofocusing techniques for automated whole slide imaging workflows [14, 15]. It remains unanswered, however, whether optical microscopy can be empowered by AI one day to extract and synthesise sufficient information so that humans can be replaced in the decision making process.

Finally, although the use of advanced high-resolution optical techniques for image-guided surgery is still at its infancy, translation from lab to clinic is of great importance for the wider society [16]. In recent years, much effort has been put into evaluating the effectiveness of confocal endoscopes in preclinical and clinical studies to distinguish between healthy and cancerous tissue [17–20]. In 2012, the first in-depth real-time intraoperative endoscopic analysis of histopathological features for common brain tumours was performed [21]. In 2016, the first application of two-photon excitation microscopy for intraoperative procedures in the human brain was also achieved [22]. Combined with fluorescence lifetime imaging, it showed great potential for rapid *in vivo* identification of native glioma tissue on a cellular and subcellular scale. Despite so, many technological and practical challenges still need to be overcome to promote the widespread usage of high-resolution surgical microscopy, such as developing autofocusing functions to keep the surgical site in focus, designing more compact systems to improve surgical mobility, preventing potential contamination, and lowering overall system cost etc. [16].

To solve aforementioned biomedical questions, novel instrumentation needs to be developed with consideration of practical limitations. These include choosing an optimal laser wavelength according to properties of light-tissue interaction, obtaining sufficient image contrast for a higher diagnostic quality, maintaining a suitable power level for minimal photodamage, as well as using a suitable fluorescent dye to label target structures. In particular, the process of fluorescence labelling in the human brain leads to additional risk and complexity, the reason for which label-free imaging is of increasing demand.

In all aspects of biomedical imaging, however, the intrinsic heterogeneous properties of biological tissue itself ultimately limit the extent to which high quality images can be acquired. A glass substrate is commonly used to suppress tilted and unflat surfaces, such as using cranial windows for *in vivo* animal experiments, fixing a cover glass to a specimen slide, and pressing the glass tip of an endoscope against the tissue during surgery. Although these approaches are effective, they can be inconvenient when intervention of the imaging region is required, such as during intraoperative procedures. It is therefore of special interest to find methods that maintain sufficient image quality after abandoning these glass substrates. Besides aberrations arising from the sample interface, those introduced from within the turbid tissue also pose limi-

tations on the depth at which images of appreciable signal-to-noise ratio can be obtained. Here, adaptive optics can be introduced as a technique that holds the potential of addressing the above problems. Finally, the capability to image large fields of view is desirable to increase the throughput of finding diseased cells and tissue structures, the reason for which algorithms that correct for spatially-variant aberrations need to be developed.

Last but not least, rapid image acquisition in three dimensions is especially important for real-time applications. Ideally, this is to be achieved with minimal aberrations throughout the full depth. Moreover, in many clinical applications, the specimen of interest may require continuous autofocusing in order to obtain high contrast and in-focus images while dynamically tracking 3D topographical variations of the sample surface over large lateral regions. The axial scanning technique then needs to be implemented with consideration of these requirements.

1.1 Optical microscopy in biomedical imaging

Due to the diverse scope of biomedical imaging, a broad range of microscope modalities have been developed. For the interest of this thesis, we will only introduce those reported for use in the human brain, the confocal microscope, the two-photon excitation (2PE) microscope, and optical coherence tomography (OCT). Their historical background, imaging principle and setup, unique features, and biomedical applications will be discussed, and comparisons will be made.

1.1.1 Confocal microscopy

Compared to conventional widefield microscopes, the main advantage of the confocal microscope lies in its optical sectioning abilities [23], such that image signal will be confined to a single layer of the specimen without out-of-focus blur. The first confocal scanning microscope was built and patented by Marvin Minsky in the 1950s for the desire of imaging neurological events in unstained preparations of the living brain [24]. Later on, scientists such as Paul Davidovits, Colin Sheppard, Tony Wilson, and Fred Brakenhoff carried out intensive work in the pursuit of developing the device for practical use and to answer biological questions [23, 25–27]. Some of these developments enabled stage translation and computerised control, and led to the first

practical laser scanning confocal microscope developed by John White and William Amos in 1987 [28], which greatly promoted the widespread usage of confocal microscopes in the modern day.

The schematic of a confocal microscope is shown in Figure 1.1(a) in an epi-illumination configuration. Laser light forms a point source after illuminating the first confocal pinhole, and is then scanned over a region of interest within the thick sample. Backscattered or fluorescence light emitting from the focal region is reflected off a beam-splitter and diverted to a second confocal pinhole placed at the conjugate focal plane before reaching the photodetector, which normally comes in the form of a photo-multiplier tube or avalanche photo-diode. Pinholes set in both the illumination and detection path help to block out-of-focus light from either side of the focal plane inside the specimen, which is extremely beneficial for 3D imaging in thick and turbid biological tissues. 2D images at a single depth can be obtained by maintaining a stationary beam while translating the sample stage along the lateral directions, or performing a raster scan of the laser focus as driven by galvanometer or resonant mirrors. Images at different layers of the specimen can then be acquired by axial refocusing for volumetric imaging. Figure 1.1(b) is an image of a single layer of mouse kidney cells acquired using a confocal fluorescence microscope, showing clear structural details with minimal out-of-focus blur.

According to the image contrast mechanism, there are mainly two types of confocal microscopes, the fluorescence mode and the reflectance mode. The former involves a linear excitation process where a fluorescent molecule within the specimen is invoked to a higher energy state by photon absorption before emitting fluorescence at a wavelength longer than that of the excitation (illumination). Fluorescence confocal microscopy has been widely appreciated in clinical settings, both for *ex vivo* imaging of tumour biopsies [29–34] and in vivo during surgical procedures [7, 19, 21, 35–41]. However, the need for fluorescent labelling, especially in humans before operation, greatly adds to the complexity and risk of the workflow.

For the above reason, reflectance confocal microscopy is of special interest due to its intrinsic label-free nature. By using back-scattered illumination light for image formation, contrast originates from differences in the refractive index of different biological components. Its capability for in vivo brain imaging has been validated by observing myelinated axons down to a depth of

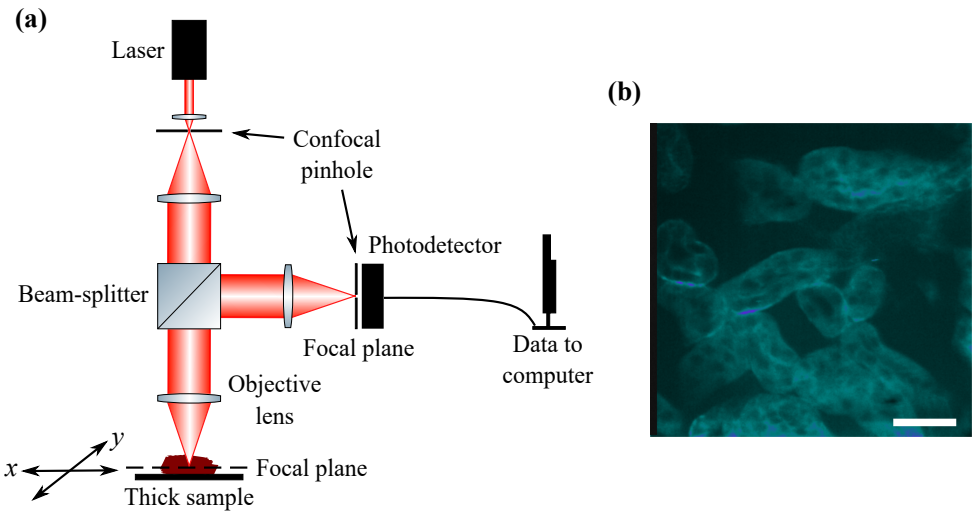


Figure 1.1: Concept of a confocal microscope. (a) Schematic diagram in an epi-illumination configuration. Pinholes set in both the illumination and detection path help to block out-of-focus light from either side of the focal plane inside the specimen. (b) A single layer of mouse kidney cells imaged using a confocal fluorescence microscope showing clear structural details with minimal out-of-focus blur. Scale bar: 10 µm.

400 µm using illumination at 400∼600 nm [42] and the mouse visual cortex down to 1.3 mm at 1700 nm [43]. It has also been successfully implemented for clinical purposes to detect individual cancerous cells both for histological analysis [29–32, 34] and intraoperative guidance [17].

1.1.2 Two-photon excitation microscopy

The first instance of 2PE microscopy was reported by Denk *et al.* in 1990 [44]. It involves a nonlinear excitation process where two low energy photons, typically in the near-infrared (NIR) region, are absorbed simultaneously by a fluorescent molecule to invoke its transition into a higher energy state, before inducing fluorescence in the UV or visible light region, as shown in the Jablonski energy diagram given in Figure 1.2(a).

Compared to single-photon fluorescence microscopy, 2PE provides three major benefits for deep tissue imaging [44–46]. First, it takes advantage of the NIR wavelength, which enjoys better penetration abilities over UV and visible light due to reduced scattering and absorption, later explained in Section 1.2.1. Secondly, 2PE depends on the time-averaged intensity squared and enables confinement of fluorescence generation to within a diffraction-limited focal volume, leading to inherent optical sectioning properties. Photobleaching drops quadratically

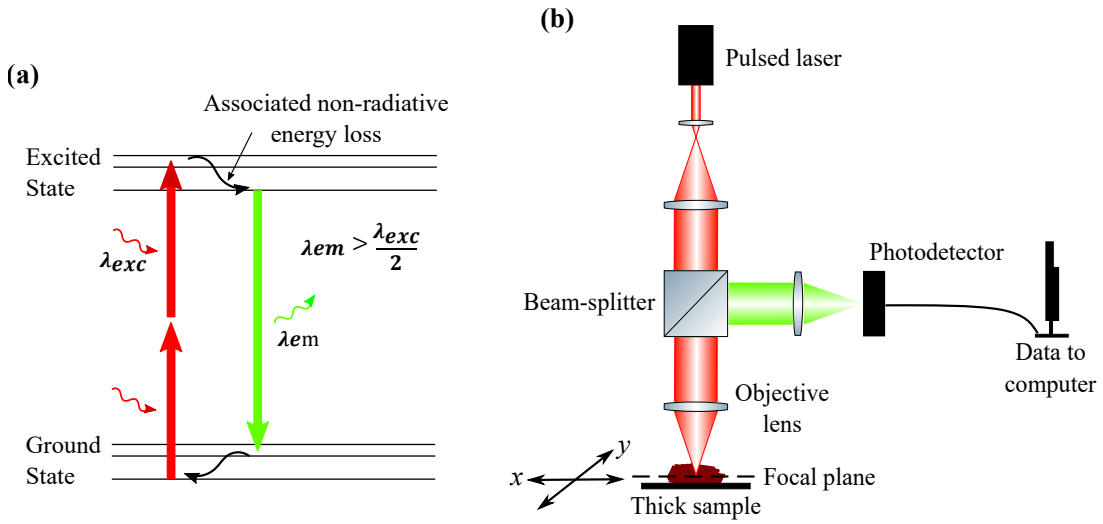


Figure 1.2: Concept of a two-photon excitation microscope. (a) Jablonski energy diagram showing the process involved for two-photon excitation where two low energy photons are absorbed simultaneously by a fluorescent molecule to invoke its transition into a higher energy state before inducing fluorescence. (b) Schematic diagram of a two-photon microscope with confocal pinholes eliminated.

with distance, illustrating a distinct advantage over single-photon excitation, where the entire illumination cone within the specimen is bleached even when only a single plane is imaged. Finally, the localisation of excitation enables all fluorescent photons to constitute useful signal, which can be especially beneficial in highly scattering tissue; whereas in confocal microscopy, fluorophores generated in out-of-focus positions are either blocked by the detection pinhole or contribute to background, in either way leading to signal loss.

Systematic differences between a confocal and 2PE microscope mainly lie in the laser source and detection path [46]. In confocal microscopy, the imaging beam travels back through the same path as the illumination beam, becomes de-scanned by the scan mirrors and arrives at a pinhole before detection to block out-of-focus light. In 2PE microscopy, as all fluorescent photons collected by the objective can be assumed to originate from the focal volume and constitute useful signal, the need for a detection pinhole is eliminated [44], as is shown in Figure 1.2(b). Ideally, a minimum number of optical lenses is preferred to maximize detection efficiency, but in order to reduce the effect of spatial heterogeneities in the photocathode sensitivity and also to collect more fluorescent photons from the scattering tissue, the emission light is focused onto the active

area of the detector by a high power focusing lens [27]. In contrast to continuous wave lasers commonly used for confocal microscopy, a mode-locked femtosecond laser is usually adopted in 2PE microscopy to generate a pulse stream of high instantaneous intensity and temporal concentration required for sufficient fluorescent signal levels.

2PE microscopy is most widely used in neuroscience for deep brain morphological and functional imaging [5, 6, 46, 47]. In clinical settings, it has been used for excitation of autofluorescence [48–52] and 5-aminolevulinic acid (5-ALA) [53] within brain tumour biopsies and the *in vivo* mouse brain, as well as autofluorescence lifetime imaging during human neurosurgical procedures [22, 41]. However, the higher average power required to enable non-linear excitation leads to more severe photobleaching at the focal plane, and the significant cost and size of femtosecond lasers make it difficult to promote 2PE microscopy for general clinical use.

1.1.3 Optical coherence tomography

OCT is a label-free imaging technique based on low-coherence interferometry that was pioneered by Fercher [54], Hitzenberger [55], and Huang [56] in the early 1990s. It typically uses a low-coherence NIR light source that is split into two arms to form a Michelson interferometer, and an interference pattern will only be formed if the difference in optical path length (OPL) between the reference and sample arm is less than the detection bandwidth [57]. According to the domain in which scanning is performed to construct a 2D image, OCT can be divided into Time Domain OCT (TD-OCT) and Fourier Domain OCT (FD-OCT). The former changes the OPL of the reference arm in time to create a depth profile of reflectivity; while the latter takes advantage of wavelength-dependent variations and can be further categorised into Spectral Domain OCT (SD-OCT) or Swept Source OCT (SS-OCT). The former uses a broadband light source and a spectrometer as detector; while the latter uses a narrowband light source that is rapidly tuned over a large optical bandwidth and a balanced detector [57]. The main advantage of FD-OCT over TD-OCT is its high sensitivity and imaging speed.

Application of OCT to brain imaging has allowed *in vitro* and *in vivo* visualisation of individual myelinated fibres [58, 59] and myelinated fibre bundles [60] in the rodent nervous system, as

well as *in vivo* and *ex vivo* volumetric imaging of the cytoarchitecture and myeloarchitecture [61, 62] within rodent brain. In particular, full-field OCT, a high resolution and large field of view (FOV) variation, has differentiated features in normal and tumorous human brain tissue with $1\,\mu m^3$ resolution [63]. However, depth penetration of this technique is highly sensitive to the refractive index mismatch (RIM) between immersion medium and tissue [58]. In general, the lateral resolution of OCT is comparable to that of confocal microscopy, while the axial resolution depends on the spectral properties of either the light source or detector.

1.2 Practical considerations for biomedical imaging

Some practical considerations need to be made when developing optical systems for biomedical purposes, mainly originating from the interactions between light and biological tissue. They can fundamentally affect our choice for both system hardware and software algorithms. In this section, four main considerations are addressed, the influence of laser wavelength, image contrast formation and enhancement, the laser power level, and the choice of fluorophore.

1.2.1 Influence of laser wavelength

For label-free imaging modalities that form the core of this thesis, the illumination wavelength is primarily determined by optical properties of the biological tissue. From this point of view, optical attenuation and phototoxicity are the main aspects of consideration. In fluorescence microscopy, another limiting factor is the excitation wavelength of approved fluorophores, which will be explained more explicitly in Section 1.2.4.

Optical attenuation

The optical attenuation properties of biological tissue are described in terms of the scattering coefficient $\mu_s(\mathrm{cm}^{-1})$, and absorption coefficient $\mu_a(\mathrm{cm}^{-1})$. In 2013, a thorough review by Jacques [64] summarised the wavelength-dependent behaviour of scattering and absorption in various human tissues. When the sample thickness is smaller than the scale of one mean free path (mfp $= 1/\mu_s$), typically $100\,\mu m$ or less, few scattering events occur. Otherwise, multiple

scattering should be considered, and the reduced scattering coefficient $\mu_s^{'}(\mathrm{cm}^{-1})$ should be used. This takes into account the angular scattering of light, i.e., the relative forward versus backward direction of scatter, which is characterised by the anisotropy factor g.

The scattering process is commonly described by two models, the first from particles that are comparable to or larger than the wavelength of light, usually referred to as Mie scattering; and the second from small particles or mass density fluctuations much smaller than the wavelength of light, known as Rayleigh scattering [64]. When evaluating the wavelength dependence of scattering in biological tissues, both models are considered with regard to a reference wavelength of $\lambda_{\mathrm{Ref}} = 500$ nm, and the reduced scattering coefficient $\mu_s^{'}(\lambda)(\mathrm{cm}^{-1})$ can be expressed by

$$\mu_s^{'}(\lambda) = a^{'}\left(f_{\mathrm{Ray}}\left(\frac{\lambda}{\lambda_{\mathrm{Ref}}}\right)^{-4} + (1 - f_{\mathrm{Ray}})\left(\frac{\lambda}{\lambda_{\mathrm{Ref}}}\right)^{-b_{\mathrm{Mie}}}\right), \tag{1.1}$$

where scaling factor $a^{'}$ equals $\mu_s^{'}(\lambda_{\mathrm{Ref}})$, f_{Ray} represents the fraction of Rayleigh scattering, and b_{Mie} is the scattering power of Mie scattering. Eq. (1.1) shows that $\mu_s^{'}(\lambda)(\mathrm{cm}^{-1})$ scales inversely with wavelength, suggesting longer wavelengths to be less affected by scattering effects.

On the other hand, a fraction of light will also be absorbed when travelling through tissue. The absorption coefficient $\mu_a(\mathrm{cm}^{-1})$ is defined as

$$\mu_a = -\frac{1}{T} \cdot \frac{\partial T}{\partial L}, \tag{1.2}$$

where T is the fraction of light transmitted after an incremental pathlength $\partial L\,(\mathrm{cm})$. From Eq. (1.2) it can be solved that light intensity decreases exponentially with the optical pathlength L, such that

$$T = e^{-\mu_a L}. \tag{1.3}$$

In a generic tissue, many chromophores contribute to the absorption of light, including water, blood, fat, melanin etc., and different tissues exhibit distinct optical properties. Figure 1.3 [64] shows how the absorption coefficient μ_a would ideally increase as water, blood, bilirubin, fat and melanin are sequentially added, at the same time predicting an inverse relationship between the absorption coefficient μ_a and wavelength. Together with the reduced scattering coefficient $\mu_s^{'}(\lambda)$, one could conclude that longer wavelengths contribute to a deeper penetration depth.

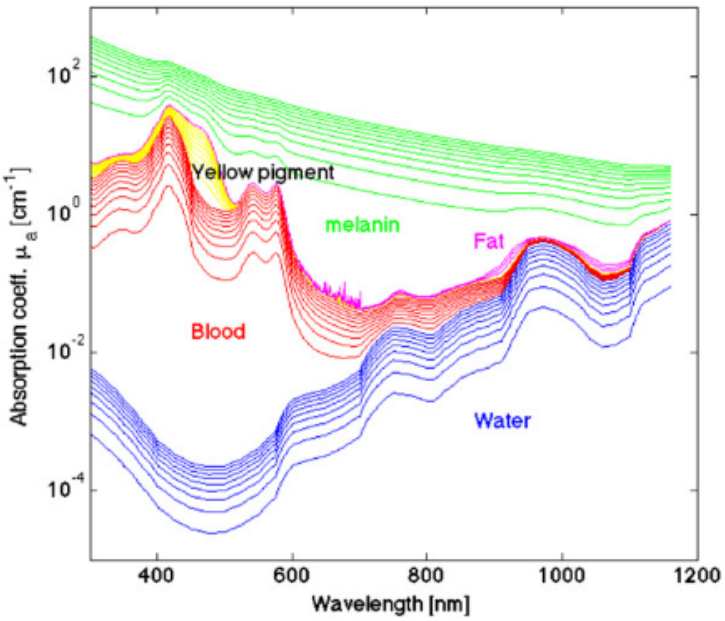


Figure 1.3: Total absorption coefficient $\mu_a(\text{cm}^{-1})$ as water, blood, bilirubin, fat and melanin are sequentially added [64].

However, a more complicated scenario is presented in the brain with water and blood absorption playing a more active role. For preclinical brain imaging and *in vivo* animal experiments, the sample of interest is carefully prepared for optimum imaging conditions eliminating excessive blood, making water absorption and scattering the major sources of attenuation. As can be seen in Figure 1.3, converse to the trend of scattering, water absorption aggravates with increasing wavelength. Studies show that the penetration depth in brain tissue continues to deepen using longer wavelengths [43, 45], with exceptions around 1450 nm, where a strong water absorption peak is present [65].

In clinical settings, operational procedures make blood absorption a more severe factor of light attenuation. Figure 1.3 shows two windows with minimum blood absorption, the first around 700 nm and the second 810 nm. Overall consideration of both scattering and absorption suggests a wavelength in the 770∼850 nm regime for maximum penetration. For reflectance confocal microscopy, without limitations from choice of fluorophore, an 830 nm illumination wavelength is commonly approved [34, 66–68].

Phototoxicity

Light can be absorbed by cellular components and induce alterations in their molecular structures, which is the main cause of phototoxicity [27]. Studies show that this process is especially pronounced in the UV and visible light region, where DNA damage is a factor of prime concern [69]. Direct excitation of DNA, which is responsible for mutagenic and carcinogenic effects, is mainly caused by short-wave UV light; while visible light leads to DNA damage and genotoxic effects through indirect mechanisms due to weak absorption. As cellular absorbers have no efficient NIR transitions, phototoxicity is limited to a minimum in the 700∼1200 nm spectral region. This property is especially beneficial for label-free imaging in the NIR regime (Section 1.2.1) and multi-photon excitation, making NIR wavelengths especially preferable for biomedical imaging.

1.2.2 Image contrast formation and enhancement

The image quality in optical microscopy is much affected by the ratio of signal power to noise power, namely the signal-to-noise ratio (SNR). When the SNR is above 5, image quality is determined by the system modulation transfer function [70]. Below this value, however, as is normally the case in turbid media like brain tissue, it is important to understand the source of image contrast, and find ways to enhance it.

Image contrast is generally understood as how well structures of interest can be differentiated from adjacent background. Only in the presence of appreciable contrast can meaningful information be interpreted. The contrast mechanism varies for different imaging modalities. In fluorescence microscopy, the detectability of fluorescence from a voxel relies on the incident power level, fluorophore brightness (governed again by its concentration, extinction coefficient, and quantum yield [71]), and the effective numerical aperture (NA) of the objective lens [27]. Most importantly, fluorescence contrast is dependent upon the fluorophore localisation, which will be further explained in Section 1.2.4. As for reflectance microscopy, contrast is determined by two factors. The first is scattering, of which the theoretical model in biological tissues was given in Section 1.2.1. This is mainly applicable to structures smaller than or comparable in size to organelles, the affects of which have been simulated in [72] and experimentally validated

in [73]. When the structure is much larger than the wavelength of light and presents a smooth interface, contrast is primarily determined by the magnitude of RIM, and increases with a larger difference [27, 42, 67, 70].

Contrast enhancement can be achieved using either additional hardware components or computational strategies. In terms of the former, efforts have been made to place apertures of different configurations at either the conjugate pupil or image plane [74–76]. Comparison shows that only certain configurations, such as split detection, are able to yield higher contrast; whereas other aperture types, such as annular, filament, and knife-edge apertures, do not make a substantial difference. Split detection, however, requires the use of multiple detectors, which greatly adds to the complexity and cost of the system, ultimately limiting its widespread usage. On the other hand, computational enhancements, such as gamma correction, are easy to implement and will be discussed in Section 7.5.

1.2.3 Power considerations

The laser power incident on the sample should be carefully controlled to prevent both instantaneous and long-term damage. For diagnostic imaging in humans, this is even more important. Photodamage is ultimately dictated by the long-term damage of mutagenicity [77]. Ideally, we would like the laser power to be as low as possible. But in practice, as described previously, this is limited by the image SNR, which depends on amongst others the amount of RIM, the fluorescent probe brightness and the laser dwell time [78]. Both single-photon (SPE) and multi-photon excitation (MPE) can cause photodamage, albeit through different mechanisms.

For SPE, power limits for NIR and visible light are governed by temperature rise and phototoxicity, and absorption occurs at all positions along the beam path [27]. For *in vivo* imaging of the mouse brain, a continuous wave post-objective incident power of 24 mW has been reported for NIR wavelengths [43]. But for preclinical studies in the human brain, most experiments have been carried out using laser powers less than 1 mW [21, 33, 37, 42].

MPE is different in that heating and nonlinear phototoxicity is localised to the focal volume. Outside the focal volume, because the interpulse interval is much shorter than the thermal time

constant, incremental temperature rise during a single pulse is in fact much less appreciable than the steady-state temperature rise under SPE conditions, and relaxation between consecutive pulses makes it even less apt to cause severe heating problems [27]. However, one must note the difference between "excitation power post-objective" and "focused laser power". The former does not take into account the imaging depth and objective NA, and power levels of up to 87 mW have been reported for *in vivo* imaging of the mouse brain at a depth of 700 µm and wavelength of 810 nm [47]. The latter, however, is more defined in the literature, and many studies have shown that an average power of over 2 mW would lead to cell damage using a NIR femtosecond laser [48, 79–81].

1.2.4 Choice of fluorophore

The range of fluorophores approved for *in vivo* imaging of the human brain and other body parts, *in vivo* imaging of the mouse brain, and assessment of biopsies differ substantially, due to the different degrees of fluorophore toxicity. Ideally, one should choose a fluorescent marker consistent with the goal of their research for justified conclusions. However for preliminary experiments, practical requirements are usually to find a dye that is stable enough to give reliable results over time. In cell biology and neuroscience, green fluorescent proteins (GFP), carbocyanines, and the Alexa Fluor family are more widely used. For clinical brain imaging, however, although exogenous markers still dominate the field of fluorescence guided surgery, the efficient use of auto-fluorescence also represents one of the many trends towards label-free imaging [8, 48, 77, 82, 83].

Exogenous fluorophores

Only three fluorescent markers are commonly approved for *in vivo* imaging of the human brain: sodium fluorescein (FNa), indocyanine green (ICG), and 5-aminolevulinic acid (5-ALA) [83]. Many other markers such as acridine orange [10, 18, 30, 33, 34], acriflavine [7, 10, 18, 33], methylene blue [10, 31], cresyl violet [10, 33], and sulforhodamine 101 [33] etc., have been

applied in biopsies and the *in vivo* mouse brain, but not directly in the human brain due to higher levels of toxicity.

Many factors govern the choice of fluorescent dyes for cancer treatment and research. One of prime importance is the fluorophore localisation. The main objective of adopting fluorescent markers is to provide contrast for visualising fine details in the specimen. For brain cancer research, it is ideal that the fluorophore binds to a cellular component and provides enough contrast to enable differentiation between cancerous and healthy tissue at a cellular level. These components may include the membrane, cytoplasm, mitochondria, lysosome, and DNA. In addition, as a change in nuclei morphology is a typical sign of malignancy for certain types of brain cancer, such as glioma, glioblastoma and brain metastasis [7, 21], it would be ideal for the fluorophore to also provide information of the cell nuclei.

Endogenous fluorophores

Biological tissues contain many sub-cellular components that are fluorescent by nature, which allows us to induce fluorescence without application of external agents. The main endogenous fluorophores associated with brain imaging is nicotinamide adenine dinucleotide (NADH) and flavin adenine dinucleotide (FAD) [8]. NADH and FAD fluoresce in their reduced and oxidised states respectively [82] and are both primarily found in the mitochondria with the excitation band of the former being 300∼380 nm and the latter 420∼500 nm [8]. During carcinogenesis, increased cellular metabolism occurs, leading to a drop in FAD production and therefore a decreased redox ratio between [FAD+] and [NADH]. This indicator of cellular metabolic activity is often assessed for its potential in discriminating between normal, precancerous and cancerous tissues by using multi-photon excitation in the NIR spectra, and has led to the first instance of fluorescence lifetime imaging in the human brain [22].

However, there are currently many limitations in using intrinsic fluorophores for *in vivo* cancer diagnostics [8]. First, signal generation relies on the nonlinear process of ultra-short NIR laser pulses due to the reason mentioned in Section 1.2.1 that UV wavelength imaging is associated with increased photodamage and poor tissue penetration. Therefore, the potential negative effects that high peak power and multi-photon processes may bring cannot be ignored.

Second, of all the information that these endogenous labels provide, nuclear details are the most limited, which prevents evaluation of the tumour grade. Finally, the reliability of these fluorophores as a cancer diagnostic tool for *in vivo* animal studies have been witnessed to drop substantially compared to its *ex vivo* counterparts, giving lower resolution and less cellular details [8]. In view of this, it remains unknown the extent to which it will facilitate discrimination between cancerous and healthy cells intraoperatively in human.

1.3 Aberrations and adaptive optics

Section 1.1 described how optical sectioning microscopes led to improved image contrast and benefit 3D imaging. The context of this, however, was that the focal spot at the specimen is diffraction-limited, i.e., its shape and size is determined only by the physics of diffraction for ideal optical components. In practice, disturbances in the beam path can cause different parts of the wavefront to travel differently in media of varying refractive index, introducing distortions to the focal spot and causing it to deviate from its ideal form. These distortions are commonly known as aberrations, the presence of which will lead to a loss in resolution, as well as reduced image intensity and contrast, regardless of the microscope modality.

Adaptive optics (AO) is a technique that can correct for aberrations and restore the image quality [84]. The concept was first introduced in the field of astronomy by Horace W. Babcock in the 1950s [85, 86] to remove wavefront distortions caused by atmospheric turbulence and reach diffraction-limited imaging with large astronomical telescopes. Since then, AO has also been widely adopted in vision science [87, 88], biological microscopy [89–91], and laser processing [92].

The implementation of AO varies slightly for different applications and microscope modalities. However, they all share the same need of applying an equal but opposite phase aberration to an appropriate adaptive device, such as a deformable mirror (DM) or spatial light modulator (SLM) [89]. For confocal microscopy, this device is ideally incorporated in a common illumination and emission path for optimum correction [93]; while for 2PE microscopy, it needs only be placed in the illumination path, as aberrations in the emission path have no effect on resolution or contrast, so long as the detection light reaches the detector [94].

To apply a suitable phase pattern, one needs to have prior knowledge of the distorted wavefront. This can be accomplished in two ways, leading to two large branches of AO. The first method uses a dedicated sensor, such as a Shack-Hartmann wavefront sensor (SHWS) [95], to directly measure the wavefront. This is known as sensor-based AO [96]. The second takes a sequence of image measurements when subjectively applying certain bias phase patterns on the adaptive element to indirectly retrieve the wavefront, commonly referred to as sensorless AO [97]. An image quality metric is usually adopted, such as total intensity or sharpness, to analyse these images and find the optimum aberration correction.

Both sensor-based and sensorless approaches possess unique pros and cons, such that it depends upon the application to choose which is more preferable. In general, the former is more broadly appreciated when the speed of wavefront retrieval and aberration correction is of paramount importance, provided that enough signal reaches the SHWS. By contrast, the latter is easier to implement into existing microscopes and works for highly scattering samples, but can be slow and may not always reach optimal correction [98].

1.4 Axial scanning techniques

3D imaging is of great importance for biomedical purposes to fully appreciate the association between cells and tissue layers. This requires the focal spot to move not only in the lateral direction, but also in the axial to image at different depths within the specimen. Two requirements are generally entailed. First, sufficient speed should be enabled to minimise photodamage and increase imaging throughput. Second, the same spatial resolution should be retained at different imaging depths, i.e., the refocusing technique should not inherently introduce aberrations. In this section, different axial scanning techniques will be discussed and comparisons will be made.

1.4.1 Conventional axial scanning techniques

Nearly all microscopes are equipped with axial scanning functions in the modern day. Most commonly, this is achieved by axial translation of the sample stage or objective lens using piezoelectric actuators. No extra effort is required in terms of either the hardware or software, making

easy integration its most appealing feature. However, the speed at which these heavy components can be translated is much limited by their large inertia to the scale of a few micrometers per millisecond. In cases where low laser power is used to image a thin and static sample, this technique may be sufficient. But for other applications, such as those that require real-time imaging to capture transient signals over large depth ranges or to track moving samples, much faster axial scanning speeds are demanded.

Techniques that control the objective lens for fast axial scanning generally modify the way they are driven in order to steer the beam along a trajectory that maximally samples the features of interest [3], such as oscillating the objective in a sinusoidal pattern [99], or at even higher frequencies that match the resonance frequency of the objective lens [100]. However, these techniques require significant software investments and 3D trajectories need to be carefully designed according to the spatial distribution of biological structures.

Axial refocusing without moving the objective lens can be realised by changing the incident beam divergence using electrically tunable lenses [101], the focal length of which changes with the shape or refractive index, or acousto-optic deflectors [102, 103] that can refocus at rates up to 10 kHz [102]. The drawback, however, is that most microscope systems are equipped with infinity-corrected objective lenses, upon which the incidence of a converging or diverging beam induces aberrations at a few tens of microns away from the natural focal plane [101, 102, 104].

1.4.2 Remote focusing for fast aberration-free focus control

Remote focusing (RF) was thus introduced to avoid slow movements of the sample stage and objective lens during real-time applications while providing the option to compensate for system aberrations introduced by beam divergence to permit high-speed aberration-free focus control [3]. A number of RF techniques have been reported.

The first technique involves constructing a perfect imaging system that obeys the sine condition [105, 106]. By positioning two objective lenses back-to-back and mapping their pupil planes together, spherical aberration can be cancelled out. Axial scanning can then be performed by keeping the objectives stationary and moving a light-weight mirror behind the second objec-

tive lens to change the focusing plane within the sample. As a result, spherical-aberration-free RF was achieved over 200 µm at a rate of 2.7 kHz [107]. While this a superior step towards rapid aberration-free focus control, the technique is highly sensitive to the precision of the optical alignment, and studies show that even a 1% deviation from the theoretical magnification of relay lenses imaging the two objective lens pupil planes can lead to a 50% decrease in the diffraction-limited RF range [108].

Alternatively, a DM or SLM can be used to perform RF and simultaneously compensate for residual aberrations [104, 109–113]. Advantages of using a DM over an SLM first lies in its fast update rate of several kilohertz compared to around 200 Hz for a typical SLM [3]. In addition, commonly used continuous membrane mirrors provide 100% wavefront modulation, while SLMs exhibit lower light efficiency due to the pixelated liquid crystal molecules [113]. SLMs also have high wavelength and polarisation dependency. Although this can be beneficial for certain applications, it can cause problems in a double-pass system, such as a confocal microscope, where the illumination and detection light are either of different wavelengths or polarisation states. However, SLMs accommodate a much larger number of pixels to enable phase wrapping for extended RF ranges [112]. Determination of the RF control signals can be obtained in two ways, either by empirical calibration using AO techniques [110], or predictive calculation from the theory of image formation. The former is useful for correction of system aberrations, but requires an additional SHWS and calibration procedures. The latter is practically more convenient without needing additional hardware, but should take into consideration the objective NA and RIM between different layers of the sample [114]. The final remark is especially important, as the optical model for a low-NA and high-NA lens is noticeably different [106].

1.5 Motivation and structure of thesis

The above sections described how optical microscopy promotes biomedical research with considerations for practical requirements, optical aberrations, and fast focus control. This thesis mainly concerns the development of novel microscopic devices and the investigation of using adaptive optics methods to address outstanding problems in clinical settings. Special focus was

placed on application towards intraoperative brain imaging, for which practical requirements in surgical scenarios, such as device compactness, label-free imaging, and speed and efficiency of algorithms etc., were considered throughout this work.

The design, construction, and development of a compact and contactless reflectance confocal microscope (CCRCM) for neurosurgery forms the core of this project. The device aims to provide label-free image guidance for human brain surgery at a cellular level resolution without direct contact with tissue so as to allow for manipulation of surgical tools. Special design concepts were given to its miniaturisation for additional mobility in the operating theatre.

A major development upon this is a novel autofocusing technique that provides system-aberration-free imaging over an extended defocus range using remote focusing and bi-directional long short term memory network prediction. This was demonstrated in the CCRCM by introducing sensor-based adaptive optics using a DM and SHWS. Real-time autofocusing was enabled for continuous axial movement over a variety of sample types.

Remote focusing was then further discussed in the context of a high-NA system when focusing through refractive-index-mismatched media. A generalised adaptive optics method using QR decomposition was developed to perform independent remote focusing and correction of refractive index mismatch. Two distinct control strategies were introduced and generalisation is provided for multiple interfaces.

The remainder of this thesis is structured as follows. The basics of image formation in optical microscopy is introduced in Chapter 2 from the diffraction theory to image formation in the confocal and 2PE microscope. Chapter 3 discusses the principles of aberrations and adaptive optics using direct wavefront sensing. The design and characterisation of the compact and contactless reflectance confocal microscope (CCRCM) for neurosurgery is demonstrated in Chapter 4. Chapter 5 describes the development of a Python-based closed-loop sensor-based adaptive optics and remote focusing control software that has been made open-source on GitHub. Chapter 6 presents thorough characterisation and calibration results after making hardware modifications to enable sensor-based adaptive optics and remote focusing in the CCRCM. Some post-processing techniques for removing image artefacts and enhancing contrast during real-time image display in the CCRCM is described in Chapter 7. Details of implementing the

extended range aberration-free autofocusing technique in the CCRCM is given in Chapter 8, along with validation results in different sample types and experiments performed for real-time surface tracking of continuous axial motion. The generalised adaptive optics method for high-NA aberration-free refocusing in refractive-index-mismatched media is discussed in Chapter 9. Finally, Chapter 10 describes the development of a multi-purpose adaptive optical microscope, and presents preliminary results of performing multi-conjugate adaptive optics in HeLa cells.

Chapter 2

Image formation in optical microscopy

2.1 Overview

This chapter discusses the theory behind image formation as a consequence of light diffraction and propagation in an optical system. The Huygens-Fresnel principle is first introduced to describe the distribution of light after diffraction within a paraxial region of the optical axis. Next, the lens is considered as a diffractive element, and the field distribution within a paraxial region of the optical axis at the focal plane is evaluated. Here, we will understand the fundamental difference compared to estimations using geometrical optics. The amplitude point spread function is then derived as the result of imaging a point object using a single lens. This is the basis of image formation, as every real object can be considered as the summation of many point objects, and will be discussed in the following section for both coherent and incoherent imaging systems. Finally, we demonstrate how the conclusions obtained in previous sections relate to the formation of images in optical sectioning microscopes introduced in Chapter 1.

2.2 Diffraction theory

Image formation is fundamentally affected by the process of diffraction during light propagation. This can be appreciated by the Huygens-Fresnel principle, which describes how each point on a wavefront can be considered as a point source that emits spherical secondary wavelets of the same frequency, and that the wavefront at positions thereafter could be constructed by taking

the envelope of secondary wavelets [115]. If the complex field distribution at a point (x_1, y_1) in the diffraction plane is denoted by $U_1(x_1, y_1)$, according to the geometry illustrated in Figure 2.1, one can express the complex field distribution $U_2(x_2, y_2)$ at a point (x_2, y_2) in the observation plane as [116],

$$U_2(x_2, y_2) \approx \iint_{-\infty}^{+\infty} \frac{\exp(-jkr)}{j\lambda r} U_1(x_1, y_1)\, \mathrm{d}x_1 \mathrm{d}y_1, \tag{2.1}$$

where $k = \dfrac{2\pi}{\lambda}$ is the wavenumber at wavelength λ, r is the geometrical distance between (x_1, y_1) and (x_2, y_2), and summation is made over the full diffraction field.

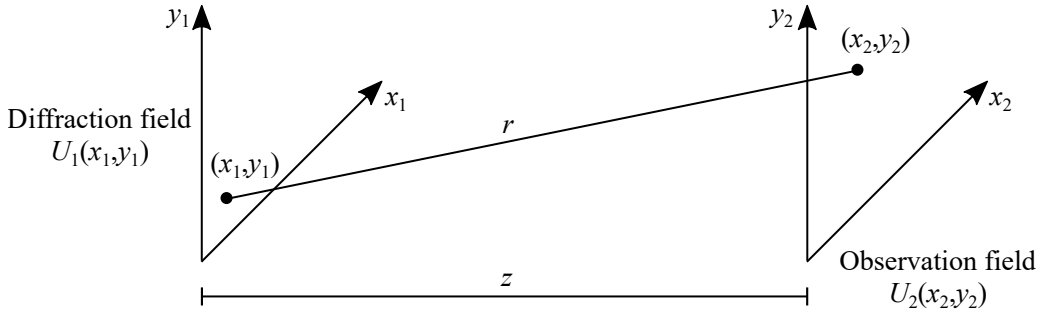


Figure 2.1: The geometry for calculating the complex field distribution at an arbitrary point in the observation plane by taking the envelope of all secondary wavelets in the diffraction field according to Huygens-Fresnel principle.

Considering only the forward propagating light field within a paraxial region of the optical axis, if z represents the distance between the diffraction and observation plane, then the assumption of $\sqrt{(x_2 - x_1)^2 + (y_2 - y_1)^2} \ll z$ can be made, and r can be approximated using binomial expansion $\sqrt{1 + x} \approx 1 + \dfrac{x}{2}$,

$$r = \sqrt{z^2 + (x_2 - x_1)^2 + (y_2 - y_1)^2} \approx z \left[1 + \frac{(x_2 - x_1)^2 + (y_2 - y_1)^2}{2z^2}\right]. \tag{2.2}$$

By substituting Eq. (2.2) into Eq. (2.1), one can derive the Fresnel diffraction integral,

$$\begin{aligned} U_2(x_2, y_2) = & \frac{\exp(-jkz)}{j\lambda z} \iint_{-\infty}^{+\infty} U_1(x_1, y_1) \\ & \exp\left\{-\frac{jk}{2z}\left[(x_2 - x_1)^2 + (y_2 - y_1)^2\right]\right\} \mathrm{d}x_1 \mathrm{d}y_1, \end{aligned} \tag{2.3}$$

which describes the near-field distribution of light under the paraxial approximation.

Further analysis can be made for the far-field distribution by assuming that,

$$z \gg \frac{k\left({x_1}^2 + {y_1}^2\right)}{2}. \tag{2.4}$$

In such case, the term $\exp\left[-\frac{jk}{2z}\left({x_1}^2 + {y_1}^2\right)\right]$ in Eq. (2.3) integrates to unity over the diffraction field, and can be neglected to yield the Fraunhofer diffraction integral,

$$\begin{aligned} U_2\left(x_2, y_2\right) = & \frac{\exp\left(-jkz\right)}{j\lambda z} \exp\left[-\frac{jk}{2z}\left({x_2}^2 + {y_2}^2\right)\right] \\ & \iint_{-\infty}^{+\infty} U_1\left(x_1, y_1\right) \exp\left[\frac{jk}{z}\left(x_1 x_2 + y_1 y_2\right)\right] \mathrm{d}x_1 \mathrm{d}y_1. \end{aligned} \tag{2.5}$$

2.3 Diffraction of a thin lens

This section discusses the phenomenon of how a lens affects the propagation of light under the diffraction theory. This can be understood by considering the lens as a diffractive element, and the optical field immediately after the lens as a diffraction field $U_1\left(x_1, y_1\right)$, similarly to that described in Section 2.2. We are then interested in evaluating the distribution of light within the paraxial region of the optical axis at the focal plane $U_2\left(x_2, y_2\right)$. Note that here we only discuss the case of using a low NA lens, such that the focusing angle is small enough for the paraxial approximation to hold.

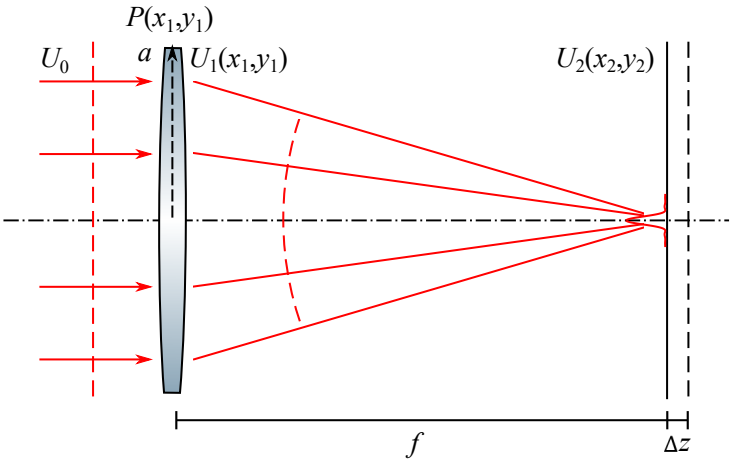


Figure 2.2: The geometry for calculating the complex field distribution within the paraxial region of the optical axis at the focal plane of a thin lens.

As illustrated in Figure 2.2, assume that a planar wavefront U_0 is incident upon a thin lens, such that rays meet both faces of the lens at approximately the same lateral coordinates (x_1, y_1). As the lens varies in thickness, the phase delay it introduces to the propagating wavefront will vary accordingly. In the case of a thin convex lens, the wavefront will encounter larger phase delays towards the centre and a spherical wave will emerge from the lens. This property can be described as the complex transmittance function $t(x_1, y_1)$ by,

$$t(x_1, y_1) = P(x_1, y_1) \exp\left[\frac{jk}{2f}\left(x_1^2 + y_1^2\right)\right], \tag{2.6}$$

where f is the focal length of the thin lens, $P(x_1, y_1)$ is a complex pupil function that takes into account the amplitude change of the light field, and the quadratic phase factor describes the transformation to a spherical wavefront. By multiplying the incident field with the complex transmittance function, one can obtain the diffraction field $U_1(x_1, y_1)$,

$$U_1(x_1, y_1) = U_0 P(x_1, y_1) \exp\left[\frac{jk}{2f}\left({x_1}^2 + {y_1}^2\right)\right], \tag{2.7}$$

which is then used to generate the optical field at an arbitrary distance z away from the thin lens. Substitution of Eq. (2.7) into the Fresnel diffraction integral Eq. (2.3) yields,

$$\begin{aligned} U_2(x_2, y_2) = & \frac{\exp(-jkz)}{j\lambda z} \iint_{-\infty}^{+\infty} P(x_1, y_1) \exp\left[\frac{jk}{2f}\left({x_1}^2 + {y_1}^2\right)\right] \\ & \exp\left\{-\frac{jk}{2z}\left[(x_2 - x_1)^2 + (y_2 - y_1)^2\right]\right\} \mathrm{d}x_1 \mathrm{d}y_1, \end{aligned} \tag{2.8}$$

where U_0 is set to unity without loss of generality.

Eq. (2.8) now allows us to evaluate the field distribution at positions within close proximity of the focal plane $z = f + \Delta z$. First expand Eq. (2.8) by,

$$\begin{aligned} U_2(x_2, y_2) = & \frac{\exp(-jkz)}{j\lambda z} \exp\left[-\frac{jk}{2z}\left({x_2}^2 + {y_2}^2\right)\right] \iint_{-\infty}^{+\infty} P(x_1, y_1) \exp\left[\frac{jk}{2f}\left({x_1}^2 + {y_1}^2\right)\right] \\ & \exp\left[-\frac{jk}{2z}\left({x_1}^2 + {y_1}^2\right)\right] \exp\left[\frac{jk}{z}\left(x_1 x_2 + y_1 y_2\right)\right] \mathrm{d}x_1 \mathrm{d}y_1. \end{aligned} \tag{2.9}$$

When $z = f$, the terms in x_1^2 and y_1^2 are seen to cancel such that,

$$U_2(x_2, y_2) \propto \iint_{-\infty}^{+\infty} P(x_1, y_1) \exp\left[\frac{jk}{f}\left(x_1 x_2 + y_1 y_2\right)\right] \mathrm{d}x_1 \mathrm{d}y_1, \tag{2.10}$$

which is just the Fourier transform of the complex pupil function. For the common case of using a rotationally symmetric lens, Eq. (2.9) can be simplified via polar coordinates, such that $r_1 = \sqrt{{x_1}^2 + {y_1}^2}$, $r_2 = \sqrt{{x_2}^2 + {y_2}^2}$, and $P(x_1, y_1) = P(r_1)$. Eq. (2.9) can then be rewritten as,

$$\begin{aligned} U_2(r_2) =& \frac{\exp(-jkz)}{j\lambda z} \exp\left(-\frac{j\pi r_2^2}{\lambda z}\right) \\ & \int_0^{+\infty} P(r_1) \exp\left[\frac{j\pi r_1^2}{\lambda}\left(\frac{1}{f} - \frac{1}{z}\right)\right] J_0\left(\frac{2\pi r_1 r_2}{\lambda z}\right) 2\pi r_1 \mathrm{d}r_1, \end{aligned} \tag{2.11}$$

where J_0 is a Bessel function of the first kind of order zero that is expressed by,

$$J_0(x) = \frac{1}{2\pi} \int_0^{2\pi} exp(jx\cos\phi)\,\mathrm{d}\phi. \tag{2.12}$$

Since we are only interested in a small region about the focal plane, assume $\Delta z \ll f$ such that $1/z \approx 1/f - \Delta z/f^2$ holds, and one can define the following parameters for a uniform circular lens of radius a [117],

$$\begin{cases} \nu \approx \dfrac{2\pi a r_2}{\lambda f} & \text{radial optical coordinate,} \\ u = \dfrac{2\pi a^2}{\lambda}\left(\dfrac{1}{f} - \dfrac{1}{z}\right) \approx \dfrac{2\pi \Delta z}{\lambda}\left(\dfrac{a}{f}\right)^2 & \text{axial optical coordinate,} \\ N = \dfrac{a^2}{\lambda f} & \text{Fresnel number,} \\ \rho = \dfrac{r_1}{a} & \text{normalised radial coordinate.} \end{cases} \tag{2.13}$$

The 3D diffraction field within near proximity of the focal plane can now be obtained given an evenly illuminated circular aperture $P(a\rho)$ that is unity within and zero outside,

$$U_2(\nu, u) = j2\pi N \exp(-jkf) \exp\left(-\frac{j\nu^2}{4N\pi}\right) \int_0^1 \exp\left(\frac{ju\rho^2}{2}\right) J_0(\nu\rho)\,\rho \mathrm{d}\rho. \tag{2.14}$$

When $u = 0$, from Eq. (2.14) we can obtain the field distribution within the focal plane,

$$U_2(\nu) = j\pi N \exp(-jkf) \exp\left(-\frac{j\nu^2}{4N\pi}\right) \left[\frac{2J_1(\nu)}{\nu}\right], \tag{2.15}$$

where J_1 is a Bessel function of the first kind of order unity. To further evaluate the intensity distribution, the modulus squared of Eq. (2.15) can be taken to yield,

$$I(\nu) = |U_2(\nu)|^2 = (\pi N)^2 \left[\frac{2J_1(\nu)}{\nu}\right]^2. \tag{2.16}$$

And when $\nu = 0$, the intensity distribution along the optical axis can be obtained from Eq. (2.14),

$$I(u) = |U_2(\nu = 0, u)|^2 = (\pi N)^2 \left[\frac{\sin(u/4)}{u/4}\right]^2. \tag{2.17}$$

Eq. (2.16) and Eq. (2.17) clearly show that under the diffraction theory, light focused by a lens does not converge to an infinitely small point, as estimated using geometrical optics, but varies in intensity within a finite region of the optical axis at the focal plane. Figure 2.3(a) gives the 2D intensity distribution within the focal plane, showing a circular Airy diffraction pattern with a central bright disk (also known as Airy disk) surrounded by weaker concentric rings; and Figure 2.3(b) depicts that for the $u\nu$-plane with distinct side-lobes. Figures 2.3(c) and (d) take the normalised intensity plot along the radial direction and optical axis, respectively, and suggests that light is more dispersed in the axial direction compared to its radial counterpart.

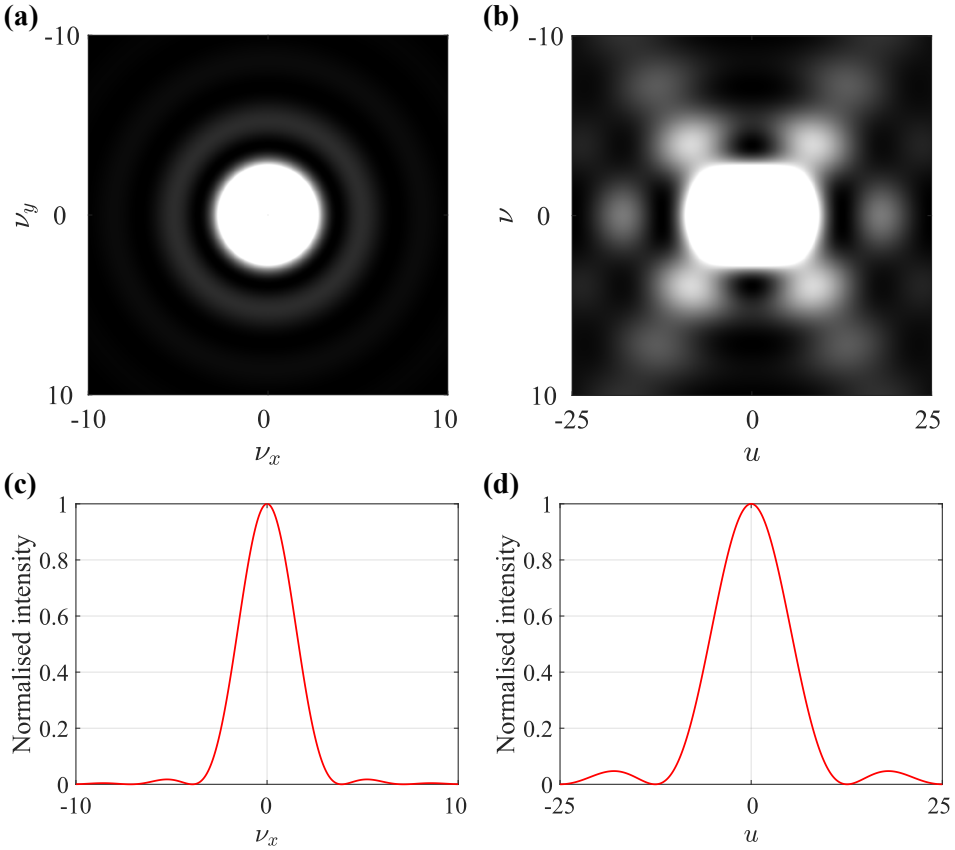


Figure 2.3: Intensity distribution within a finite region of the optical axis at the focal plane (home-made). 2D profile plots in the (a) focal plane and (b) $u\nu$-plane show an Airy pattern with distinct side-lobes. The central lobe is saturated to show outer side-lobes. Normalised intensity plots along the (c) radial direction and (d) optical axis are also given.

The results above fundamentally explain why there is a limit to the resolution of conventional widefield microscopes, i.e., only objects above a certain dimension can be resolved. The lateral and axial resolution are determined by the diameter of the first minima $d_{lateral,widefield}$ and $d_{axial,widefield}$ in the normalised intensity plots given in Figures 2.3(c) and (d), and can be expressed by the Rayleigh criterion as [27],

$$d_{\text{lateral,widefield}} = \frac{1.22\lambda}{\text{NA}}, \tag{2.18}$$

$$d_{\text{axial,widefield}} = \frac{4\lambda n}{\text{NA}^2}, \tag{2.19}$$

where λ is the illumination wavelength, n is the refractive index of the objective medium, and NA is the numerical aperture of the objective lens.

2.4 The amplitude point spread function

The previous section discussed how a thin lens diffracts light such that the optical field at the focal plane is not a geometrically defined point, but a finite distribution. In this section, we will look into the process of image formation via a single lens, i.e., how an object is imaged by a thin lens. The geometry in Figure 2.4 will be used for reference.

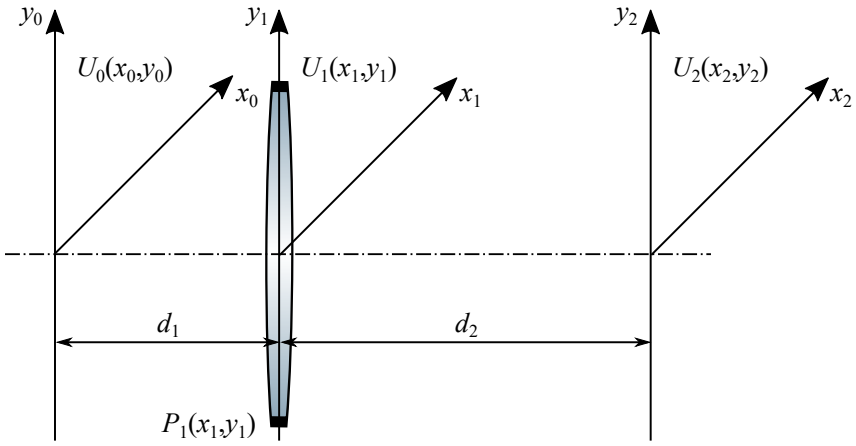


Figure 2.4: The coordinate system for analysing image formation via a single lens. $U_0(x_0, y_0)$ describes the optical field immediately after the object, $U_1(x_1, y_1)$ describes that immediately after a lens placed at a distance d_1 away from the object, $U_2(x_2, y_2)$ describes the field distribution at the image plane.

In the case that an object at plane (x_0, y_0) is illuminated by a uniform planar wavefront, the optical field immediately after the object can be denoted as $U_0(x_0, y_0) = o(x_0, y_0)$, also known as the object function. Then according to the Fresnel diffraction formula derived in Eq. (2.3), the field before the lens at a distance d_1 away from the object plane can be expressed as,

$$\begin{aligned} U_1(x_1, y_1) =& \frac{\exp(-jkd_1)}{j\lambda d_1} \iint_{-\infty}^{+\infty} U_0(x_0, y_0) \\ & \exp\left\{-\frac{jk}{2d_1}\left[(x_1 - x_0)^2 + (y_1 - y_0)^2\right]\right\} \mathrm{d}x_0 \mathrm{d}y_0, \end{aligned} \tag{2.20}$$

Considering the complex transmittance function given in Eq. (2.6), the optical field immediately after the lens can be obtained by,

$$\begin{aligned} U_1'(x_1, y_1) =& \frac{\exp(-jkd_1)}{j\lambda d_1} P(x_1, y_1) \exp\left[\frac{jk}{2f}\left({x_1}^2 + {y_1}^2\right)\right] \\ & \iint_{-\infty}^{+\infty} U_0(x_0, y_0) \exp\left\{-\frac{jk}{2d_1}\left[(x_1 - x_0)^2 + (y_1 - y_0)^2\right]\right\} \mathrm{d}x_0 \mathrm{d}y_0, \end{aligned} \tag{2.21}$$

One can now examine the optical field at a distance d_2 away from the lens, which we define as our image plane (x_2, y_2), by applying the Fresnel diffraction formula a second time,

$$\begin{aligned} U_2(x_2, y_2) =& \frac{\exp[-jk(d_1 + d_2)]}{\lambda^2 d_1 d_2} \iiiint_{-\infty}^{+\infty} P(x_1, y_1) U_0(x_0, y_0) \\ & \exp\left[\frac{jk}{2f}\left({x_1}^2 + {y_1}^2\right)\right] \exp\left\{-\frac{jk}{2d_1}\left[(x_1 - x_0)^2 + (y_1 - y_0)^2\right]\right\} \\ & \exp\left\{-\frac{jk}{2d_2}\left[(x_2 - x_1)^2 + (y_2 - y_1)^2\right]\right\} \mathrm{d}x_0 \mathrm{d}y_0 \mathrm{d}x_1 \mathrm{d}y_1, \end{aligned} \tag{2.22}$$

Assuming that distances d_1 and d_2 satisfy the lens law formula,

$$\frac{1}{f} = \frac{1}{d_1} + \frac{1}{d_2}, \tag{2.23}$$

if we introduce a magnification factor $M = d_1/d_2$, and define a function $h(x, y)$ which is the 2D Fourier transform of the pupil function $P(x_1, y_1)$ at spatial frequencies $m = x/\lambda d_1$ and $n = y/\lambda d_1$ [117], as introduced in Eq. (2.10),

$$h(x, y) = \iint_{-\infty}^{+\infty} P(x_1, y_1) \exp\left[\frac{jk}{d_1}(x_1 x + y_1 y)\right] \mathrm{d}x_1 \mathrm{d}y_1, \tag{2.24}$$

the image field described in Eq. (2.22) can be rewritten as,

$$\begin{aligned} U_2(x_2,y_2) =& \frac{M\exp\left[-jkd_1\left(1+1/M\right)\right]}{\lambda^2{d_1}^2}\exp\left[-\frac{jkM}{2d_1}\left({x_2}^2+y_2^2\right)\right]\iint_{-\infty}^{+\infty}U_0(x_0,y_0) \\ & \exp\left[-\frac{jk}{2d_1}\left({x_0}^2+{y_0}^2\right)\right]h(x_0+Mx_2,y_0+My_2)\,\mathrm{d}x_0\mathrm{d}y_0. \end{aligned} \tag{2.25}$$

In the ideal case of the object being a point source that takes the form of a delta function in both dimensions, then $U_0(x_0,y_0)=o(x_0,y_0)=\delta(x_0,y_0)$, and Eq. (2.25) becomes,

$$U_2(x_2,y_2)=\frac{M\exp\left[-jkd_1\left(1+1/M\right)\right]}{\lambda^2{d_1}^2}\exp\left[-\frac{jkM}{2d_1}\left({x_2}^2+y_2^2\right)\right]h(Mx_2,My_2). \tag{2.26}$$

Here, we see that the term $h(x,y)$ contains the complex amplitude of the optical field for the image of a point object. We therefore call $h(x,y)$ the 2D amplitude point spread function (APSF) of the optical system, which also describes its inherent imaging properties.

Now assume that distances d_1 and d_2 don't satisfy the lens law formula, and let

$$\frac{1}{f}-\frac{1}{d_1}-\frac{1}{d_2}=\frac{1}{\Delta d}. \tag{2.27}$$

We can introduce a defocused pupil function,

$$P'(x_1,y_1)=P(x_1,y_1)\exp\left[\frac{jk}{2\Delta d}\left({x_1}^2+{y_1}^2\right)\right], \tag{2.28}$$

such that the defocused APSF, now also referred to as the 3D APSF, can be expressed by,

$$h'(x,y)=\iint_{-\infty}^{+\infty}P(x_1,y_1)\exp\left[\frac{jk}{2\Delta d}\left({x_1}^2+{y_1}^2\right)\right]\exp\left[\frac{jk}{d_1}\left(x_1x+y_1y\right)\right]\mathrm{d}x_1\mathrm{d}y_1. \tag{2.29}$$

Again, if we consider a rotationally symmetric lens, polar coordinates can be introduced such that $r_1=\sqrt{{x_1}^2+{y_1}^2}$ and $P(x_1,y_1)=P(r_1)$. Eq. (2.29) can then be reduced to,

$$h'(x,y)=\int_0^{+\infty}P(r_1)\exp\left(\frac{jk{r_1}^2}{2\Delta d}\right)J_0\left(\frac{2\pi r_1 r}{\lambda d_1}\right)2\pi r_1\mathrm{d}r_1. \tag{2.30}$$

For a uniform circular lens of radius a, parameters similar to Eq. (2.13) can be defined [117],

$$\begin{cases} \nu\approx\dfrac{2\pi ar}{\lambda d_1} & \text{radial optical coordinate,} \\ u=\dfrac{2\pi a^2}{\lambda}\left(\dfrac{1}{f}-\dfrac{1}{d_1}-\dfrac{1}{d_2}\right)\approx\dfrac{2\pi a^2}{\lambda\Delta d} & \text{axial optical coordinate,} \\ \rho=\dfrac{r_1}{a} & \text{normalised radial coordinate,} \end{cases} \tag{2.31}$$

thus Eq. (2.30) will obtain the final form of,

$$h^{'}(\nu, u) = \int_0^1 P(\rho) \exp\left(\frac{ju\rho^2}{2}\right) J_0(\nu\rho)\, 2\pi\rho \mathrm{d}\rho. \tag{2.32}$$

If we let $u = 0$, then the 2D APSF for a circular lens of finite aperture can be derived as,

$$h(\nu) = \pi \left[\frac{2J_0(\nu)}{\nu}\right]. \tag{2.33}$$

2.5 Coherent and incoherent image formation

In the previous section, we looked into the image formation process of a single lens, and derived the 2D APSF for the special case of imaging a point object. In this section, we will continue to investigate how an image is formed for a general object emitting either coherent or incoherent light. Ideally, the 2D APSF in Eq. (2.24) should retain point-like properties of the object. This implies that variables x and y should be small. In such case, we can assume that $x_0 + Mx_2 \approx 0$ and $y_0 + My_2 \approx 0$ in Eq. (2.25). Consider also that for a point object the exponential term $\exp\left[-\frac{jk}{2d_1}\left({x_0}^2 + {y_0}^2\right)\right]$ integrates to unity, then the following relationship can be observed,

$$U_2(x_2, y_2) \propto \iint_{-\infty}^{+\infty} U_0(x_0, y_0)\, h(x_0 + Mx_2, y_0 + My_2)\, \mathrm{d}x_0 \mathrm{d}y_0. \tag{2.34}$$

The expression above superimposes the amplitude image of each point [23], indicating a coherency in the light emanating from the object. The image field can therefore be described by the 2D convolution of the object function with the 2D APSF of the optical system. We refer to this as coherent imaging, where the amplitude response of the optical system determines the image formation process. A typical example is when a narrow bandwidth laser is used for reflectance confocal imaging. In this case, the image field can be simply denoted by,

$$U_2 \propto U_0 \otimes h, \tag{2.35}$$

where $\otimes$ is the convolution operator. The image intensity can thus be obtained by taking the modulus squared of the image field,

$$I_2 \propto |U_0 \otimes h|^2. \tag{2.36}$$

In the case that there is no correlation in phase between the light field emitted from each point of the object, such as imaging with fluorescence signal, the image is formed solely by adding the intensity response of each object point. This process is known as incoherent imaging. The image intensity can be expressed by,

$$I_2(x_2, y_2) \propto \iint_{-\infty}^{+\infty} U_0(x_0, y_0)\, h(x_0 + Mx_2, y_0 + My_2)^2 \,\mathrm{d}x_0 \mathrm{d}y_0, \tag{2.37}$$

which is the 2D convolution of the object function with the 2D intensity point spread function (IPSF) of the incoherent optical system, and can be further simplified to give,

$$I_2 \propto U_0 \otimes h^2. \tag{2.38}$$

2.6 Image formation in optical sectioning microscopes

In Section 1.1.1 and Section 1.1.2, we introduced the principle and optical setup of the confocal and two-photon excitation (2PE) microscope. In this section, we will discuss the mathematical representation of their image formation processes using conclusions obtained in the previous section for a general thin object in both coherent and incoherent imaging systems.

2.6.1 The confocal microscope

Both backscattered and fluorescence light can constitute useful signal in a confocal microscope. The former corresponds to coherent image formation, commonly known as reflectance mode, where the detection wavelength λ_{det} is equal to that of the illumination λ_{ill}. Due to Stokes shift, $\lambda_{\mathrm{det}} > \lambda_{\mathrm{ill}}$ holds in the latter case, and incoherent fluorescence imaging takes place. Figure 2.5 depicts the typical image formation process for both the reflectance (Figure 2.5(a)), and fluorescence (Figure 2.5(b)) confocal microscope in a epi-illumination configuration.

The laser first illuminates a confocal pinhole to create a point source in the illumination path, which is imaged onto the objective focal plane within a thick sample of object function $o(x_1, y_1)$. This image is also known as the illumination point spread function, denoted by h_{ill}. For reflectance mode imaging, the emission field $U_1(x_1, y_1)$ immediately after interaction

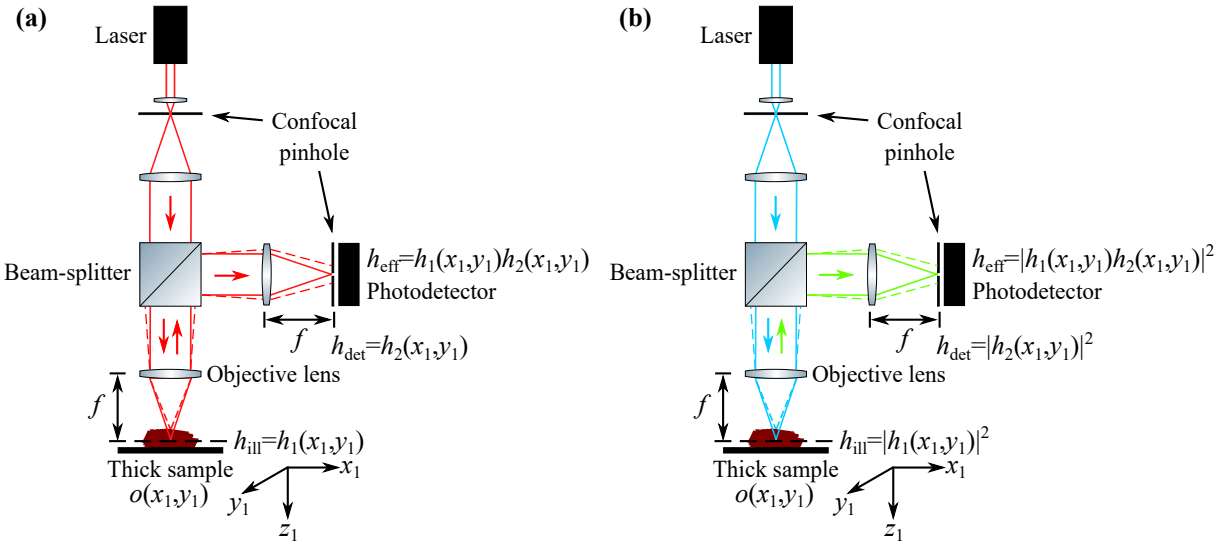


Figure 2.5: Image formation in confocal microscopes for (a) reflectance imaging, and (b) fluorescence imaging.

with sample structures preserves the coherence of h_{ill}, similarly to a coherent imaging system discussed in Section 2.5. The APSF thus determines the generation of image signal, such that $h_{\text{ill}} = h_1(x_1, y_1)$. Now consider the sample reflectivity function $o\,(x_1 - x_s, y_1 - y_s)$, where (x_s, y_s) represents the current scan position, and $U_1(x_1, y_1)$ can be expressed as,

$$U_1(x_1, y_1) \propto h_1(x_1, y_1) o\,(x_1 - x_s, y_1 - y_s)\,, \tag{2.39}$$

By contrast, in fluorescence mode this coherent nature is destroyed when molecules fluoresce spontaneously and act as new point sources. Fluorescence excitation is proportional to the focal intensity, which results in a relationship of $h_{\text{ill}} = |h_1(x_1, y_1)|^2$. If $o\,(x_1 - x_s, y_1 - y_s)$ now represents the density of fluorescent molecules at sample point (x_1, y_1), the intensity distribution immediately after illumination can be derived as,

$$I_1(x_1, y_1) \propto |h_1(x_1, y_1)|^2 o\,(x_1 - x_s, y_1 - y_s)\,. \tag{2.40}$$

Upon image detection, signal light is first diverted to a second pinhole at the image plane (x_2, y_2) by a beam-splitter before reaching the photodetector. As this is in a descanned position, i.e., the lateral location of image points is fixed regardless of the raster scan taking place in the sample plane, each point in the sample forms an image at (x_2, y_2), and the detection pinhole

rejects background light from out-of-focus positions inside the sample. Assuming system magnification between (x_1, y_1) and (x_2, y_2) is unity for simplicity, the detection point spread function h_{det} can be expressed as $h_{\text{det}} = h_2(x_2 - x_1, y_2 - y_1)$ and $h_{\text{det}} = |h_2(x_2 - x_1, y_2 - y_1)|^2$ in reflectance and fluorescence mode, respectively. The effective point spread function at the photodetector h_{eff} can then be obtained by multiplying h_{ill} and h_{det}, which yields the image field distribution of a single sample point in a reflectance confocal microscope,

$$U_2(x_2, y_2) \propto h_1(x_1, y_1) o\,(x_1 - x_s, y_1 - y_s)\, h_2(x_2 - x_1, y_2 - y_1). \tag{2.41}$$

The final field distribution can then be expressed as the summation of all sample points,

$$U_2(x_2, y_2) \propto \iint_{-\infty}^{+\infty} h_1(x_1, y_1) o\,(x_1 - x_s, y_1 - y_s)\, h_2(x_2 - x_1, y_2 - y_1) \mathrm{d}x_1 \mathrm{d}y_1. \tag{2.42}$$

As $\lambda_{\text{ill}} = \lambda_{\text{det}}$ in reflectance imaging, if we also assume the illumination and detection path to be similar such that $h_1(x_1, y_1) = h_2(x_2 - x_1, y_2 - y_1) = h$, Eq. (2.42) can be simplified using the convolution operand,

$$U_2 \propto h^2 \otimes o. \tag{2.43}$$

Taking the modulus squared thus gives the final intensity distribution for reflectance imaging,

$$I_2 \propto |h^2 \otimes o|^2. \tag{2.44}$$

In the case of fluorescence imaging, the image intensity distribution of a single sample point is,

$$I_2(x_2, y_2) \propto |h_1(x_1, y_1)|^2 o\,(x_1 - x_s, y_1 - y_s)\, |h_2(x_2 - x_1, y_2 - y_1)|^2, \tag{2.45}$$

and summation over all points in the sample gives the final image intensity distribution,

$$I_2(x_2, y_2) \propto \iint_{-\infty}^{+\infty} |h_1(x_1, y_1)|^2 o\,(x_1 - x_s, y_1 - y_s)\, |h_2(x_2 - x_1, y_2 - y_1)|^2 \mathrm{d}x_1 \mathrm{d}y_1. \tag{2.46}$$

Considering a small Stokes shift such that we can make the approximation of $\lambda_{\text{ill}} \approx \lambda_{\text{det}}$, Eq. (2.46) can be rewritten as,

$$I_2 \propto |h|^4 \otimes o. \tag{2.47}$$

It is worth mentioning that when using a single-mode fibre for coupling of incident (emission) light, the fibre itself can be considered as the illumination (detection) pinhole.

In Section 2.3, the lateral and axial resolution of a conventional widefield microscope was given in terms of the Airy diffraction pattern. For confocal microscopes, as the illumination and detection pinholes further restrict collection of light to the focus centre, they lead to a squared PSF of tighter confinement that can be given as [27, 118],

$$d_{\text{lateral,confocal}} = \frac{0.8\lambda}{\text{NA}}, \tag{2.48}$$

$$d_{\text{axial,confocal}} = \frac{2.8\lambda n}{\text{NA}^2}, \tag{2.49}$$

Note that the above equations strictly correspond to approximations within the paraxial region of the optical axis (very low NA) and slight deviations occur with high-NA lenses, especially when calculating axial resolution.

Thus one can observe the importance of choosing an optimum pinhole size in order to take full advantage of confocal imaging. A pinhole diameter of 0.7∼1.5 Airy units is often adopted [27, 119] in consideration of the trade-off between optical sectioning and signal level. In practice, the detection Airy unit is often calculated as

$$\text{AU} = \frac{1.22\lambda f_{\text{det}}}{d_{\text{det}}}, \tag{2.50}$$

where f_{det} is the focal length of the focusing lens in front of the detector and d_{det} is the detection beam diameter. However, one must note the preservation of coherence in the detection signal when using reflectance confocal microscopy. As phase information is not lost at the detection pinhole, it can lead to speckle noise which comes from multiply scattered light, and is especially noticeable when imaging in turbid media. It is shown in [120] that the choice of a suitable detection pinhole size of $3 \sim 5$ Airy units can help maintain adequate optical sectioning while reducing the effect of speckle noise, resulting in images with improved contrast.

2.6.2 The two-photon excitation microscope

As outlined in Section 1.1.2, the principle of a 2PE microscope involves a nonlinear process where two low energy photons are absorbed simultaneously by a fluorescent molecule to emit fluorescence at a wavelength longer than half the excitation, i.e., $\lambda_{\text{det}} > \frac{1}{2}\lambda_{\text{ill}}$. As such, the fluorescence excitation is proportional to the focal intensity squared, and the illumination point

spread function can be expressed as $h_{\text{ill}} = |h_1(x_1, y_1)|^4$, which is illustrated in Figure 2.6. Due to second order nonlinear excitation being much less likely to occur, it will only be confined to regions of the focal spot with sufficient energy levels. Therefore, 2PE microscopes possess inherent optical sectioning properties and the need for pinholes to obstruct out-of-focus light is eliminated. The effective point spread function h_{eff} is then equivalent to h_{ill}, and the final image intensity distribution can be obtained as,

$$I_2 \propto |h|^4 \otimes o. \tag{2.51}$$

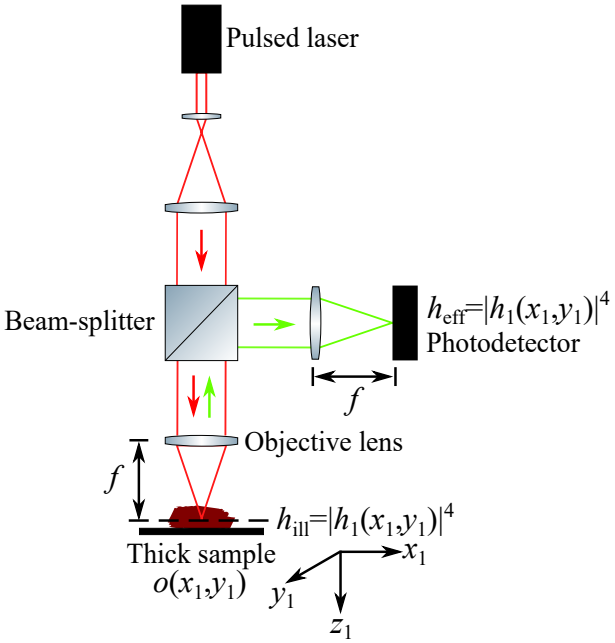


Figure 2.6: Image formation in a two-photon excitation microscope.

It could be seen from Equations 2.44, 2.47, and 2.51 that the final image intensity of all three imaging modalities discussed in this section is proportional to $|h|^4$, suggesting that if a sufficiently small pinhole was used for confocal imaging, and images were formed at the same wavelength, the theoretical optical resolution for all three microscopes would also be the same.

Chapter 3

Aberrations and sensor-based adaptive optics

3.1 Overview

As previously mentioned in Chapter 1, the presence of optical aberrations lead to a decrease in resolution, image intensity and contrast, which greatly impairs the image quality. Adaptive optics (AO) is a technique developed to compensate for these optical deformations. This chapter discusses in more detail the definition, source, representation, and evaluation of aberrations. The practical implementation of direct wavefront sensing is introduced, including the principle of the Shack-Hartmann wavefront sensor (SHWS), and associated algorithms that recover the wavefront profile. Sensor-based AO is further discussed with special focus on the deformable mirror (DM) calibration procedure and closed-loop AO control routine. Next, it is demonstrated how remote focusing (RF) can be achieved using a DM for rapid system-aberration-free focus control. Finally, the limitations of pupil AO (PAO) is discussed and the concepts of conjugate AO (CAO) and multi-conjugate AO (MCAO) is presented.

3.2 Aberrations in optical microscopy

To overcome aberrations in biomedical imaging, one needs to understand its properties in the context of a real optical system. Here, we focus on distortions in the wavefront known as phase aberrations, which is the most detrimental source of aberration in the case of using a narrowband

light source. This is in contrast to chromatic aberrations, which are artefacts due to dispersion when a broadband light source propagates through media with varying refractive indices (RI).

3.2.1 Definition of phase aberrations

In Section 2.3, we introduced the concept of a complex pupil function $P(x, y)$ in a diffraction-limited imaging system, and how it takes into account the amplitude change of the light field upon incidence of a planar wavefront. We call this the aberration-free pupil function, which produces a perfect spherical wavefront, also known as the Gaussian reference sphere, and is transformed into the image space via Fourier transform. In a general case, the wavefront can be represented by,

$$P'(x, y) = P(x, y)\exp(-j\Phi), \tag{3.1}$$

where Φ is an additional phase term that considers the aberrations introduced in the optical system, and makes the wavefront deviate from the Gaussian reference sphere [84, 121]. This phenomenon is illustrated in Figure 3.1, where the pupil plane can be defined within a unit circular aperture A that corresponds to the maximum semi-aperture angle α converging to the Gaussian focus O of reference sphere G. This is often related to the numerical aperture (NA) of the imaging lens by $\mathrm{NA} = n\sin\alpha$, where n is the image space RI. β is then the semi-aperture angle of an arbitrary meridional ray that intersects with G at point P and an aberrated wavefront G' at P'. The optical path difference (OPD) between PP', which we denote as $\Delta\phi$, then contributes to the phase aberration at angle β, which can be mapped onto A by the normalised radial coordinate ρ with the relation of $\rho = \sin\beta/\sin\alpha$. For an incident wavelength λ, the aberrated pupil function can thus be expressed in terms of ρ by,

$$P'(\rho) = P(\rho)\exp(-jk\Delta\phi), \tag{3.2}$$

where k is the image space wavenumber given by $k = 2\pi n/\lambda$.

3.2.2 Source of phase aberrations

In practice, phase aberrations arise from a series of factors, which can be divided into two categories. The first category reflects aberrations induced by imperfections of the optical system,

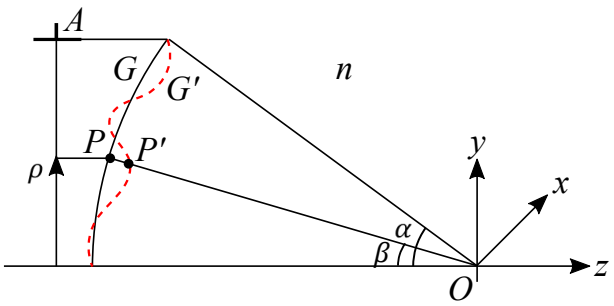


Figure 3.1: Definition of phase aberration in terms of optical path difference (OPD) between the aberrated wavefront G' (dotted red line) and Gaussian reference sphere G (solid black line). A is a unit circular aperture in the pupil plane which corresponds to the maximum semi-aperture angle α that converges to the Gaussian image point O. β is then the semi-aperture angle of an arbitrary meridional ray that intersects with the Gaussian reference sphere G at point P and aberrated wavefront G' at P'. The OPD between PP', which we denote as $\Delta\phi$, then contributes to the phase aberration.

which are known as system-induced aberrations. One such instance is when the design or manufacturing of certain optical components inherently lead to aberrations. This is most typical for high-NA objective lenses, where the geometrical design is prone to inducing spherical aberration. Another instance is when residual misalignments are present in the system, such as spherical lenses positioned at off-axis positions in a tilted orientation.

The second type of phase aberrations originates from the specimen of interest, commonly known as specimen-induced aberrations, which can occur even in a perfect optical system. One typical case is the presence of refractive index mismatch (RIM) [122–124]. Focal shift and spherical aberration proportional to the focusing depth are introduced when imaging through planar interfaces between media that have different RI, such that rays in the converging cone of light refract at different angles, and do not intersect at the same axial location [114]. This can happen when the objective lens is immersed in medium with a different RI to that of the nominal, or if the cover glass is of a different thickness to what the objective lens corrects for. A more complex source of specimen-induced aberration comes from non-foreseeable variations in RI within biological specimens. The phenomenon is more pronounced when focusing deeper into the specimen, seeing larger and more complex aberrations, as well as using high-NA objective lenses, such that effects are exacerbated by the large focusing angles.

3.2.3 Zernike representation of phase aberrations

Phase aberration Φ as defined in Section 3.2.1 can be expanded into a series of Zernike polynomials which are orthogonal over a unit circle. The concept of Zernike polynomials was first introduced by Frits Zernike in 1934 [125], and given detailed analysis by Born & Wolf in 1975 [115]. It was further developed by Noll [126] who first suggested its orthonormal form and ordering in describing atmospheric turbulence, and later by Mahajan [127] who developed a system that allows each polynomial to be uniquely defined by either a single index i or dual index (n, m). n and m represent radial and azimuthal indices respectively, where $n \geq |m|$ and $n - |m|$ is even. Zernike polynomials consist of a radial and an azimuthal component, and can be explicitly expressed as a function of normalised radial coordinate ρ and azimuthal angle θ by,

$$Z_n^m(\rho, \theta) = \begin{cases} \sqrt{2} R_n^{-m}(\rho) \sin(-m\theta) & m < 0 \\ R_n^0(\rho) & m = 0 \\ \sqrt{2} R_n^m(\rho) \cos(m\theta) & m > 0, \end{cases} \tag{3.3}$$

$$R_n^m(\rho) = \sqrt{n+1} \sum_{s=0}^{(n-m)/2} \frac{(-1)^s (n-s)!}{s! \left[(n+m)/2 - s\right]! \left[(n-m)/2 - s\right]!} \cdot \rho^{n-2s}. \tag{3.4}$$

Normalisation is performed such that, for $n \neq 0$, the mean of each polynomial over the unit circle is zero and the variance is unity. When $n = 0$, the opposite is applied. Many standards define the mapping algorithm between dual index and single index systems, the two most widely adopted being Noll's convention [126, 127] and the OSA/ANSI standard [128]. For Noll's convention, index i increases with n. Within a given n, lower values of $|m|$ obtain a lower i, while at the same time ensuring that a negative m obtains an odd i and a positive m obtains an even i. The OSA/ANSI standard is slightly different in that within a given n, indices increase with the value of m from negative to positive. For the remainder of this thesis, the OSA/ANSI standard is used unless otherwise stated, and the first 21 polynomials are given in Table 3.1. It should be noted that the piston mode only adds a constant offset to the phase without changing its profile and does not affect the image quality. It is therefore neglected such that $i = 1$ starts with tilt.

Table 3.1: The first 21 Zernike polynomials numbered according to the OSA/ANSI standard.

i	n	m	$Z_i(\rho,\theta)$	Classical name
1	0	0	1	piston
2	1	-1	$2\rho\sin\theta$	tilt
3	1	1	$2\rho\cos\theta$	tip
4	2	-2	$\sqrt{6}\rho^2\sin 2\theta$	oblique astigmatism
5	2	0	$\sqrt{3}(2\rho^2-1)$	defocus
6	2	2	$\sqrt{6}\rho^2\cos 2\theta$	vertical astigmatism
7	3	-3	$2\sqrt{2}\rho^3\sin 3\theta$	vertical trefoil
8	3	-1	$2\sqrt{2}(3\rho^3-2\rho)\sin\theta$	vertical coma
9	3	1	$2\sqrt{2}(3\rho^3-2\rho)\cos\theta$	horizontal coma
10	3	3	$2\sqrt{2}\rho^3\cos 3\theta$	oblique trefoil
11	4	-4	$\sqrt{10}\rho^4\sin 4\theta$	oblique quadrafoil
12	4	-2	$\sqrt{10}(4\rho^4-3\rho^2)\sin 2\theta$	oblique secondary astigmatism
13	4	0	$\sqrt{5}(6\rho^4-6\rho^2+1)$	primary spherical
14	4	2	$\sqrt{10}(4\rho^4-3\rho^2)\cos 2\theta$	vertical secondary astigmatism
15	4	4	$\sqrt{10}\rho^4\cos 4\theta$	vertical quadrafoil
16	5	-5	$2\sqrt{3}\rho^5\sin 5\theta$	vertical pentafoil
17	5	-3	$2\sqrt{3}(5\rho^5-4\rho^3)\sin 3\theta$	vertical secondary trefoil
18	5	-1	$2\sqrt{3}(10\rho^5-12\rho^3+3\rho)\sin\theta$	vertical secondary coma
19	5	1	$2\sqrt{3}(10\rho^5-12\rho^3+3\rho)\cos\theta$	horizontal secondary coma
20	5	3	$2\sqrt{3}(5\rho^5-4\rho^3)\cos 3\theta$	oblique secondary trefoil
21	5	5	$2\sqrt{3}\rho^5\cos 5\theta$	oblique pentafoil

An arbitrary wavefront Φ can then be decomposed into a series of Zernike polynomials by,

$$\Phi(\rho,\theta)=\sum_{i=2}^{\infty}a_i Z_i(\rho,\theta), \tag{3.5}$$

where a_i is the coefficient of the ith Zernike polynomial that represents its root-mean-square (RMS) phase value, and can be obtained using the orthogonality of Zernike polynomials,

$$a_i=\frac{1}{\pi}\int_0^1\int_0^{2\pi}\Phi(\rho,\theta)Z_i(\rho,\theta)\rho\mathrm{d}\rho\mathrm{d}\theta. \tag{3.6}$$

The convention of expanding an aberration function into orthogonal Zernike polynomials over a unit circle enjoys the following advantages. First, the coefficients of these expansion terms represent their RMS phase value, such that the contribution of each Zernike mode can be evaluated using the same benchmark. They can then be assigned the same weight when used to calculate certain image metrics, which will be further discussed in Section 3.2.4. Second, their smooth profiles allow them to be applied onto common adaptive elements, such as continuous membrane deformable mirrors, which will be introduced in Section 3.4.1. Third,

common primary aberrations, such as defocus, astigmatism, coma, and spherical aberration, can be represented by a single low-order Zernike polynomial, which allows them to be adjusted independently of other aberration modes. Figure 3.2 shows the 2D (Figure 3.2(a)) and 3D (Figure 3.2(b)) phase profiles of common low-order Zernike polynomials with single-index numbering. 0.5 µm amplitude RMS was applied and the OPD at each point of the unit circle with regard to a planar wavefront is indicated in the colorbar.

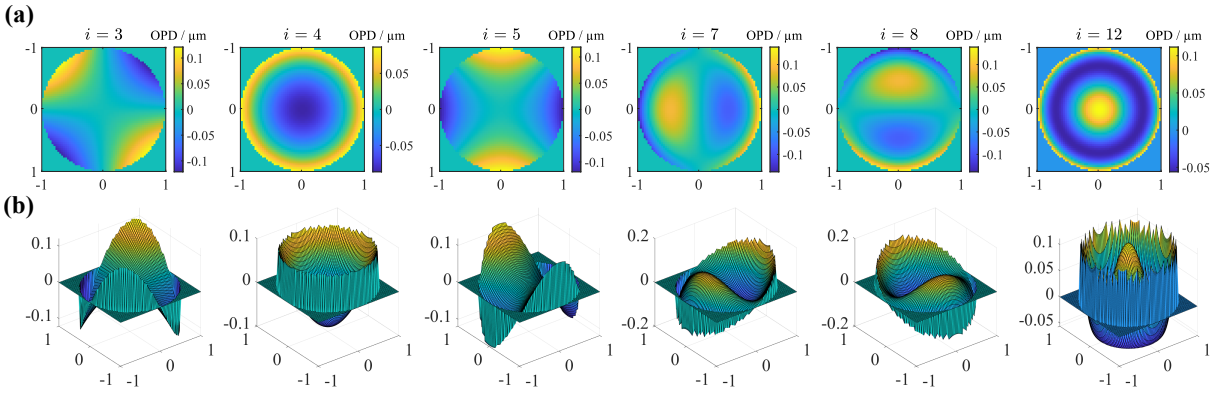


Figure 3.2: Phase profiles of common low-order Zernike polynomials with single-index numbering. (a) 2D and (b) 3D phase profiles of each mode with 0.5 µm amplitude RMS applied. The colourbar indicates the OPD at each point of the unit circle with regard to a planar wavefront.

3.2.4 The Strehl ratio

As described in Section 3.2.1, an aberration-free image is formed by the convergence of a perfect spherical wavefront. All light waves propagate in phase over the same optical path length (OPL) and constructively interfere to generate a tight focal spot (Figure 3.3(a)). However, when the wavefront is distorted, light waves in phase do not arrive at O at the same time, thus cannot constructively interfere, which leads to a much dispersed focus, as illustrated in Figure 3.3(b).

The Strehl ratio (SR) is defined as the ratio of intensity on-axis between an aberrated and unaberrated beam [84, 129], which is less than 1 in all practical systems. For small aberrations, the SR can be used as an image quality metric approximated by [129]

$$\mathrm{SR} \approx \exp\left(-\Phi^2\right) \approx 1 - \Phi^2, \tag{3.7}$$

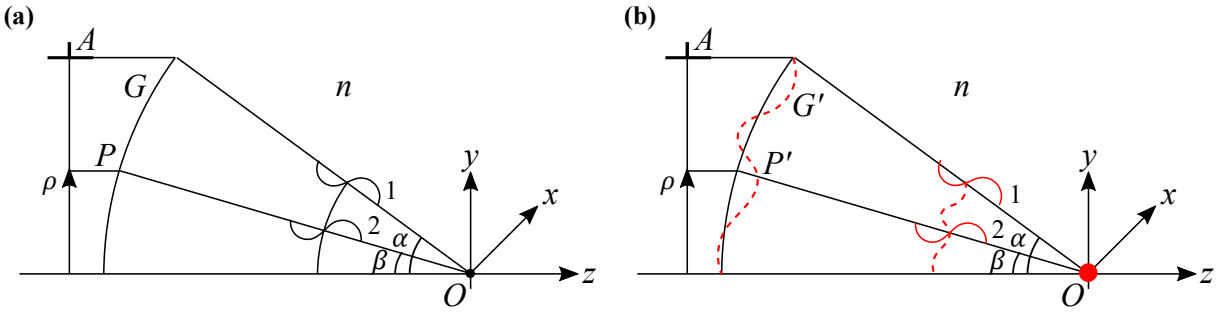


Figure 3.3: Diagram showing how light waves (a) constructively interfere at the Gaussian image point O for a perfectly spherical wavefront (solid black line), and (b) do not constructively interfere in the case of a distorted wavefront (dotted red line).

where Φ^2 is the wavefront variance. To obtain a diffraction-limited image, let SR > 0.8 such that the standard deviation of the wave aberration is smaller than $\lambda/14$. This is commonly referred to as the Maréchal criterion [129, 130].

As was discussed in Section 3.2.3, Zernike coefficients represent the RMS phase of Zernike polynomials that contribute to the aberrated wavefront. The geometric sum of all non-piston terms then yield the wavefront variance that directly estimates the SR [84, 115]. For a diffraction-limited image, according to the above Maréchal criterion, this yields

$$\text{SR} \approx \exp\left(-\Phi^2\right) = \exp\left(-\sum_{i=2}^{N} a_i^2\right) > 0.8, \tag{3.8}$$

where N is the total number of non-piston term Zernike coefficients. Eq. (3.8) can then be used as the image quality metric for assessing small aberrations represented by Zernike polynomials. In practice, however, it should be noted that the various shapes and inhomogeneities of cells and tissue layers in biological samples may lead to cross-coupling between Zernike modes, such that the adjustment of one mode may also lead to changes in another.

3.3 Direct wavefront sensing

Evaluation of the image quality requires a feedback system of how much aberration is present in the system. This can be obtained by either directly measuring the wavefront using a dedicated sensor, which is referred to as direct wavefront sensing, or taking a sequence of image measurements when subjectively applying certain bias phase patterns to indirectly retrieve the

wavefront. This work focuses on the former, due to its rapid wavefront inference process, which is extremely important for real-time applications.

3.3.1 The Shack-Hartmann wavefront sensor (SHWS)

If the aberrated wavefront is spatially divided into an array of small zones within the pupil plane, then the wavefront inside each zone can be represented by a local tilt with respect to a planar wavefront perpendicular to the optical axis. If the local tilt inside all zones of a finite aperture can be recorded, then the entire wavefront can be sampled and reconstructed [84]. This is the basic principle of an SHWS. The concept of using local tilt as an indicator of the phase profile was first introduced to test the quality of a lens or mirror, which was called the Hartmann test [84]. An opaque mask with holes was placed behind the optical element, such that each hole acted as an aperture to create an array of spots. Later, Shack replaced the holes by lenses, and the device was given the name Shack-Hartmann wavefront sensor [95].

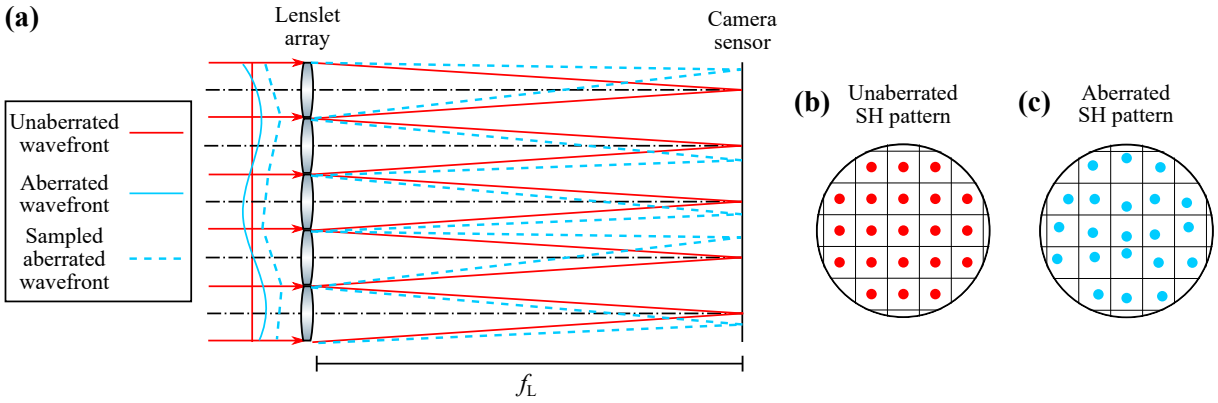


Figure 3.4: Diagram showing the geometry of a SHWS and SH spot pattern when sampling an unaberrated and aberrated wavefront. (a) Geometry of SHWS with a lenslet array placed at a conjugate pupil plane of the optical system and camera sensor at the focal plane of the lenslet array. (b) Regular SH spot pattern on the camera sensor for an unaberrated wavefront. (c) Irregular SH spot pattern in the case of an aberrated wavefront.

Nowadays, typically an array of square lenses called a lenslet array, each with a focal length of f_L, is placed at a conjugate pupil plane of an optical system. Light coming from a point source in the sample will form an array of spots on a camera sensor placed at the lenslet focal plane, as illustrated in Figure 3.4(a). When an unaberrated wavefront is incident upon the SHWS,

each lenslet samples a portion of the wavefront and focuses it at a local on-axis position of the camera sensor. A regular SH spot pattern, given in Figure 3.4(b), is then generated and used as reference. Figure 3.4(c) depicts the case of an aberrated wavefront, where the local tilt at each lenslet causes a proportional shift in the SH spot position relative to the lenslet centre. By analysing the direction and amplitude of the focal shift behind each lenslet, one can reconstruct the full wavefront [84, 91, 98]. For the remainder of this thesis, a region on the camera sensor that analyses the aberration information behind one lenslet is referred to as a search block (SB).

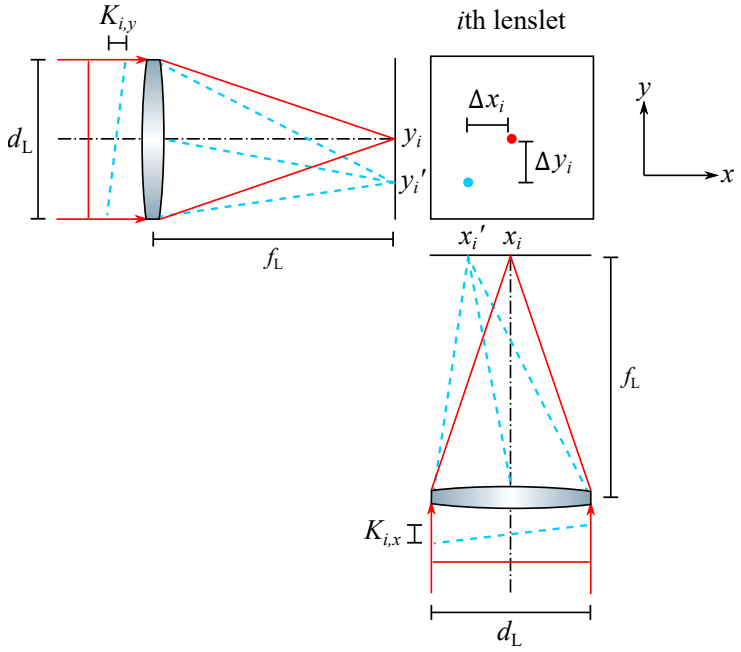


Figure 3.5: Relationship between local wavefront tilt and the amount of focal shift for the ith lenslet along the x- and y-axis.

Figure 3.5 describes the relationship between the amount of local wavefront tilt and focal shift for one lenslet along the x- and y-axis. Assume that lenslets are numbered in row-major order and the diameter of each lenslet is d_L. Take the ith lenslet as an example. When the wavefront is unaberrated, an SH spot would form at point (x_i, y_i) within the corresponding SB. If there exists a local wavefront tilt along both the x- and y-axis, the SH spot would shift to point (x_i', y_i') within the same SB. The amount of focal shift $\Delta x_i = x_i' - x_i$ and $\Delta y_i = y_i' - y_i$, also known as the x- and y-slope values, can then be used to calculate the local wavefront tilt

$\frac{\partial(\Phi_i)}{\partial x}$ and $\frac{\partial(\Phi_i)}{\partial y}$ using the following relationship,

$$\begin{aligned}\frac{\partial(\Phi_i)}{\partial x} &\simeq \frac{K_{i,x}}{d_{\mathrm{L}}} = \frac{\Delta x_i}{f_{\mathrm{L}}} \\ \frac{\partial(\Phi_i)}{\partial y} &\simeq \frac{K_{i,y}}{d_{\mathrm{L}}} = \frac{\Delta y_i}{f_{\mathrm{L}}}\end{aligned} \tag{3.9}$$

3.3.2 Centroiding of SH spot patterns

In order to determine the x- and y-slope values Δx_i and Δy_i, one needs to locate the centroid of the SH spot. This is based upon the assumption that the wavefront variation behind each lenslet is simple enough to be approximated as a tip or tilt [84], as is often the case when using a sufficient number of lenslets to sample a wavefront originating from superficial layers of the biological specimen. For wavefronts that are so severely distorted that the portion of wavefront sampled by each lenslet cannot be considered with this approximation, one should also consider the SH spot's shape and maximum intensity [84]. Here it should be noted that when designing an SHWS in practice, one should take into account the number and size of lenslets in relation to the number of correction modes, so as to measure the wavefront with both a sufficiently high sampling rate and signal-to-noise ratio.

The centroid (x_c, y_c) is defined as the first moment of the SH spot, which can be calculated using the centre of gravity (CoG) method. As the camera sensor consists of discrete pixels and we are only interested in one SB for calculation of each centroid position, we can calculate (x_c, y_c) using the following equation,

$$\begin{aligned}x_c &= \frac{\sum_{m=1}^{M} x_m I_m}{\sum_{m=1}^{M} I_m} \\ y_c &= \frac{\sum_{m=1}^{M} y_m I_m}{\sum_{m=1}^{M} I_m},\end{aligned} \tag{3.10}$$

where the mth pixel within a given SB has a coordinate of (x_m, y_m) and intensity of I_m, and M is the total number of pixels within the SB.

Although the CoG method is easy to implement and computationally fast, its accuracy can be affected by background noise. Some existing methods, including the thresholding centre of gravity (TCoG) and weighted centre of gravity (WCoG) algorithms, can help to reduce this effect [131]. The TCoG method first determines the maximum intensity value $I_{\max}$ within each

SB. Then a parameter T is chosen such that only pixels above value $I_T = TI_{\max}$ are used as valid pixels for CoG computation while others are set to zero. This algorithm is effective for low and uniform background levels. However, when suppression of spurious noise is required, the WCoG algorithm should be adopted such that pixels are assigned with different weights centred at the most likely centroid position [131].

It should be noted that in order to acquire centroid positions that accurately reflect the local wavefront tilt, sufficient light should emanate from a point source within the specimen, as the SH spots are in effect images of the specimen space focal spot, and scattered and out-of-focus light may lead to ambiguous measurements [97]. In practice, this can be achieved by using a fluorescent bead as "guide star" [132, 133] or a spatial filter to block out-of-focus light [134, 135]. Alternatively, 2PE microscopy benefits from its intrinsic optical sectioning properties by confining fluorescence emission to the focal region and generating a nonlinear "guide star" [47, 136, 137], thus allowing for 700 µm penetration depth within the *in vivo* brain [47]. The use of this nonlinear "guide star" is advantageous for two reasons, the first being its non-invasiveness and the second being that it can be created at any desired position.

3.3.3 Calculation of Zernike coefficients using slope values

Slope values Δx_i and Δy_i provide sampled approximations of the aberrated wavefront after segmenting it into discrete regions. Indeed this is sufficient for quantitative analysis. However, for the reasons explained in Section 3.2.3, it is also advantageous to convert raw slope values into modular Zernike coefficients, the method of which will be described below.

As camera pixels are rectangular, here we rewrite Eq. (3.5) and represent phase aberration Φ using Zernike polynomials in the Cartesian coordinate with consideration of $\rho = \sqrt{x^2 + y^2}$ and $\theta = \tan \frac{y}{x}$,

$$\Phi(x, y) = \sum_{j=2}^{\infty} a_j Z_j(x, y). \tag{3.11}$$

Assume (x_i, y_i) are now normalised coordinates of the ith lenslet on a unit circle, the local wavefront tilt behind the ith lenslet can then be expressed using Zernike polynomials as,

$$\begin{aligned}\frac{\partial(\Phi_i(x_i,y_i))}{\partial x} &= \frac{\Delta x_i}{f_{\mathrm{L}}} \equiv \sum_{j=2}^{N} a_j \overline{\frac{\partial Z_j(x_i,y_i)}{\partial x}} \\ \frac{\partial(\Phi_i(x_i,y_i))}{\partial y} &= \frac{\Delta y_i}{f_{\mathrm{L}}} \equiv \sum_{j=2}^{N} a_j \overline{\frac{\partial Z_j(x_i,y_i)}{\partial y}},\end{aligned} \tag{3.12}$$

where N is the total number of Zernike polynomials used to represent the aberrated wavefront. $\overline{\frac{\partial Z_j(x_i,y_i)}{\partial x}}$ and $\overline{\frac{\partial Z_j(x_i,y_i)}{\partial y}}$ are the averaged x and y derivatives of the jth Zernike polynomial given as,

$$\begin{aligned}\overline{\frac{\partial Z_j(x_i,y_i)}{\partial x}} &= \frac{1}{N_s}\sum_{k=1}^{N_s} \frac{\partial Z_j(x_k,y_k)}{\partial x} \\ \overline{\frac{\partial Z_j(x_i,y_i)}{\partial y}} &= \frac{1}{N_s}\sum_{k=1}^{N_s} \frac{\partial Z_j(x_k,y_k)}{\partial y},\end{aligned} \tag{3.13}$$

where (x_k, y_k) represents the normalised coordinates of the kth segment after partitioning each lenslet into N_s segments. If we collect the local wavefront tilt behind all N_{L} lenslets into a single vector $\mathbf{W}$, Eq. (3.12) can be expressed in matrix form as,

$$\mathbf{W} = \nabla \mathbf{Z}\mathbf{a}, \tag{3.14}$$

where,

$$\mathbf{W} = \begin{bmatrix} \Delta x_1/f_{\mathrm{L}} \\ \Delta x_2/f_{\mathrm{L}} \\ \vdots \\ \Delta x_{N_{\mathrm{L}}}/f_{\mathrm{L}} \\ \Delta y_1/f_{\mathrm{L}} \\ \Delta y_2/f_{\mathrm{L}} \\ \vdots \\ \Delta y_{N_{\mathrm{L}}}/f_{\mathrm{L}} \end{bmatrix}, \mathbf{a} = \begin{bmatrix} a_1 \\ a_2 \\ \vdots \\ a_N \end{bmatrix}, \tag{3.15}$$

and

$$\nabla\mathbf{Z} = \begin{bmatrix} \overline{\partial Z_1(x_1,y_1)}/\partial x & \overline{\partial Z_2(x_1,y_1)}/\partial x & \dots & \overline{\partial Z_N(x_1,y_1)}/\partial x \\ \overline{\partial Z_1(x_2,y_2)}/\partial x & \overline{\partial Z_2(x_2,y_2)}/\partial x & \dots & \overline{\partial Z_N(x_2,y_2)}/\partial x \\ \vdots & \vdots & \ddots & \vdots \\ \overline{\partial Z_1(x_{N_\mathrm{L}},y_{N_\mathrm{L}})}/\partial x & \overline{\partial Z_2(x_{N_\mathrm{L}},y_{N_\mathrm{L}})}/\partial x & \dots & \overline{\partial Z_N(x_{N_\mathrm{L}},y_{N_\mathrm{L}})}/\partial x \\ \overline{\partial Z_1(x_1,y_1)}/\partial y & \overline{\partial Z_2(x_1,y_1)}/\partial y & \dots & \overline{\partial Z_N(x_1,y_1)}/\partial y \\ \overline{\partial Z_1(x_2,y_2)}/\partial y & \overline{\partial Z_2(x_2,y_2)}/\partial y & \dots & \overline{\partial Z_N(x_2,y_2)}/\partial y \\ \vdots & \vdots & \ddots & \vdots \\ \overline{\partial Z_1(x_{N_\mathrm{L}},y_{N_\mathrm{L}})}/\partial y & \overline{\partial Z_2(x_{N_\mathrm{L}},y_{N_\mathrm{L}})}/\partial y & \dots & \overline{\partial Z_N(x_{N_\mathrm{L}},y_{N_\mathrm{L}})}/\partial y \end{bmatrix}. \tag{3.16}$$

a can then be obtained by,

$$\mathbf{a} = (\nabla\mathbf{Z})^{\dagger}\mathbf{W}, \tag{3.17}$$

where $(\nabla\mathbf{Z})^{\dagger}$ is the pseudo-inverse of $\nabla\mathbf{Z}$. As the columns of $\nabla\mathbf{Z}$ are linearly independent, $(\nabla\mathbf{Z})^{\mathrm{T}}(\nabla\mathbf{Z})$ is invertible, and thus $(\nabla\mathbf{Z})^{\dagger}$ can be computed as,

$$(\nabla\mathbf{Z})^{\dagger} = [(\nabla\mathbf{Z})^{\mathrm{T}}(\nabla\mathbf{Z})]^{-1}(\nabla\mathbf{Z})^{\mathrm{T}}. \tag{3.18}$$

Note that in practice, one can validate the correctness of the above computation by right multiplying Eq. (3.18) with factor $\nabla\mathbf{Z}$ to obtain an identity matrix $\mathbf{I}$.

3.4 Sensor-based adaptive optics

By using a dedicated sensor to measure the aberrated wavefront and using this information to determine the phase pattern applied on an adaptive element, sensor-based AO can be achieved. In all areas of astronomy [86], vision science [96, 138], and microscopy [47, 139], sensor-based AO has played a crucial role for its unique ability to provide rapid updates of the aberrated wavefront. Here, we focus on the example of using a DM for wavefront correction.

3.4.1 The electrostatic and electromagnetic deformable mirror

According to the surface continuity, DMs can be divided into segmented or continuous membrane devices. A main disadvantage of the former is that all actuators are attached to inde-

pendent mirrors, such that gaps exist between each mirror, leading to light loss and diffraction effects [140]. Continuous membrane mirrors are therefore more commonly used. DMs can be further categorised according to their actuator control mechanisms into 3 major categories, namely electrostatic, electromagnetic, and piezoelectric mirrors. The first two were adopted in this thesis and will be introduced below.

Electrostatic mirrors consist of a thin membrane suspended over an actuator pad array that deflects when voltages are applied to a high-voltage driver. To avoid possible "snap-down" that occurs as a result of the membrane and actuator distance being too small, the mirror can only be pulled in one direction, and the amount of actuator displacement is linearly proportional to the applied control voltage squared [141]. Mirrors of this type enjoy better performance in terms of wavefront correction with a tighter actuator packing [141].

Electromagnetic mirrors attach magnets behind the mirror surface which generate a magnetic field when a voltage is applied to the coil. Depending on its sign, the magnet is attracted to or repelled from the coil, which causes the mirror surface to be pulled or pushed away from the neutral position. Consequently, these devices are bi-directional and the amount of actuator displacement is approximately linear to the applied control voltage [142]. Mirrors of this type are particularly beneficial for their large stroke [143], which is the amount of actuator displacement with regard to their neutral position.

3.4.2 Deformable mirror calibration

To accurately apply phase patterns, one needs to have prior knowledge of how each DM actuator reacts to given control signals, and how its movement contributes to the overall mirror shape. This is known as the actuator influence function (IF). When using direct wavefront sensing, the IF can be obtained with respect to both the raw slope values and Zernike coefficients.

In a direct wavefront sensing system, the SHWS is often used to monitor the DM membrane during calibration so as to understand the mutual interaction between the two devices. This also eliminates the need to rely on separate calibration modules. For an electromagnetic mirror, as the amount of actuator displacement scales linearly with the applied control voltage, it can be

sampled with a minimum number of bias values. The IF with respect to raw slope values can be obtained by applying a positive and negative bias voltage of the same magnitude $\pm V_b$ sequentially to each DM actuator, and recording the x- and y-slope values of each lenslet $(\Delta x^+_{i,n}, \Delta y^+_{i,n})$ and $(\Delta x^-_{i,n}, \Delta y^-_{i,n})$, where i denotes the ith lenslet, n the nth DM actuator, and $+, -$ the sign of the applied voltage. The IF can then be obtained in matrix form $\mathbf{I}_s$ with each column representing the IF of one actuator,

$$\mathbf{I}_s = \begin{bmatrix} \frac{\Delta x^+_{1,1}-\Delta x^-_{1,1}}{2V_b} & \frac{\Delta x^+_{1,2}-\Delta x^-_{1,2}}{2V_b} & \cdots & \frac{\Delta x^+_{1,N_\mathrm{A}}-\Delta x^-_{1,N_\mathrm{A}}}{2V_b} \\ \frac{\Delta x^+_{2,1}-\Delta x^-_{2,1}}{2V_b} & \frac{\Delta x^+_{2,2}-\Delta x^-_{2,2}}{2V_b} & \cdots & \frac{\Delta x^+_{2,N_\mathrm{A}}-\Delta x^-_{2,N_\mathrm{A}}}{2V_b} \\ \vdots & \vdots & \ddots & \vdots \\ \frac{\Delta x^+_{N_\mathrm{L},1}-\Delta x^-_{N_\mathrm{L},1}}{2V_b} & \frac{\Delta x^+_{N_\mathrm{L},2}-\Delta x^-_{N_\mathrm{L},2}}{2V_b} & \cdots & \frac{\Delta x^+_{N_\mathrm{L},N_\mathrm{A}}-\Delta x^-_{N_\mathrm{L},N_\mathrm{A}}}{2V_b} \\ \frac{\Delta y^+_{1,1}-\Delta y^-_{1,1}}{2V_b} & \frac{\Delta y^+_{1,2}-\Delta y^-_{1,2}}{2V_b} & \cdots & \frac{\Delta y^+_{1,N_\mathrm{A}}-\Delta y^-_{1,N_\mathrm{A}}}{2V_b} \\ \frac{\Delta y^+_{2,1}-\Delta y^-_{2,1}}{2V_b} & \frac{\Delta y^+_{2,2}-\Delta y^-_{2,2}}{2V_b} & \cdots & \frac{\Delta y^+_{2,N_\mathrm{A}}-\Delta y^-_{2,N_\mathrm{A}}}{2V_b} \\ \vdots & \vdots & \ddots & \vdots \\ \frac{\Delta y^+_{N_\mathrm{L},1}-\Delta y^-_{N_\mathrm{L},1}}{2V_b} & \frac{\Delta y^+_{N_\mathrm{L},2}-\Delta y^-_{N_\mathrm{L},2}}{2V_b} & \cdots & \frac{\Delta y^+_{N_\mathrm{L},N_\mathrm{A}}-\Delta y^-_{N_\mathrm{L},N_\mathrm{A}}}{2V_b} \end{bmatrix}, \tag{3.19}$$

where N_A and N_L represent the total number of DM actuators and lenslets, respectively. The process of obtaining the IF with respect to Zernike coefficients is similar to the above, with the additional step of converting x- and y-slope values acquired at each bias control voltage to Zernike coefficients $a^+_{j,n}$ and $a^-_{j,n}$ using Eq. (3.17) before generating the IF matrix $\mathbf{I}_z$ to yield,

$$\mathbf{I}_z = \begin{bmatrix} \frac{a^+_{1,1}-a^-_{1,1}}{2V_b} & \frac{a^+_{1,2}-a^-_{1,2}}{2V_b} & \cdots & \frac{a^+_{1,N_\mathrm{A}}-a^-_{1,N_\mathrm{A}}}{2V_b} \\ \frac{a^+_{2,1}-a^-_{2,1}}{2V_b} & \frac{a^+_{2,2}-a^-_{2,2}}{2V_b} & \cdots & \frac{a^+_{2,N_\mathrm{A}}-a^-_{2,N_\mathrm{A}}}{2V_b} \\ \vdots & \vdots & \ddots & \vdots \\ \frac{a^+_{N,1}-a^-_{N,1}}{2V_b} & \frac{a^+_{N,2}-a^-_{N,2}}{2V_b} & \cdots & \frac{a^+_{N,N_\mathrm{A}}-a^-_{N,N_\mathrm{A}}}{2V_b} \end{bmatrix}, \tag{3.20}$$

where N is the total number of Zernike polynomials used to reconstruct the wavefront.

After acquiring the IF matrices $\mathbf{I}_s$ and $\mathbf{I}_z$, one needs to determine the set of control voltages that can be applied to the DM in order to generate a phase aberration equal but opposite to that detected by the SHWS. This is a least squares problem assuming that the squared error between the set of generated and detected slope values or Zernike coefficients is ε^2. The IF matrices Eq. (3.19) and Eq. (3.20) essentially reflect the change in slope value or Zernike coefficient per

unit voltage of each actuator. By computing its pseudo-inverse, the set of control voltages that generate one unit of phase aberration can be acquired, and is known as the DM control matrix (CM). It should be noted that in order to obtain a unique solution, the IF matrices must have more rows than columns.

The pseudo-inverse problem can be accurately computed using singular value decomposition (SVD), which decomposes a real IF matrix of size $m \times n$ and rank n into the product of three matrices $\mathbf{U}\mathbf{\Sigma}\mathbf{V}^{\mathrm{T}}$, where $\mathbf{\Sigma}$ is a square diagonal matrix of size $n \times n$, and $\mathbf{U}$ and $\mathbf{V}$ are semi-unitary matrices of size $m \times n$ and $n \times n$, such that $\mathbf{U}^*\mathbf{U} = \mathbf{V}^*\mathbf{V} = \mathbf{I}_n$. As the IF matrix is real, $\mathbf{U}$ and $\mathbf{V}$ are also column-orthogonal matrices and both form a set of orthonormal vectors. Each column of $\mathbf{V}$ represents a set of control voltages that generate an independent system mode, which are orthogonal modes that can be created by the DM considering its mechanical limitations and actuator layout [144]. Note that system modes are different to Zernike modes in the sense that they compromise for the break down of Zernike mode orthogonality in the case of pixelated actuators. A linear combination of system modes is then used to generate Zernike modes in practice. Each column of $\mathbf{U}$ represents the system mode as seen by the SHWS when unit voltage is applied to each actuator. If we take matrix $\mathbf{I}_z$ as example, then the diagonal entries σ_i of $\mathbf{\Sigma}$ are positive singular values of $\mathbf{I}_z$ ordered in descending order from top left to bottom right, and links orthonormal vectors of $\mathbf{U}$ and $\mathbf{V}$, denoted as $\mathbf{u}_i$ and $\mathbf{v}_i$, by

$$\mathbf{I}_z\mathbf{v}_i = \sigma_i\mathbf{u}_i. \tag{3.21}$$

A large singular value would indicate that the linear transformation from $\mathbf{v}_i$ to $\mathbf{u}_i$ is significant for $\mathbf{I}_z$, while modes with small singular values possess negligible significance. They generally contribute to noise or less-critical high-order system modes, and can severely limit the dynamic range of critical low-order modes, leading to instabilities during device control. For this reason, small singular values after which a substantial drop is seen on the diagonal of $\mathbf{\Sigma}$ are often set to zero when performing pseudo-inverse. The corresponding CMs $\mathbf{C}_s$ and $\mathbf{C}_z$ that convert between raw slope values $\mathbf{S}$ or Zernike coefficients $\mathbf{a}$ and DM control voltages can then be expressed as the product of three matrices $\mathbf{V}\mathbf{\Sigma}^{\dagger}\mathbf{U}^{\mathrm{T}}$. Finally, DM control voltages can be computed as

$$\mathbf{c}_s = \mathbf{C}_s\mathbf{S}, \tag{3.22}$$

and

$$\mathbf{c}_z = \mathbf{C}_z \mathbf{a}. \tag{3.23}$$

3.4.3 Closed-loop adaptive optics control

Eq. (3.22) and Eq. (3.23) allows for one-time aberration correction, which is termed as open-loop AO control. A disadvantage is that it lacks a feedback mechanism, i.e., the system does not know how well the aberration has been corrected. Closed-loop control is therefore introduced to provide feedback of the residual aberration and decide whether subsequent iterations of AO correction is required.

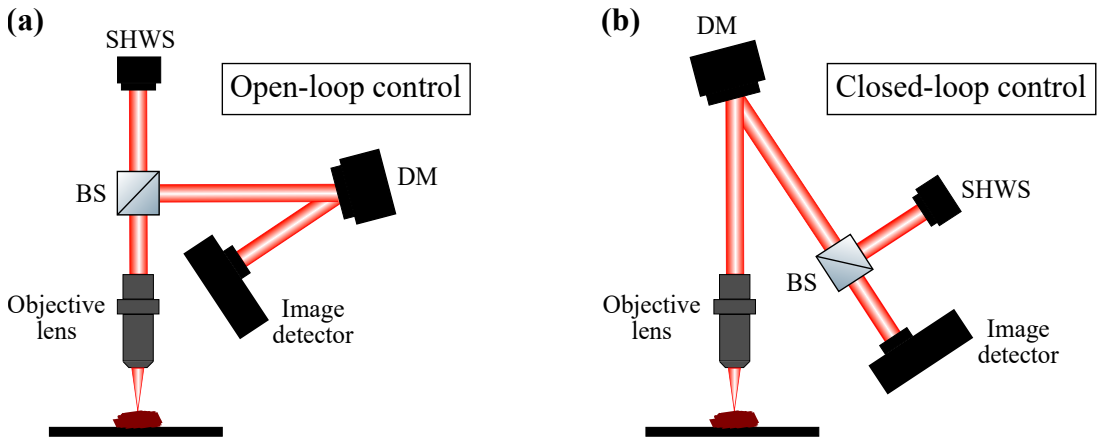


Figure 3.6: Typical system setups for open-loop and closed-loop AO control. (a) Open-loop control. The SHWS is placed closer to the objective lens than the DM and directly measures the amount of phase aberration at the objective pupil plane. (b) Closed-loop control. The SHWS is placed further away from the objective lens than the DM, such that it measures the residual phase aberration after DM correction.

The main difference in system setup is given in Figure 3.6. In an open-loop control system, the SHWS is placed closer to the objective lens than the DM and directly measures the amount of phase aberration at the objective pupil plane (Figure 3.6(a)); whereas in a closed-loop control system, the SHWS is placed further away from the objective lens, such that it measures the residual phase aberration after DM correction (Figure 3.6(b)). The control voltages are therefore determined by not only the current SH measurements, but also the control voltages of the

previous correction loop via the following relationship [145],

$$\begin{cases} \mathbf{c}_{s,l} = \mathbf{c}_{s,bias} - g\mathbf{C}_s\mathbf{S}_l & , l = 1, \\ \mathbf{c}_{s,l} = \mathbf{c}_{s,l-1} - g\mathbf{C}_s\mathbf{S}_l & , l > 1, \end{cases} \tag{3.24}$$

in the case of using the raw slope values, and

$$\begin{cases} \mathbf{c}_{z,l} = \mathbf{c}_{z,bias} - g\mathbf{C}_z\mathbf{a}_l & , l = 1, \\ \mathbf{c}_{z,l} = \mathbf{c}_{z,l-1} - g\mathbf{C}_z\mathbf{a}_l & , l > 1, \end{cases} \tag{3.25}$$

in the case of using Zernike coefficients, where l represents the lth correction loop. g is a loop gain between [0,1] that determines the proportion of control voltages calculated from the current SH measurements that will be added to the control voltages of the previous correction loop, and $\mathbf{c}_{*,bias}$ are bias voltages that are applied at the beginning of a closed-loop correction process. More details of how to determine the bias voltages will be discussed in Section 3.4.4. It should be mentioned that as Zernike tip/tilt only lead to a lateral shift of the focal spot and do not degrade the image quality, they can be removed from the correction loop by subtraction of the mean slope values in each direction. Finally, an image metric can be used to evaluate the effectiveness of the aberration correction process by taking the average value over a small lateral region around the optical axis (typically smaller than 50 µm), and a threshold is set to terminate the control loop. For small aberrations, the SR can be used in a similar way as mentioned in Section 3.2.4 with a termination threshold of SR > 0.8.

Performing aberration correction using closed-loop control is more accurate in the following ways. First, it takes into account hysteresis and drift of the DM membrane that cause the relationship between control voltage and membrane deformation to deviate from the linear case during AO correction. Second, it takes into account non-linearities of the SHWS due to its limited dynamic range, i.e., the magnitude of phase aberrations that can be detected by the SHWS is limited due to the finite lenslet diameter and lenslet focal length. This dictates that acquired slope values do not scale linearly with increments of the local wavefront tilt, i.e., the detected slope values are more sensitive to variations of smaller wavefront tilts as compared to larger ones. In such case, depending on the magnitude of the bias voltages applied during DM

calibration, one-time SH measurements can be either larger or smaller than the true value. This can be compensated for by continuously adjusting the control voltage according to the residual phase aberration. Third, when dynamic aberrations are present, i.e., when the magnitude of aberrations is continuously changing, the control voltages as determined by Eq. (3.24) and Eq. (3.25) can be divided into a static term (left-hand side) and dynamic term (right-hand side) to follow the dynamics of the aberration.

3.4.4 Correction of system aberrations

In the previous section, we introduced a set of bias control voltages $\mathbf{c}_{*,bias}$ that were applied before the closed-loop AO correction process. In practice, these are in fact the control voltages that correspond to system-induced aberrations. As they are normally stationary over a long period of time, they can be applied as a bias value.

The process of acquiring the bias control voltages can be considered as performing closed-loop AO correction on an aberration-free sample. For fluorescence imaging, this can be a fluorescent bead embedded in a thin layer of immersion medium; whereas for reflectance imaging, this can simply be a piece of white card to avoid specular reflections [146]. In either case, the aberration-free sample is placed at the objective focal plane and the control voltages as determined by Eq. (3.24) and Eq. (3.25) are continuously updated from $\mathbf{c}_{*,bias} = 0$ (electromagnetic) or $\mathbf{c}_{*,bias} = 0.7$ (electrostatic) until the SR calculated using Zernike coefficients satisfies the criteria in Eq. (3.8). The corresponding control voltages are then saved and loaded upon software initialisation to compensate for system-induced aberrations and provide a DM system flat file.

3.5 Remote focusing using a deformable mirror

It was discussed in Section 1.4.2 how RF can enable fast axial scanning to avoid slow movements of the translation stage during real-time applications and simultaneously correct for system aberrations. Here, a DM was used to compensate for other aberrations besides spherical during the RF process [106, 108]. Alternatively, the DM can be replaced with an SLM for systems that require polarisation control or fine AO correction [104, 113].

3.5.1 Remote focusing calibration

Voltages that control DM actuators to deform the membrane for fine axial refocusing were calibrated by axially displacing a piece of white card an amount Δd µm away from the objective focal plane using a sample translation stage, and compensating for this displacement via closed-loop AO control [110]. This allows simultaneous correction of system aberrations induced at each calibration step. Displacements were introduced uni-directionally from the natural focal plane to the furthest axial position sequentially along both $+z$-axis and -z-axis to enable refocusing on either side of the natural focal plane. DM control voltages $\mathbf{c}_1, \mathbf{c}_2, ..., \mathbf{c}_K$ after compensating for the kth displacement were saved, and the process was repeated for each calibration step. The magnitude of Δd was chosen with the following considerations: 1) to avoid large accumulative errors arising from small step displacements; 2) to avoid surpassing the dynamic range of the SHWS; 3) to enable sufficient sampling of non-linearity between DM control voltage and membrane deformation. Linear interpolation was subsequently performed between voltages acquired at each calibration step to acquire those for finer axial steps.

3.5.2 Real-time system-aberration-free remote focusing

After DM control voltages have been calibrated with simultaneous correction of system aberrations in air, a look-up table (LUT) can be created and loaded upon software initialisation. During real-time applications, control voltages corresponding to each RF depth are individually addressed from the LUT and applied to the DM. For most modern devices, the membrane settling time is below 1 ms regardless of the deformation amplitude, thus imaging can be performed almost immediately with an axial scan rate of > 1 kHz. This is in contrast to mechanical translation stages where larger axial displacements require a longer update time due to the uniform translation speed. As a result, both volumetric and depth-wise random access imaging can be easily performed by RF, which will be explained in more detail in Section 5.3.5. It should be emphasised that as the above RF calibrations were performed in air for standard practice, it only corrects for aberrations of the optical system, and does not take into account the RIM between immersion media and sample (see Section 3.2.2). This may not be detrimental when

using low-NA objective lenses (typically less than 0.5 NA), but special considerations need to be taken for high-NA lenses, which will be thoroughly discussed in Chapter 9.

3.6 Multi-conjugate adaptive optics

In Section 2.4 and Section 3.2.1, it was discussed that the system amplitude point spread function (APSF) could be calculated as the Fourier transform of the complex pupil function, and that phase aberrations were most commonly corrected for in the conjugate pupil plane. This can also be referred to as pupil AO (PAO). In microscopy, PAO proves effective when the aberrations are spatially invariant, thus the same pattern of correction can be applied to all points within a certain field of view (FOV). However, it has been demonstrated both theoretically and experimentally in microscopy that limitations occur with spatially-dependent aberrations [147]. When the sample of interest is spatially variant, as is normally the case with biological specimens, the FOV to which a single correction can be applied is very limited. Thus a better solution would be to place the DM at a plane conjugate to that where aberrations are most dominant in the sample, namely conjugate AO (CAO) [147–150], or better still, to use dual or multiple adaptive elements for different layers of correction, ultimately leading to multi-conjugate AO (MCAO) [151, 152]. It is important to understand the rationale behind each of these concepts to fully appreciate the potential of MCAO, as will be highlighted in Figure 3.7.

3.6.1 Limitations of pupil adaptive optics (PAO)

In PAO, a phase conjugate wavefront correction provided by the DM is measured from one object point (below referred to as "guide star") and applied uniformly to all points across the focal plane. However, for those displaced from the guide star, the correction rapidly becomes uncorrelated with localised aberrations, leading to the presence of two uncorrelated phase variations in the imaging optics, in which case the image quality would actually be degraded compared to when no corrections were applied, as seen in Figure 3.7(a). It has been theoretically derived that for RMS phase variations Φ of one radians or larger, correlated in a Gaussian manner over a length l_Φ that characterises the lateral variation frequency, and located a distance z away from

the object, the FOV over which PAO proves effective has a diameter of $a_0 \approx 2l_\Phi/\sqrt{1+2\Phi^2}$ [147]. This FOV becomes narrower with larger phase variations, ultimately approaching the limit of $\sqrt{2}l_\Phi/\Phi$, and is independent of the location z of the phase variation relative to the object.

3.6.2 Considerations for conjugate adaptive optics (CAO)

The disadvantage of PAO for large and spatially variant aberrations arises from the way a pupil-conjugate wavefront correction tracks multiple points in the FOV while aberrations in the sample are static [147]. This problem can be solved by locking the wavefront correction to a plane of dominant phase variation, as is the case with CAO, which will in effect expand the FOV to the DM aperture size demagnified onto this plane by imaging optics in between. The FOV advantage of CAO has been experimentally demonstrated in [150], seeing a 32-fold improvement in FOV for a phantom using non-transparent adhesive tape as turbid medium to image fluorescent beads, and a 15-fold improvement while imaging through 150 µm thick intact skull. However, several factors must be noted in order to take full advantage of CAO.

First of all, the effective FOV in CAO can be compromised in practice by the objective NA, which determines the maximum cone of light that can be collected from any object point. If the cone is large enough to span the demagnified DM at the plane of dominant phase variation for all object points, then CAO would work equally well throughout this FOV. On the other hand, if it is smaller than the demagnified DM, the DM will cause vignetting effects to the edge of the FOV dependent on the distance z, as is indicated in Figure 3.7(b).

Secondly, one should pay attention to the system tolerance of axial and lateral displacements in optimal wavefront correction relative to the nominal. An axial displacement can also be understood as the extent to which correction for a single layer of phase variation would be effective within a volume of tissue layers. This is of special importance, as in real samples the probability is very small that aberrations would take the form of a single dominant layer. This has been thoroughly investigated in [148], demonstrating that the maximum lateral displacement $\delta_{x_{max}} \approx l_\Phi/\Phi$ depends on the characteristic slope of the aberration itself, while the tolerance of axial displacement also depends on the objective NA and is greater than the lateral range by

a factor of around NA^{-1}. This finding has the implication of potential benefits in deep tissue imaging where a single conjugate correction would be effective for a large axial depth. However, one should notice that when using objectives with an NA larger than 1, as is the case with water and oil immersion objectives, the axial extent to which corrections are tolerated is less than that in the lateral direction and is therefore even more sensitive to the characteristic slopes of the aberration, suggesting low NA objectives for long axial range correction.

Finally, when applying CAO to point-scanning microscopy, there is an inherent compromise in the correction resolution as the beam translates within the DM aperture and only a sub-region can be used for wavefront correction at a single scan position. In this sense, the spatial frequency of the aberration correction is lower in comparison to performing PAO with the same DM. This final remark is one of the major considerations for implementing MCAO.

3.6.3 Introduction of multi-conjugate adaptive optics (MCAO)

The concept of MCAO was first proposed by Dicke [153] and further developed by Beckers [154] to correct for multiple turbulent layers of the atmosphere. In recent years it has also been adopted in the field of vision science [151], enabling the imaging of retinal features down to a few microns over a FOV three times larger than that in conventional AO systems. In the microscopy community, however, despite numerical simulations have been carried out [152], practical application is yet to be explored. Its basic concept will be introduced below and comparisons will be made with PAO and CAO.

An MCAO setup is much like the combination of PAO and CAO such that in addition to a DM set at the pupil plane, multiple DMs are placed in non-pupil planes conjugate to different depths in the sample that impart severe phase variations. Light corresponding to each object point passes through different sections of the conjugate DM and picks up varying phase patterns to correct for field-dependent aberrations. Two DMs are indicated in Figure 3.7(c) for simplicity. In practice, however, for the reason explained in Section 3.6.2, except for a small number of examples where a layer of dominant phase variation is present, such as atmospheric turbulence

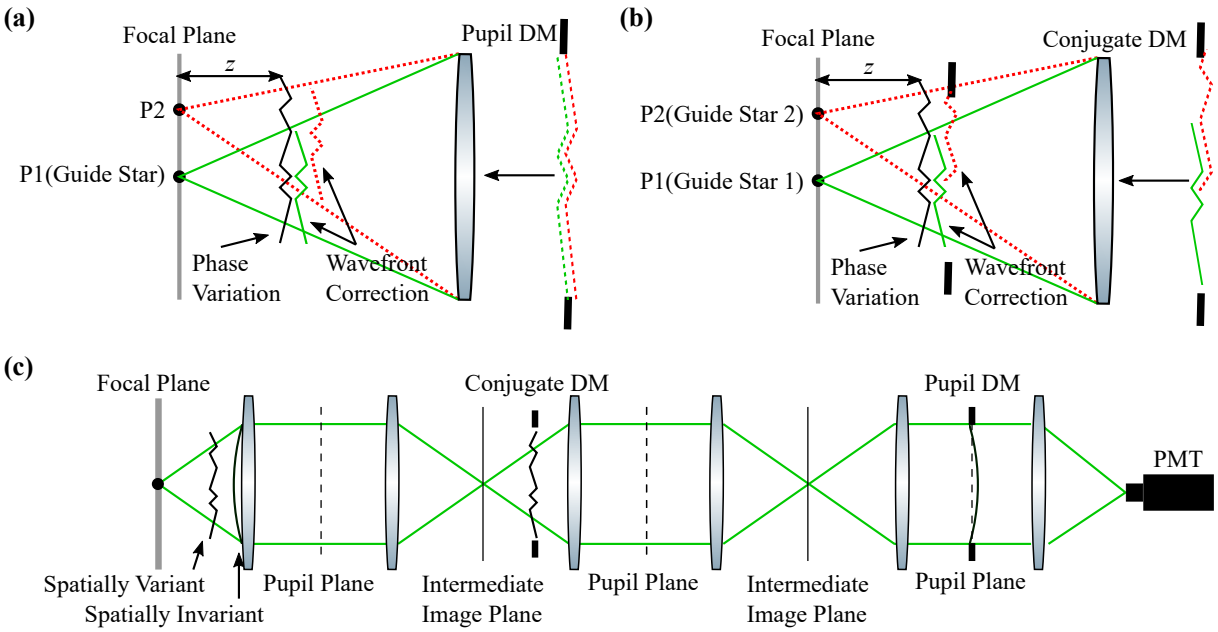


Figure 3.7: Rationale behind using MCAO. (a) In PAO, the wavefront correction of a displaced object point becomes uncorrelated with the localised phase variation. (b) In CAO, the wavefront correction of a displaced object point is correlated with the localised phase variation, but can get vignetted by the demagnified DM aperture. (c) System setup of MCAO using two DMs. Green solid line: central guide star. Red dotted line: displaced object point.

or the retina, in general aberrations can originate from all depths within the sample, for which reason multiple DMs or calculation of the depth-wise correction range would be required.

Apart from the significant FOV advantage MCAO possesses over PAO, compared to CAO its main difference lies in the presence of a pupil-conjugate correction. Why do we still need this? As previously mentioned, in CAO the beam is scanned across sub-sections of the conjugate DM, leading to a limited spatial resolution in the applicable phase correction. When a pupil-conjugate DM is employed, however, the beam is fixed on the full DM aperture, in effect being able to correct for high order residual aberrations, compensating for the loss of spatial resolution inherently brought by CAO. Another consideration is that when a DM with smaller actuator pitch and similar actuator count is used for the conjugate plane, its stroke (maximum amplitude of deformation) will inevitably decrease, making it incapable of correcting for large spatially invariant aberrations, justifying the need of a pupil-conjugate DM. Therefore, an MCAO system incorporating both a sample- and pupil-conjugate DM is theoretically more idealised for complete correction of both spatially variant and invariant aberrations.

Chapter 4

A compact and contactless reflectance confocal microscope (CCRCM) for neurosurgery

4.1 Overview

Visual guidance at the cellular level during neurosurgical procedures is essential for complete tumour resection. This chapter demonstrates the development of a compact reflectance confocal microscope with a 20 mm working distance (WD) that operates in the near-infrared and provides <1.2 µm spatial resolution over a 600 µm × 600 µm field of view (FOV).

The following sections are arranged as follows. The current status of image-guided brain surgery is first introduced along with limitations that motivate this project. Next, the design concept is discussed before presenting the microscope setup in detail. The performance of the optical design is then evaluated using Zemax software. System capability and robustness is systematically assessed in three biological specimens. First, 60-µm thick fixed mouse brain is used to validate spatial resolution and imaging fidelity in biological tissue. Optical sectioning abilities are then demonstrated through axial stack imaging and 3D reconstruction of frozen mouse calvaria. Live tissue imaging capability is verified through maximum intensity projections of 100-µm deep axial stacks in the rat organotypic hippocampus. Finally, novelties as well as space for future development of the system is discussed in view of the practical needs for next generation neurosurgical microscopes.

4.2 Current status of image-guided brain surgery

The primary aim in the treatment of brain cancer is maximal tumour resection with minimal damage to adjacent brain tissue. Numerous technologies have been developed to provide real-time intraoperative guidance in order to achieve this goal [17, 22, 155, 156]. In particular, specialised optical microscopes have shown to provide valuable morphological information during surgery, such as the ARveo Glow 800 surgical microscope (Leica Microsystems, Wetzlar, Germany) [19], the OPMI S5 (Carl Zeiss, Germany) [157], and the Pentero 900 (Carl Zeiss, Germany) [41]. However, most of these systems were not optimised to enable visualisation of individual cells. Low numerical aperture (NA) was used, normally below 0.07, to offer a WD of over 200 mm [53], and thus allow space for surgical manipulations. In addition, the bulky design of some systems makes it inconvenient for use in small operating rooms, suggesting the need for compact systems with a smaller footprint.

To overcome the limitation in spatial resolution, endoscopic probes have emerged and proven effective in delineating the tumour margin with higher precision [7, 18–20, 30, 33, 36, 37, 158]. In addition to improving the discrimination between diseased and normal cells, endoscopic probes are more compact than most specialised surgical microscopes, making them convenient for deployment in operating rooms. However, some practical complications have also been encountered during their use in clinical applications [19, 36]. One major drawback is that endoscopic devices require direct contact with tissue. They are therefore susceptible to erythrocyte contamination, and frequent cleaning of the probe tip is unavoidable [36]. Another caveat originates from the difficulty to stabilise and apply uniform pressure on the probe when held by hand [19].

In summary, it would be ideal to combine the highly desirable features of both endoscopes and specialised surgical microscopes into a single, compact system such that cellular level resolution can be achieved while eliminating the need for direct contact between instrument and tissue. This configuration would further allow for manipulation of surgical tools below the microscope objective using both hands as in conventional surgical microscopes.

Apart from system configuration, the employed contrast mechanism also affects the feasibility of adopting an imaging modality for intraoperative use. Fluorescence guided surgery, as

one of the most commonly exploited techniques, has provided useful information on the cellular and molecular scale for brain tumour resection [19, 21, 35, 38–41]. However, one intrinsic drawback of fluorescence imaging is the lack of tissue detail aside from the labelled features, which may lead to reduced specificity and unwanted damage to normal tissue [159]. In addition, the use of fluorescent dyes in the human brain is limited by many factors, such as tumour selectivity, fluorophore uptake due to the blood-brain-barrier, fluorophore brightness and toxicity, photobleaching, injection timings, dose constraints, etc. [83, 159–161]. Consequently, only three markers have been approved for neurosurgical procedures in humans, as introduced in Section 1.2.4. In particular, 5-ALA as a precursor of PpIX, which contributes to the heme synthesis pathway, has proven especially effective for high-grade glioma detection, contributing to substantially more complete resections than standard techniques, but shows less efficacy in low-grade gliomas and other tumour types [20, 161]. On the other hand, endogenous fluorophores, e.g. NADH and FAD, enable label-free fluorescence detection. However, low signal level and spectral specificity has prevented its common usage till the modern day [48]. Furthermore, most fluorophores mentioned in Section 1.2.4, except for ICG, excite and fluoresce in the visible light spectrum (VIS) where scattering effects are more prominent (see Section 1.2.1). Therefore, novel label-free intraoperative devices are in high demand.

Reflectance confocal microscopy (RCM) has for long been of special clinical interest due to its favourable optical sectioning abilities and label-free nature [17, 31, 34, 42]. The implementation of a pinhole in both the illumination and detection paths helps to eliminate out-of-focus light adjacent to the focal plane. Without being constrained by the excitation spectrum of a specific fluorophore, the choice of illumination wavelength is primarily dependent on optical properties of the tissue itself, with additional considerations for spatial resolution. Furthermore, compared to fluorescence microscopy, the signal level for RCM is usually much higher for a given incident power. Less light is required at the tissue, reducing potential possibilities of photodamage; while stringent requirements imposed on the detection sensitivity of fluorescence imaging can be loosened as well [40]. Most importantly, owing to a contrast mechanism based on differential refractive indices, RCM has recently been found to provide information on cellularity,

architecture, and morphological features simultaneously for tumour discrimination in *ex vivo* studies [17], showing great potential for surgical translation.

4.3 Materials and methods

4.3.1 Design concept

The design of the confocal reflectance microscope aims to overcome limitations of currently available neurosurgical systems, while considering the ease of translation from bench-top to clinic. Communication with clinicians suggested some requirements for improved surgical imaging, which are listed in Table 4.1. Specifically, a system WD sufficient for preventing direct contact with tissue and permitting insertion of surgical tools was a main priority. Second, an imaging FOV of around 1 mm was desirable. Another major goal was to provide a spatial resolution of $\sim$1 µm across the whole FOV such that cellular or even subcellular level examination could be accomplished. In addition, the image update rate should ideally be above 6 Hz or even approach 16 Hz for video rate display. Furthermore, system compactness was given special consideration to enable easy manoeuvring of the microscope in the operating theatre. Finally, to make this system affordable and reproducible, off-the-shelf rather than custom-designed lenses were used.

Table 4.1: Requirements for improved surgical imaging.

Parameters	Values
Working distance	few centimetres
Field of view (mm)	1
Resolution (µm)	1
Frame rate (Hz)	6

4.3.2 System setup

The main microscope design is illustrated in Figure 4.1(a). For reduced scattering, minimal blood absorption, minimal detection of hemoglobin, as well as negligible tissue autofluorescence, a near-infrared (NIR) wavelength of 830 nm was chosen [19, 64, 162] (see Section 1.2). A low coherence superluminescent diode (SLD, SLD830S-A20, Thorlabs) was used to suppress speckle

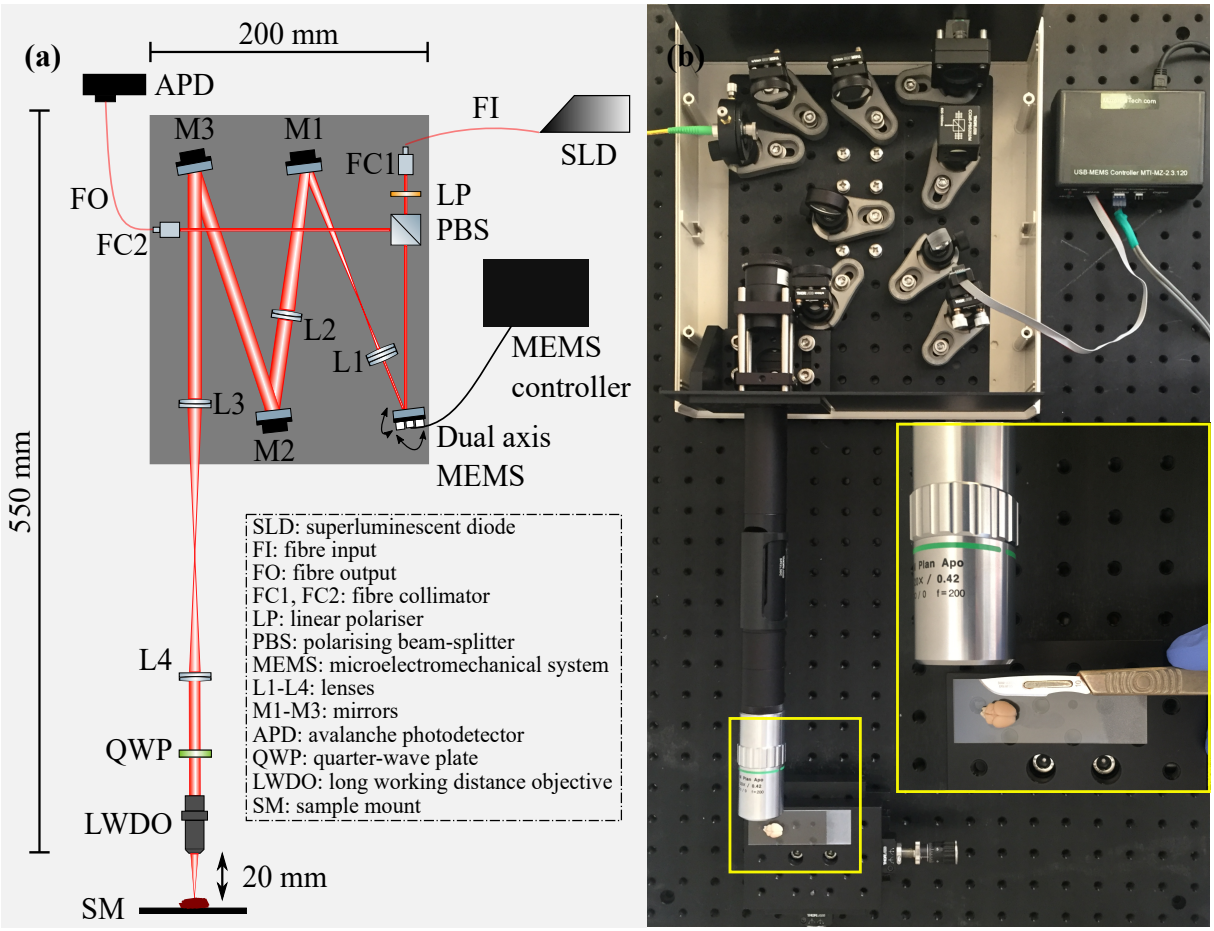


Figure 4.1: Microscope design and physical layout. (a) Schematic of the imaging system. Full description of components is given in the dotted box. (b) Physical layout of microscope system taking up a 200 mm × 550 mm bench-top footprint. Magnified view of a scalpel inserted between the microscope and sample is given in the inset.

noise without increasing the pinhole size [120]. Light was coupled into the system via a single mode fibre and power after the objective was set to 5 mW for all experiments. To minimise detection of backscattered light from components along the optical path, a quarter-wave plate (QWP) was implemented in combination with a linear polariser (LP) and a polarising beam-splitter (PBS). The LP generated horizontally-polarised illumination light, which transmitted through the PBS, before passing the QWP whose fast-axis was oriented 45° relative to the polarisation direction. The PBS then reflected vertically-polarised signal light into the detection path while any spurious horizontally-polarised light would be eliminated [43]. A compact gimbal-less dual-axis MEMS scan mirror (S31155, Mirrorcle Technologies) with a clear aperture of 2 mm

was integrated for system miniaturisation, providing a maximum mechanical scan angle (MSA) of ± 4.8° in both the horizontal and vertical directions. The choice of objective was most critical. The desire was to achieve a few centimetres WD between the microscope and tissue while maintaining an approximately 1 µm image resolution. A longer WD generally indicates a smaller NA which downgrades resolution. Taking into account also the NIR wavelength that suffers from a lower resolution compared to its VIS counterparts, a 20× magnification, 0.42 NA air immersion plan-apochromat objective (LWDO, MY20X-804, Mitutoyo) with a WD of 20 mm and clear aperture of 8.4 mm was chosen. Some practical constraints limited the choice of lens design. Above all, the objective back aperture (OBA) was 8.4 mm, a near 5× magnification relative to the 1.74 mm output diameter of the illumination source. In addition, some further developments of the system were in mind, such that the beam size needed to be expanded beyond 8.4 mm before demagnification to slightly overfill the OBA. For system miniaturisation, this required a lens with a reasonably small effective focal length (EFL), usually with a smaller diameter as well, immediately after the MEMS mirror. To prevent large magnitude aberrations during the raster-scanning process, a Hastings achromatic triplet was chosen for L1 as opposed to achromatic doublets used for L2–L4. In addition, special care was taken to prevent beam clipping from lenses in adjacent paths and vignetting due to large scan angles and magnifications. A full description of the chosen lens parameters is given in Table 4.2. In the detection path, backscattered signal light was coupled into an adjustable aspheric fibre collimator (FC2, CFC-11X-B, Thorlabs) with a focal length of 10 mm. A single mode fibre with a core size of 5 µm, equivalent to 0.7 Airy unit (AU), was used as a confocal pinhole to couple signal light into a silicon avalanche photodetector (APD, APD430A/M, Thorlabs). Components within the main microscope body were separately mounted on a 200 mm × 250 mm breadboard (MB2025/M, Thorlabs) and further enclosed in a protective casing. L4 and the QWP were mounted into lens tubes that extended from the microscope body and could be easily unscrewed for portable transit. A fibre-in fibre-out (FIFO) configuration was implemented for miniaturisation. The system footprint was kept to 200 mm × 550 mm and the physical layout of the system with a magnified view indicating the insertion of a scalpel between the microscope and sample is depicted in Figure 4.1(b).

Table 4.2: System lens parameters.

Lens No.	Lens Type	EFL (mm)	Lens Diameter (mm)	Model No.	Manufacturer
L1	Achromatic Triplet	25.4	15	30120	Edmund Optics
L2	Achromatic Doublet	175	25.4	49363	Edmund Optics
L3	Achromatic Doublet	125	25.4	49361	Edmund Optics
L4	Achromatic Doublet	100	25.4	49360	Edmund Optics

Scanning control and image acquisition were performed using a custom-developed Python software (Dr. Matthew Wincott made initial developments) via a standard laptop (XPS 15 7590, Dell) and FPGA (USB-7855R, National Instruments). Analog triangle wave scan signals were sent to the MEMS mirror controller and the analog detection signal from the APD was used for image construction. Distortion due to the non-linear velocity of the scan mirror was corrected using a pre-calibrated look-up table, the method of which will be discussed in Section 7.3. Images were displayed on the GUI interface at 1 Hz and later processed using ImageJ software.

4.3.3 Zemax evaluation of system aberrations

A compact optical system exclusively using commercial lenses is prone to aberrations, especially when large scan angles are required such that oblique beams enter short focal length lenses at peripheral positions. In order to determine a lens combination that causes minimal accumulation of system-induced aberrations using commercially available lenses throughout the whole FOV, the design was modelled and evaluated using Zemax software 18.9. As the objective lens model was not available, it was considered as an ideal lens, and imaging performance was analysed at the objective back focal plane. While this is not possible in reality, considering the choice of a low NA plan-apochromat objective, which is optimised for low order spherical aberration and field curvature, the estimations should permit high system resemblance.

Ideally, diffraction-limited performance (DLP) is highly desirable in microscopic systems. However, depending on the application, this is not always necessary. For our purpose, cellular level resolution is easily achievable within a 1 µm regime. As substantial beam expansions were required to fill the OBA, taking into consideration the use of relatively short focal length commercial lenses with a standard 1-inch diameter where large angle scan beams are prone to

entering some lenses at peripheral positions, rather than aiming for DLP that was likely to be achieved within only a narrow region about the optical axis, we slightly relaxed the criterion to obtain more uniform image quality across the whole FOV. A Strehl ratio of > 0.7 was sustained for the maximum $\pm$ 4.8° MSA, equivalent to an FOV of approximately 600 µm $\times$ 600 µm. Assuming a linear relationship between MSA and FOV using small angle approximation, system performance was evaluated at a series of MSAs across the full scan range with increments equivalent to 100 µm at the sample. The Strehl ratio, diffraction encircled energy, and Huygens point spread function (PSF) were individually assessed.

Strehl ratio

The Strehl ratio (SR) is commonly used as a performance criterion for high resolution imaging systems, as discussed in Section 3.2.4. The theoretical SR variations with different MSAs across both the x- and y-directions are shown in Figure 4.2(a), where the x- and y-axis were horizontal and vertical to the base plate, respectively. The Maréchal criterion of SR = 0.8 was used as reference for DLP. It could be seen that for all scan angles along both the x- and y-axis, the SR was kept well above 0.7. A symmetrical variation could be noticed across the FOV in both scan directions, most likely to have originated from the balancing of field flatness distortion at different lateral positions when optimising for the highest uniform SR. Comparison between the x-scan and y-scan curves indicated similar degrees of system-induced aberration such that the same SR was achieved for a certain scan angle. It could be noticed, however, that the system was slightly more aberrated along the x-axis at large angles, which may have originated from the fact that beams were folded multiple times in the horizontal plane at arbitrary angles, which led to larger magnitudes of horizontal tilt.

Diffraction encircled energy

Next, variations in the illumination PSF's size and energy distribution were examined by plotting the diffraction encircled energy diagram, as demonstrated in Figure 4.2(b), which is the percentage of total energy enclosed as a function of distance from the image centroid of a point object. Each curve referred to the gain of cumulative energy with radius for a different MSA,

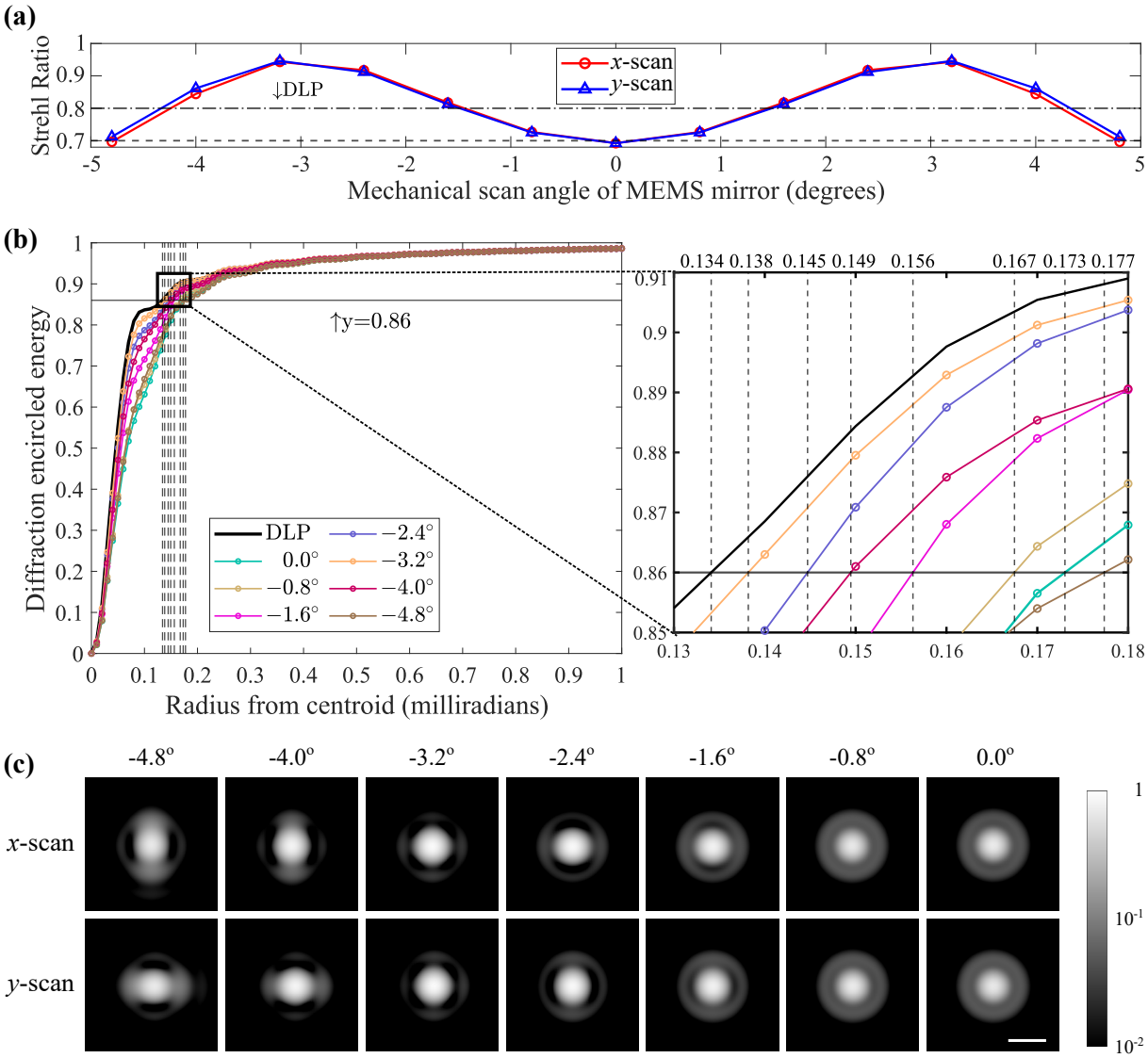


Figure 4.2: Zemax evaluation of system imaging performance. (a) Theoretical SR variation as a function of MEMS mirror MSAs in both x-(red) and y-directions (blue). The DLP of 0.8 SR at the objective back aperture and system optimisation result of 0.7 SR for all MSAs along both scan directions are indicated with horizontal lines. (b) Diffraction encircled energy versus radius from centroid in milliradians for different MSAs. Black curve is shown for DLP. Solid black line marks 86% of the total energy. Magnified plot highlights radius values at which the diffraction encircled energy reach 86% of the total energy for DLP and all other MSAs. (c) Huygens PSF profiles across a half FOV for both x- and y-scans. Intensity is individually normalised and displayed on a logarithmic scale. Scale bar: 200 milliradians.

and that for DLP was highlighted in black as reference. Only results for negative scan angles were plotted due to the symmetry witnessed in Figure 4.2(a). It could be found that all scan angles followed a similar steep accumulation trend of energy comparable to that of DLP, and

the degree of similarity closely followed the trend of the SR value seen in Figure 4.2(a). To assess the degree of deterioration in PSF size brought by relaxation of the SR, with consideration that the far field emission profile of an SLD does not closely resemble that of a Gaussian laser beam [163], the PSF's full width at half maximum (FWHM) was calculated at different MSAs by first taking the $1/e^2$ width of the PSF, within which 86% of total beam power was contained, and further considering a conversion factor of $\sqrt{2}/\sqrt{\ln 2}$. The radius values in milliradians at which the diffraction encircled energy curves reached 86% of the total energy for DLP and all other MSAs were highlighted in the magnified plot of Figure 4.2(b). Considering a focal length of $f = 100$ mm for L4, and a $20\times$ demagnification introduced by the objective lens, as well as assuming a similar intensity PSF (IPSF) for both the illumination and detection paths, the effective system IPSF $1/e^2$ width and FWHM was calculated and given in Table 4.3.

Results showed that despite system optimisation resulted in an SR of 0.7, the FWHM of the illumination IPSF was kept well within 1 µm across the whole 600 µm × 600 µm FOV, and the largest deviation relative to DLP was ∼100 nm, a negligible amount for cellular level imaging.

Huygens PSF

Finally, to understand the main aberration components in the system, the Huygens PSF, which is the PSF directly integrated using the Huygens wavelets method, was assessed for half the FOV along both x- and y-scan directions. It could be observed in Figure 4.2(c) that for both cases, the shape of the PSF started to deviate from an ideal circular spot for larger angles between $-3.2°$ and $-4.0°$ and became elongated in one direction, showing moderate astigmatism. Defocus and spherical aberrations were the main on-axis aberration components, as could be seen from the annular structures surrounding the bright central region. However, no significant variations in

Table 4.3: Theoretical $1/e^2$ width and FWHM of effective IPSF for DLP and different MSAs in the proposed confocal system.

	DLP	$-4.8°$	$-4.0°$	$-3.2°$	$-2.4°$	$-1.6°$	$-0.8°$	$-0.0°$
$1/e^2$ width (µm)	1.16	1.33	1.22	1.17	1.20	1.25	1.30	1.32
FWHM (µm)	0.68	0.78	0.72	0.69	0.71	0.74	0.76	0.77

PSF profile were noticed in either directions, indicating a reasonably uniform image quality for the entire 600 µm × 600 µm FOV.

4.3.4 Reflectance imaging

Spatial resolution was calibrated using a stage micrometer with 1 µm line width (AGL4202, Agar Scientific) placed at the central FOV. A profile plot of the line showed a FWHM of around 1.10 µm (please refer to Figure 7.4(b), right; and Figure 7.5(a)) with a ±5% measurement error. Figure 7.4(b), right showed no noticeable difference in resolution between the central and edge regions within a 50 µm FOV. However, for a more rigorous examination of field effects, a profile plot should also be acquired at the edge of the 600 µm FOV. Effective image intensity in a reflectance confocal microscope is given by $I_{eff} = |(h_{ill} \cdot h_{det}) \otimes o_r|^2$, where h_{ill} and h_{det} denote the illumination and detection amplitude PSF (APSF) and o_r represents the object reflectance profile, as discussed in Section 2.6.1. For simplicity, a Gaussian approximation was used for h_{ill}, h_{det} and o_r, and a similar distribution of the illumination and detection APSF was assumed such that $h_{ill} = h_{det} = h_a$. Further considering the relation of $h_{eff} = |h_a|^4$ between effective system IPSF h_{eff} and single path APSF h_a in a confocal system, the FWHM of h_{eff} was calculated to be 0.84 µm. Comparison was made between the experimentally derived effective IPSF and the result in Table 4.3 for FWHM at 0.0° MSA. It could be seen that the built confocal system provided an effective IPSF consistent with that of the theoretical system, with only a 7% increase in size. Additionally, a spatial resolution of <1.2 µm could be resolved in the reflectance images. Axial resolution was not specifically examined within this chapter, but can be referred to Chapter 7.

During experiments, a manual translation stage (PT3A/M, Thorlabs) was used for 3D translation of specimens. Imaging took place with the microscope mounted both horizontally and vertically on a mechanical arm. No visible difference in image quality was noticed, indicating the microscope's ability to perform reliably in all orientations. In the results below, the pixel spacing was decreased to ∼1.17 µm to image a 600 µm × 600 µm FOV with 512 × 512 pixels, such that a near 2 µm lateral resolution was expected according to Nyquist sampling, and lim-

ited by the pixel resolution only. For a smaller FOV with finer pixel spacing, a <1.2 µm optical resolution was obtained.

4.3.5 Sample preparation

System capability and robustness were systematically validated using three biological specimens: 1) 60-µm thick fixed brain slice from a Thy1-GFP mouse; 2) excised mouse calvaria; 3) 350-µm thick organotypic hippocampal slice from a male Wistar rat. All animal work was carried out in accordance with the Animals (Scientific Procedures) Act, 1986 (UK), and samples were prepared by Carla Schmidt and Dr. Raphaël Turcotte.

Thy1-GFP mice were overdosed with pentobarbital before transcardial perfusion with phosphate buffered saline and 4% paraformaldehyde (PFA). Subsequently, the fixed brain was extracted and immersed in PFA for 24 hours. Finally, the fixed brain was cut into 60-µm thick coronal slices and mounted between a microscope slide and a 170-µm coverslip for imaging.

Calvaria was extracted from frozen mouse cadavers using scissors. The left portion of the calvarial bone between the frontal and coronal suture was then cut and glued onto a microscope slide for imaging. Imaging was performed in air.

Organotypic hippocampal slices (350-µm thick) were prepared from male Wistar rats (P7) and cultured on Millicell CM membranes (Millipore). Slices were maintained in culture media (Life Technologies/Sigma Aldrich), at 37°C for 7∼14 days prior to use. Culture media was replaced every 2∼3 days. Cultured slices were transferred to a petri dish, fixed with vacuum grease and kept in physiological Tyrode's solution for imaging (in mM: 120 NaCl, 2.5 KCl, 30 glucose, 2 $CaCl_2$, 1 $MgCl_2$, and 20 HEPES; Sigma Aldrich; pH = 7.2∼7.4; $n = 1.33$).

4.4 Experimental results

4.4.1 *Ex vivo* imaging of fixed mouse brain

Taking advantage of the well-known anatomy and morphology of the mouse brain, fixed slices were imaged to characterise system spatial resolution and imaging fidelity in biological tissue.

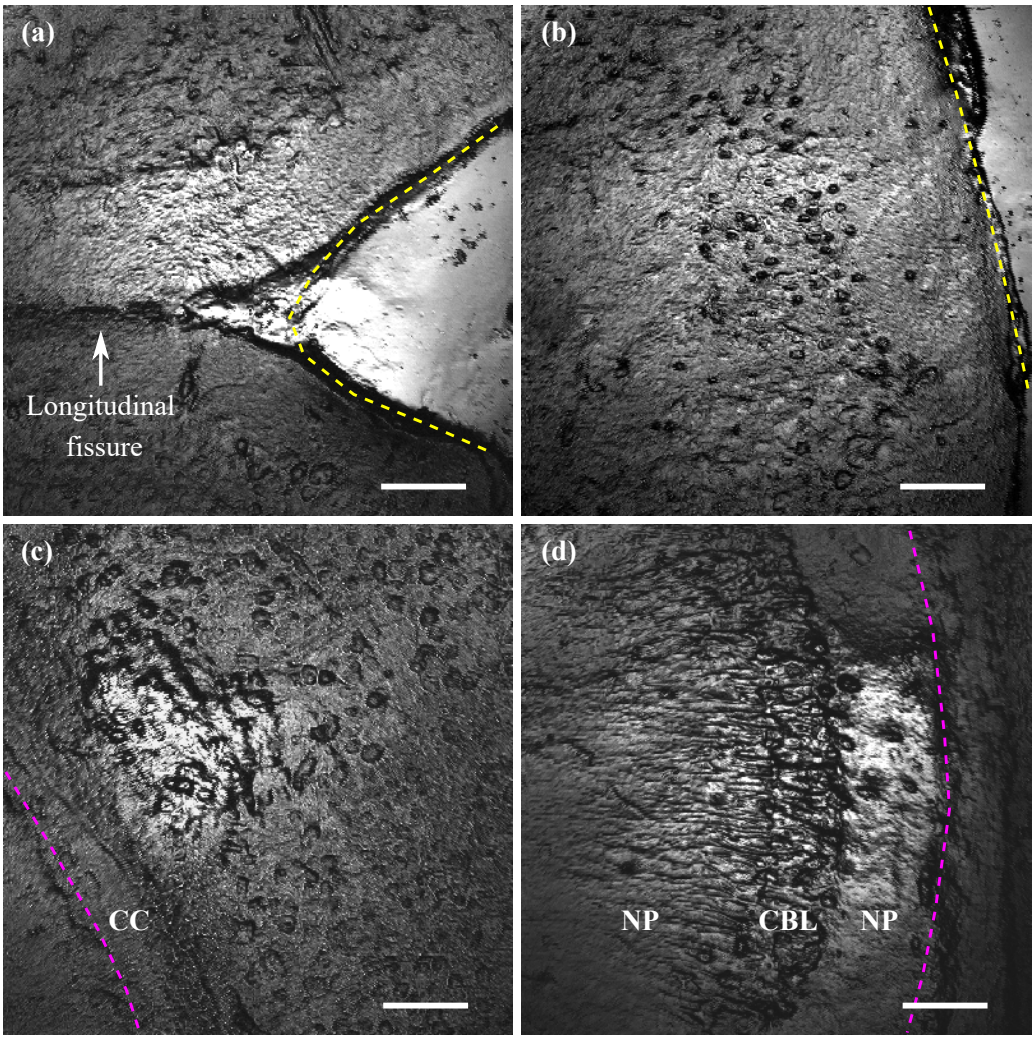


Figure 4.3: Single depth imaging of 60-µm thick fixed brain slice from a Thy1-GFP mouse. (a) Top-most border of cerebral cortex showing longitudinal fissure. Yellow line: edge of sample. (b) Upper cortical region displaying densely packed dark neurons. Adjacent regions above and below featured sparser distributions of scattered cells. (c) Lower cortical region featuring the corpus callosum (CC) and neurons of varying sizes. Magenta line: outer border of the hippocampus. (d) CA1 field of the hippocampus. Pyramidal cells formed a neat hypo-reflective cell body layer (CBL). Neuronal processes (NP) were distinguished as distinct dark grooves projecting from the CA1 neurons, as well as regions with high reflective signal. Scale bar: 100 µm.

The longitudinal fissure, separating the left and right hemispheres, was located at the top-most border of the cerebral cortex (Figure 4.3(a)). Figure 4.3(b) shows prominent dark neurons within the upper cortical region. Adjacent regions above and below featured much sparser distributions of scattered cells. The corpus callosum (CC) was recognised as a clearly discernable fibre tract in the lower cortical region (Figure 4.3(c)), separating the outer cortex from the

hippocampus. Just before reaching the CC, sparsely distributed neurons of varying sizes were witnessed. Figure 4.3(d) shows the CA1 field of the hippocampus. As expected, a neatly defined hypo-reflective cell body layer (CBL) was formed by CA1 pyramidal cells; while adjacent neuronal processes (NPs) were distinguished as distinct dark grooves projecting from the CA1 neurons in a parallel configuration, as well as regions with high reflective signal.

The results above suggested high spatial resolution and imaging fidelity of the microscope within biological tissue. The 170-µm coverslip is liable to introduce spherical aberration when used with an air immersion objective without coverslip correction. Although this effect is more detrimental with high-NA objectives, especially in the presence of sample tilt [164], slight blurring effects are still likely to be present during imaging. Also, a slight pixel shift is noticed between consecutive lines which may have been a residual artefact from the MEMS scanning after distortion compensation. Nevertheless, it is demonstrated that the proposed system utilising RCM, has the potential of imaging morphological features of the mouse cortex and hippocampus without any form of labelling [165, 166].

4.4.2 *Ex vivo* imaging of frozen mouse calvaria

The mouse calvaria is known to be highly scattering, and its significant surface curvature causes further deterioration of the light field for optical microscopy [167]. Here it is shown that the RCM system maintained sufficient optical sectioning, even when severe optical distortions were present, to achieve 3D imaging at the cellular level. Two different locations were imaged: the first where the bone surface was approximately normal to the optical axis, and the second where it was tilted by several degrees. Distinct features in hard bone and bone marrow demonstrated the axial sectioning ability when volumetric data was acquired with 5-µm axial steps (Figure 4.4).

At the first location, the hard bone matrix covered the entirety of the FOV (Figure 4.4(a)). A magnified view of osteocytes is given in the inset, visualised by negative contrast with the strongly reflective collagen bone matrix [168]. The transition between hard bone and bone marrow was clearly discernable as a sharp and curved interface (Figure 4.4(b); dotted line), confirming the microscope's optical sectioning ability, and suggesting an axial resolution of

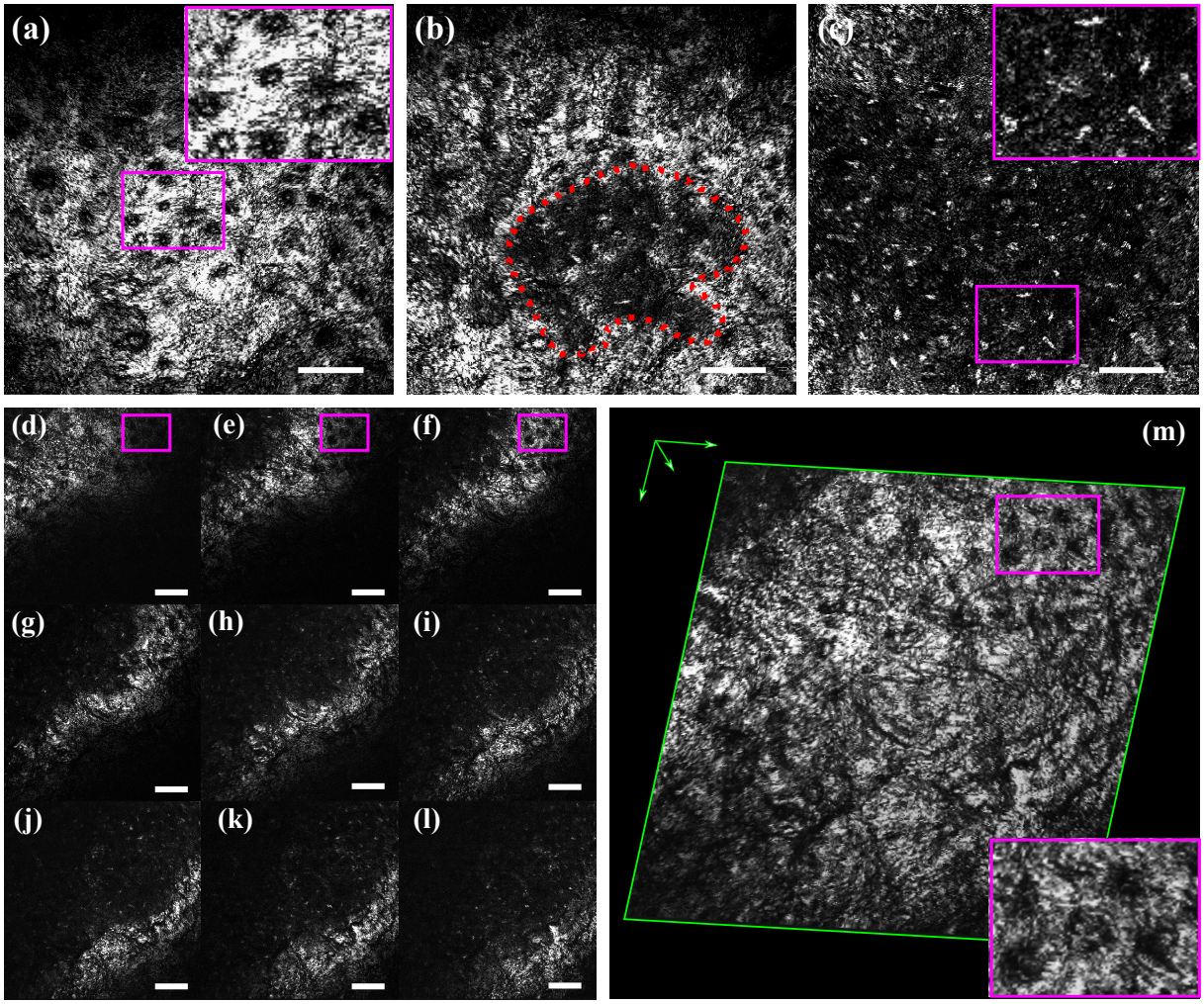


Figure 4.4: Volumetric imaging of the mouse calvaria at locations where the bone surface was approximately (a)–(c) normal to the optical axis and (d)–(m) tilted by several degrees. (a) In the hard bone, the locations of osteocytes were revealed by negative contrast from the bright hard bone matrix. (b) The top surface of a bone marrow cavity was observed 45 µm below the hard bone surface. A sharp interface was visible between the hard bone and bone marrow (dotted line). (c) A further 5 µm deeper, the bone marrow cavity was larger, occupying almost the entirety of the FOV. (d)–(l) Consecutive slices within the calvaria showing a distinct cross-section of the hard bone matrix at each depth. Osteocytes within magenta boxes gradually come into focus from (d) to (f). (m) 3D reconstruction of (d)–(l) showed a smooth transition of the bone surface. The similar osteocyte pattern as in (d)–(f) was observed. Scale bar: 100 µm.

about 5 µm within highly scattering biological tissue, which is in the region of the theoretical axial resolution of 6.5 µm. The bone marrow cavity appeared to be less reflective than hard bone, likely as a consequence of the freezing process (Figure 4.4(c)), while scattered bright cells

were nonetheless clearly identifiable. Nine 5-µm thick stack images were taken before reaching the transition zone, indicating a hard bone thickness of approximately 45 µm.

At the second location, nine consecutive axial-stack images were taken (Figure 4.4(d)–(l)) and due to surface tilt, only a distinct cross-section of the hard bone matrix was visible within the focal plane at each incrementing depth, showing a diagonal progression pattern from the top left corner to bottom right. After performing 3D reconstruction of the consecutive stack images, the surface of the hard bone matrix could be visualised (Figure 4.4(m)), showing smooth transition and featuring the same osteocyte pattern indicated within boxes in Figure 4.4(d)–(f). Note how the osteocytes gradually come into focus from Figure 4.4(d) to Figure 4.4(f).

The above results provided validation of the microscope penetration through optically dense and highly scattering media, as well as its optical sectioning capability across the whole FOV.

4.4.3 Live tissue imaging of the rat hippocampus

In the final experiment, to verify the live tissue imaging capability of the microscope, a 350-µm thick organotypic hippocampal slice was chosen and a thick layer of Tyrode's solution was inserted between air and tissue to mimic an aqueous physiological interface.

Figure 4.5(a) illustrates the rat hippocampus highlighting three biologically significant regions, namely the dentate gyrus (DG), CA3 field, and CA1 field. A 100-µm deep axial-stack with 5-µm intervals was taken for each region and a maximum intensity projection (MIP) was performed to build the 100-µm thick volume. Demonstration of the maximum projected hippocampal slice is given with rotational views at 0°, 30°, and 60° relative to the normal projection (Figures 4.5(b)–(d)). An image from a single location 100 µm deep in the sample is also shown.

Imaging started at the DG (Figure 4.5(b)) which was acutely bent in shape. A dark granular cell layer was visible in the central region of interest. Adjacent regions of NPs showed high reflectivity and dense fibrillarity, forming strong contrast against the neuronal cell bodies. MIP of the CA3 field revealed a narrower layer of NPs towards the edge of the hippocampus, surrounding a region of dark pyramidal cells (Figure 4.5(c)). Visible reflective signal contrast was also seen

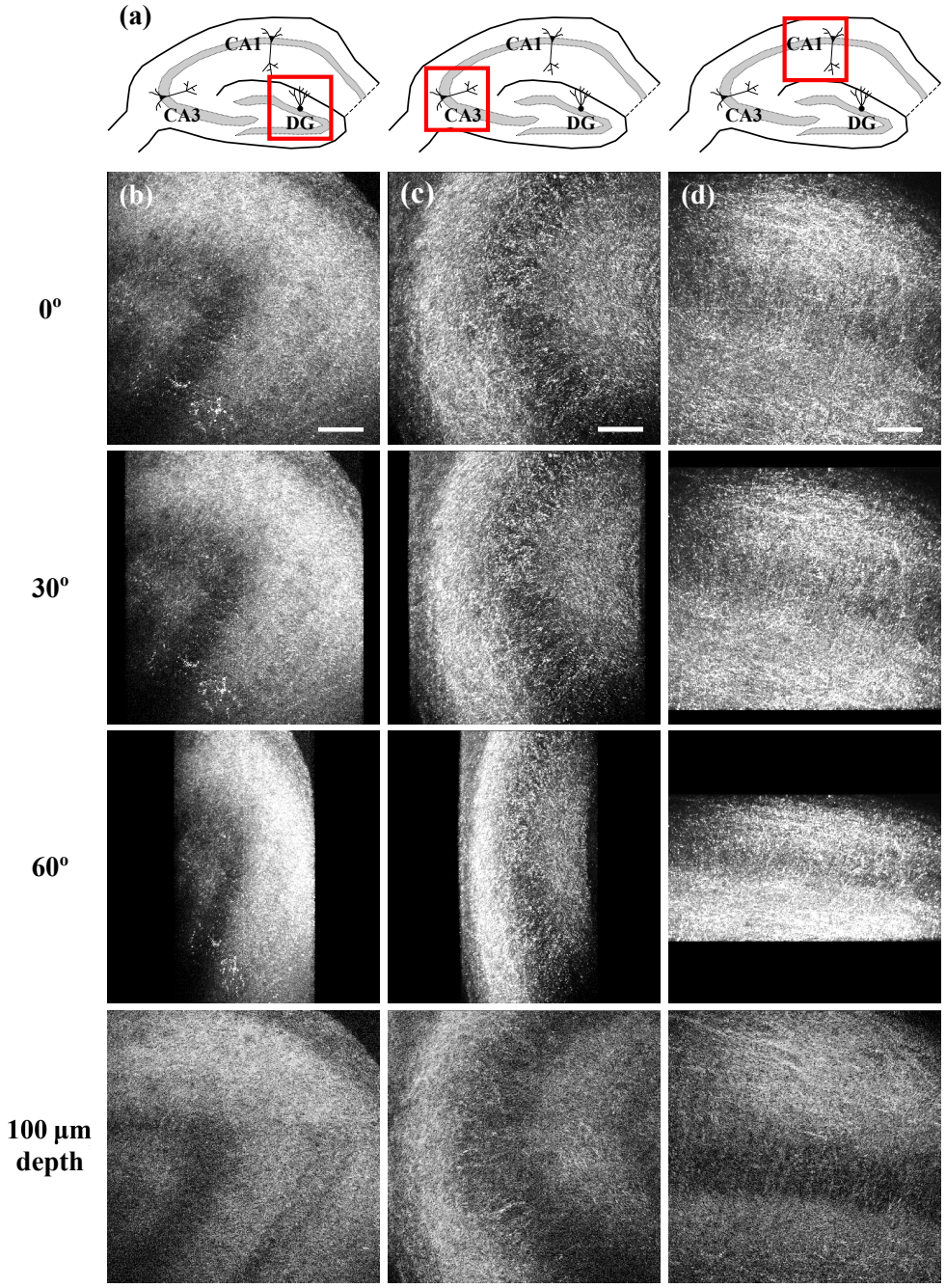


Figure 4.5: Rotational views of maximum projected 100-µm deep organotypic hippocampal slices at 0°, 30°, and 60° relative to the normal projection. (a) Schematic diagram of the rat hippocampus. Solid red boxes indicate imaging regions for (b)–(d). DG: dentate gyrus. (b) MIP of the DG showed a dark granular cell layer and adjacent regions of NPs with high reflectivity and dense fibrillarity. (c) MIP of the CA3 field showed a narrower layer of NPs surrounding a region of dark pyramidal cells. (d) Visible reflective signal contrast was also seen between the cell bodies and NPs in the CA1 field. An image from 100 µm deep in the sample is shown for each imaging region. Scale bar: 100 µm.

between the cell bodies and NPs in the CA1 field, though lower than its CA3 counterpart (Figure 4.5(d)).

Successful imaging of the live hippocampus up to 100 µm in depth validated the capability of the proposed microscope for live tissue imaging before translation to pre-clinical experiments. It should be mentioned that although RCM has been previously reported for live tissue and *in vivo* imaging of the mouse brain [43, 169], as well as imaging of the fresh human cadaver [170], rather than using a high NA objective lens for deep brain imaging, we have adopted a low NA (0.42) air immersion objective. In addition, compared with results obtained in Section 4.4.1, it can be found that due to the fixation method for *ex vivo* imaging, as well as a loss of aqueous tissue contents, different characteristics were observed between fixed and live brain tissue. This took the form of a highly reflective background with individual dark cells seen in the fixed brain slice, as opposed to the dark background, bright fibrous filaments, and dark band of cells in the live hippocampus.

4.5 Discussion and conclusion

This chapter presented the development, characterisation, and biological demonstrations of a compact microscope using off-the-shelf components for image guidance during neurosurgery. The system achieved a lateral spatial resolution of $<1.2\,\mu m$ and imaging speed of 1 Hz while leaving a 20 mm WD between the device and tissue to prevent direct contact and enable easy manipulation of surgical tools. Taking advantage of RCM, the proposed system is label-free and possesses three-dimensional imaging capabilities. The potential for pre-clinical translation is experimentally validated in distinct biological specimens: fixed mouse brain, frozen mouse calvaria, and organotypic hippocampal slice. This study provides initial ground for future development towards next generation neurosurgical microscopes while also leaving space for prospects in other areas of surgical imaging, which will be discussed in detail below.

Many factors influence the effectiveness of a device for image-guided brain surgery, which can be briefly split into two categories. The first incorporates intrinsic functionality features of the instrument, such as resolution, FOV, imaging depth, frame rate, contrast mechanism, etc.

The second, however, is equally important but much easier to neglect, which is the fact that instrumentation should be designed in such a way that its full functional advantage could be exerted with minimum effort in real life scenarios.

The RCM presented in this work fills a substantial gap in surgical practice. Specifically, key features of conventional surgical microscopes and endoscopic probes were combined such that cellular level resolution was achieved, while enough space was left between device and tissue to prevent direct contact and frequent probe cleaning, as well as allow for insertion of surgical tools. A minimal number of off-the-shelf components was used with considerations for compactness, affordability and reproducibility. Sufficient resolution was provided both laterally and axially to discern fibrillar structures as well as delineate the border of tissue layers, and imaging was achieved at least 100 µm within live tissue, suggesting the system's competence for clinical translation. Comparison between images of fixed and live brain tissue revealed instructive information on how variations in cell and tissue morphology could possibly change the refractive index to give different textures under the proposed microscope. This has interesting clinical implications and agrees with findings described in [17, 31, 34].

In addition, the concept entails some practical advantages. A combination of NIR illumination with fibre-based detection reduces the system's susceptibility to room light interference, which is normally in the visible light spectrum [171], implying that surgical procedures could be performed under normal lighting conditions [40]. Longer wavelengths would further decrease interference of ambient light as well as increase the imaging depth [43, 64, 172], but at the expense of a reduced spatial resolution. In addition, benefiting from a label-free and contactless concept, imaging requires no additional labelling of the tissue or excessive sterilization processes of endoscopic probes, enabling simplification of pre-surgical procedures.

Further system development should mainly address the following aspects: imaging speed and depth. First of all, the current frame rate is limited by the analog sampling rate to 1 Hz at 600 µm × 600 µm FOV. The implementation of a scanning module with position feedback would enable operation in resonant mode and thus substantially increase the frame rate to around 6 Hz [173]. To achieve this, a high-speed digitiser could be used to increase capture speed, through which images of higher diagnostic quality could be displayed with pixel res-

olutions higher than 512 × 512. In the current system, for the maximum imaging FOV of 600 µm × 600 µm, resolution is limited by pixel count rather than optical restrictions. A faster scan mirror could further enhance imaging speed, but current integrated MEMS technology would require using mirrors with smaller clear apertures, thus needing larger beam expansions before the OBA, ultimately introducing stronger system aberrations. In addition, a drawback entailed to faster imaging speed is that less signal will be collected for a single frame and a drop in image contrast may be experienced. The refractive index mismatch of cells and tissue structures [27, 42, 67, 68, 70] as well as scattering from smaller organelles [72, 73] that together generate reflectance contrast will not change. Consequently, the imaging depth may be compromised such that its extent of trade-off for imaging speed would require further investigation.

Secondly, the implementation of a wavefront shaping device, such as a deformable mirror (DM), would be extremely beneficial for performing simultaneous adaptive optics (AO) and remote focusing (RF), see Chapter 3. Correction of both sample- and system-induced aberrations would allow a tighter focal spot to arrive at the specimen and more signal to be delivered through the detection pinhole so as to improve signal-to-noise ratio and permit deeper imaging into the highly heterogeneous brain tissue [89, 91]. This can be related to the results obtained in Section 4.4.3, where the limiting factor was low contrast throughout the imaging session. It would be ideal to image deeper so as to prevent unnecessary resection of normal tissue beneath. Taking advantage of the DM also for RF abandons the need for a piezo objective scanner to refocus along the axial direction. In comparison, the DM enjoys much higher dynamic speed and resolution, which would contribute towards a more compact system design, and the ability to rapidly and precisely refocus within the tissue. The combination of a deeper imaging depth and a more accurate refocusing unit together with the optical sectioning abilities of the confocal microscope would be especially useful for finding the three-dimensional tumour margin.

Some variations of OCT, such as spectral/Fourier domain optical coherence microscopy (see Section 1.1.3), can potentially provide a deeper tissue penetration depth of over 1 mm [59, 61, 62]. However, system complexity is higher, and a high-NA water immersion objective is required to obtain a comparable lateral resolution of ∼1 µm. In addition, the corresponding FOV of a single image is approximately 620 µm [60, 61], which is similar to the proposed system, though

mosaic imaging can be implemented for expansion of the FOV [60]. The use of mosaic imaging would be a promising direction to explore for this application as well.

Upon the results discussed in this chapter, apart from further system development, more intensive work should also be conducted on pre-clinical validation of the instrument's sensitivity and specificity in detecting different types of tumour, which is likely to be in comparison with more mature and standardised techniques known to the current day, such as biopsies stained with hematoxylin and eosin (H&E) and 5-ALA. Special focus should be placed on the instrument's ability to extract sufficient information for decision making, by exerting its potential to provide a full scope of cellular and tissue level details. It is most likely that certain types of tumour prone to giving more contrast will benefit more from the application. Acquisition of empirical verification on this hypothesis is of great importance. Functionality tests of the microscope under intraoperative procedures need also be performed to search for underlying pitfalls. One example of this may be an inadequateness to tackle overhanging margins [159]. Although the microscope has been verified to sustain similar image quality under both horizontal and vertical orientations, considering that the problem is common also to endoscopic imaging, it might well be the case here. An optional solution is to switch to a flexible probe for this specific purpose, as a practical add on to the surgical procedure.

Although this work most addresses the needs of brain surgery, the application is by no means confined to this field, but relates to all scenarios that would benefit from label-free, contactless, and high resolution imaging. Ideally, this includes all surgical procedures. However, two criteria should be met in order for the system to perform effectively during cancer treatment: 1) distinct changes in cell or tissue structure that lead to variations in the refractive index should occur to provide contrast for diagnostics, either in the form of morphology or distribution; 2) traditional treatment procedures should involve exposing the wound to open air. Therefore, in some particular areas it would see more effectiveness than others. One of these fields is dermatology. RCM has seen great promise for detection of skin cancer margins due to unique sources of contrast delivered by melanin in melanocytes and pigmented keratinocytes, as well as keratin and collagen [66–68, 174]. However, contact is usually required between the microscope and skin either via a tissue ring attached with a polycarbonate optical window or a small tip. In the case of an

open wound, multiple layers of immersion and sterilisation agents are also applied between the wound and objective lens, which significantly complicates the imaging procedure. By adopting the proposed contactless technique, optical window inserts and excessive agent administration processes can be eliminated, with the additional convenience of simultaneous imaging and resection at the cellular level. Some other applicable areas may include pancreatic cancer [175], liver cancer [176], and microscopic confirmation of tumour clearance for bone tumour [177]. Finally, one application that would be of interest to the wider audience is simultaneous imaging of tissue morphology and microcirculation [178, 179]. In comparison to fluorescence techniques, the proposed system incorporates the ability to visualise blood cells, vessels, tissue structures and other functional cells at the same time without application of multiple fluorescent agents and immersion media, paving the path for general diagnostic potential.

Chapter 5

SenAOReFoc: A closed-loop sensor-based adaptive optics and remote focusing control software

5.1 Overview

It was discussed in the previous chapter that the compact and contactless reflectance confocal microscope would benefit from adaptive optics (AO) and remote focusing (RF). *SenAOReFoc* is a closed-loop sensor-based AO and RF control software that was originally developed for this purpose and works with a deformable mirror (DM) and a Shack-Hartmann wavefront sensor (SHWS). Later, a general need was identified for the wider community. Background research showed that a range of software serving for different astronomical purposes have been introduced over time, including those for simulation of AO systems [180, 181], control with atmospheric tomography [182], and fast control using GPU hardware [183]. In the microscopy community, software is also openly available for AO modelling and analysis [184], as well as general AO control [185]. However, there is not yet an existing open-source software that serves the purpose of performing both closed-loop AO and RF within the single package, despite that the techniques are widely used. As a result, time and effort has to be spent reimplementing existing techniques for different hardware systems. In addition, although many less conventional algorithms that aim to solve particular problems have been reported in various papers, without a software to integrate them into the mainstream workflow, they are less likely to be widely adopted.

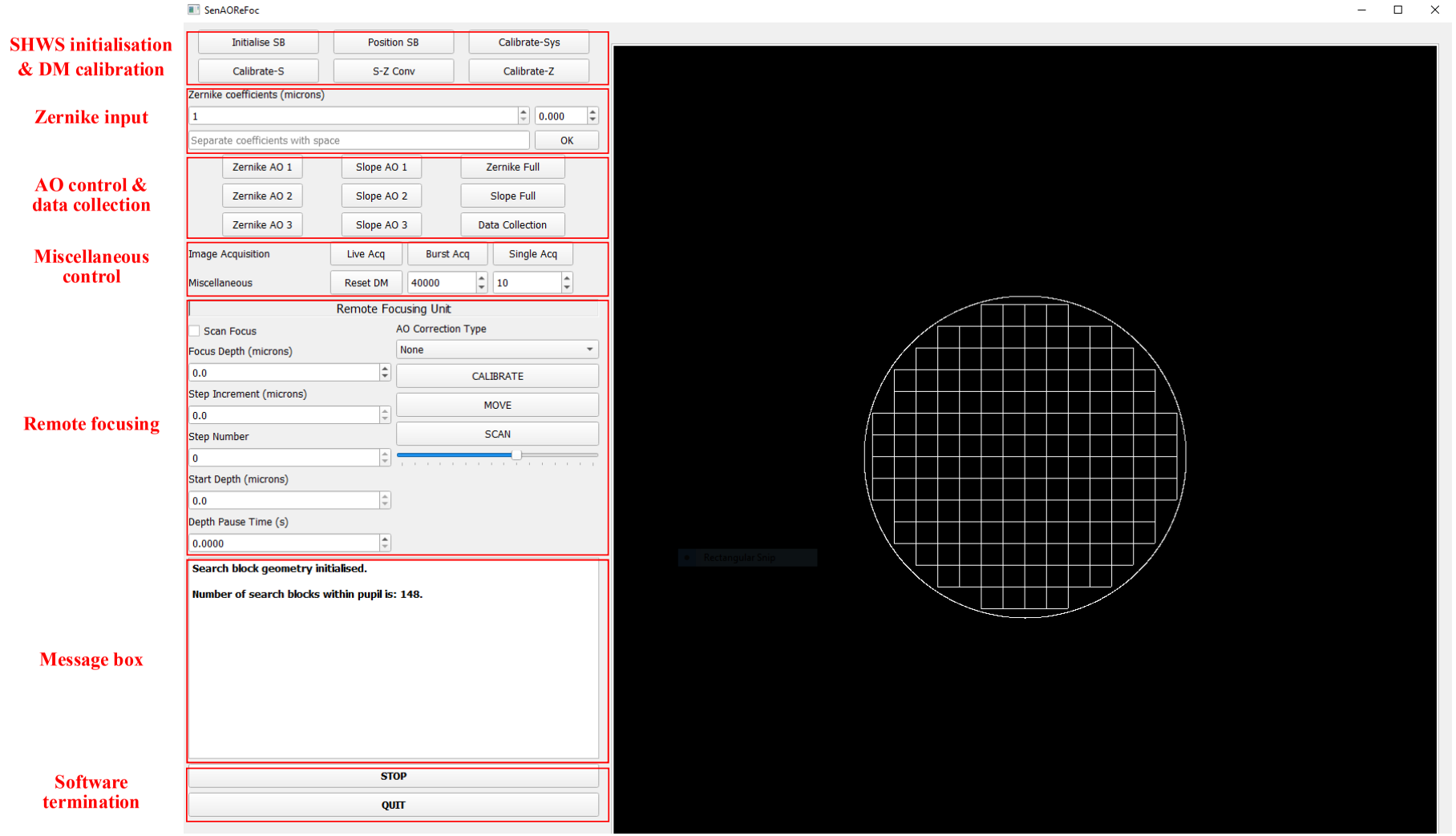


Figure 5.1: Graphic user interface (GUI) of *SenAOReFoc* with individual functional units indicated in red boxes.

SenAOReFoc aims to fill this gap and to make closed-loop sensor-based AO [145] and RF more easily accessible to the microscopy community, while at the same time integrate algorithms that aim to solve specific problems into the mainstream workflow. It has been designed for open development and easy integration into existing adaptive optical microscopes with a simple and user-friendly architecture. Software functionality has been tested on different operating systems (Windows/Linux/macOS) for generality. Finally, *SenAOReFoc* takes care of some reported issues in the field, such as the thermal effects of electromagnetic DMs [186], and obscured search blocks in the case of severely distorted pupils [187–189]. In the former case, an option is provided to exercise the DM membrane by sending routine sets of random control voltages to the actuators upon software initialisation. In the latter case, control algorithms for both the zonal and modal methods are modified as compared to the standard case to ensure the orthogonality of control.

The software is written in Python and is now publicly available on GitHub `https://github.com/jiahecui/SenAOReFoc`. In the following sections, a brief description of the software functionalities is first given before discussing the details of each modular unit in sequence.

5.2 Description of software functionalities

SenAOReFoc consists of 5 main units, the SHWS initialisation and DM calibration unit, the Zernike aberration input unit, the AO control and data collection unit, the miscellaneous control unit, and the remote focusing unit, as shown in Figure 5.1. The software can be run in either 'debug mode' to perform functionality tests without connected hardware (DM and SHWS), or 'standard mode' on a well-aligned optical sectioning microscope (confocal, multiphoton, etc.). The software fully operates in Windows under both 'debug mode' and 'standard mode' for hardware control. For Linux and macOS, functionality tests in 'debug mode' passes for both systems when hardware packages are not imported. Python-bindings for Ximea cameras and Python 3.8-binding for Alpao DMs are compatible with Linux systems, and other Python-bindings for Alpao DMs in Linux should also be compatible following their release. User-controllable system parameters can be freely accessed and modified in a separate configuration file that is loaded upon software initialisation, and parameters that require continuous user input can be modified

from the GUI. Parameters calculated when running the software, as well as important result data, are grouped and saved in a separate HDF5 file that can be read with HDFView software. Automated AO performance characterisations can be performed in 'standard mode' to assess the correction ability of the optical system. If the adopted DM is designed with a large stroke, i.e., is capable of large deformations, both the closed-loop AO correction and RF functionalities can be exploited. On the other hand, if the DM exhibits insufficient stroke for RF, by ignoring the remote focusing unit, closed-loop AO correction functionalities will still be fully functional without additional modifications.

Closed-loop AO correction can be performed using both the zonal method, which updates DM control voltages in terms of the raw SHWS slope values; and the modal method, which updates DM control voltages in terms of orthogonal Zernike polynomials. There are four sub-modes tagged to each of the two methods: 1) standard closed-loop AO correction; 2) closed-loop AO correction with consideration of obscured search blocks; 3) closed-loop AO correction with partial correction excluding defocus; and 4) closed-loop AO correction with both consideration of obscured search blocks and partial correction excluding defocus.

RF can be performed by scanning the focus axially with a pre-determined axial range, step increment and step number, or by manually adjusting a toggle bar on the GUI for random access RF. The former also incorporates options of whether or not to perform closed-loop AO correction at each RF depth.

5.3 GUI modular software functions

5.3.1 SHWS initialisation and DM calibration unit

The SHWS initialisation and DM calibration unit is given in Figure 5.2.

[**Initialise SB**] determines the search block (SB) geometry given user informed parameters of the lenslet pitch (the diameter of one lenslet), the dimension and pixel size of the camera sensor, as well as the incident pupil diameter. Using this information, the software first calculates the number of pixels across one SB and the number of SBs across the camera sensor, before determining the number and geometrical arrangement of the SBs within the pupil region of the

incident beam. Then, their reference centroid coordinates with regard to the camera sensor is calculated, before the full SB region is displayed on the GUI, as shown in Figure 5.1. This button also exercises the DM membrane by generating a user specified number of random patterns on the DM, which helps to combat the thermal effects of electromagnetic DMs upon initialisation.

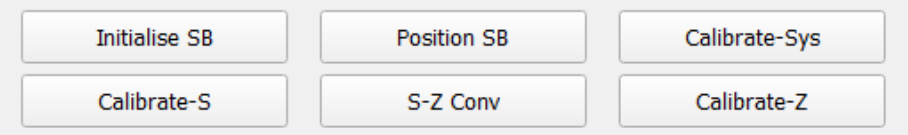


Figure 5.2: SHWS initialisation and DM calibration unit.

[**Position SB**] repositions the SB region on the camera sensor such that it is concentric with the incident beam to allow for maximum dynamic range. This can be achieved in two ways depending on whether or not the DM requires recalibration. User input is needed at this stage by entering '**y**' or '**n**' on the keyboard. By entering '**y**', the user can reposition the SB region by entering $\uparrow$, $\downarrow$, $\leftarrow$, $\rightarrow$, which will shift the entire SB region by one pixel at a time and display it at its new location. When the central SH spot(s) is centred within its corresponding SB, by pressing '**Enter**' on the keyboard, the user can confirm the new SB position and trigger the process of automatically calculating new SB reference centroid coordinates according to the number of pixels shifted in each direction. Upon entering '**n**', SB and DM calibration related parameters from the last session will be automatically loaded from the HDF5 file.

[**Calibrate-Sys**] performs system aberration calibration in three modes. Mode 0 automatically loads the DM control voltages that correct for system aberrations (DM system flat file) from last calibration session onto the DM. Mode 1 runs closed-loop AO correction (zonal control) using the procedure outlined in Section 3.4.4 until the Strehl ratio (SR) is above the given tolerance factor and saves final DM control voltages (DM system flat file) to the HDF5 file. Mode 2 is designed to ignore system aberration correction for small stroke DMs by saving current centroid coordinates as reference for convergence during closed-loop AO correction.

[**Calibrate-S**] performs the DM calibration procedure as specified in Section 3.4.2 to retrieve the control matrix (CM) for direct slopes (zonal) control. The positive and negative bias control voltages provided by the user are sequentially applied to each DM actuator to retrieve the x-

and y-slope values, which are then used to calculate the DM influence function (IF) matrix using Eq. (3.19), and slope CM by computing its pseudo-inverse.

[**S-Z Conv**] calculates the conversion matrix between raw slope values and Zernike coefficients as given in Eq. (3.15) and Eq. (3.16). This can be used to calculate the SR using Eq. (3.8) for evaluation of the image quality during direct slope (zonal) control, or to further acquire the DM IF matrix and CM for Zernike (modal) control.

[**Calibrate-Z**] retrieves the CM for Zernike (modal) control by first calculating the DM IF matrix as given in Eq. (3.20) using the raw slope values acquired in [**Calibrate-S**] and slope-Zernike conversion matrix calculated in [**S-Z Conv**]. Before performing pseudo-inverse of the DM IF matrix, the results after singular value decomposition are first evaluated to identify a cutoff value for small singular values. As suggested in Section 3.4.2, this is usually selected as the value after which a significant drop is seen in the diagonal entries of $\mathbf{\Sigma}$. System modes below this value are removed during pseudo-inverse for acquisition of a stable Zernike CM.

5.3.2 Zernike aberration input unit

The Zernike aberration input unit as shown in Figure 5.3 is mainly used for thorough characterisation of the system AO performance by specifying certain amounts of Zernike modes to generate on the DM membrane. Zernike modes are ordered according to the OSA/ANSI standard given in Table 3.1 and piston is removed such that mode 1 starts with tip. [**Zernike mode spin box**] allows the user to specify a single mode number, the amplitude of which is given in [**Zernike value spin box**] in the unit of microns. Mode combinations can be specified in [**Zernike array edit box**] by providing an array of coefficients in the correct order. Irrelevant modes can be set as zero and only modes up to the maximum mode number controlled during AO correction (user-defined) can be generated. More details on the use of this unit in practice is provided in Section 6.3.

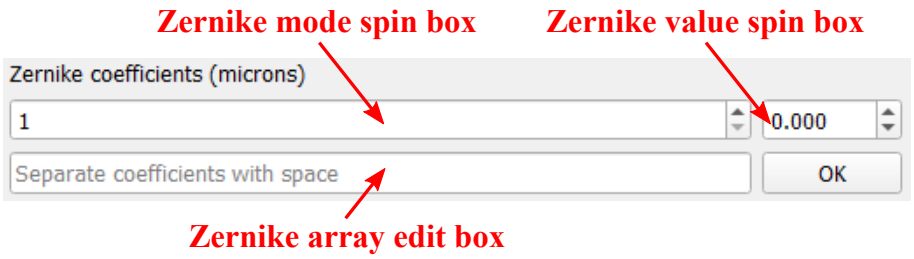


Figure 5.3: Zernike aberration input unit.

5.3.3 AO control and data collection unit

This is the core software unit responsible for closed-loop AO control and automated data collection. Both Zernike (modal) and direct slopes (zonal) control can be performed in 4 different modes, as shown in Figure 5.4.

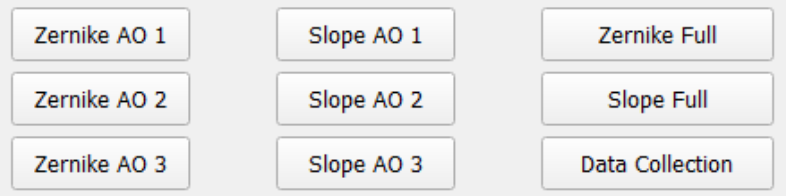


Figure 5.4: AO control and data collection unit.

[**Zernike AO 1**] performs basic closed-loop Zernike (modal) AO control by updating DM control voltages using Eq. (3.25) with the Zernike CM obtained in [**Calibrate-Z**]. Termination of the control loop is realised after the SR satisfies the Maréchal criterion given in Eq. (3.8) or the number of iterations exceeds the maximum limit (user-defined). The same criteria is used for subsequent AO control modes. There are 2 sub-modes under this button that can be specified using mode flags in the parameter configuration file. Sub-mode 1 does not generate Zernike aberration modes before closed-loop AO correction. Sub-mode 2 generates aberrations specified in the Zernike aberration input unit on the DM membrane before performing closed-loop AO correction. The latter is especially useful for characterisation of the system AO performance.

[**Zernike AO 2**] is a modified version of [**Zernike AO 1**] that takes into account missing or ill-formed spots (obscured SBs) detected by the SHWS due to arbitrarily shaped pupils [187–189]. In this case, Zernike polynomials which are defined over a unit circle lose orthogonality and original calibration matrices lead to unreliable interpretations of the wavefront. Therefore, a

new set of orthogonal modes need to be established and an updatable control method is required to dynamically modify the CM during closed-loop AO correction.

Assume $\mathbf{Z}$ is a set of Zernike polynomials consisting of N non-piston terms and $\mathbf{Q}$ is a new set of modes orthogonal over the arbitrarily shaped pupil. Then $\mathbf{Q}$ can be expressed as a linear combination of $\mathbf{Z}$,

$$Q_l = \sum_{i=2}^{N} D_{li} Z_i, \tag{5.1}$$

where D_{li} is a conversion coefficient between the ith Zernike polynomial and the lth new orthogonal mode. If N_{L} represents the total number of lenslets (SBs), then the above equation can be given in matrix form as,

$$\mathbf{Q} = \mathbf{Z}\mathbf{D}, \tag{5.2}$$

where $\mathbf{Q}$ and $\mathbf{Z}$ are two $N_{\mathrm{L}} \times N$ matrices, and $\mathbf{D}$ is an $N \times N$ matrix. $\mathbf{Z}$ is evaluated at the centre of the N_{L} SBs, and $\mathbf{Z}^{\mathrm{T}}\mathbf{Z}$ is a symmetric positive-definite matrix. Let $\mathbf{D} = (\mathbf{P}^{\mathrm{T}})^{-1}$, then $\mathbf{P}$ can be obtained uniquely by computing the Cholesky decomposition of $\mathbf{Z}^{\mathrm{T}}\mathbf{Z}$ [188], where $\mathbf{P}$ is an upper triangular matrix, and $\mathbf{D}$ is a lower triangular matrix. The slope-Zernike conversion matrix is then updated from $(\nabla\mathbf{Z})^{\dagger}$ to $\mathbf{P}(\nabla\widetilde{\mathbf{Z}})^{\dagger}$ and the following equations hold,

$$\widetilde{\mathbf{I}}_z = \mathbf{P}(\nabla\widetilde{\mathbf{Z}})^{\dagger}\widetilde{\mathbf{I}}_s, \tag{5.3}$$

$$\widetilde{\mathbf{a}} = \mathbf{P}(\nabla\widetilde{\mathbf{Z}})^{\dagger}\widetilde{\mathbf{S}}, \tag{5.4}$$

$$\widetilde{\mathbf{c}}_z = \widetilde{\mathbf{I}}_z^{\dagger}\widetilde{\mathbf{a}}, \tag{5.5}$$

where $\widetilde{\mathbf{I}}_s$, $\nabla\widetilde{\mathbf{Z}}$, and $\widetilde{\mathbf{S}}$ are obtained using valid SBs in a similar way as Eq. (3.19), Eq. (3.16), and Eq. (3.15). More details are given in **[Slope AO 2]**. As the pupil shape changes, matrix $\mathbf{P}$ should always be updated by the Cholesky decomposition of $\widetilde{\mathbf{Z}}^{\mathrm{T}}\widetilde{\mathbf{Z}}$.

[Zernike AO 3] is a modified version of **[Zernike AO 1]** that neglects the correction of Zernike defocus such that refocusing of the focal spot is minimised. For Zernike (modal) control, this is simply achieved by setting the detected value of Zernike mode 4 to zero before updating the DM control voltages using the original Zernike CM obtained in **[Calibrate-Z]**.

[**Slope AO 1**] performs basic closed-loop direct slopes (zonal) AO control by updating DM control voltages using Eq. (3.24) with the direct slope CM obtained in [**Calibrate-S**]. The 2 sub-modes described in [**Zernike AO 1**] also apply.

[**Slope AO 2**] is a modified version of [**Slope AO 1**] fulfilling the same purpose as [**Zernike AO 2**]. Without needing to establish a new set of orthogonal modes, the procedure of generating a new CM is much simpler in comparison. Slope values of invalid SBs are removed from $\mathbf{S}$ to obtain $\widetilde{\mathbf{S}}$ and rows corresponding to invalid SBs in $\mathbf{I}_s$ are removed to obtain $\widetilde{\mathbf{I}}_s$. Control voltages are then updated using the following equation,

$$\widetilde{\mathbf{c}}_s = \widetilde{\mathbf{I}}_s^{\dagger}\widetilde{\mathbf{S}}. \tag{5.6}$$

[**Slope AO 3**] is a modified version of [**Slope AO 1**] fulfilling the same purpose as [**Zernike AO 3**]. In order to suppress Zernike defocus using direct slopes control, a suppression gain g_s is introduced [187]. The row corresponding to Zernike defocus in the Zernike IF matrix is multiplied with g_s and concatenated to the end of the original slope IF matrix to form a new slope IF matrix $\mathbf{I}_s^{'}$. The new CM $(\mathbf{I}_s^{'})^{\dagger}$ is then used to update DM control voltages thereon.

[**Zernike Full**] and [**Slope Full**] perform closed-loop AO control taking into account both obscured SBs and suppression of Zernike defocus at the same time.

[**Data Collection**] is designed to perform automated AO performance characterisations of the microscope system, though any data collection process that benefits from automation can be written beneath the hood. Each operation mode is identified by a unique mode flag in the parameter configuration file, which should be determined before software initialisation. Integrated modes have been used to generate the data presented in Sections 6.3.2, 6.3.3, 6.3.4, and 6.3.5, which will be individually discussed in corresponding sections.

5.3.4 Miscellaneous control unit

This unit controls independent image acquisition when no other background process thread is running, as well as miscellaneous functions that are either used by multiple units or do not fit into any unit (Figure 5.5).

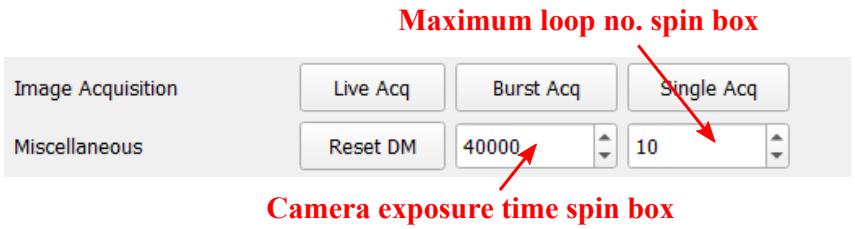


Figure 5.5: Miscellaneous control unit.

Independent image acquisition can be performed in 3 modes. [**Live Acq**] continuously acquires images and displays them on the GUI at the user-defined frame rate and exposure time until manual termination. [**Burst Acq**] acquires a user-defined number of frames in burst mode before automatically terminating. [**Single Acq**] only acquires one image when clicked.

[**Reset DM**] resets the actuators to their neutral position. [**Camera exposure time spin box**] controls the exposure time of the SHWS given in units of microseconds. [**Maximum loop no. spin box**] determines the maximum number of iterations before control loop termination.

5.3.5 Remote focusing unit

The remote focusing unit controls all parameters and procedures relevant to the calibration and execution of RF using a DM.

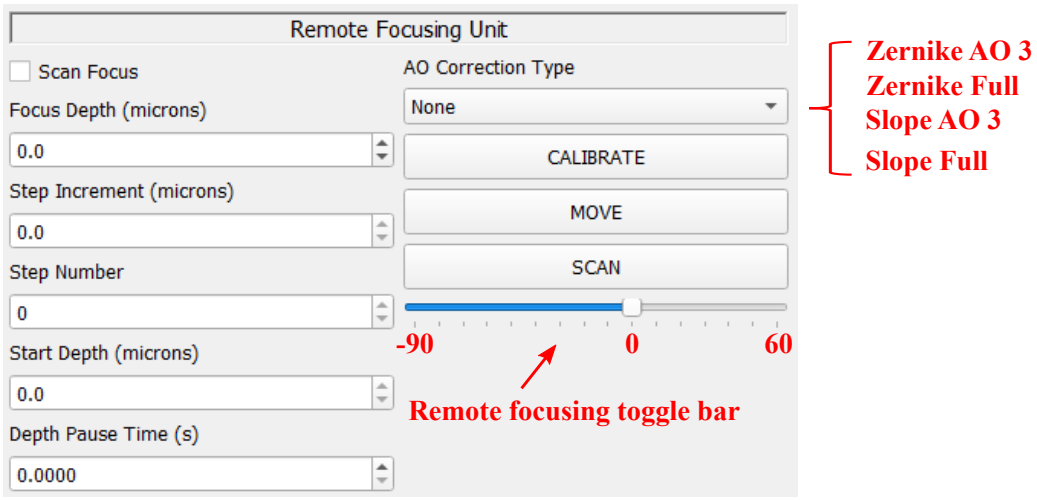


Figure 5.6: Remote focusing unit.

[**CALIBRATE**] triggers the calibration of DM control voltages for RF. Details of the RF calibration process were given in Section 3.5.1. The software performs this as a 2-step process

that proceeds along the negative direction before the positive. The direction of calibration should be determined within the configuration file prior to software initialisation. Other important parameters include the number of and axial distance between incremental steps. Messages are displayed in the message box to inform users of the current calibration direction and step number, as well as to provide users with options to: 1) confirm that the sample has been moved to the next calibration step; and 2) save or discard calibrated voltages and exit the thread. Commands can then be entered via the keyboard. A typical example of the interactive command message is: **Move sample to positive position 2. Press [y] to confirm. Press [s] to save and exit. Press [d] to discard and exit.** The software automatically saves calibrated voltages to the HDF5 file after reaching the maximum user-defined step number, or does so on request at an arbitrary step. It also saves results of the slope values, Zernike coefficients, and SR acquired before and after performing closed-loop AO correction at each calibration step for further analysis of the wavefront. After interpolation of DM control voltages acquired at each calibration step, a look-up table can be loaded upon software initialisation.

[**Scan Focus**] controls whether RF is to be performed at only one depth or at multiple depths. When unticked, only the first spin box on the left-hand-side panel is accessible while others are disabled. When ticked, the otherwise is true.

[**MOVE**] performs RF at only one depth by first retrieving control voltages corresponding to that specified in [**Focus Depth (microns)**], and then applying those voltages on the DM to move the focus relative to the natural focal plane. Negative values move towards -z-axis and positive ones +z-axis.

[**SCAN**] performs RF sequentially at multiple depths by applying different sets of voltages to the DM membrane and scanning the focus depth-wise. [**Step Increment (microns)**] controls the displacement interval between consecutive RF planes, [**Step Number**] the number of planes to be accessed, [**Start Depth (microns)**] the depth at which to start the RF process relative to the natural focal plane, and [**Depth Pause Time (s)**] the time for which the focal spot remains stable at each RF plane. Entering a negative value for [**Step Increment (microns)**] permits RF in the -z-direction.

[**AO Correction Type**] allows the user to choose whether or not to apply AO correction at each RF plane and which type to apply. Four options are available from the drop box, [**Zernike AO 3**], [**Zernike Full**], [**Slope AO 3**], and [**Slope Full**], the features of which have been discussed in Section 5.3.3. All options are applicable to the RF process behind both [**MOVE**] and [**SCAN**], default is set to [**None**].

[**Remote focusing toggle bar**] permits random access of different RF planes during imaging by simply dragging the bar to a desired depth. Default is set to the natural focal plane and max/min limits are provided by the user according to the RF calibration results. [**Remote focusing toggle bar**] and [**MOVE**]/[**SCAN**] perform similar tasks with different pros and cons. The former is more flexible and can be used to randomly examine certain specimen features during imaging. However, it is more difficult to place the focus at specific depths due to manual toggling. The latter is less flexible as parameters in the left-hand-side panel need to be given prior to starting RF and cannot be changed afterwards. However, it enables the focus to be parked at precise locations relative to the natural focal plane with fixed increments, which is more optimal for collecting volumetric stack images for 3D imaging. Results acquired using this function will be discussed in Section 6.4.2.

5.4 Discussion and conclusion

This chapter described the development of a python-based closed-loop sensor-based AO and RF control software that has been designed for open development and easy integration into existing adaptive optical microscopes with modular functional units. Main processes are executed as separate worker threads from a main script used as the central navigation centre to allocate and recycle resources. Communication of events during processes are then handled using Qt's signals and slots mechanism. Common events between different threads, such as displaying an image or error message, reuse the same slots. This neat control arrangement hopefully makes it more convenient for microscope developers to adapt the software for use on their own microscopes.

Further development of the software should focus on two aspects. First of all, it would benefit from synchronisation with the image acquisition software such that results of the closed-

loop aberration correction process could be better appreciated by evaluating specimen images directly after each iteration. The additional access to acquired specimen images would provide possibilities of using image-related metrics, such as image intensity and sharpness, etc., to guide the correction process. Integration of these metrics with direct wavefront sensing may further lead to new hybrid adaptive optics algorithms. Secondly, the current software gives an example for using an electromagnetic DM where the actuator displacement is linearly proportional to the applied control voltage, as was described in Section 3.4.1. In this case, the device can be driven linearly in both the negative and positive directions by applying a normalised control voltage of $\frac{V}{V_{\max}}$. To use it with a electrostatic DM, the actuator displacement should be proportional to the applied control voltage squared, such that $(\frac{V}{V_{\max}})^2$ should be used to drive the device in a linear manner.

Chapter 6

Sensor-based adaptive optics and remote focusing in the CCRCM

6.1 Overview

Developments were made upon the compact and contactless reflectance confocal microscope (CCRCM) for neurosurgery described in Chapter 4 to incorporate necessary components for adaptive optics (AO) and remote focusing (RF). In the following sections, the system hardware modifications and software control is first outlined. Thorough AO characterisation results of the CCRCM are then presented in a 5-step process. Next, the implementation of RF in the CCRCM is demonstrated by first analysing the RF calibration results before performing RF for acquisition of volumetric stacks in frozen mouse calvaria.

6.2 System setup and software control

Hardware modifications were made to the setup described in Section 4.3.2 and the updated microscope schematic is illustrated in Figure 6.1. A large-stroke DM (DM-69, Alpao) with a settling time of 1 ms and comprising of 69 actuators replaced planar mirror M3 at a pupil plane conjugate to the back aperture of the 0.42 NA, 20 mm working distance dry objective lens (MY20X-804, Mitutoyo). This allowed RF to be performed with simultaneous correction of low frequency aberrations. A separate wavefront sensing path was included at a descanned

position diverted by a 10:90 non-polarising plate beam-splitter (BS, BSN11, Thorlabs) in the detection path. A 150 µm pitch, 5.2 mm focal length lenslet array (MLA150-7AR-M, Thorlabs) was attached to a xiQ CMOS camera (11.27 mm × 11.27 mm active area, 5.5 µm pixel size, MQ042MG-CM, Ximea) to form a custom Shack-Hartmann wavefront sensor (SHWS). It was positioned at a conjugate pupil plane to the DM membrane and relayed by lenses L5 (f = 100 mm) and L6 (f = 150 mm) from the surface of the dual-axis MEMS.

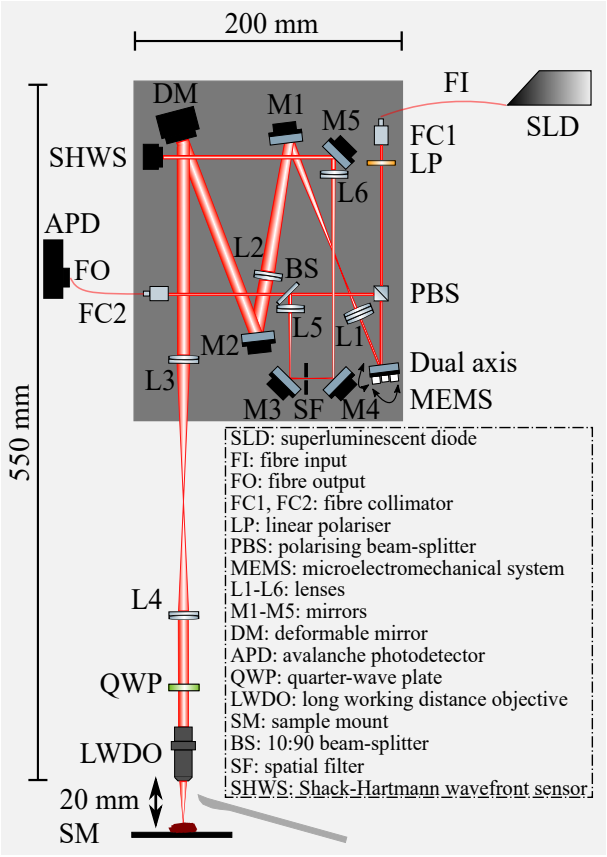


Figure 6.1: Schematic diagram of the CCRCM incorporating a large-stroke DM and custom SHWS for sensor-based AO control and RF.

To enable optimum performance, the SHWS should be designed with careful consideration of the incident beam size, the pitch and focal length of the lenslet array, as well as the pixel size of the camera sensor. Long focal length lenslet arrays lead to larger beam shifts on the camera sensor for the same amount of aberration, and increases sensitivity. The lenslet pitch should be chosen such that the incident beam is sampled by a sufficient number of lenslets, and that the

region behind each lenslet (search block) is sampled by a sufficient number of camera pixels. As the lenslet array and DM are in conjugate pupil planes, we can also regard the lenslet array to be sampling DM actuators. Based on the Nyquist criteria, a 2:1 lenslet-actuator ratio should be allowed to effectively evaluate the effect of each DM actuator on the wavefront profile, such that the following relationship can be satisfied,

$$D/d \approx 2 \cdot N_{\mathrm{A}}, \tag{6.1}$$

where D is the incident beam diameter, d is the lenslet pitch, and N_{A} is the number of DM actuators across the pupil diameter. In the current microscope, this led to 14 lenslets illuminated across the pupil diameter (148 lenslets in total) and 27 pixels across each lenslet. It should be noted that in theory, the maximum number of Zernike modes a DM can correct is equal to the number of DM actuators (degrees of freedom), but in reality only a much smaller number of Zernike modes can be accommodated due to deficiencies in the actuator arrangement, inter-actuator coupling, etc. In addition, an acceptable signal-to-noise ratio should be considered for the number of lenslets sampling the wavefront as well as the number of camera pixels sampling each lenslet. In the case of low signal level, a lower lenslet and pixel count should be used.

Closed-loop sensor-based AO and RF control was achieved in the CCRCM using the Python-based *SenAOReFoc* software developed in Chapter 5. For the remainder of this chapter, the direct slopes (zonal) correction method was used to account for the relatively low actuator count of the chosen DM, which may lead to under-sampling of ideal Zernike modes, thus cause imperfections during conversion from detected slope values to Zernike coefficients, especially for modes with higher frequencies. Zernike modes are nevertheless used for wavefront reconstruction and AO performance characterisation, as a direct and easily-interpretable analysis tool set.

6.3 Characterisation of adaptive optics performance

The AO performance of the CCRCM was characterised in a 5-step process by first calibrating the DM and system aberrations. Next, the dynamic range of the SHWS was assessed by generating each Zernike mode independently with increasing amplitudes. The degree of Zernike mode

coupling was then evaluated using a heatmap illustrating the amplitude of each detected Zernike mode when a single mode of given amplitude was applied on the DM membrane. Evaluation of the correction performance for different amplitudes of Zernike defocus was then carried out before performing similar tests for combinations of multiple odd and even Zernike modes. To enable routine characterisation, Step 2 to Step 5 were implemented as automated procedures in *SenAOReFoc* under the **[Data Collection]** button as described in Section 5.3.3.

6.3.1 Calibration of deformable mirror and system aberration

The DM calibration procedure as described in Section 3.4.2 was implemented to acquire the DM influence function (IF) and control matrix (CM) by applying a bias voltage of $V_b = 0.1$ V (10% of the maximum 1 V drive voltage) and scanning over a piece of white card placed at the natural focal plane. System aberration was calibrated by setting the **[Calibrate-Sys]** button to Mode 1 and acquiring a DM system flat file using the procedure set out in Section 3.4.4. The result is given in Figure 6.2.

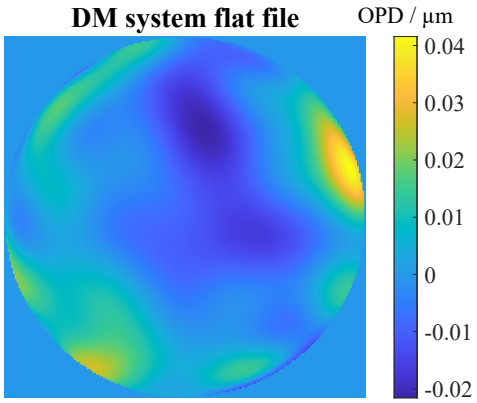


Figure 6.2: DM system flat file acquired by scanning over a piece of white card placed at the natural focal plane during closed-loop AO correction.

6.3.2 Evaluation of SHWS dynamic range

The dynamic range of the SHWS was calibrated for the first 20 Zernike modes as given in Table 3.1 (excl. piston) by generating each mode individually on the DM membrane in increments of 0.02 µm RMS until the amplitude detected by the SHWS did not further increase.

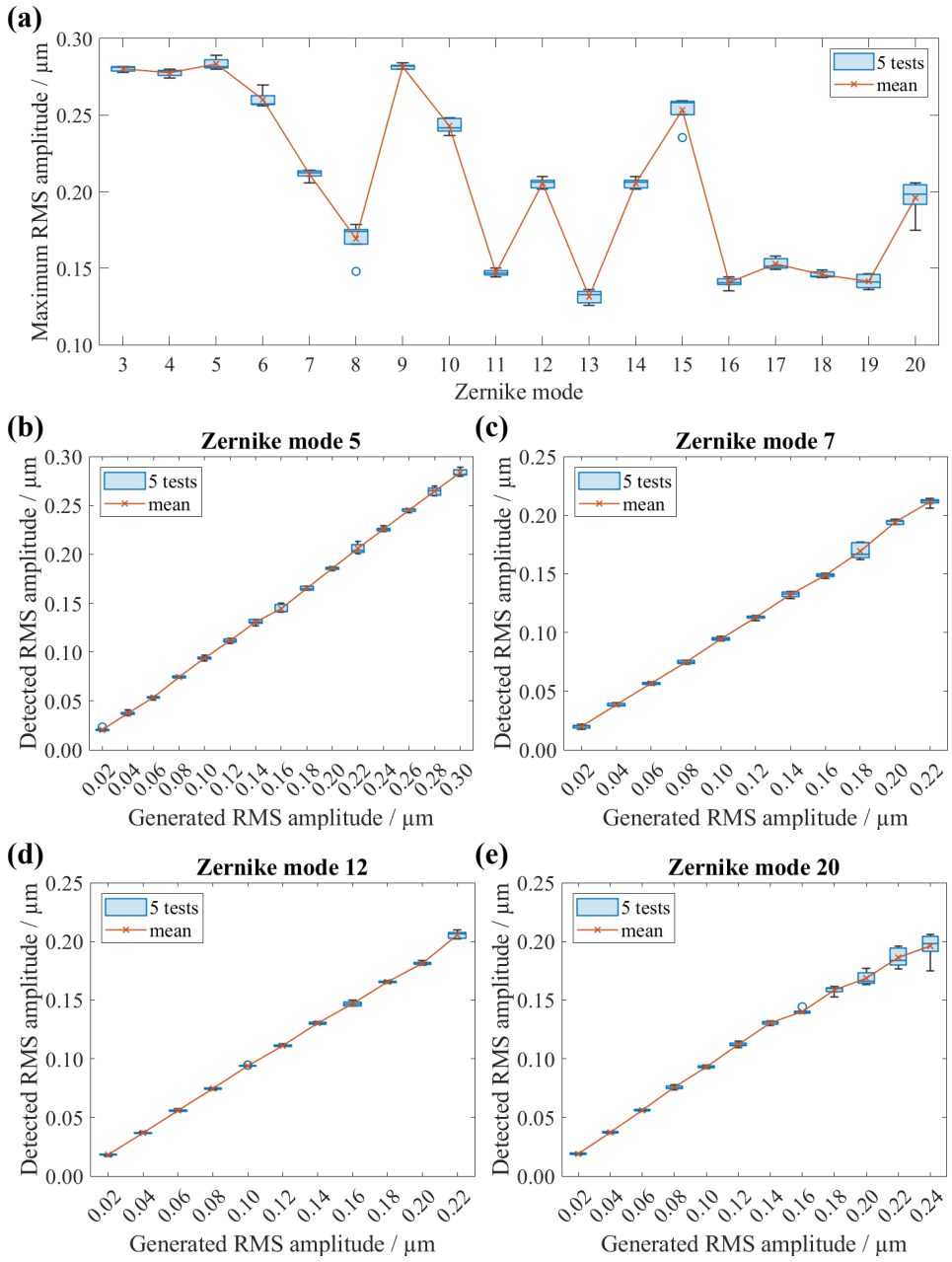


Figure 6.3: Characterisation results of system AO correction performance. (a) Dynamic range of the SHWS for Zernike modes 3-20 (excl. tip/tilt). (b)–(e) Generated and detected RMS amplitudes of odd/even Zernike modes (b) 5, (c) 7, (d) 12, and (e) 20, in increments of 0.02 µm. Error bars represent the maximum/minimum/median, as well as the 25th and 75th percentiles of the data.

This was implemented in closed-loop to account for non-linearities of the SHWS, as discussed in Section 3.4.3. As tip/tilt only cause a lateral shift in the focal position and do not affect the image quality, they were neither calibrated nor corrected for during closed-loop control. Results

with error bars over 5 measurements are shown in Figure 6.3(a) and examples of the generated and detected RMS amplitudes in increments of 0.02 µm for Zernike modes 5, 7, 12, and 20 is demonstrated in Figures 6.3(b)–(e). A variation in the dynamic range of each Zernike mode could be seen with an RMS amplitude of above 0.13 µm achieved for all of the first 20 modes. Many factors can lead to this phenomenon, such as the capability of the DM actuator layout to accurately produce each mode shape, the relative geometry between the DM actuator layout and lenslet array configuration, and the difference in magnitude of local gradients for each Zernike polynomial. Finally, the detected RMS amplitude is equivalent to that generated, demonstrating high fidelity prior to the limit. Data was acquired using Mode 1 of [**Data Collection**].

6.3.3 Evaluation of Zernike mode coupling

To assess the degree of Zernike mode coupling upon detection at the SHWS, 0.1 µm RMS of the first 20 Zernike modes was individually generated (excl. tip/tilt), and a heatmap was constructed from the detected Zernike coefficients (Figure 6.4). All values were normalised by 0.1 to acquire the correlation coefficient between detected and generated mode amplitudes. From the heatmap, we observe an apparent diagonal indicating a strong correlation between the same generated and detected Zernike mode. All other modes were generally well suppressed leading to a low correlation coefficient, despite with a noticeably larger cross-talk for Zernike defocus (second row), due to a better capability and higher tendency of the DM to create this mode shape. It is also explicit from this heatmap that specular reflections were not present [146], as a similar Zernike mode amplitude to that generated was detected for both the odd and even Zernike modes. Data was acquired using Mode 1 of [**Data Collection**].

6.3.4 Correction of Zernike defocus

Figure 6.5 validates the closed-loop zonal correction performance (loop gain $g = 0.2$) for incrementing amplitudes of Zernike mode 4 (defocus). With the white card placed at the natural focal plane, the DM was instructed to first generate the corresponding amount of Zernike defocus and then correct for it in closed-loop. This is critical for evaluating the feasibility of the

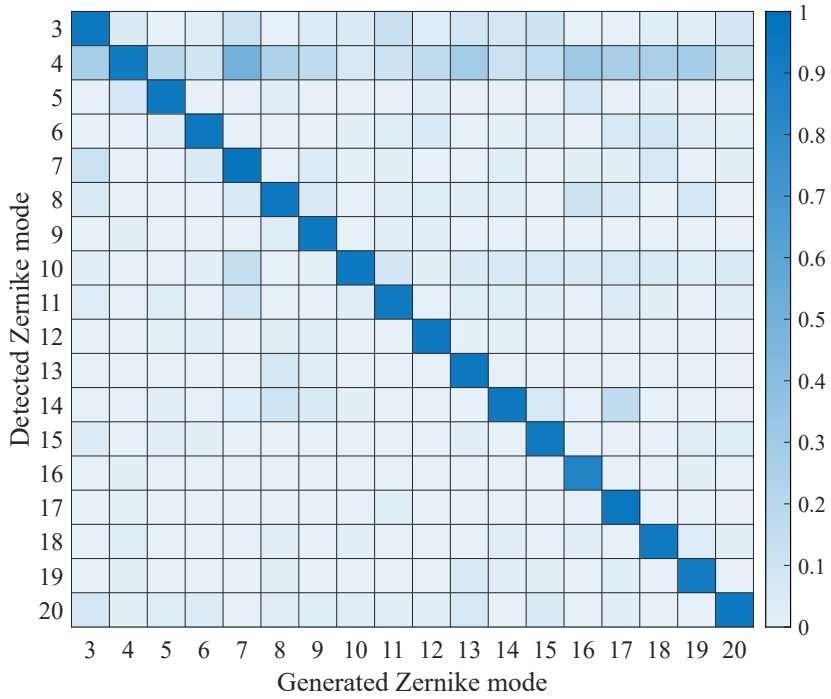


Figure 6.4: Heatmap of correlation coefficients between detected and generated mode values for 0.1 µm of Zernike modes 3-20 (excl. tip/tilt). A strong correlation was observed between the same generated and detected Zernike mode, while all other modes were generally well suppressed.

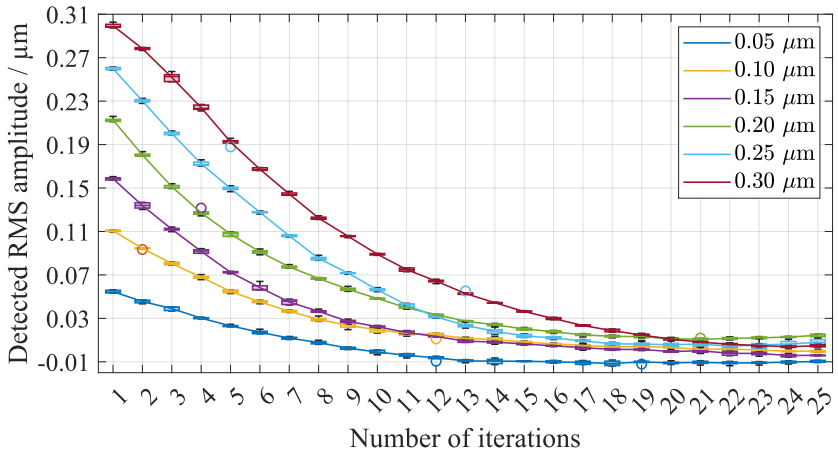


Figure 6.5: Detected amplitudes of Zernike mode 4 (defocus) at each iteration during closed-loop zonal correction for different generated amplitudes.

RF calibration process described in Section 3.5.1. In all cases, the correction curve converged monotonically to zero within 20 iterations for all generated amplitudes up to 0.30 µm RMS, with small amplitude aberrations converging earlier than larger ones. Correction of amplitudes above

this may also be possible, but was not assessed as the system was limited in its capability to give an accurate absolute measurement, shown in the results of Figure 6.3. In addition, the narrow error bars indicated high stability between independent tests, a loop gain larger than $g = 0.2$ would introduce faster convergence with more noticeable instability. Data was acquired using Mode 1 of [**Data Collection**].

6.3.5 Correction of multiple Zernike mode combinations

Finally, to ensure the system could correct for multiple Zernike modes with good stability and minimal mode coupling, different combinations of odd and even Zernike modes (0.1 µm RMS) were generated and corrected for using closed-loop zonal control (Figure 6.6). In all cases, the amplitude of each generated aberration mode decreased monotonically with an increasing number of iterations, and a smooth curve was obtained for the Strehl ratio (SR) calculated using the first 69 detected Zernike coefficients via Eq. (3.8). The Maréchal criterion of SR = 0.8 was achieved for diffraction-limited performance (DLP) within 7 iterations in all cases, as indicated by dashed lines. Data was acquired using Mode 3 of [**Data Collection**].

6.4 Remote focusing in the CCRCM

RF was implemented in the CCRCM not only for its rapid system-aberration-free axial scanning properties, but also that it allowed elimination of the piezo actuator that would otherwise be incorporated for axial translation of the objective lens, which would take up more space and lead to additional hardware costs.

6.4.1 Remote focusing calibration results

RF calibration to acquire control voltages for fine axial refocusing was performed in both the negative and positive directions of the natural focal plane according to the procedure in Section 3.5.1 and using the [**CALIBRATE**] button. A displacement of Δd = 10 µm was used between each calibration step, and interpolation was performed for fine refocusing steps of 0.1 µm.

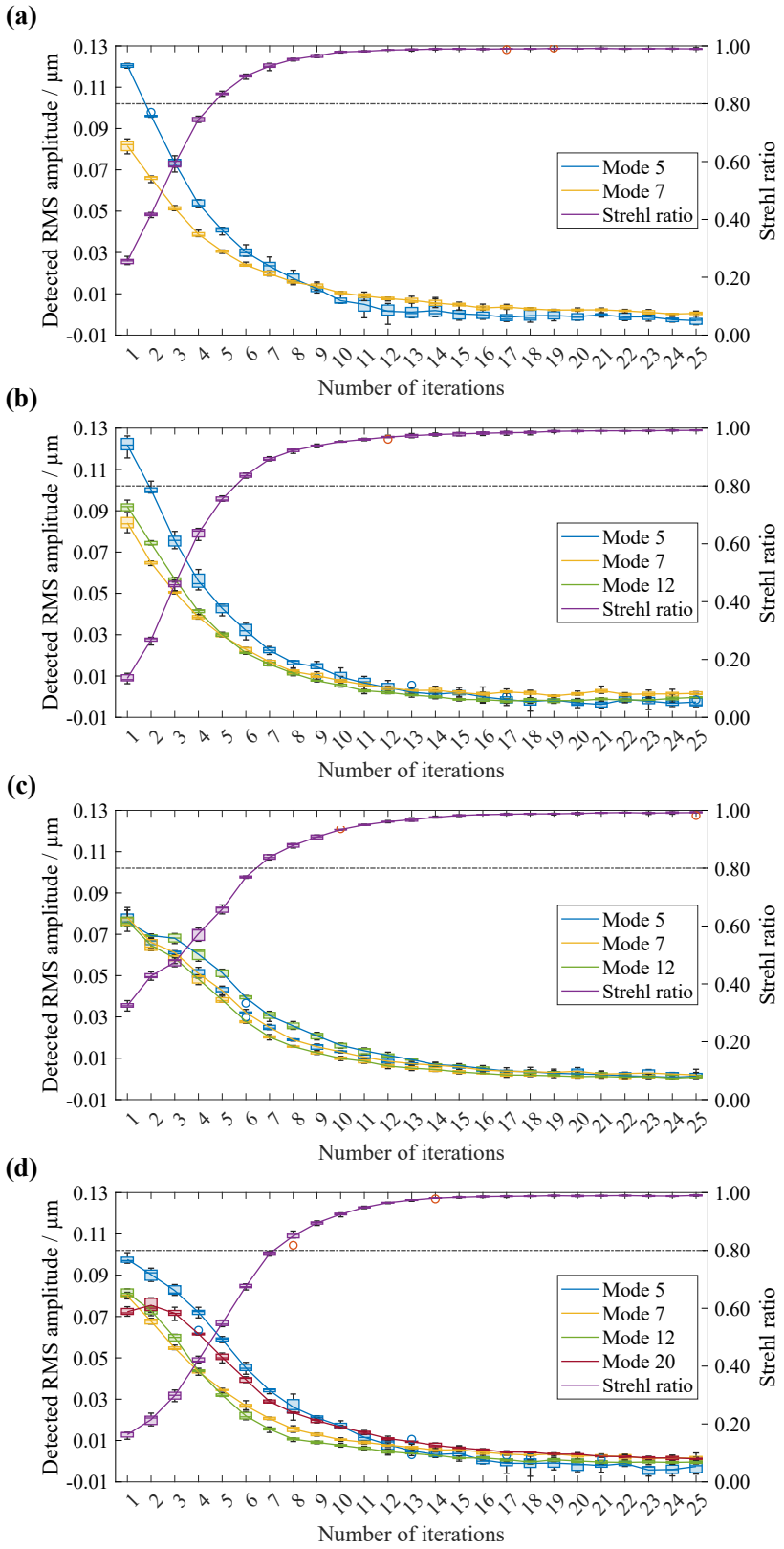


Figure 6.6: Detected amplitudes of generated odd and even Zernike mode combinations and SR calculated using first 69 Zernike modes (excl. tip/tilt) during closed-loop zonal correction.

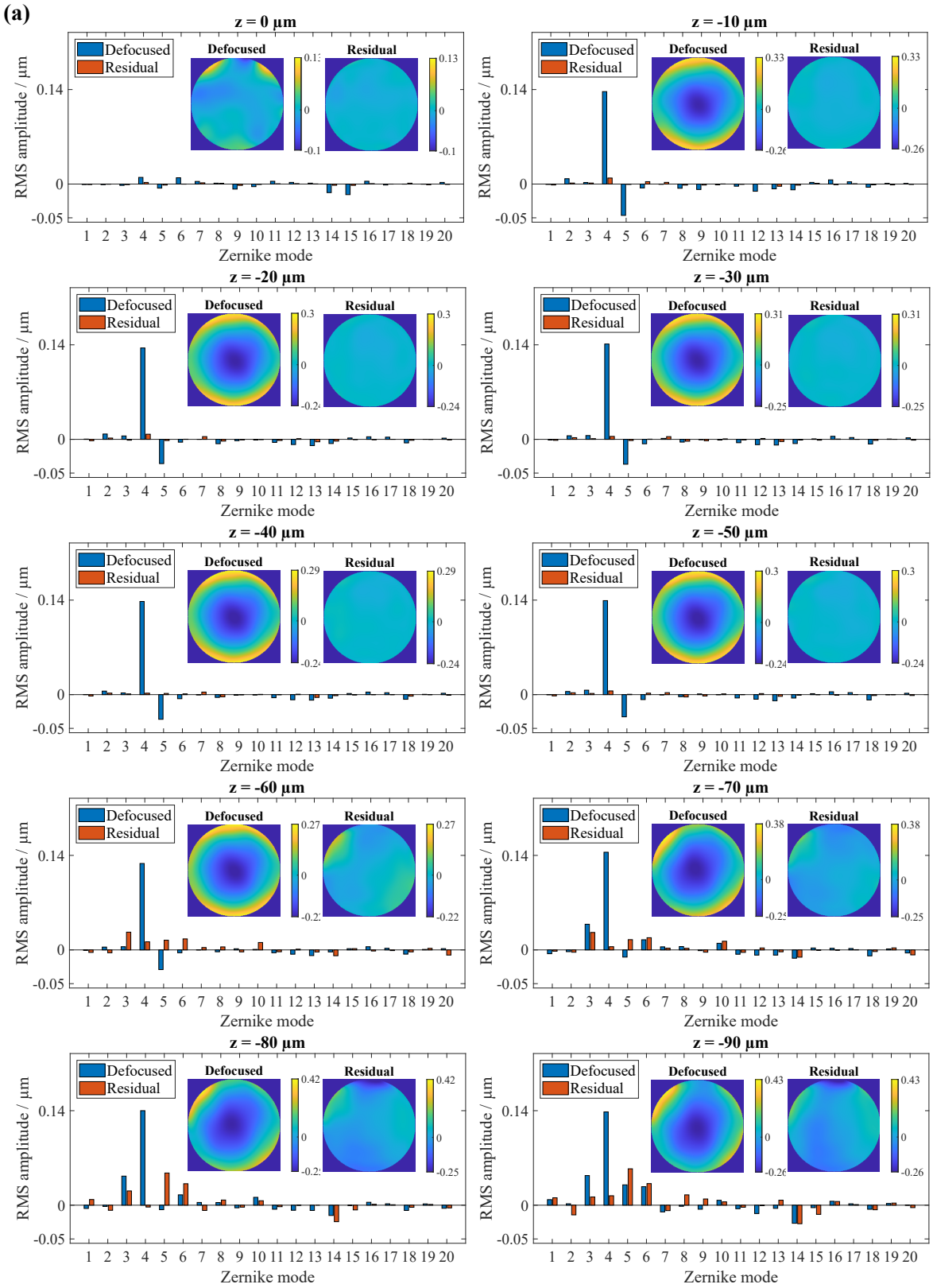


Figure 6.6: Remote focusing calibration results. (a) Defocused and residual wavefront maps and Zernike coefficients detected using the SHWS at each 10 µm calibration step from the natural focal plane (0 µm) to −90 µm axial displacement along the -z-axis.

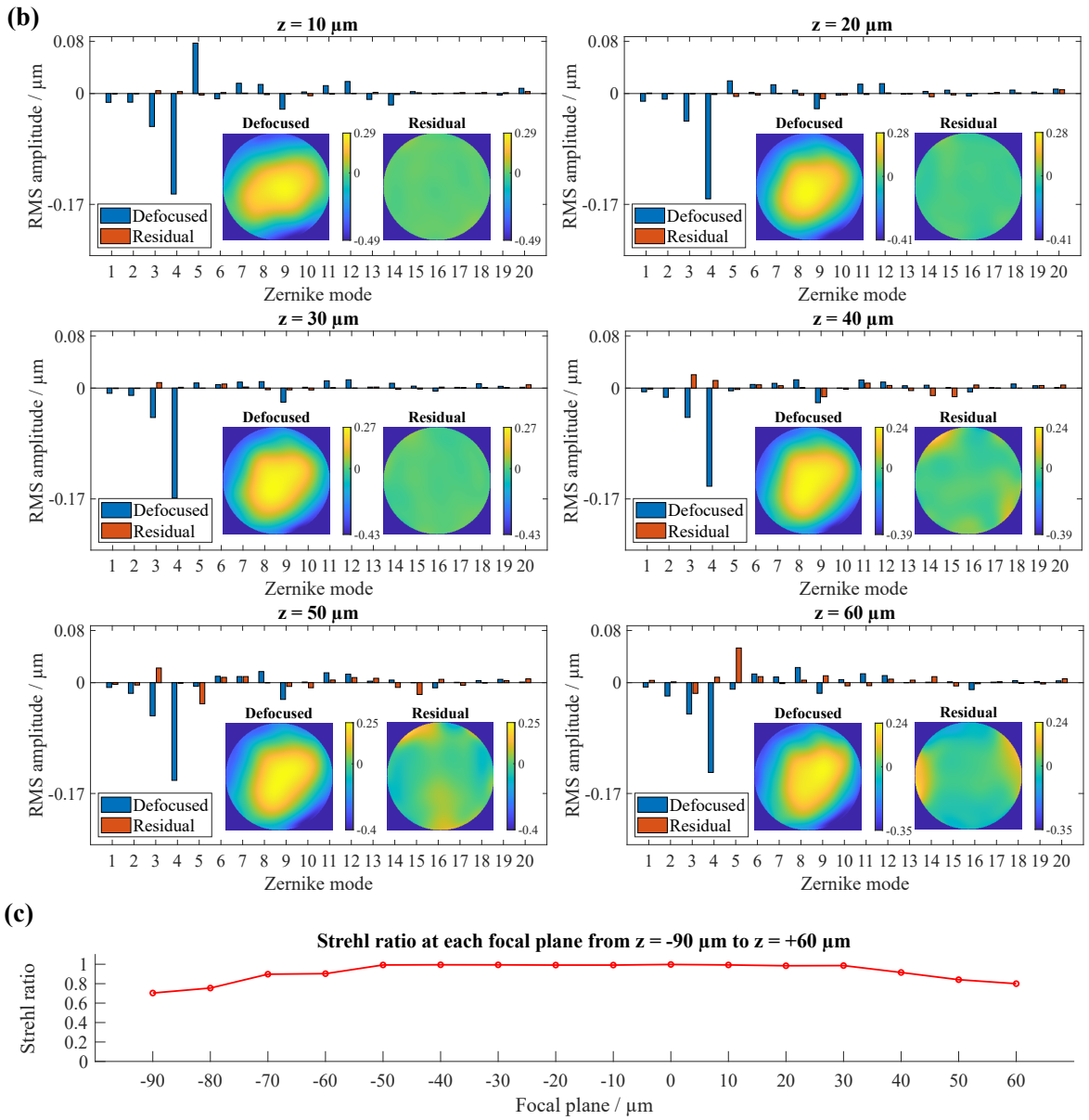


Figure 6.6: Remote focusing calibration results. (b) Defocused and residual wavefront maps and Zernike coefficients detected using the SHWS at each 10 µm calibration step from 10 µm to 60 µm axial displacement along the $+z$-axis. Both the defocused and residual wavefront maps are normalised to the maximum amplitude of the defocused wavefront map. (c) SR calculated using first 69 Zernike modes (excl. tip/tilt) at each calibration step. An SR of above 0.7 was maintained throughout the -90 µm $\sim$ +60 µm RF range.

Results were characterised by analysis of the first 20 Zernike coefficients and reconstruction of the detected wavefront at each calibration step. Comparison was made between results of the defocused wavefront for an axial displacement of 10 µm, and that of the residual wavefront after

closed-loop correction. Results for each calibration step from the natural focal plane (0 µm) to −90 µm axial displacement along the -z-axis and from 10 µm to 60 µm axial displacement along the +z-axis are given in Figure 6.6(a) and Figure 6.6(b), respectively. In all cases (excl. $z = 0$ µm), Zernike mode 4 was the dominant constituent of the defocused wavefront, accompanied by noticeable amounts of Zernike modes 3 and 5. This most likely originates from system aberrations induced when a divergent beam is incident upon an infinity-corrected objective lens in the presence of residual misalignment.

The diffraction-limited RF range was defined as the distance over which SR > 0.8 as given in Eq. (3.8), resulting in a ±60 µm range with negligible aberration. However, as DLP is not critical for cellular level imaging, the SR criterion was further relaxed to 0.7 to obtain a larger axial refocusing range of −90 µm $\sim$ +60 µm. The slight degradation in correction ability seen at larger displacements is most likely due to two reasons. First, although with electromagnetic mirrors the amount of actuator displacement is approximately linear to the applied control voltage, as introduced in Section 3.4.1, certain amounts of non-linearity can begin to develop when the actuator approaches its maximum stroke. Second, as this non-linearity was not seen by the SHWS during DM calibration, it would lead to inaccuracies in the closed-loop correction process, eventually preventing convergence to zero. This, however, should not noticeably effect the RF performance, as the SR of above 0.7 that was maintained across the full depth range was also the lower bound of the image quality achieved on the CCRMC without aberration correction at the natural focal plane (Chapter 4). Results of the SR for each calibration step throughout the −90 µm $\sim$ +60 µm RF range are given in Figure 6.6(c).

6.4.2 Remote focusing within frozen mouse calvaria

After calibrating the RF control voltages according to Section 3.5.1 and characterising the RF wavefront as shown in Section 6.4.1, RF performance was evaluated within frozen mouse calvaria.

Volumetric stacks were first obtained by acquiring images with 10 µm axial steps over a 90 µm depth range from the surface of the calvaria. Comparison was made between scanning sequentially through multiple depths using RF (Figure 6.7(a), top rows), and axially translating

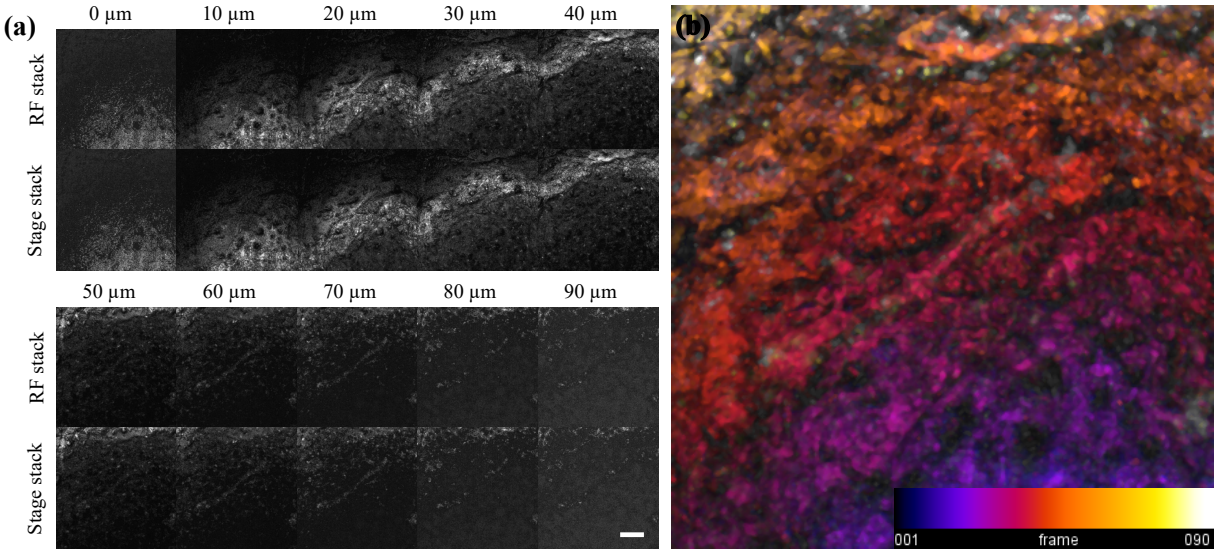


Figure 6.7: RF results within frozen mouse calvaria. (a) Stack images acquired with 10 µm axial steps over a 90 µm depth range from the surface of the calvaria. Top rows: results obtained by scanning sequentially through multiple depths using calibrated RF control voltages. Bottom rows: comparison results obtained by axially translating the sample stage with a DM system flat file. (b) Colour-coded MIP of 90 frames with 1 µm intervals. Scale bar: 100 µm.

the sample stage with a DM system flat file (Figure 6.7(a), bottom rows). Results validated that refocusing via deformation of the DM membrane with simultaneous correction of system aberrations was capable of precisely locating the target focal plane throughout the full 90 µm depth range with no noticeable decrease in spatial resolution or field of view (FOV).

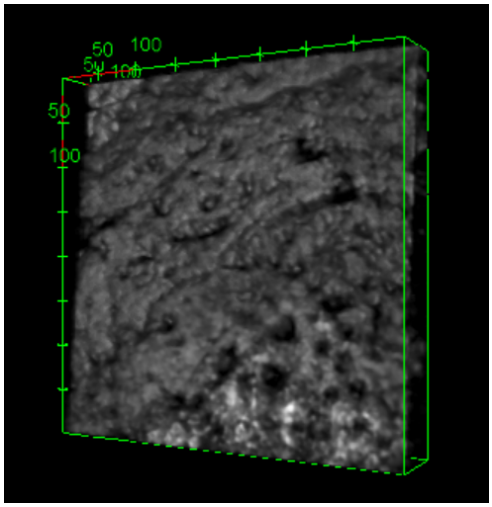


Figure 6.8: Snapshot of reconstructed 3D volume over 90 µm depth range within frozen mouse calvaria rotating around the y-axis.

To fully appreciate the fine refocusing ability of the DM enabled by linear interpolation of control voltages at each calibration step, a second volumetric stack was automatically acquired at the same region with 1 µm axial steps. A colour-coded maximum intensity projection (MIP) of all 90 frames (Figure 6.7(b)) shows smooth transition between layers and no spurious artefacts such as tip/tilt or lateral shifts. A 3D volume was reconstructed to better appreciate connections between cells and tissue structures, and a snapshot of it rotating around the y-axis is given in Figure 6.8. Acquisition time for one volumetric stack is determined by that of one lateral image, limited by the FPGA sampling rate to 4 fps for a 256×256 image. In the axial direction, speed is solely dependent on the DM settling time, being 1 ms for the DM used in this work.

6.5 Discussion and conclusion

In this chapter, experimental characterisation and imaging results validated the feasibility and effectiveness of performing closed-loop sensor-based AO and RF in the CCRCM after incorporating a large stroke DM and custom SHWS.

A small amount of system aberration was seen at the natural focal plane of the objective lens and control voltages for a DM system flat file was obtained after closed-loop AO correction at this plane. The dynamic range of the SHWS was different for each Zernike mode but an RMS amplitude of above 0.13 µm was generally achieved for the first 20 Zernike modes. Minimal mode coupling was demonstrated by strong correlation between the same generated and detected Zernike mode, and weak correlation between different modes in the obtained heatmap. Closed-loop correction of Zernike defocus converged monotonically to zero for all generated amplitudes up to 0.30 µm RMS and minimum mode coupling was experienced when correcting for combinations of odd and even Zernike modes.

RF calibration results demonstrated a diffraction-limited RF range of ± 60 µm and an SR > 0.7 RF range of -90 µm $\sim +60$ µm. Experiments within frozen mouse calvaria showed no noticeable decrease in spatial resolution or FOV over the full 90 µm RF depth, and no spurious artefacts such as tip/tilt or lateral shifts were noticed between consecutive depth layers.

Due to the unavailability of diseased tissue and the use of a low-NA objective lens which exhibited minimal specimen-induced aberration within samples at hand, performance of the closed-loop AO control was not validated for correction of specimen-induced aberrations. However, the effectiveness of AO to improve the diagnostic quality of cancerous cells within tissue biopsies, as well as to assist decision-making during image-guided surgery remain as a critical step of introducing AO to the clinic.

Chapter 7

Post-processing and image enhancement techniques for real-time display

7.1 Overview

The image quality during real-time display fundamentally affects decision-making in clinical settings. Images of appreciable diagnostic quality should be of sufficient contrast and free of artefacts such as distortion. However, due to limitations in the system hardware, images acquired without any post-processing seldom fulfil these requirements. In addition, different imaging modes that allow clinicians to switch between macroscopic and close-up views of the tissue can greatly accelerate the diagnostic process.

It is therefore of great importance to introduce image post-processing and enhancement techniques that improve the quality of real-time image display. They should not require a substantial computational effort so as to maintain sufficient image update rates. In the following sections, different imaging modes are incorporated in the compact and contactless reflectance confocal neurosurgical microscope to fulfil clinical requirements. Methods of removing image artefacts induced by the sinusoidal behaviour of the MEMS scanner and bi-directional scanning are then thoroughly discussed before calibrating the spatial resolution of the system. Finally, the effects of introducing real-time gamma correction for image contrast enhancement is demonstrated.

7.2 Different imaging modes for clinical requirements

Scanning control and image acquisition were performed using readily-developed software via a standard laptop (XPS 15 7590, Dell) and FPGA (USB-7855R, National Instruments). Analog triangle scan signals were sent to the MEMS controller for fast bi-directional scanning along the x-axis and sawtooth signals were used for uni-directional scanning along the y-axis.

Modifications were made upon the existing software such that four imaging modes with different fields of view (FOV) were incorporated to fulfil clinical requirements. Mode 1 enables large FOV access of 600 µm at a frame rate of 1 fps. With a pixel count of 512 × 512, approximately 2 µm spatial resolution is provided according to Nyquist sampling. Mode 2 gives a close-up view of 200 µm with the same pixel count, enabling a theoretical spatial resolution of ∼1 µm. Mode 3 is designed to provide magnified views of target structures with ∼1 µm spatial resolution at higher frame rates of 4 fps. An adjustable FOV within the range of 50 ∼ 100 µm with 10 µm increments can be selected from a drop-down box on the graphic user interface (GUI). Mode 4 scans over a very small region (<20 µm) for use during deformable mirror (Section 3.4.2) and remote focusing (Section 3.5.1) calibration. A screenshot of the GUI for different imaging modes is given in Figure 7.1.

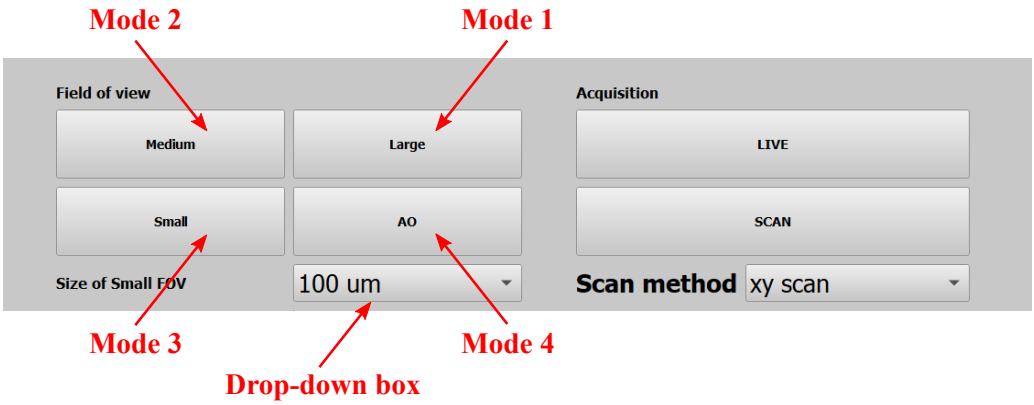


Figure 7.1: GUI showing four imaging modes with different FOVs to fulfil clinical requirements.

7.3 Removal of image artefacts

Due to the sinusoidal behaviour of the MEMS scanner, significant image distortion was present along the fast-scan axis. To remove the distortion artefact during real-time display, a mapping function for pixel-reassignment was developed. A silicon grid test specimen (AGS1930, Agar Scientific) with a periodicity of 10 µm was used both for calibration of the scanning FOV and sampling of image distortion. The procedure was repeated for each imaging mode described in Section 7.2 except Mode 4, which was not used for imaging purposes. An example of the mapping function generation process is given for the case of 60 µm FOV.

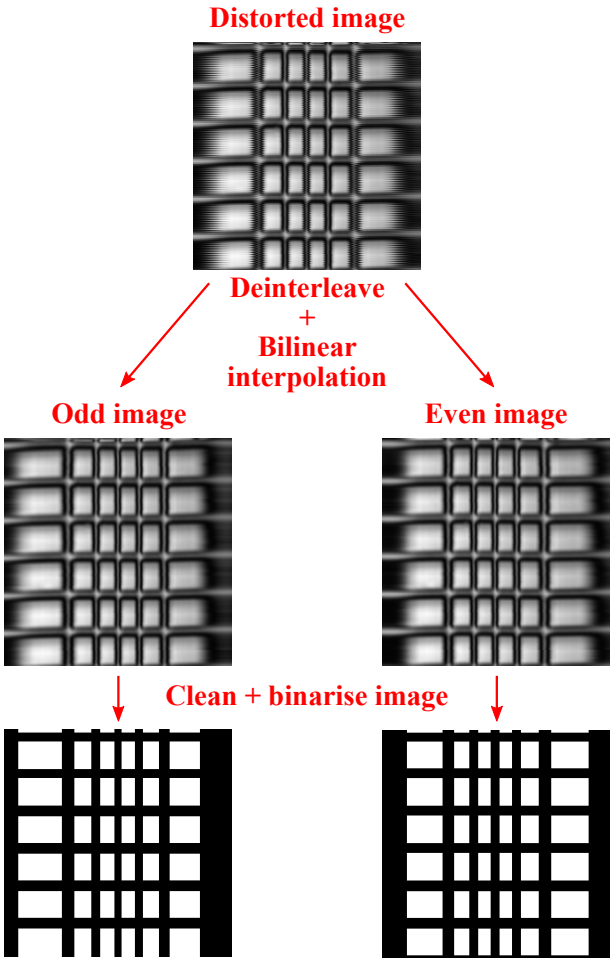


Figure 7.2: Intermediate results during image pre-processing when generating the mapping function for pixel-reassignment of distorted images along the fast-scan axis.

An image of the distorted grid was first acquired by adjusting the MEMS scanner control voltage and sample translation stage such that 6 full grids equivalent to 60 µm FOV were seen and approximately centred in both directions. Image pre-processing was then performed as follows. To account for the discrepancy in forward- and backward-scan patterns due to a generally different scanner acceleration and deceleration speed [190], the distorted image was deinterleaved and bi-linearly interpolated into one forward-scan (odd) image and one backward-scan (even) image for separate calibration. Both the odd and even images were then cleaned by smoothing and sharpening the rough grid edges, and binarised to display regular grid structures. Intermediate results of the above procedure is given in Figure 7.2. Subsequent procedures were performed separately for odd and even images with consideration that the image distortion was only noticeable along the fast-scan axis.

Edge detection was applied to the binarised images to retrieve a set of distorted square grid coordinates after removing the black regions on either side of the image. As they corresponded to positions at which the MEMS scanner came to a halt in between grid structures before changing scan direction, they were not of significance when generating the mapping function. Pixels with similar x-coordinates within a certain tolerance were considered in the same column and only columns with pixel counts above a given threshold were considered as a grid edge. In order to reassign pixels for removal of distortion artefacts, another set of ideal square edge coordinates was generated according to the scanning FOV and nominal grid periodicity.

Having obtained two separate sets of edge coordinates, one for the distorted grid image and the other for an ideal grid image, the next step was to generate a mapping function from the former to the latter. Here, a continuously differentiable interpolant was constructed using a Clough-Tocher scheme [191], which provides local support and takes advantage of piecewise cubic interpolation to approximatively minimise the curvature of the interpolating surface. Odd and even images were remapped separately and a final undistorted image could be reconstructed by combining the two images. Results of the odd, even, and full image before and after distortion correction using the generated mapping function is demonstrated in Figure 7.3.

During real-time imaging, the mapping function was loaded upon software initialisation to execute distortion correction on a millisecond timescale for a standard laptop, and a Gaussian

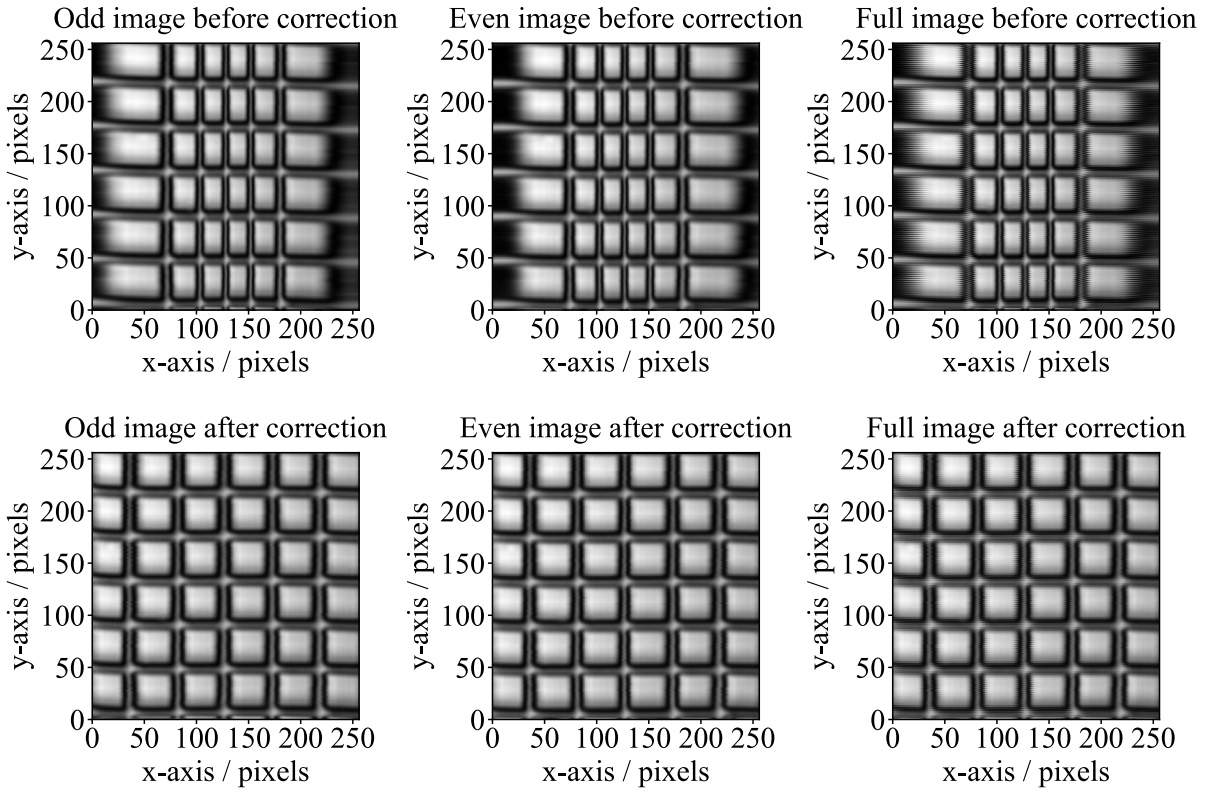


Figure 7.3: Results of the odd, even, and full image before and after distortion correction using the generated mapping function.

kernel ($\sigma = 0.8$) was then applied to remove the residual jitter effect between forward- and backward-scan lines due to bi-directional scanning. The resulting effect of distortion correction and Gaussian filtering on the silicon grid specimen in real time over a 60 µm FOV is given in Figure 7.4(a). Finally, to evaluate the effectiveness of the mapping functions on different specimens, tests were also performed over 50 µm FOV on a stage micrometer (AGL4202, Agar Scientific), as demonstrated in Figure 7.4(b).

7.4 Calibration of spatial resolution

Calibration of lateral and axial spatial resolution was performed after removal of all image artefacts. Lateral resolution was calibrated by plotting the intensity profile along a line drawn perpendicular to a 1-µm wide stage micrometer graticule (Figure 7.4(b), right). Axial measurements were acquired by translating the objective focal spot axially through a planar mirror in

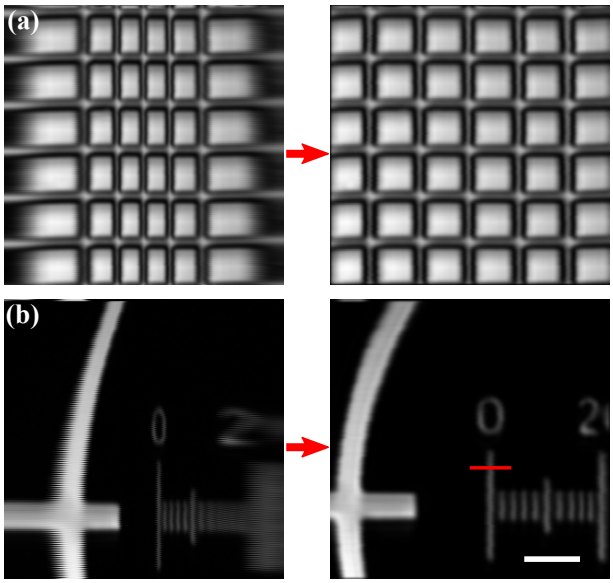


Figure 7.4: Real-time image distortion correction and Gaussian filtering results for (a) silicon grid specimen over 60 µm FOV and (b) stage micrometer over 50 µm FOV. Scale bar: 10 µm.

steps of 0.5 µm, and plotting the detected intensity at each axial location. Figure 7.5 shows the calibration results with a lateral FWHM of 1.14 µm and axial FWHM of 5.85 µm, the latter corresponding also to the size of the axial intensity PSF. Using the method discussed in Section 4.3.4, the effective lateral intensity PSF was calculated to be 0.89 µm. The slight asymmetrical shape of the axial intensity distribution indicates typical signs of residual spherical aberration and astigmatism in the system [192, 193], which is consistent with the remote focusing calibration results obtained in Section 6.4.1.

7.5 Gamma correction for image contrast enhancement

Gamma correction, or power-law transformation, is a formula applied on image intensity to manipulate contrast for better visualisation of structural details within the image. It can be expressed mathematically as

$$I_{\mathrm{o}} = I_{\mathrm{max}} \cdot (I_{\mathrm{i}}/I_{\mathrm{max}})^{1/\gamma}\,, \tag{7.1}$$

where I_{i} is the input intensity, I_{o} is the output intensity after gamma correction, I_{max} is the maximum intensity for a given bit-depth, and γ is the adjustable gamma value. A gamma value of 1.0 outputs the original image, while that smaller and larger than 1.0 moves the image

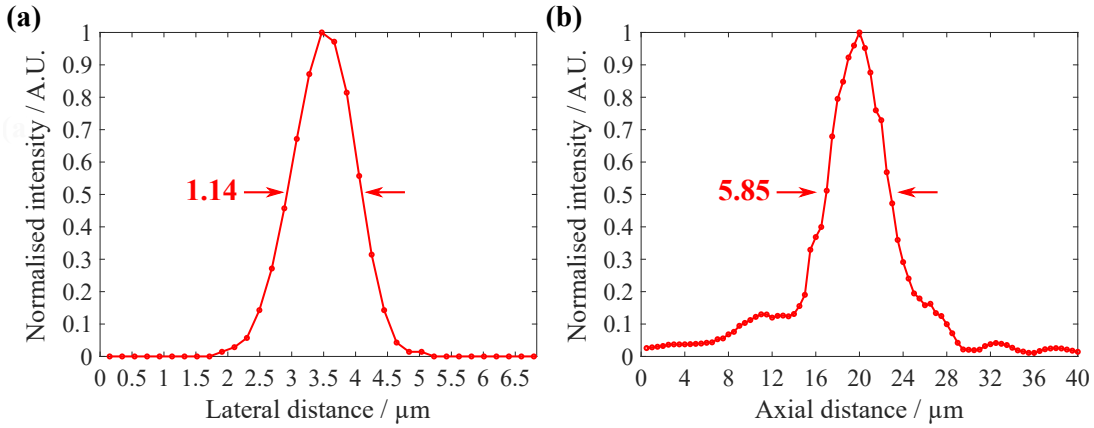


Figure 7.5: Spatial resolution calibration results after removal of image artefacts. (a) Intensity profile plot along red line drawn perpendicular to 1-µm wide stage micrometer graticule in Figure 7.4(b), right. (b) Detected intensity plot of objective focal spot scanned axially through a planar mirror in steps of 0.5 µm.

histogram towards darker and whiter tones, respectively. A toggle bar as shown in Figure 7.6 was incorporated in the software GUI for flexible adjustment during real-time imaging.

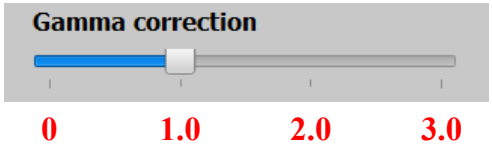


Figure 7.6: GUI showing toggle bar for adjustment of gamma value during real-time imaging.

To find the optimum gamma value for better visualisation of structural details within scattering biological specimens, comparison was made at the surface of frozen mouse calvaria. The optimum value was determined in two steps. A histogram was first generated for each image and those without shadow- or highlight-clipping (which would otherwise indicate a loss of detail) would enter the second step while others were abandoned. Critical structural details within the focal plane of these images were then chosen, and an intensity profile plot was generated across the selected structures. The contrast ratio (CR) was further calculated for each plot and comparison was made to find the gamma value with the highest CR.

Characterisation results of gamma correction within frozen mouse calvaria is demonstrated in Figure 7.7. For simplicity, side-by-side comparison is made between 4 raw images with gamma values of 1.0, 1.5, 2.0, and 2.5 in Figure 7.7(a). From direct perception of the human eye, raw

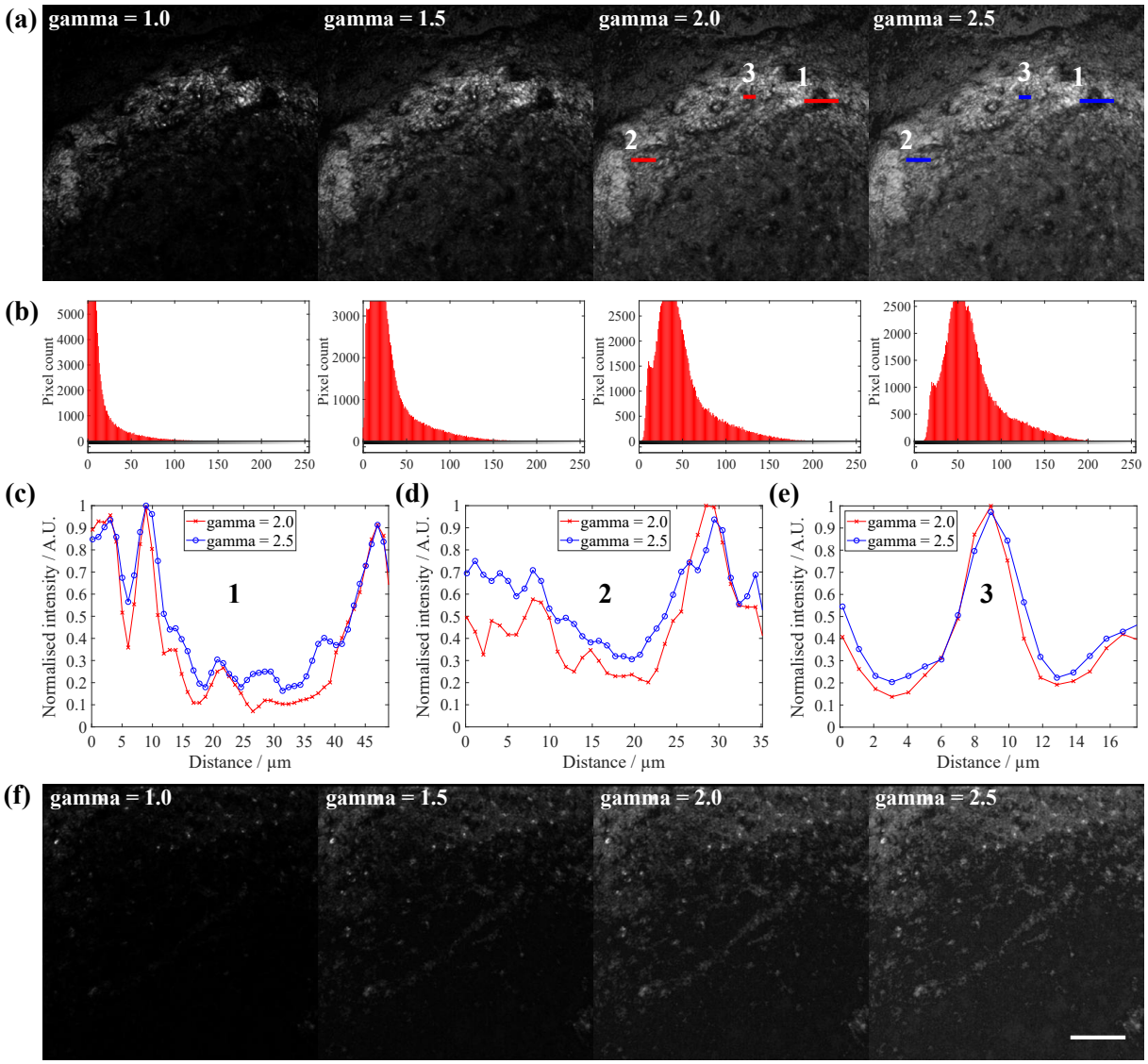


Figure 7.7: Characterisation results of gamma correction in frozen mouse calvaria. (a) Comparison of raw images obtained at the surface of frozen mouse calvaria for gamma values of 1.0 (original image), 1.5, 2.0, and 2.5. (b) Histograms obtained from corresponding raw images. (c)–(e) Intensity profile plots along red lines (gamma = 2.0) and blue lines (gamma = 2.5) at different positions of the natural focal plane as shown in (a). (f) Validation images at ∼80 µm depth for gamma values of 1.0 (original image), 1.5, 2.0, and 2.5. Scale bar: 100 µm.

images with gamma values of 1.0 and 1.5 are dark and minimal information can be appreciated from layers adjacent to the focal plane. Images become brighter with gamma values of 2.0 and 2.5, revealing more constructive details that can be separated from the background tissue matrix. This is further analysed using corresponding histograms, given in Figure 7.7(b), where

Table 7.1: Contrast ratios calculated from normalised intensity profiles plots at 3 different positions for gamma values of 2.0 and 2.5.

Position	1		2		3	
Gamma value	2.0	2.5	2.0	2.5	2.0	2.5
Contrast ratio	14.00	6.13	4.97	3.07	7.28	4.77

those for gamma values of 1.0 and 1.5 are noticeably "shadow-clipped" on the left. By contrast, gamma values of 2.0 and 2.5 lead to a full histogram, validating the findings above.

Prominent structures at 3 different locations were then arbitrarily chosen and normalised intensity profile plots were generated along the lines drawn in Figure 7.7(a), the results of which are given in Figures 7.7(c)–(e). The CR of each plot was calculated as CR = $I_{\max}/I_{\min}$, with results given in Table 7.1. For all 3 positions, a gamma value of 2.0 led to much higher CRs compared to that of 2.5. This phenomenon was further validated at depths of $\sim$80 µm (Figure 7.7(f)). Therefore, a gamma value of 2.0 was used for acquisition of images within frozen mouse calvaria throughout the remainder of this work. It should be noted that the optimum gamma value varies according to the specific sample. This can be determined using the same procedure as described above, though an easier solution would be to adjust the toggle bar shown in Figure 7.6 and determine the best contrast in real time.

7.6 Discussion and conclusion

In this chapter, it was demonstrated how raw images with artefacts or low contrast could be post-processed with minimal computational effort to improve quality before real-time display without affecting the image update rate. Sinusoidal image distortions during the bi-directional scan process were optimally corrected for using pre-calibrated mapping functions generated with a grid sample and a Clough-Tocher interpolant for pixel-reassignment. The CR of images from severely scattering samples was enhanced by finding the optimum gamma value that compromises for the "shadow-clipped" histograms of low contrast images. Four imaging modes with different FOVs and image update rates were also implemented to facilitate the process of switching between macroscopic and close-up views during clinical diagnosis.

One of the main limitations during this work was that the FPGA had a low sampling rate and all software for scanning control and image acquisition were ran from a laptop for portable transit. This was also discussed in Section 4.5. More intensive methods such as line-by-line pixel registration were also tested but led to a prolonged image processing time which prevented images from being updated within pre-assigned time slots and caused the software to freeze. As it was not ideal to lower the image update rate for the purpose of this microscope, these methods were not further investigated into. However, their effectiveness should be exploited if more powerful devices were used. In particular, residual jitter between forward- and backward-scan lines may be overcome in a way that did not sacrifice the image resolution.

Chapter 8

Extended range aberration-free autofocusing via remote focusing and Bi-LSTM network prediction

8.1 Overview

Rapid autofocusing over long distances is critical for tracking 3D topographical variations and sample motion in real time. This chapter describes an extended range autofocusing technique that combines remote focusing (RF) with sequence-dependent learning via bi-directional long short term memory (Bi-LSTM) network prediction. A deformable mirror (DM) and a Shack-Hartmann wavefront sensor (SHWS) were used to record phase information, as well as to correct for system-induced aberrations during axial scanning. Three sequential shift measurements consisting of specific Zernike coefficients acquired at pre-determined axial positions were used to predict RF voltages for fast autofocusing.

The following sections start with an introduction of the status and limitations of existing autofocusing techniques. Next, a thorough description of the autofocusing workflow proposed in this work is presented. The distribution curves of specific Zernike modes are further evaluated as a feasibility study. The structure of the developed Bi-LSTM network is then presented with offline optimisation results for critical parameters. Experimental validations were performed both in air and refractive-index-mismatched media, such as arbitrary-thickness liquid layers up to 1 mm. This is especially advantageous for clinical applications where the sample is typically

immersed in a buffer or physiological fluid. Network generality was evaluated for fields of view (FOVs) of different sizes, as well as sample types not seen during network training. Proof-of-concept experiments were carried out for tracking of continuous axial motion in real time. Finally, the technique's ability to autofocus at target depths was validated using organotypic hippocampal slices immersed in liquid.

8.2 Status and limitations of existing autofocusing techniques

Autofocusing to automatically acquire in-focus images is of wide interest for applications such as whole slide imaging [14, 194], digital holography [195], and surgical microscopy [16]. Whole slide imaging systems typically use a dry high numerical aperture (NA) objective for imaging thin tissue slices. The main challenge lies in the need to acquire high quality images while dynamically tracking 3D topographical variations of the sample surface over large lateral regions [194]. Conventionally, a set of axial-stack (z-stack) images is taken at different positions and a figure of merit is calculated for each image to find the focal plane corresponding to the peak or valley of the figure of merit [14]. This operation is time-consuming as the number of images required in each z-stack rapidly increases for a higher positioning accuracy [14, 196]. In addition, the range is constrained to less than 40 µm due to the lack of structural details at severely out-of-focus positions where meaningful figure of merit calculations cannot be obtained [196, 197]. To increase the autofocusing range, approaches that use dual-pinhole masks before the sensor [198], dual-LED illumination [199], as well as image-based wavefront sensing [200, 201] have been introduced, successfully accommodating for defocus ranges above 80 µm. Reflection-based methods that track the angle of reflectance from a laser can enable fast autofocusing, but the objective focus can only be maintained at a fixed axial position above the reference plane, such that topographical variations of the sample surface cannot be examined, inherently limiting its scope of application [194]. Finally, in terms of digital holography, autofocusing has significantly improved the speed of distance prediction and phase recovery [202, 203].

More recently, machine learning methods applied to autofocusing have been particularly advantageous for enhancing speed and throughput [15, 202–208], accuracy by means of combining

information from different domains [205], as well as robustness towards non-ideal scenarios such as sample tilt [15, 206], cylindrical curvature [206], and unevenly distributed focal points [208]. For the majority of applications, convolutional neural network (CNNs) were used to interpret defocus information from acquired sample images or holograms [15, 202, 203, 205, 206, 208]. An in-focus image was then acquired by either mechanical adjustment of the sample stage and objective lens [203], or virtual refocusing [15, 206, 208]. Despite their many advantages, deep learning methods possess some inherent drawbacks that cannot be neglected. First, networks that directly use sample images as input need to make interpretations from sufficient structural details, which dictates a relatively short defocus range of at most $\pm 20\,\mu m$ [204] and typically around $\pm 10\,\mu m$ [15, 205, 206, 208]. To obtain a larger defocus range, structural information can be embedded within holograms using interference [202], or a Fourier transform can be performed on the sample image [207]. For imaging of thick tissue with severely tilted or unflat surfaces, as well as applications where sample movement is likely to occur [16], much larger defocus ranges are desired. Second, despite the short prediction time, a significant amount of computational power is required during the training stage on image data, which can typically take over a day even on powerful GPUs [15, 202, 204, 205]. Third, networks that rely on information from specimen images can be difficult to generalise towards untrained sample types [207–209].

To address the above limitations while preserving merits of the network prediction speed, one possible solution is to extract positional information from sources other than sample images, and adopt less computationally intensive networks [207] that make use of non-image-based input data. Techniques proposed in [200, 201] inferred phase information by solving the transport of intensity equation and demonstrated a much extended defocus range, though at the expense of using multiple correction loops. Alternatively, optical phase can be directly measured at the pupil plane using specialised devices such as an SHWS [95]. The latter eradicates dependency on structural details, which fundamentally overcomes limitations to the defocus range, while greatly enhancing generality towards different sample types. Apart from defocus, other aberrations that degrade the image quality can be measured simultaneously, and an adaptive device such as a DM can be used to correct for these aberrations using adaptive optics (AO) techniques. The Zernike expansion of phase aberrations further allows its representation to be reduced from a

2D phase function into a short list of Zernike coefficients. Such data can be well interpreted by a much simpler network, such as a multilayer perceptron [207] or recurrent neural network.

8.3 Materials and methods

In the context of this work, the use of a bidirectional long short term memory (Bi-LSTM) network [210, 211] was exploited. Bi-LSTM networks are designed to learn from both directions of an input sequence for prediction of the output at the current data point, or shift, and extract maximum information from the sequential ordering [211]. It has high noise tolerance and requires fewer operations when updating weights that connect adjacent units for each shift. This is of special importance as these weight parameters essentially determine how much of the information gathered in preceding units is passed on to later units and how new information should be formed. Compared to CNN networks, as the input data for Bi-LSTM networks is usually a 1D sequence rather than a 2D image, the weight updating process is much simpler, making Bi-LSTM networks faster to train, easier to generalise, and less dependent on parameter fine tuning [210].

Data collection and experimental demonstrations were performed in the compact and contactless reflectance confocal microscope (CCRCM) after incorporating the large-stroke DM and custom SHWS. Details of the microscope setup were discussed in Section 4.3.2 and Section 6.2, with the schematic diagram given in Figure 6.1. DM and RF calibration were performed according to procedures outlined in Section 3.4.2 and Section 3.5.1, which allowed simultaneous correction of system aberrations induced at each calibration step. The diffraction-limited RF range of $\pm 60\,\mu m$ discussed in Section 6.4.1 dictates the maximum autofocusing range for the technique described in this work, and all axial distances refer to the mechanical distance as determined by the sample translation stage.

8.3.1 Autofocusing workflow

The workflow of the proposed autofocusing scheme is illustrated in Figure 8.1 for the typical case of surface tracking. Figure 8.1(a) depicts the main procedure for network training, including

data collection and preprocessing, and pairing of input-ground truth data. Training data was collected by first applying a DM system flat file and adjusting the sample stage axially such that the tissue surface coincided with the objective natural focal plane. Then, RF voltages were applied to the DM for axial scanning with 0.5 µm steps from −60 µm focal displacement to +60 µm. At each axial step z_d, phase aberration measurements were taken with the SHWS when scanning over a small lateral region (<20 µm) to form one dataset. This was repeated multiple times on mouse skull exposed to air, as well as that beneath an arbitrary-thickness liquid layer within 1 mm. Various surface conditions were taken into account, such as regions with different surface roughness, curvature, and signal levels.

Collected datasets were then preprocessed by sampling at 3 sequential shifts τ_1, τ_2, τ_3 for each axial step. Sampling in the negative and positive directions were considered as the past and future states, respectively. The full RF range was partitioned into 3 regions, namely the central, negative, and positive regions, as defined by stride length Δz. The central region incorporated axial steps within $[-60 + \Delta z, 60 - \Delta z]$ µm range of the tissue surface, the negative region $[-60, -60 + \Delta z)$ µm, and the positive region $(60 - \Delta z, 60]$ µm. For all 3 regions, τ_1 corresponded to the currently evaluated position z_d. In the case of the central region, τ_2 corresponded to an axial step Δz in the negative direction $z_d - \Delta z$, and τ_3 corresponded to an axial step Δz in the positive direction $z_d + \Delta z$. The Zernike coefficients as retrieved by the SHWS at each of the 3 axial positions $[a_{1,1}, a_{1,2}, ..., a_{1,N}]$, $[a_{2,1}, a_{2,2}, ..., a_{2,N}]$, and $[a_{3,1}, a_{3,2}, ..., a_{3,N}]$, were then reorganised into one input training sample that consisted of 3 shifts and N features. For the negative region, τ_2 was sampled at $z_d + \Delta z$, while τ_3 corresponded to positions further away from z_d, denoted by $z_d + \Delta z + \Delta z_-$. For the positive region, τ_2 was sampled at $z_d - \Delta z$, while τ_3 was sampled at $z_d - \Delta z - \Delta z_+$. Finally, input training samples were paired with a set of ground truth RF voltages corresponding to the opposite amount of focal displacement $-z_d$, denoted as V_{-z_d}, to form one training sample. Separate networks of the same architecture were trained for each of the central, negative, and positive regions.

Figure 8.1(b) demonstrates how the trained networks enable RF voltage prediction during real-time autofocusing. At any arbitrary axial position z_d, RF voltages corresponding to z_d, $z_d - \Delta z$, and $z_d + \Delta z$ were first sequentially applied to the DM. At each position, in parallel to

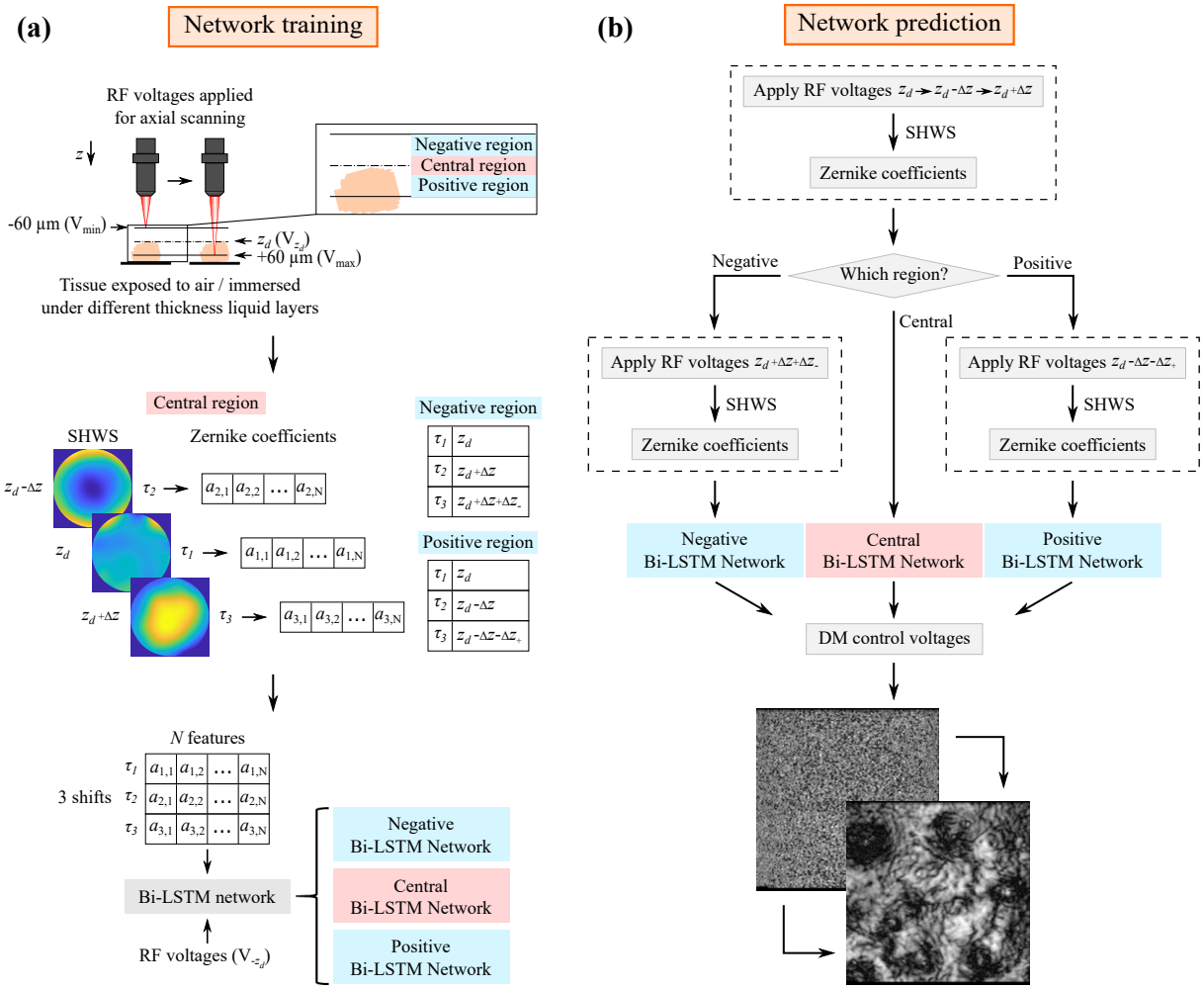


Figure 8.1: Autofocusing workflow via RF and sequence-dependent learning. (a) During data collection, RF voltages V_{z_d} were first applied for axial scanning. At each axial step, Zernike coefficients $a_{j,i}$, where j represents the jth shift and i the ith Zernike coefficient, sequentially measured at 3 axial positions, were used as network input and paired with RF voltages corresponding to the opposite amount of focal displacement. Separate Bi-LSTM networks of the same architecture were trained for each of the central, negative, and positive regions. (b) During experiments, Zernike coefficients measured at the same axial positions were passed into the corresponding Bi-LSTM network for direct prediction of DM control voltages.

image acquisition, Zernike coefficients retrieved by the SHWS were analysed to make a decision based upon the consecutive measurements of Zernike defocus (Z_2^0) on which region the currently evaluated position fell within. In the case of the central, retrieved Zernike coefficients were then reorganised into a matrix of 3 shifts and N features as in the training stage and passed into the central Bi-LSTM network. For the negative region, a 4th phase measurement would be made

at $z_d + \Delta z + \Delta z_-$, and these Zernike coefficients would be used along with those acquired at z_d and $z_d + \Delta z$ to form input data for the negative Bi-LSTM network. Similar procedures apply to the positive region at positions sampled during network training. Predicted RF voltages were then directly used for refocusing.

8.3.2 Evaluation of Zernike distribution curves

The distribution of primary Zernike modes over the full ±60 µm defocus range as interpreted by the SHWS was evaluated for all datasets (Figure 8.2). In addition to Zernike defocus (Z_2^0), which provides the most critical positional information, other low order Zernike modes such as primary spherical aberration (Z_4^0), vertical astigmatism (Z_2^2), horizontal coma (Z_3^1), vertical coma (Z_3^{-1}), and oblique astigmatism (Z_2^{-2}), can also be present due to the data being acquired in both air and liquid under different surface conditions. A 90% data distribution interval was calculated to show how the majority of data was distributed, while the remaining 10% which possibly included outliers and extremely noisy data, was also used during network training to improve generality. A 95% confidence interval was obtained from the full dataset to represent the level of uncertainty in the curve estimation process, and the smoothed mean was also calculated to understand the overall distribution trend.

The 90% distribution interval is simply the raw data of the Zernike coefficients obtained at each axial location used for network training. It is broad because the data was collected both in air and liquid, which have different refractive indices; and under varying surface conditions, which affected the measurement of the Zernike coefficients with respect to that of the theoretical value. Despite so, the goal was to predict the distance between the current focal position and the specimen surface regardless of the imaging medium and surface condition. Therefore, as a feasibility study it was important to examine the confidence in doing so, given the variability and size of the training dataset, which was the reason for calculating the 95% confidence interval. This was obtained by first computing the standard error of the mean for the Zernike coefficients at each axial location, multiplying it by the calculated 95% values of the t-distribution, and then adding and subtracting those values from the mean.

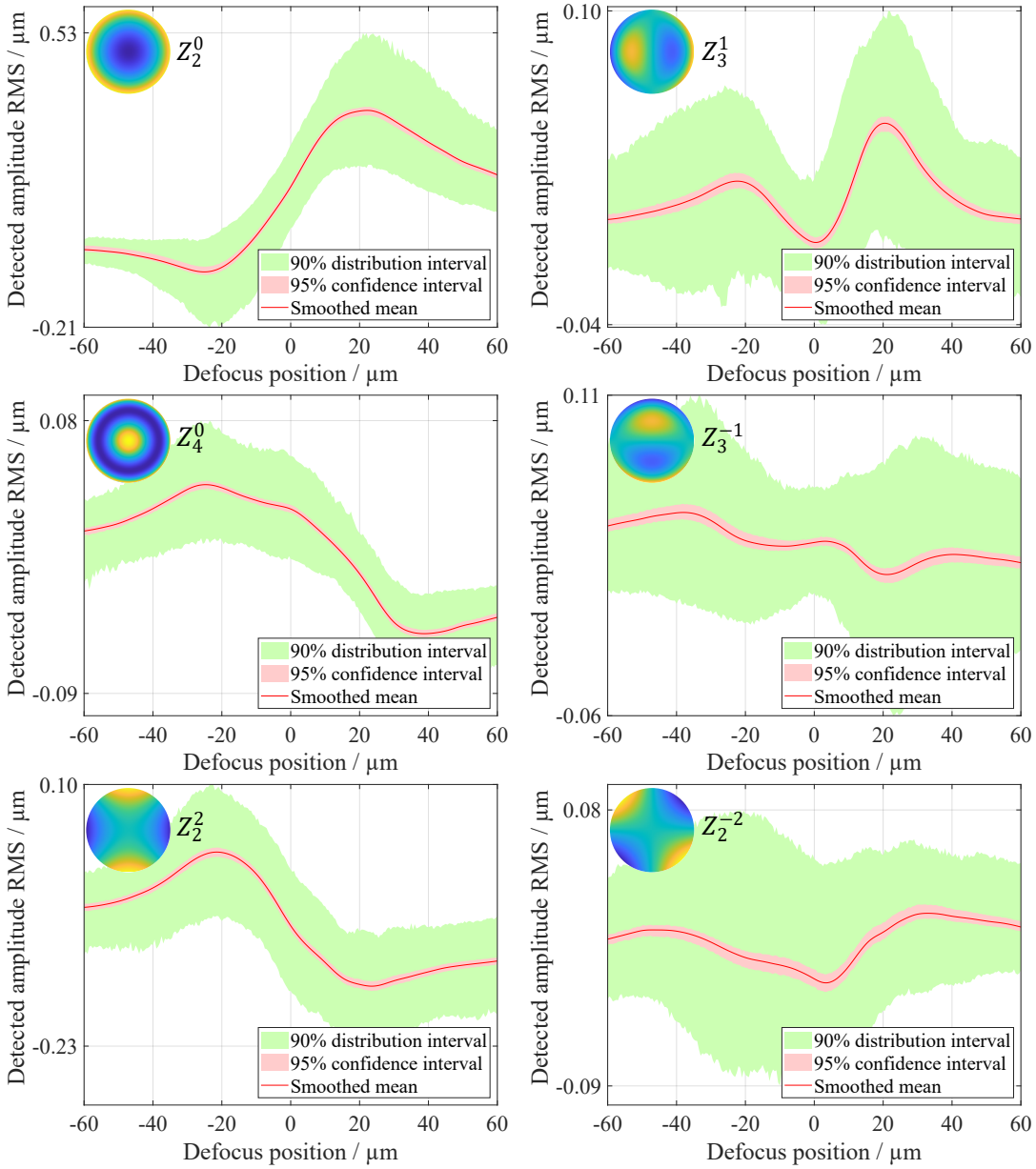


Figure 8.2: Wavefront maps and distribution plots of primary Zernike modes (Zernike defocus (Z_2^0), primary spherical (Z_4^0), vertical astigmatism (Z_2^2), horizontal coma (Z_3^1), vertical coma (Z_3^{-1}), and oblique astigmatism (Z_2^{-2})) as a function of defocus position incorporating data from all datasets. Green shade: 90% data distribution interval; pink shade: 95% confidence interval; red line: smoothed mean.

Results showed that despite the diversity of surface conditions and liquid layer thicknesses, Zernike coefficients could be inferred with a reasonably high accuracy throughout the full defocus range. It could be seen that although some of the curves were monotonic within a small defocus

range, none of them were monotonic within the full defocus range. Therefore, in order to predict our precise location at an arbitrary point within the full defocus range, multiple shifts were required. During experiments, discrimination of the currently evaluated region was inferred from the 3 sequential measurements of Zernike defocus (Z_2^0) according to asymptotes of the distribution curve via the following criterion,

$$\begin{cases} \text{negative} & \text{if } a_3 \leq a_1 \leq a_2 \text{ and } a_2 < 0.1 \\ \text{positive} & \text{if } a_3 \leq a_1 \leq a_2 \text{ and } a_3 > 0 \\ \text{central} & \text{otherwise,} \end{cases} \tag{8.1}$$

where a_1, a_2, and a_3 represent measured Zernike defocus values at positions z_d, $z_d - \Delta z$, and $z_d + \Delta z$, respectively. In practice, this means that Zernike defocus predominantly determines the current focal position, albeit with a degree of uncertainty due to the variation in imaging medium and liquid layer thickness. However, this uncertainty can then be decreased by simultaneous measurement of other Zernike modes that together allow for a more precise prediction.

8.3.3 Bi-LSTM network

The Bi-LSTM network architecture is illustrated in Figure 8.3. It comprises of 4 Bi-LSTM layers each with 64 units and a dense layer with 69 nodes for each of the 69 DM actuators. The optimal network architecture was determined by gradually increasing the number of network layers and the number of units in each layer to find that with the lowest validation loss. It was found that two- and three-layer networks performed similarly, four-layer networks saw a noticeable improvement, and more layers thereafter did not lead to substantial improvement. Thus a four-layer structure was decided upon. Input features were individually normalised between [-1,1] and batch normalisation was performed before each Bi-LSTM layer. ReLU activation was used to introduce non-linearity in Bi-LSTM layers and linear activation was used in the dense layer for direct voltage prediction. Random weights were initialised with a He uniform kernel and the adaptive moment estimation (Adam) optimiser [212] was adopted to iteratively update weights and biases with a learning rate of 1×10^{-3}. The network was implemented using Keras with a Tensorflow backend.

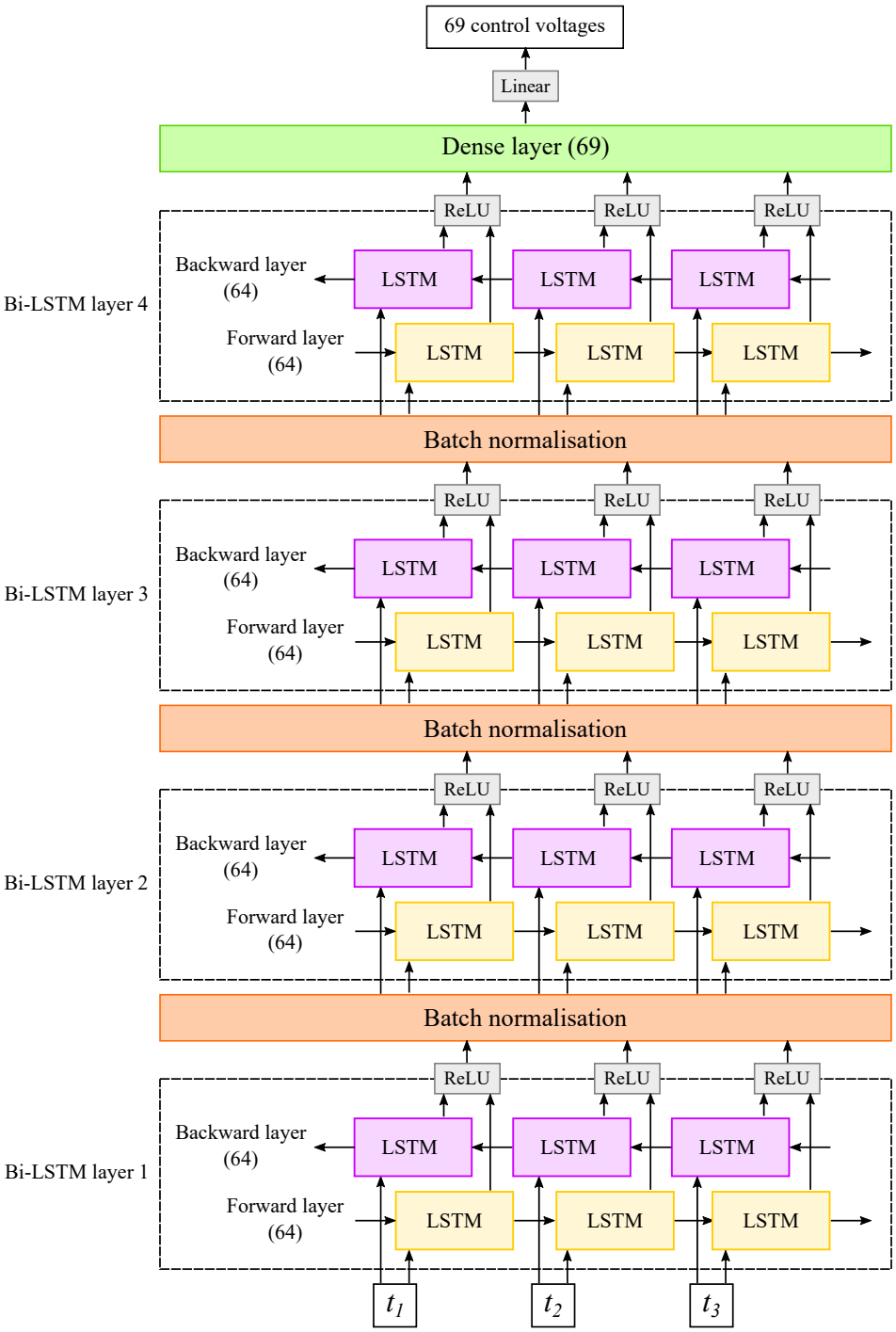


Figure 8.3: Architecture of the proposed bidirectional long short term memory (Bi-LSTM) network comprising of 4 Bi-LSTM layers each with 64 units, batch normalisation, and a dense layer with 69 nodes to control 69 DM actuators. ReLU and linear activation functions were used in the Bi-LSTM layers and final dense layer, respectively.

Offline optimisation routines were performed to find the optimum stride lengths Δz, Δz_-, and Δz_+, the number of Zernike modes to use as input features, as well as the batch size and number of datasets for network training (Figure 8.4). Here we demonstrate validation results after all above parameters had been obtained such that only one parameter was interrogated at a time with other parameters set as the optimum value. 160 datasets were used in the first 3 tasks, 140 for network training with a validation split of 0.2, and 20 as test data for blind inference, which is process of predicting RF voltages with input data not used during the training stage. Samples were shuffled between epochs to prevent the model from learning order dependence between independent samples. In all cases, the root mean square error (RMS error) between predicted and ground truth RF voltages defined the loss function and was compared with the root mean square difference (RMS difference) between RF voltages corresponding to calibrated axial step intervals. The central Bi-LSTM network was empirically trained for 30 epochs and the positive and negative Bi-LSTM networks 70 epochs, while more epochs led to overfitting.

8.3.4 Sample preparation

The following protocol was carried out for preparation of mouse skull immersed beneath arbitrary thick liquid layers. 1% agar gel was prepared by dissolving 0.2 g agar powder (Sigma Aldrich) in 20 mL of distilled water and heating the suspension until a clear solution is obtained. A small amount of hot agar gel was transferred to a mold and a piece of mouse skull was embedded within the gel using tweezers while exposing a portion of the surface to air. Then the sample was left to set for around 30 minutes until the agar gel fully hardened before transferring the agar sample to a petri dish. In order to overcome the surface tension of water that prevents it from spreading out on the surface of the petri dish, 0.06% cetrimonium bromide solution (CTAB, molar mass: 364.45 g/mol, critical micelle concentration in water: 0.0009 mol/L) was prepared by dissolving 0.03 g CTAB powder in 50 mL of distilled water. Precise adjustment of the liquid thickness in all relevant experiments was enabled by calculating the equivalent liquid volume with prior knowledge of the petri dish dimension and applying the liquid using a micropipette. All other samples were prepared using similar procedures to that in Section 4.3.5.

8.4 Network optimisation and experimental validation results

8.4.1 Offline network optimisation results

To determine stride length Δz, the central Bi-LSTM network was individually trained using samples generated with stride length increments of 5 µm within the range of 5 µm to 30 µm. The optimum stride length Δz_{op} corresponding to the smallest RMS error was then employed to find $\Delta z_{-\text{op}}$ and $\Delta z_{+\text{op}}$ using the negative and positive Bi-LSTM networks. As outlined in Section 8.3.1, Δz determined the size of the 3 defocus regions. Therefore, the amount of training and test samples varied with a fixed number of datasets during optimisation of Δz, while this number remained constant for that of Δz_- and Δz_+. The number of training and test samples used for optimisation of Δz, Δz_-, and Δz_+ is given in Table 8.1, and the mean RMS error over 5 test runs for each examined stride length is plotted in Figure 8.4(a) with corresponding error bars. Results suggested an optimum value of 25 µm for all stride lengths Δz_{op}, $\Delta z_{-\text{op}}$, and $\Delta z_{+\text{op}}$. A complete summary of the raw RMS error data is provided in Table 8.2.

Table 8.1: Number of training and test samples used for optimisation of Δz, Δz_+, and Δz_-.

Stride length (µm)	Δz						Δz_+	Δz_-
	5	10	15	20	25	30		
Training data	30800	28000	25200	22400	19600	16800	6860	6860
Test data	4400	4000	3600	3200	2800	2400	980	980

Table 8.2: RMS error over 5 test runs for different values of Δz, Δz_+, and Δz_-.

RMS error (V)		Δz			Δz_+			Δz_-		
		Mean	Max	Min	Mean	Max	Min	Mean	Max	Min
Stride length	5 µm	0.0198	0.0203	0.0187	0.0139	0.0148	0.0125	0.0168	0.0186	0.0148
	10 µm	0.0138	0.0143	0.0131	0.0122	0.0135	0.0113	0.0125	0.0140	0.0114
	15 µm	0.0115	0.0128	0.0107	0.0109	0.0116	0.0103	0.0114	0.0134	0.0105
	20 µm	0.0092	0.0099	0.0087	0.0091	0.0100	0.0084	0.0107	0.0118	0.0096
	25 µm	0.0077	0.0082	0.0072	0.0091	0.0098	0.0083	0.0107	0.0126	0.0094
	30 µm	0.0077	0.0081	0.0074	0.0106	0.0110	0.0103	0.0118	0.0135	0.0108

The optimum number of input features was determined by choosing combinations of the primary Zernike modes evaluated in Section 8.3.2 according to their azimuthal index orders and

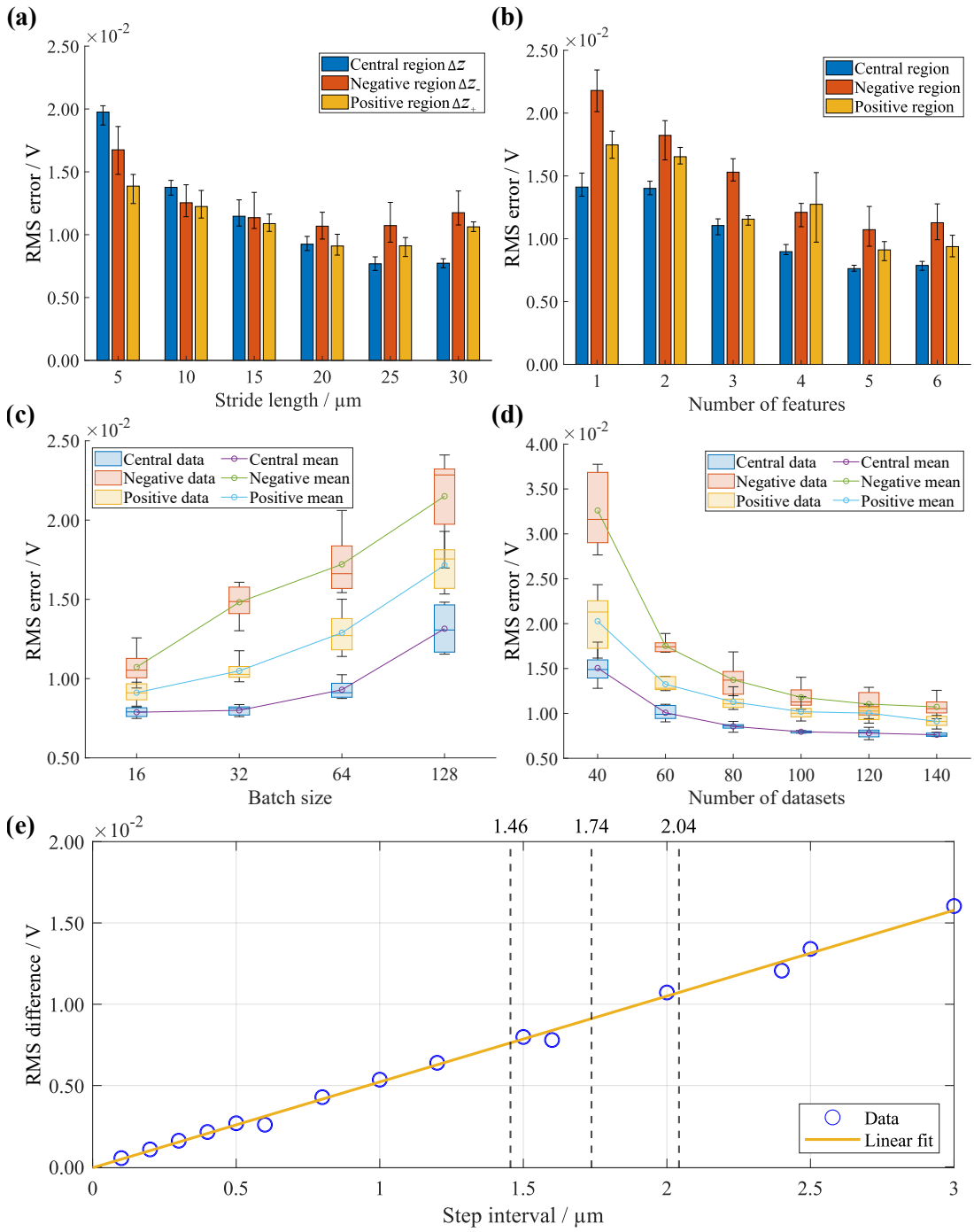


Figure 8.4: Offline network optimisation results. (a) Test RMS error as a function of stride length Δz, Δz_-, and Δz_+; (b) Test RMS error versus the number of Zernike modes incorporated as input features; (c) Test RMS error as a function of batch size for each training epoch; (d) Test RMS error versus the number of datasets used for network training. (e) Linear fit of RMS difference between RF voltages corresponding to calibrated axial step intervals. Dashed vertical lines indicate the equivalent prediction error in terms of distance for the final RMS error during offline optimisation.

level of uncertainty as indicated by the 95% confidence interval. The combination of Zernike modes used in each case is given in Table 8.3. Figure 8.4(b) shows how the RMS error changed with increasing input features over 5 test runs for each of the 3 defocus regions. A summary of the raw RMS error data is provided in Table 8.4. Results showed that in all 3 cases, prediction accuracy was highest when 5 Zernike modes were included as input features. This conclusion suggested that the incorporation of other primary Zernike modes in addition to Zernike defocus can indeed provide useful information for enhancement of network performance. However, there is an extent to which more input features can be beneficial, dependent upon system-specific phase aberrations, and driving beyond this limit may lead to higher chances of overfitting to noisy data. The 3 network models were then trained with different batch sizes of 16, 32, 64, and 128. A monotonic decrease in RMS error was seen with smaller batch sizes in all 3 cases, suggesting an optimum value of 16 (Figure 8.4(c)).

Table 8.3: Combination of Zernike modes evaluated for the optimum number of input features.

Number of features		1	2	3	4	5	6
Zernike modes	Z_2^0	✓	✓	✓	✓	✓	✓
	Z_4^0		✓	✓	✓	✓	✓
	Z_2^2			✓	✓	✓	✓
	Z_3^1				✓	✓	✓
	Z_3^{-1}					✓	✓
	Z_2^{-2}						✓

Table 8.4: RMS error over 5 test runs for different numbers of input features.

RMS error (V)		Central Network			Positive Network			Negative Network		
		Mean	Max	Min	Mean	Max	Min	Mean	Max	Min
Number of features	1	0.0141	0.0152	0.0134	0.0175	0.0186	0.0164	0.0218	0.0234	0.0201
	2	0.0140	0.0146	0.0135	0.0165	0.0173	0.0160	0.0182	0.0194	0.0163
	3	0.0111	0.0116	0.0103	0.0116	0.0118	0.0111	0.0153	0.0164	0.0146
	4	0.0090	0.0095	0.0087	0.0127	0.0153	0.0097	0.0121	0.0128	0.0110
	5	0.0076	0.0079	0.0074	0.0091	0.0098	0.0083	0.0107	0.0126	0.0094
	6	0.0079	0.0082	0.0075	0.0094	0.0103	0.0086	0.0113	0.0128	0.0099

Finally, networks were trained with increasing numbers of datasets to find the threshold for a sufficient prediction accuracy. Results in Figure 8.4(d) showed that the RMS error dropped

rapidly between 40∼80 sets of data, while a moderate improvement was observed afterwards. Considering the trade-off between training time (effort required for data collection) and prediction accuracy, the mean RMS error after training with 140 datasets (0.0077 V, 0.0091 V, and 0.0107 V for the central, positive and negative defocus regions, respectively) was compared with the RMS difference between RF voltages corresponding to calibrated axial step intervals, as illustrated in Figure 8.4(e). Equivalent prediction error in terms of distance was inferred from the linear fit to be 1.46 µm, 1.74 µm, and 2.04 µm for the central, positive, and negative regions, which was much smaller than half the system axial resolution of 5.5 µm, indicating a sufficient accuracy according to the Nyquist criterion. Therefore, 140 datasets were used to generate final network models.

Networks were trained on a desktop computer with Intel 8-core i7-7820X 3.60 GHz CPU and 16 GB RAM, which took less than 5 mins for the central network, and 4 mins for the positive and negative networks. Real-time autofocusing was performed on a laptop with Intel 6-core i7-9750H 2.60 GHz CPU and 16 GB RAM. Blind inference took less than 0.037 s for all 3 networks. One full autofocusing cycle took 0.31 s when in the central region, and 0.40 s when in the positive and negative regions. Phase acquisition time could be flexibly adjusted.

8.4.2 Characterisations for both air-exposed and water-immersed tissue

The proposed autofocusing technique was first characterised on mouse skull exposed to air and beneath 250-µm, 500-µm, 750-µm, and 1000-µm thick liquid layers over the same FOV during data collection. With a DM system flat file applied, the sample was translated to defocused positions along the optical axis with 10 µm step intervals over the ±60 µm range. At each position z_d, 5 independent autofocusing tests were performed, and the average image intensity I_d after refocusing to the sample surface was recorded in each instance. Considering the approximate relation of $\mathrm{h_{eff}} = |\mathrm{h_a}|^4$ between the effective system intensity point spread function $\mathrm{h_{eff}}$ and single path amplitude point spread function $\mathrm{h_a}$ in a reflectance confocal microscope described in Section 4.3.4, I_d was compared with the average image intensity $\mathrm{I_{ref}}$ acquired when no defocus was induced by calculating the relative Strehl ratio, which is proportional to $\sqrt{\mathrm{I}_d/\mathrm{I_{ref}}}$. Results

showed that under all 5 scenarios, the trained Bi-LSTM network allowed tracking of the tissue surface with a relative Strehl ratio of above 0.8 for all examined positions (Figure 8.5(a)), regardless of the liquid layer thickness. Narrow error bars were obtained, indicating a good level of repeatability. Using the relative Strehl ratio as a quality metric takes into account not only defocus information, but also image quality in the presence of optical aberrations.

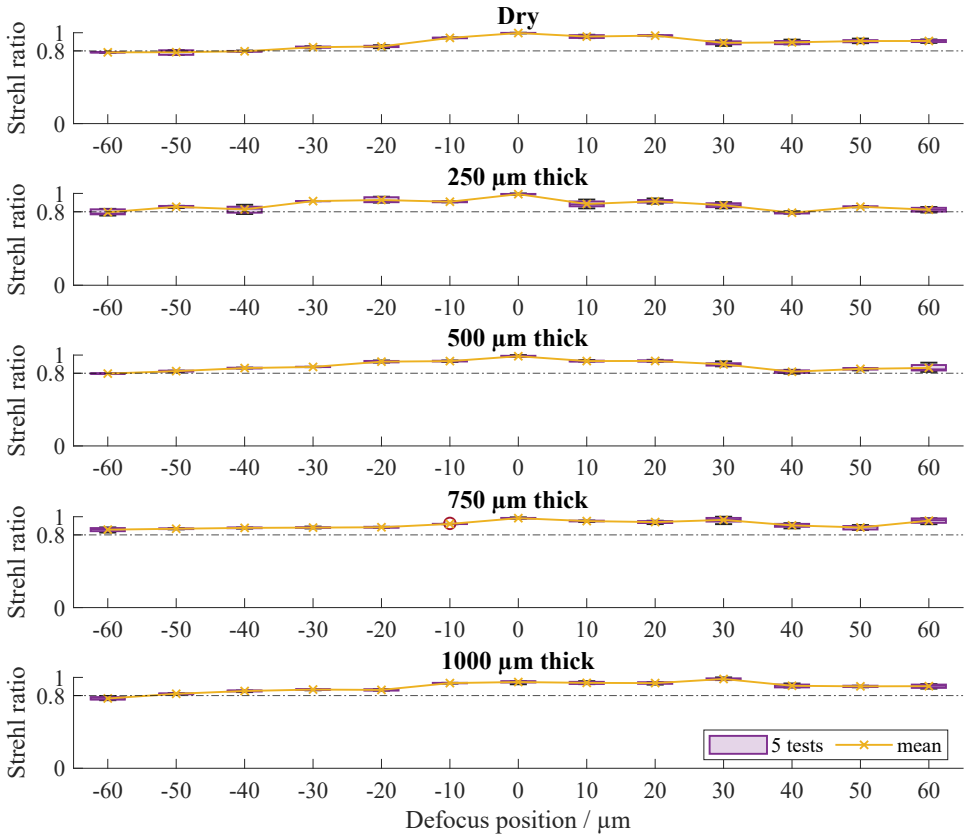


Figure 8.5: Characterisation results on mouse skull exposed to air and that beneath 250-µm, 500-µm, 750-µm, and 1000-µm thick liquid layers over lateral scan regions smaller than 20 µm. 5 independent tests were performed at each 10 µm step interval over the full ±60 µm range.

8.4.3 Generalisation towards different size imaging FOVs and sample types

Generalisation of the trained networks was evaluated over FOVs of different sizes and sample types not seen during network training. 50 µm and 100 µm FOVs were individually assessed on mouse skull exposed to air and fixed mouse brain. As illustrated in Figure 8.6(a), autofocusing was performed at each 10 µm step from −60 µm to +60 µm of focal displacement by translation

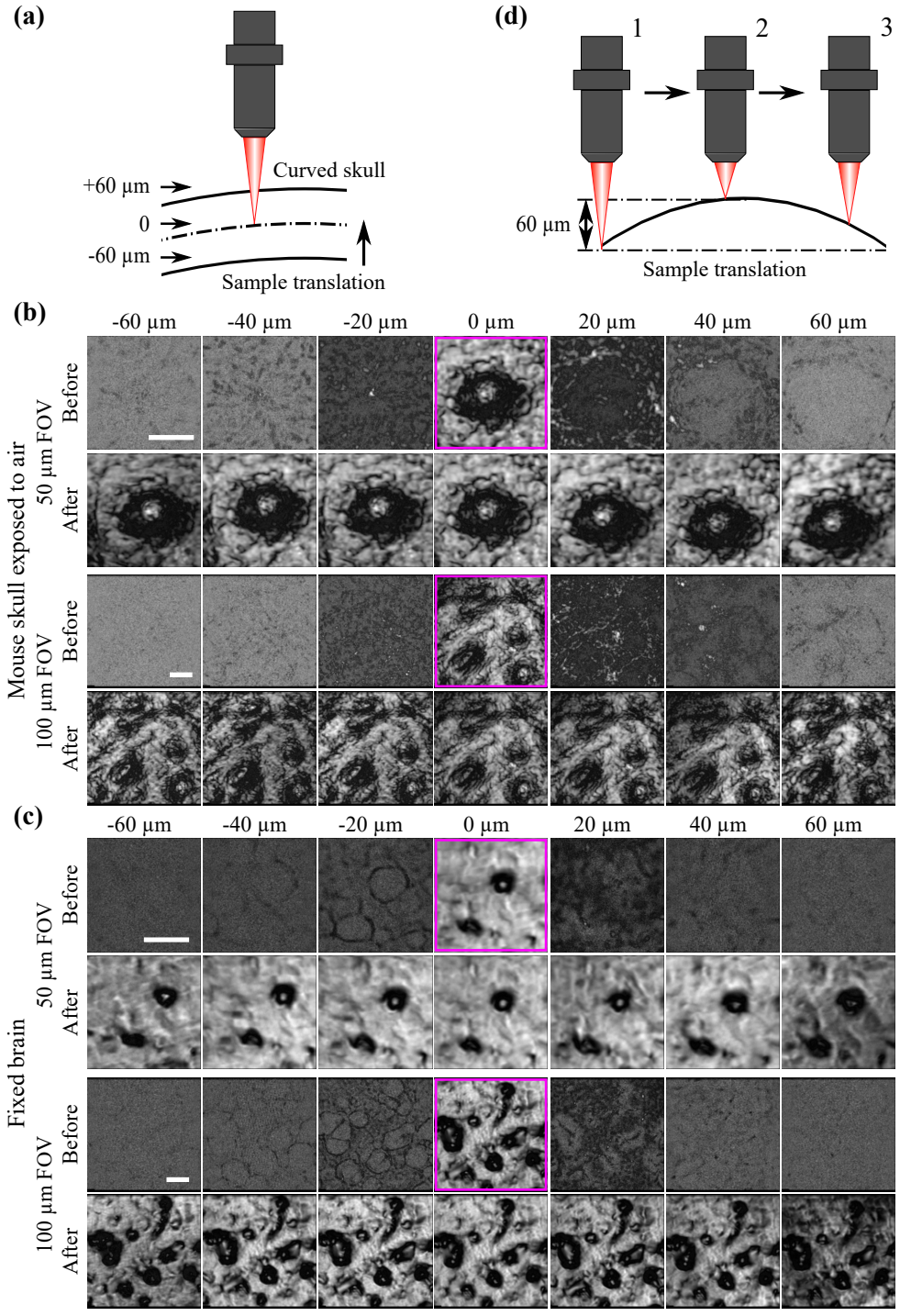


Figure 8.6: Validations of generalisation towards different imaging FOVs and sample types, and tracking of continuous axial motion. (a) −60 µm to +60 µm focal displacement introduced by sample stage translation at tilted region of curved skull during validation of different imaging FOVs. (b)–(c) Validation results over different imaging FOVs and fixed specimens. 50 µm and 100 µm FOVs individually assessed with: (b) mouse skull exposed to air; (c) fixed mouse brain. Images before and after autofocusing are displayed for comparison. Magenta box: reference image in each experiment. Scale bar: 20 µm. (d) Schematic of the relative motion between focal plane and sample surface during the course of Visualisation 1(a).

of the sample stage, and imaging was performed over a tilted region of the curved skull so as to simultaneously assess the network's resilience towards sample tilt. Exposure of the SHWS was set to 40 ms when scanning over 50 µm FOVs and 80 ms over 100 µm FOVs. Results at each 20 µm axial step are displayed in Figure 8.6(b) for the case of autofocusing on mouse skull, and Figure 8.6(c) for fixed mouse brain. Images were individually normalised between maximum and minimum pixel intensities for real-time display. Comparison was made between images before and after autofocusing, and the reference plane z_{ref} in each experiment when no defocus was introduced is highlighted in the magenta box. Results obtained after autofocusing from different defocus positions in both specimens showed comparable image quality to that obtained at the reference plane for both 50 µm and 100 µm FOVs. The focal plane remained stationary when autofocusing was performed without pre-induced defocus, and structural details at the tissue surface came into focus at all other positions, demonstrating robustness towards sample tilt, as well as validity for unseen specimens.

8.4.4 Autofocusing in real time with continuous axial motion

Next, through a series of 4 experiments we assessed the technique's ability to track continuous axial motion in real time. A 50 µm FOV was used in the first 3 experiments, and a 100 µm FOV in the final experiment. Imaging was performed at 4 fps and a predetermined number of consecutive images were recorded for each experiment. All Visualisations are played at 8 fps for demonstration purposes. The process of making sequential timestep measurements was observed as brief 'blinks'. Videos of the same process without autofocusing were recorded in each case. The first experiment showed how the proposed technique allowed continuous tracking of samples with severely tilted and unflat surfaces. With a DM system flat file applied, the natural focal plane was first positioned 60 µm deep below the peak of curved mouse skull. Next, the stage was translated laterally until a different surface region came into focus within the 50 µm FOV. This lateral position was recorded as the starting point for Visualisations 1(a) and 1(b). Then in Visualisation 1(a), autofocusing was switched on for a feedback rate of 0.5 Hz, and the stage was translated back along the same path until it reached the skull peak, before surpassing it in the

other direction, as illustrated in Figure 8.6(d). From Visualisation 1(a) it could be appreciated that the proposed technique allowed tracking of the surface morphology after each autofocusing routine and continuous examination of structural details was enabled throughout the whole period. In comparison, without autofocusing the skull surface was lost after a few frames, as seen in Visualisation 1(b).

In the second and third experiment, autofocusing was performed with a feedback rate of 1 Hz while monotonically translating the sample stage over the 120 µm range on mouse skull exposed to air and that immersed beneath a 500 µm-thick liquid layer, respectively. A total of 240 effective frames were acquired, equivalent to an axial motion rate of 2 µm/s. Observation of the skull surface was permitted throughout the recording session for both experiments in Visualisations 2(a) and 3(a), despite with slight deviations that may have been caused by rapid vibrations from manual stage translation. In comparison, Visualisations 2(b) and 3(b) only recorded structural features coming in and out of focus when the natural focal plane was within close proximity of the skull surface. In order to quantitatively analyse the imaging performance with and without autofocusing, Pearson correlation coefficients were computed for each image frame with respect to that acquired at 0 µm defocus position. Results for Visualisations 2(a) and 2(b) are given as example. Figure 8.7(a) plots correlation coefficients as a function of the defocus position. The yellow curve depicts imaging without autofocusing, showing strong correlation only within a narrow region about the reference plane, before dropping rapidly to below 0.2 [213]. The case with autofocusing on is illustrated in blue, where troughs represent 'blinking' patterns during timestep measurements. Red asterisks mark frames before (after) seeing a sudden decrease (increase) in correlation, which contain those captured in between timestep measurements, resulting in values above 0.4. This falls within expectations considering that the focal plane may not be static during the course of acquiring one image and lateral shifts may occur during manual stage translation. Figure 8.7(b) sorts the coefficients in descending order and plots the number of frames above a certain value. Dotted lines indicate a strong (>0.7) or moderate (>0.5) relationship between the reference image [213], and a significant increase can be seen when performing regular tracking routines.

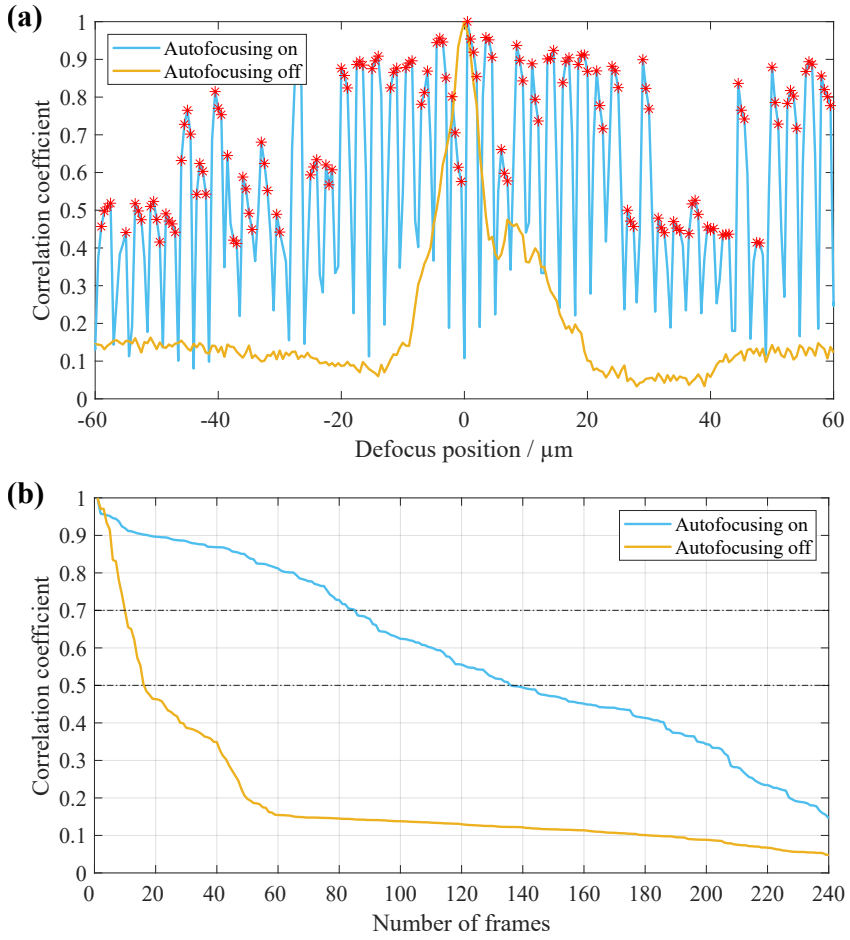


Figure 8.7: Autofocusing results in real time with continuous axial motion. (a) Pearson correlation coefficients computed for each frame in Visualisations 2(a) and 2(b) with respect to that acquired at the natural focal plane as a function of defocus position. Red asterisks: frames before (after) seeing a sudden decrease (increase) in correlation. (b) The number of frames in Visualisations 2(a) and 2(b) with a Pearson correlation coefficient above each value. Dotted lines indicate a strong (>0.7) or moderate (>0.5) relationship.

In the final experiment, the experimenter's finger was placed on a fixed mount below the objective lens while using the other hand for focus control. In Visualisation 4(a) with autofocusing, the microscope retained focus throughout the whole recording session; whereas in Visualisation 4(b) without autofocusing, the focal plane constantly moved with movements of the finger during breathing, such that it was difficult to concentrate on any specific feature.

8.4.5 Autofocusing at target depths within live tissue immersed in liquid

Finally, rather than tracking the specimen surface, we retrained the network to autofocus at target depths below the surface. This required only minor modifications during the data preprocessing stage. As described in Section 8.3.1, to autofocus at the specimen surface, RF voltages corresponding to the opposite amount of focal displacement V_{-z_d} were used as ground truth during network training. In order to refocus at a target depth z_t, the ground truth was replaced by voltages corresponding to the opposite amount of focal displacement plus the additional distance z_t below the surface, which we denote as $V_{-z_d+z_t}$. Separate networks were retrained for imaging at 5 µm, 10 µm, 15 µm, and 20 µm deep below the sample surface. Results for that at 10 µm deep are demonstrated in Figure 8.8. Autofocusing was performed over a 100 µm FOV in an organotypic hippocampal slice immersed beneath a 300-µm thick layer of Tyrode's solution. 500 µm FOV images before and after autofocusing are displayed in Figure 8.8 for better comparison of structural details. Results showed that the retrained network model was able to autofocus at the target depth with reasonable high accuracy. Images after autofocusing were comparable to that at the reference plane (magenta box) albeit with slight differences noticed between refocusing from opposite directions. It should also be pointed out that these images exhibited completely different features from the mouse skull, validating that sample morphology did not affect the network performance. In addition, as brain tissue contains extremely high water content ($n_{brain} = 1.36$), the RI difference between that and bone tissue is approximately 0.15 ($n_{bone} = 1.51$). This covers most biological tissues, and demonstrates the potential for networks trained on one specimen to be valid for a wide variety of tissue types after training.

8.5 Discussion and conclusion

In this chapter, a new autofocusing technique based on RF and sequence-dependent learning was demonstrated. By taking advantage of a DM and SHWS, system-aberration-free autofocusing was achieved in tissue both exposed to air and immersed in liquid. An extended 120 µm range was obtained with a positioning error smaller than half the axial resolution. The technique is valid for different imaging FOVs and for specimens not seen in the network training pro-

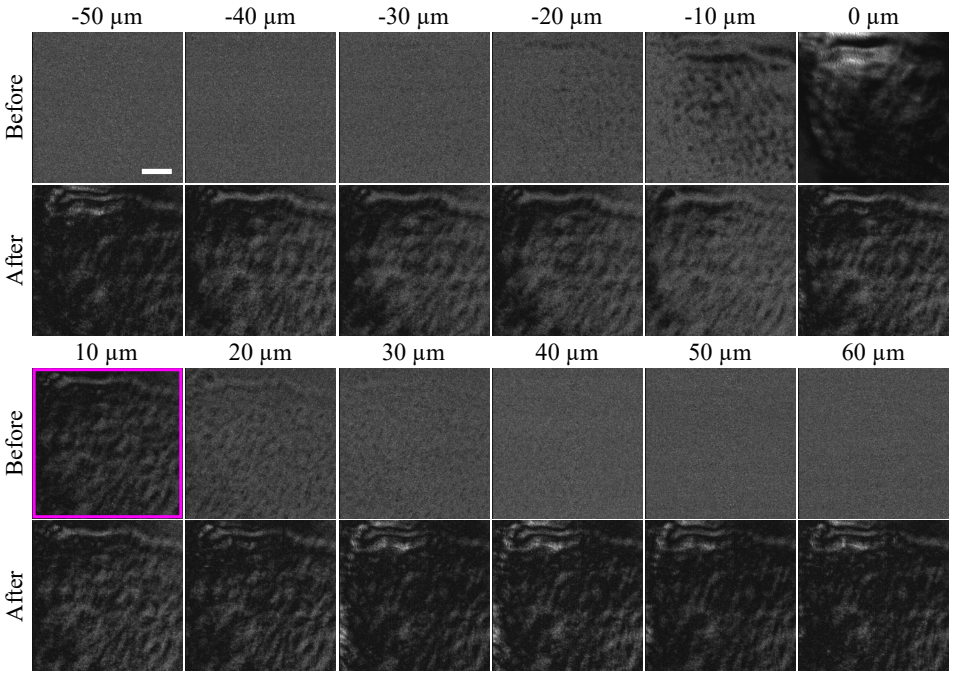


Figure 8.8: Autofocusing results at 10 µm deep below the surface in organotypic hippocampal slices. Experiments were performed when scanning over a 100 µm FOV. 500 µm FOV images before and after autofocusing are displayed. Magenta box: reference image. Scale bar: 100 µm.

cess. Continuous tracking of axial sample motion was enabled in real time using the compact neurosurgical microscope, showing great potential for transition towards clinical and surgical applications. It should be noted that although this work was demonstrated using reflectance contrast, the technique is fully applicable to fluorescence imaging by incorporating a band-pass or short-pass filter before the SHWS to detect back-scattered illumination light.

The proposed autofocusing technique is unique in a number of ways. First, we directly take phase measurements with a dedicated wavefront sensor instead of interpreting defocus information from sample images, which prevents the autofocusing range from being limited by the availability of structural details. A 120 µm range was achieved, and could be further extended by using an SHWS with larger dynamic range. In addition, the SHWS permitted simultaneous correction of system aberrations during RF by incorporating this information within calibrated DM control voltages. Therefore, any operation that involved the use of RF voltages also corrected for system aberrations at each axial location, including prior to making phase measurements when acquiring training datasets, the ground truth data itself that constituted of RF voltages,

as well as prior to making each shift measurement in real time. Other aberrations induced by non-ideal surface conditions and refractive index mismatch between different media could also be detected. Acquisition of training data under these diverse conditions greatly enhanced the trained network's generality towards non-ideal scenarios and allowed accurate repositioning of the focal plane. Moreover, as the SHWS prevented network exposure to sample structures, a second aspect of generality, that towards different specimen types, was simultaneously permitted. In contrast to implementing the proposed technique in a low NA system similar to that used in this work, high NA systems would greatly benefit from simultaneous correction of aberrations induced by refractive index mismatch and sample inhomogeneity [214] by using a similar AO correction routine to that set out in Section 3.5.1 at predetermined step intervals during training data acquisition. Second, the implementation of RF allowed not only the correction of system aberrations, but also axial refocusing to be performed in less than 1 ms, which is much faster than movements of the sample stage and objective lens. This is beneficial in particular for surgical applications to stabilise imaging during respiratory and pulsing movements over long distances. Third, compared to CNN-based approaches, the use of a Bi-LSTM network for learning of sequential aberration information from an SHWS is more tailored to the task at hand. By removing irrelevant information, such as cell morphology and size etc., from the network input, more concentration can be placed on factors that determine the position and quality of the focal spot. Consequently, the network is not only simpler and faster to train, but also leads to unique strengths such as allowing for higher generality and image quality.

It is worth mentioning that the autofocusing range depends on the NA of the objective lens, the mechanical stroke of the DM, the signal-to-noise ratio (SNR) at the SHWS, as well as the dynamic range of the SHWS. The first two factors determine the microscope's maximum permissible RF range, while the latter two determine the maximum detectable phase aberration. A lower NA, longer mechanical stroke, higher SNR, and larger dynamic range potentially lead to a more extended defocus range. Although the SNR wasn't of special concern in this system for the reported defocus range and exposure time, it can decrease at larger distances away from the specimen surface and may become a limiting factor for systems with low photon counts. A longer SHWS exposure time can then be adopted, but at the expense of speed, which may

nevertheless be favourable for applications that do not require autofocusing in real time. The maximum FOV over which the network trained with small FOVs would remain stable is dictated by the isoplanatic patch [215], within which the SHWS is able to obtain relatively constant phase measurements. At superficial layers of the specimen, its size generally decreases with a higher NA. The downside of this can be alleviated by performing imaging and phase aberration measurements alternately, such that autofocusing is performed over a small FOV (backscattered light) or at a fixed lateral position (fluorescence), while imaging is performed over much larger FOVs. This also enhances autofocusing speed by lowering the SHWS exposure time for phase measurements. Speed is then only ultimately limited by the DM settling time. For the current system, however, it was only possible to perform imaging in parallel with phase aberration measurements, which compromised the autofocusing speed in reality. Despite so, the alternation of these two processes would be a task for the future. Finally, we would like to point out that compared to existing single-shot methods, such as those reported in [15, 198, 203], although the requirement for three measurements makes the proposed method comparably slower, the additional merits of allowing for a much larger autofocusing range, and system-aberration-free imaging over the full extended range compensates for the minor decrease in speed.

Chapter 9

A generalised adaptive optics method for high-NA aberration-free refocusing in refractive-index-mismatched media

9.1 Overview

Previous chapters demonstrated how remote focusing could be performed by pre-calibrating corresponding control voltages using closed-loop adaptive optics (AO). Although this method is effective and reliable, pre-calibration is not always possible, especially in the absence of a wavefront sensor. In such cases, a predictive method is required to control common adaptive devices in performing accurate axial refocusing. Ideally, the method should be applicable to both high-NA and low-NA lenses, and be able to correct for the refractive index mismatch (RIM) when focusing through different media (Section 3.2.2). As the phenomenon is most significant for high-NA systems, it will be the main focus for this chapter. In addition, the focus position in these media can be adjusted through either optical remote-focusing or mechanical stage translation. However, no generalised control algorithm using Zernike polynomials has been presented that performs independent remote focusing and RIM correction in combination with mechanical stage translation, an important point that will also be addressed in this chapter.

The following sections first discuss the representation of high-NA defocus before considering remote focusing in a homogeneous media, where the core concept of derivations made in this

work, QR decomposition, is introduced. This concept is further developed for the operations of high-NA remote focusing and RIM correction in stratified media. Here, it is shown how optical remote focusing and mechanical stage translation are not optically equivalent processes, such that one cannot fully compensate for the other without additional aberration compensation. New orthogonal modes are further established to control high-NA remote focusing and RIM correction as independent primary modes in combination with mechanical stage translation for aberration-free refocusing. Two distinct control strategies are given for two typical experimental scenarios and numerical simulations are performed for the cases of focusing through a single-interface stratified medium and a cover glass. Finally, it is discussed how in practice the control matrix of common adaptive devices can be updated to execute the new control algorithms without affecting its previous functionalities.

9.2 Background and motivation

Precise and aberration-free focusing with high numerical aperture (NA) is essential in many applications such as microscopy [216, 217] and laser fabrication [218, 219]. Aberrations commonly lead to a distorted focal spot when focusing through refractive-index-mismatched (RIM) media with planar interfaces [122, 123]. The correction of RIM is important not only for different microscope modalities [220–223], but also for emerging applications that generate larger amounts of RIM, typically when using air immersion objectives to provide longer working distances [217], fabricating in high-RI material [224], and imaging in optically-cleared biological samples [225]. Among different RIM correction methods [217], AO approaches that use a deformable mirror (DM) or spatial light modulator (SLM) are of special interest as it can not only provide RIM correction, but also take advantage of defocus for remote focusing.

Both defocus and spherical aberration can be modelled as functions over a unit disk representing the optical pupil [126]. With a low-NA objective lens, these two functions coincide well with two of the well-known Zernike polynomials [125], which are a set of orthogonal basis functions commonly employed to decompose an arbitrary aberration function. However, when high-NA lenses are used, defocus takes the form of a spherical wavefront as opposed to the quadratic

function describing Zernike defocus [106], and RIM aberration no longer coincides with the individual Zernike spherical terms [220, 221]. Practically, this means that Zernike defocus and Zernike spherical terms of first and higher orders must be both manipulated for remote-focusing and RIM correction, such that the two operations are coupled in terms of Zernike representation.

The correction of high-NA RIM aberration using common adaptive devices has been well addressed [219, 222, 226–229]. However, there is not yet a generalised predictive method that provides simultaneous support for aberration-free remote-focusing with consideration of mechanical stage translation in a high-NA system. Ideally, a new set of mathematical modes analogous to Zernike modes should be derived, such that the new modes maintain orthogonality while allowing high-NA defocus to independently adjust the axial focus position without inducing aberrations; and the new high-NA spherical mode to independently correct for RIM aberration without shifting the focus position.

9.3 Representation of high-NA defocus Φ_d

The illumination field at the focus of a high-NA lens is accurately modelled by the Debye–Wolf diffraction integral [121], the geometry of which is illustrated in Figure 9.1(a). This integral is formulated with respect to the maximum semi-aperture angle α of the Gaussian reference sphere G, which relates to the numerical aperture and image space refractive index n by $\mathrm{NA} = n \sin \alpha$ (see Section 3.2.1). β represents the incidence angle of an arbitrary meridional ray that converges to the Gaussian focus O. Note that in this work, we only consider on-axis points in the sample for telecentric systems where the adaptive device is placed at an infinity-focused exit pupil imaged by $4f$ telescope systems from the back aperture of an infinity-corrected objective lens. By mapping the Gaussian reference sphere onto a unit aperture disk A for an objective lens obeying Abbe's sine condition [106], the radial coordinate ρ can be expressed by $\rho = \sin \beta / \sin \alpha$.

The phase representation of high-NA defocus Φ_d can be derived by referring to the dependency of the diffraction integral upon axial coordinate z. Assume the presence of an axial focal displacement Δ expressed in microns, that causes the Gaussian focus to shift to O', as illustrated

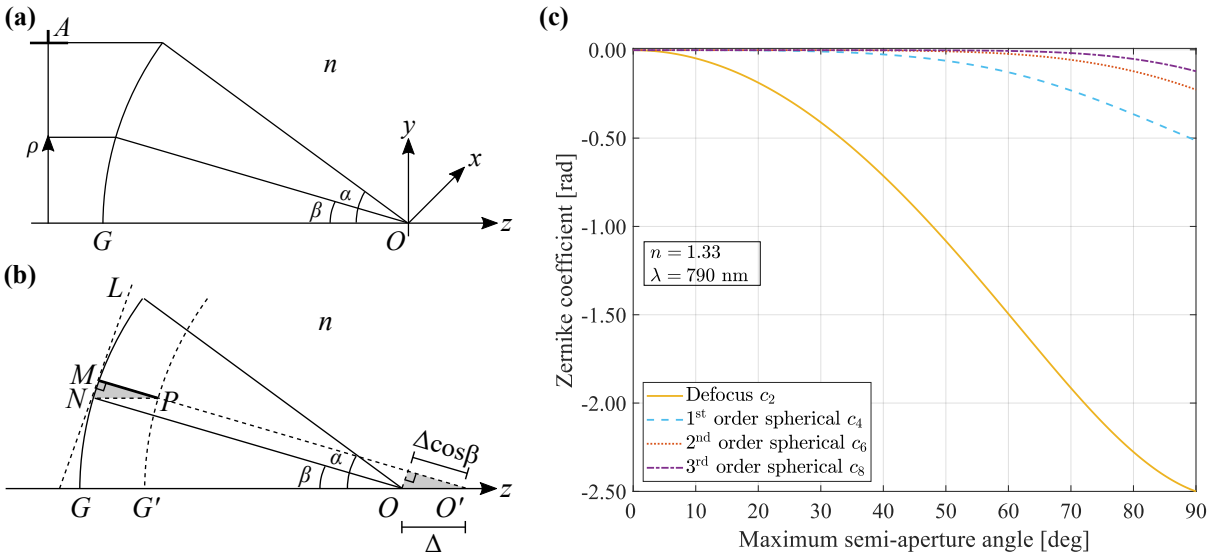


Figure 9.1: Representation of high-NA defocus Φ_d. (a) Frame of reference for the Debye–Wolf diffraction integral. (b) Geometrical derivation of Φ_d for focal displacement Δ. (c) The first four Zernike coefficients c_{2p} in Eq. (9.3) (excl. piston) evaluated as a function of α for 1 µm focal displacement in a homogeneous medium of refractive index $n = 1.33$ at wavelength $\lambda = 790$ nm.

in Figure 9.1(b). The corresponding phase in the unit aperture disk can then be obtained as

$$\Phi_d = k\Delta \cos\beta, \tag{9.1}$$

where $k = 2\pi n/\lambda$ and λ is the incident wavelength expressed also in micrometres. For convenience of representation in the unit pupil disk, using the geometrical relations given in Figure 9.1(a), one can also express Φ_d as a function of the radial coordinate ρ,

$$\Phi_d = k\Delta\sqrt{1 - (\rho \sin\alpha)^2}. \tag{9.2}$$

The operation of inducing an axial focal displacement of Δ using a DM or SLM (remote focusing), without mechanical movement of the objective lens or sample stage, can then be achieved by correcting for Φ_d, equivalent to applying a phase of $-\Phi_d$ at the pupil plane of the optical system.

9.3.1 Zernike expansion of Φ_d

Phase Φ_d can be accurately expanded into a series of radially symmetric Zernike polynomials $\mathcal{Z}_{2p}^0(\rho,\theta)$ [220, 230] using the formulas given in Appendix A, i.e.,

$$\Phi_d = k\Delta\sqrt{1-(\rho\sin\alpha)^2} = k\Delta\sum_{p=0}^{\infty} c_{2p}^0 \cdot \mathcal{Z}_{2p}^0(\rho,\theta), \tag{9.3}$$

where $\mathcal{Z}_{2p}^0(\rho,\theta)$ is normalised and ordered under the Noll's convention outlined in Section 3.2.3, and c_{2p}^0 is the Zernike coefficient that represents the root-mean-square (RMS) phase value of its corresponding Zernike mode. Both single $(\cdot)_{\#i}$ and double $(\cdot)_n^m$ index notations can be used, and the latter $(\cdot)_{n=2p}^{m=0}$ is adopted for derivations in this work using radially symmetric Zernike polynomials with radial order $n = 2p$ [126, 127]. Explicit mention of the azimuthal order $m = 0$ and azimuthal coordinate θ will also be dropped for the remainder of this work. It should be noted that except for interferometric techniques [231], Zernike piston coefficients c_0 or $c_{\#1}$ can be safely ignored during the evaluation of phase, as it only introduces a constant offset to the phase but no variations within. However, we retain the Zernike piston term in mathematical derivations throughout this work for completeness.

To appreciate the difference between low-NA and high-NA defocus, the first four Zernike coefficients c_{2p} in Eq. (9.3) (excl. piston) are evaluated in radians as a function of α for 1 µm focal displacement in a homogeneous medium of refractive index $n = 1.33$ at a wavelength of $\lambda = 790$ nm. c_{2p} can be calculated according to Appendix A as,

$$c_{2p} = \left[\frac{2p-1}{2p+3}\tan^4\left(\frac{\alpha}{2}\right) - 1\right]\frac{\sin(\alpha)\tan^{2p-1}(\alpha/2)}{2(2p-1)\sqrt{2p+1}}. \tag{9.4}$$

Results in Figure 9.1(c) show that only Zernike defocus is significantly non-zero when α is small ($\alpha \approx 22°$ for NA = 0.5 and $n = 1.33$). Therefore, refocusing using a low-NA lens in a homogeneous medium generally results in a phase contribution that is essentially equivalent to Zernike defocus $c_2\mathcal{Z}_2(\rho)$. In practice, this means that aberration-free remote focusing can be achieved in a low-NA system by solely applying Zernike defocus to the adaptive device. On the other hand, Zernike spherical terms become more significant at larger angles, such that the additional terms in Eq. (9.3) cannot be neglected, and should be applied in addition to Zernike defocus for aberration-free remote focusing. It should be noted, however, when the

focal displacement Δ is large in a low-NA system, the absolute value of Zernike spherical terms may also become non-negligible.

9.3.2 Representation using a vector of Zernike coefficients

When considering a finite sum, the Zernike coefficients in Eq. (9.3) can be collected into a vector $\mathbf{s}_l \in \mathbb{R}^{K+1}$ expressed in the following form,

$$\mathbf{s}_l = \begin{bmatrix} c_0 \\ c_2 \\ c_4 \\ \vdots \\ c_{2K} \end{bmatrix} = \begin{bmatrix} c_{\#1} \\ c_{\#4} \\ c_{\#11} \\ \vdots \\ c_{\#J} \end{bmatrix}, \tag{9.5}$$

where the double and single index notations are used for the first and second vectors, respectively. We refer to $\mathbf{s}_l$ as the vector of low-NA spherical coefficients, where the maximum radial order is $2K$, and relates to the maximum Noll's index J by $J = 1 + 2K(2K+1)/2$. When controlling an adaptive device in practice, it is also necessary to consider the complete set of Zernike coefficients $\mathbf{z}_l \in \mathbb{R}^J$, where zeros take the place of non-radially symmetric elements that appear in the Noll's single-index enumeration. High-NA defocus Φ_d can then be represented by $k\Delta \cdot \mathbf{s}_l$ or $k\Delta \cdot \mathbf{z}_l$ for a focal displacement of Δ. In practice, this means that in order to refocus from point O to O' in Figure 9.1(b) using an adaptive device, the vector $-k\Delta \cdot \mathbf{z}_l$ should be added to the vector of Zernike coefficients representing its current state of control.

9.4 Independent high-NA remote focusing in a homogeneous medium

As detailed in Section 9.3.1, due to the geometry of high-NA lenses, defocus is no longer equivalent to Zernike defocus, and consists also of Zernike spherical terms of first and higher orders (see Eq. (9.3)). In practice, this means for common adaptive devices that are conveniently controlled using Zernike polynomials, such as SLMs and membrane DMs, adjusting Zernike defocus only for refocusing would inherently induce aberrations and adjusting any Zernike spherical term of

first and higher order would shift the focus position. This is highly inconvenient, as ideally one would like to control one element only for remote focusing and correct for other aberrations without affecting the focus position. In this section, a modal decomposition method is derived for independent remote focusing and aberration correction in a homogeneous medium. A new set of orthogonal modes will be defined, which we call high-NA modes, where high-NA defocus is an independent degree of freedom (DoF) equivalent to the role of Zernike defocus in the low-NA case for aberration-free remote focusing.

Define a basis matrix $\mathbf{A} \in \mathbb{R}^{(K+1)\times(K+1)}$, where each column is a basis mode represented by a vector of low-NA spherical coefficients. When representing low-NA Zernike modes only, $\mathbf{A}$ will be an identity matrix. Now substitute the second column of $\mathbf{A}$ with the Zernike decomposition of high-NA defocus expressed in radians for 1 µm focal displacement in a homogeneous medium with refractive index n (see Eq. (9.4)), then basis matrix $\mathbf{A}$ would take the following form,

$$\mathbf{A} = \begin{bmatrix} 1 & kc_0 & 0 & 0 & \dots & 0 \\ 0 & kc_2 & 0 & 0 & \dots & 0 \\ 0 & kc_4 & 1 & 0 & \dots & 0 \\ 0 & kc_6 & 0 & 1 & \dots & 0 \\ \vdots & \vdots & \vdots & \vdots & \ddots & \vdots \\ 0 & kc_{2K} & 0 & 0 & \dots & 1 \end{bmatrix}. \tag{9.6}$$

To make all subsequent spherical modes orthogonal to high-NA defocus while being mutually orthogonal, a QR decomposition process can be applied to matrix $\mathbf{A}$ [232],

$$\mathbf{A} = \mathbf{QR} = \begin{bmatrix} \mathbf{q}_1 & \mathbf{q}_2 & \dots & \mathbf{q}_{K+1} \end{bmatrix} \mathbf{R}, \tag{9.7}$$

where $\mathbf{Q} \in \mathbb{R}^{(K+1)\times(K+1)}$ is an orthonormal matrix whose j-th column $\mathbf{q}_j$ represents the j-th new high-NA mode, and $\mathbf{R} \in \mathbb{R}^{(K+1)\times(K+1)}$ is an upper triangular matrix whose j-th column represents combinations of the basis modes in $\mathbf{A}$ that are required to create the j-th new high-NA mode. As a result, each high-NA mode is a unique linear combination of radially symmetric Zernike modes and represent the high-NA analogues of Zernike piston, defocus, 1st order spherical, and higher order spherical terms, after removal of preceding high-NA components.

We can now introduce a vector of high-NA spherical coefficients $\mathbf{s}_h \in \mathbb{R}^{K+1}$, of which the second element controls high-NA defocus, analogous to that in $\mathbf{s}_l$ in the low-NA case for device

control. The remaining elements are orthogonal to the second element, as well as being mutually orthogonal. In order to find the relation between $\mathbf{s}_h$ and $\mathbf{s}_l$, two conversion matrices $\mathbf{T}_{l\leftarrow h} \in \mathbb{R}^{(K+1)\times(K+1)}$ and $\mathbf{T}_{h\leftarrow l} \in \mathbb{R}^{(K+1)\times(K+1)}$ are defined, where the former converts from $\mathbf{s}_h$ to $\mathbf{s}_l$, and the latter from $\mathbf{s}_l$ to $\mathbf{s}_h$, expressed as

$$\begin{aligned} \mathbf{s}_l &= \mathbf{T}_{l\leftarrow h}\mathbf{s}_h \\ \mathbf{s}_h &= \mathbf{T}_{h\leftarrow l}\mathbf{s}_l. \end{aligned} \tag{9.8}$$

As matrix $\mathbf{Q}$ is orthonormal, each column represents a high-NA mode whose unit magnitude corresponds to a phase of 1 radians RMS. In practice, however, one may wish to relate high-NA defocus to the amount of focal displacement in micrometres. For this purpose, the conversion matrices can be obtained by rescaling the columns of $\mathbf{Q}$ by the diagonal elements of $\mathbf{R}$, such that

$$\begin{aligned} \mathbf{T}_{l\leftarrow h} &= \mathbf{Q}\cdot\mathrm{diag}(\mathbf{R}) \\ &= \begin{bmatrix}\mathbf{q}_1 & \mathbf{q}_2 & \cdots & \mathbf{q}_{K+1}\end{bmatrix} \begin{bmatrix} r_{11} & 0 & \dots & 0 \\ 0 & r_{22} & \dots & 0 \\ \vdots & \vdots & \ddots & \vdots \\ 0 & 0 & \dots & r_{(K+1)(K+1)} \end{bmatrix}, \\ \mathbf{T}_{h\leftarrow l} &= \mathrm{diag}(\mathbf{R})^{-1}\cdot\mathbf{Q}^{\mathrm{T}} \\ &= \begin{bmatrix} 1/r_{11} & 0 & \dots & 0 \\ 0 & 1/r_{22} & \dots & 0 \\ \vdots & \vdots & \ddots & \vdots \\ 0 & 0 & \dots & 1/r_{(K+1)(K+1)} \end{bmatrix} \begin{bmatrix} \mathbf{q}_1 \\ \mathbf{q}_2 \\ \vdots \\ \mathbf{q}_{K+1} \end{bmatrix}. \end{aligned} \tag{9.9}$$

The above process allows aberration-free remote focusing to be achieved in a high-NA system by solely adjusting the second element of vector $\mathbf{s}_h$. For example, to refocus an offset Δ away from the Gaussian focus, a vector $\mathbf{s}_h$ with zeros assigned to each element is first taken. Then, $-\Delta$ is assigned to the second element of $\mathbf{s}_h$ to set high-NA defocus. Finally, a vector of low-NA spherical coefficients $\mathbf{s}_l$ can be computed using Eq. (9.8) to reconfigure an adaptive device controlled using Zernike polynomials. It should be mentioned that as all elements in $\mathbf{s}_h$ are now mutually orthogonal, adjusting the remaining elements of $\mathbf{s}_h$ would not affect the focus position.

Simulations of the proposed control algorithm were performed for a refocusing offset of $\Delta = 20\,\mu\mathrm{m}$ with parameters NA = 1.25, $n = 1.33$, and wavelength $\lambda = 790$ nm. Figure 9.2(a)

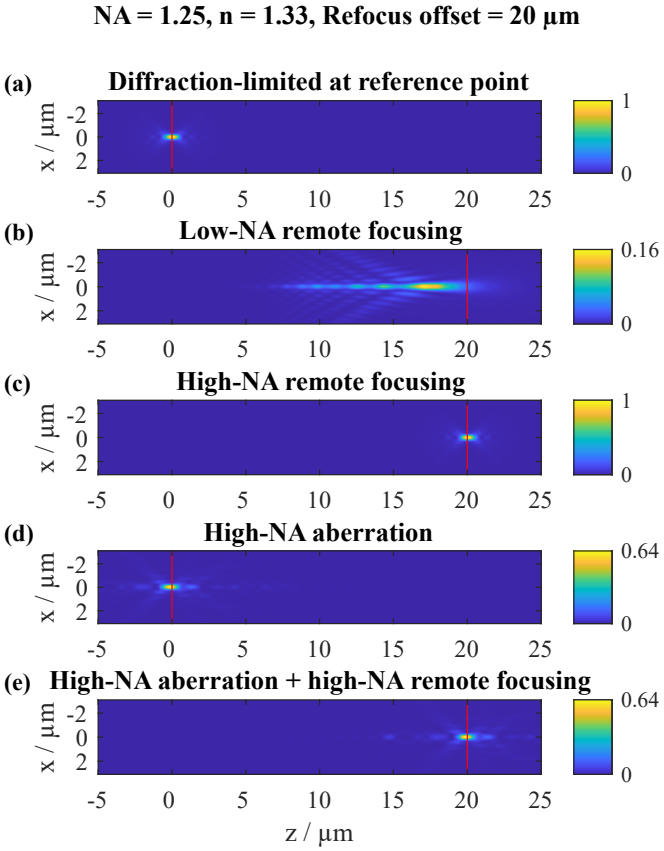


Figure 9.2: Simulation results of the proposed algorithm for refocusing offset $\Delta = 20\,\mu\text{m}$ with parameters NA $= 1.25$, $n = 1.33$, and wavelength $\lambda = 790$ nm. Plots show focal intensity distributions in the cases of: (a) applying zero phase; (b) applying low-NA approximation of $-\Phi_d$; (c) applying high-NA defocus by assigning -20 to the second element of zero vector $\mathbf{s}_h = \mathbf{0}$; (d) assigning normalised random values to all elements of $\mathbf{s}_h$ excluding the second; (e) further assigning -20 to the second element of $\mathbf{s}_h$.

simulates a diffraction-limited focal spot at the Gaussian focus, the maximum intensity of which is used to normalise all subsequent simulation plots. In Figure 9.2(b), a low-NA approximation of $-\Phi_d$ consisting of pure Zernike defocus was applied to the pupil disk. This results in the focal spot being shifted towards the desired depth albeit with significant distortions and a Strehl ratio (SR) of 0.16, since Φ_d and its low-NA approximation do not perfectly cancel. Figure 9.2(c) uses the proposed control algorithm by setting the second element of a zero vector $\mathbf{s}_h = \mathbf{0}$ to -20 and obtaining $\mathbf{s}_l$ by computing $\mathbf{s}_l = \mathbf{T}_{l \leftarrow h}\mathbf{s}_h$. Aberration-free remote focusing was thus achieved at the desired offset of 20 µm with an SR of 1, as indicated in the colorbar. To further validate that adjusting other elements of $\mathbf{s}_h$ would not affect the focus position, in Figure 9.2(d), the

second element was set to zero while all other elements were set to random values normalised to the length of the coefficient vector. This led to an aberrated focal spot centred at the Gaussian focus, confirming that elements of $\mathbf{s}_h$ excluding the second could indeed control other aberration modes without shifting the focus. Finally, Figure 9.2(e) also assigns -20 to the second element of $\mathbf{s}_h$ and demonstrates independent control of remote focusing and aberration correction.

Note that although remote focusing is controlled by the second element of $\mathbf{s}_h$, large values in the other elements may also cause distortions that shift the position of peak intensity along the optical axis, similar to the case of Zernike spherical aberration [193].

9.5 High-NA refocusing in stratified media with a single interface

In this section, we consider the case of refocusing in stratified media with a single interface, where the index of refraction is uniform within each stratum, but different between consecutive strata. The interface is assumed to be planar and orthogonal to the optical axis, and create additional spherical terms that are absent in the case of focusing in a homogeneous medium.

9.5.1 Effective numerical aperture

When focusing into stratified media, it is important to verify whether the full NA of the objective lens can be exploited. Assume a medium with N strata, and let n_i denote the refractive index of the i th stratum, due to possible total internal reflection at an interface i where $n_i > n_{i+1}$, the effective numerical aperture $\mathrm{NA_e}$ is always limited by the minimum refractive index of the stratified media, and should be used in place of the nominal numerical aperture $\mathrm{NA_n}$ after finding the index i for which the ratio $\mathrm{NA_n}/n_i$ is maximum and no larger than 1.

9.5.2 Total phase contribution of RIM and high-NA defocus Φ_d

The geometry for deriving the phase contribution due to RIM of a single interface is given in Figure 9.3, where β_1 represents the angle of propagation of a ray in stratum 1 and β_2 is the angle of this ray refracted into stratum 2. The distance h travelled by the sample translation

stage (or objective lens relative to the RIM interface) will be referred to as the stage depth, or Gaussian depth, which is also equivalent to the corresponding focal shift in a homogeneous medium without the presence of RIM. We define the phase contribution due to RIM as Φ_i, which can be obtained by computing the optical path difference (OPD) between ray 1 and ray 2. Φ_i can thus be obtained using geometrical optics and Snell's Law as [220]

$$\Phi_i = -k_1 h \cos\beta_1 + k_2 h \cos\beta_2, \tag{9.10}$$

where $k_1 = 2\pi n_1/\lambda$ and $k_2 = 2\pi n_2/\lambda$. In order to implement remote focusing in stratum 2, the phase contribution of high-NA defocus Φ_d should be expressed according to Eq. (9.1),

$$\Phi_d = k_2 \Delta \cos\beta_2, \tag{9.11}$$

Thus the total phase considering both RIM aberration and remote focusing is expressed as [114]

$$\Phi_t = \Phi_i + \Phi_d = -k_1 h \cos\beta_1 + k_2 (h + \Delta) \cos\beta_2. \tag{9.12}$$

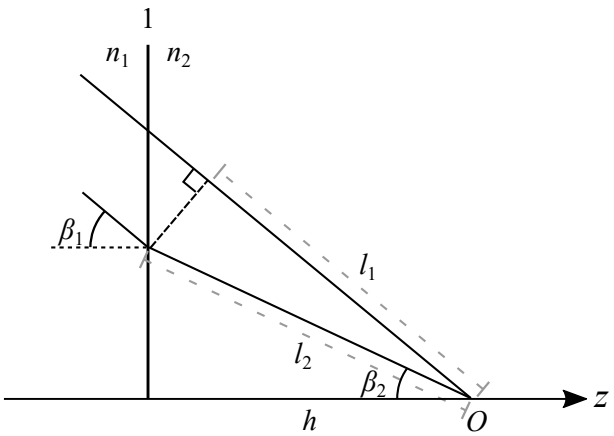


Figure 9.3: Geometry for deriving the phase contribution due to RIM when focusing through stratified media with a single interface. The refractive index on either side of the interface is denoted by n_1 and n_2. The illustration shows the case where $n_1 < n_2$. Ray 1 depicts the case of focusing at O in a homogeneous medium without RIM aberration; and ray 2 depicts the case of focusing at the same position, albeit in a stratified media such that the ray is refracted at the RIM interface before arriving at O. The two geometries have been superimposed.

If Φ_i is cancelled by an adaptive device, an aberration-free focus will form at Gaussian depth h. A subsequent adjustment of Φ_d will then allow remote focusing to an offset Δ with respect to O. Therefore, the total phase for simultaneous RIM correction and remote focusing to desired

depth $h+\Delta$ is $-\Phi_t$. It is important to realise that Φ_i is a function of both n_1, α_1 and n_2, α_2. On the contrary, Φ_d is only a function of n_2, α_2. Consequently, if Φ_i is cancelled by the adaptive device, the problem of remote focusing within stratum 2 would be identical to that outlined for the homogeneous medium in Section 9.3. Note that for derivations in this work, it is always assumed that remote focusing happens within the last stratum without total internal reflection.

According to Eq. (9.3), Eq. (9.12) can be rewritten as a function of ρ in the unit pupil disk,

$$\Phi_t = -k_1 h\sqrt{1-(\rho\sin\alpha_1)^2} + k_2(h+\Delta)\sqrt{1-(\rho\sin\alpha_2)^2}, \tag{9.13}$$

and be further expanded into a series of radially symmetric Zernike polynomials $\mathcal{Z}_{2p}(\rho)$,

$$\Phi_t = -k_1 h\sum_{p=0}^{\infty} c_{2p}\cdot\mathcal{Z}_{2p}(\rho) + k_2(h+\Delta)\sum_{p=0}^{\infty} d_{2p}\cdot\mathcal{Z}_{2p}(\rho), \tag{9.14}$$

where c_{2p} and d_{2p} are computed from Eq. (9.4) using α_1 and α_2, respectively. Following the same reasoning in Section 9.3.2, c_{2p} and d_{2p} can be collected into two vectors $\mathbf{s}_{l1}$ and $\mathbf{s}_{l2}$ (see Eq. (9.5)), and Φ_t can be represented with a vector of low-NA spherical coefficients $\mathbf{s}_t$ as,

$$\mathbf{s}_t = -k_1 h\mathbf{s}_{l1} + k_2(h+\Delta)\mathbf{s}_{l2}. \tag{9.15}$$

Applying $-\mathbf{s}_t$ to the adaptive device will simultaneously correct for the RIM aberration induced at stage depth h and remote focus to the desired depth $h+\Delta$.

In practice, it is beneficial to control high-NA defocus and RIM spherical aberration directly as independent primary modes, rather than indirectly as combinations of Zernike basis modes. This would enable the operation of remote focusing, which is equivalent to controlling high-NA defocus, and correcting for high-NA RIM spherical aberration, to be achieved by independently adjusting one mode only. As these two operations are associated with the same Zernike spherical terms for high-NA lenses, decoupling is essential for independent adjustment.

9.5.3 Independent remote focusing and RIM aberration correction

Following the derivations made in Section 9.4, we use the same QR decomposition method to achieve independent remote focusing and RIM correction in a stratified media, with slight differences only in the representation of basis matrix $\mathbf{A}$. The second column should now consist

of the Zernike coefficients associated with high-NA defocus in n_2 (last stratum). In addition, those associated with high-NA RIM spherical aberration should now be used as the primary high-NA spherical mode in the third column, such that

$$\mathbf{A} = \begin{bmatrix} 1 & k_2 d_0 & k_2 d_0 - k_1 c_0 & 0 \ldots 0 \\ 0 & k_2 d_2 & k_2 d_2 - k_1 c_2 & 0 \ldots 0 \\ 0 & k_2 d_4 & k_2 d_4 - k_1 c_4 & 0 \ldots 0 \\ 0 & k_2 d_6 & k_2 d_6 - k_1 c_6 & 1 \ldots 0 \\ \vdots & \vdots & \vdots & \vdots \ddots \vdots \\ 0 & k_2 d_{2K} & k_2 d_{2K} - k_1 c_{2K} & 0 \ldots 1 \end{bmatrix}. \tag{9.16}$$

QR decomposition will then create a high-NA spherical aberration mode that is orthogonal to high-NA defocus. Specifically, the second and third columns of orthonormal matrix $\mathbf{Q}$ now represent normalised versions of independent high-NA defocus Φ_d and RIM spherical aberration Φ_i, respectively, and conversion matrix $\mathbf{T}_{l \leftarrow h}$ can be obtained in the same way as Eq. (9.9). Now we can achieve independent remote focusing and RIM aberration correction by setting the second element of the newly-defined vector of high-NA spherical coefficients $\mathbf{s}_h$ to $-\Delta$ to refocus to an offset Δ away from the Gaussian focus, and the third element of $\mathbf{s}_h$ to $-h$ to correct for the RIM aberration induced at stage depth h. We note that in column three, using only the latter vector would also give the same results. Here both terms are retained for its physical RIM presentation.

In order to validate the proposed control algorithm for focusing in high-RI medium with a large RIM between the immersion media, Figure 9.4 demonstrates simulation results for independent remote focusing and RIM aberration correction focusing from oil ($n_1 = 1.52$) to diamond ($n_2 = 2.42$) using an oil immersion lens of NA = 1.45 with incident wavelength $\lambda = 790$ nm. Figure 9.4(a) first simulates a diffraction-limited focal spot at stage depth $h_1 = 20\,\mu$m below a conceptual interface between $n_1 = n_2 = 2.42$ for an NA = 1.45 objective lens designed for perfect operation at this refractive index. The maximum focal intensity is again used to normalise all consecutive plots. Figure 9.4(b) illustrates the RIM aberration in the case of $n_1 = 1.52$ and $n_2 = 2.42$ when zero phase is applied to the adaptive device at the same stage depth. In Figure 9.4(c), the RIM aberration is corrected for independently of its high-NA defocus component, i.e., with the defocus component removed, by assigning -20 to the third element and zero to

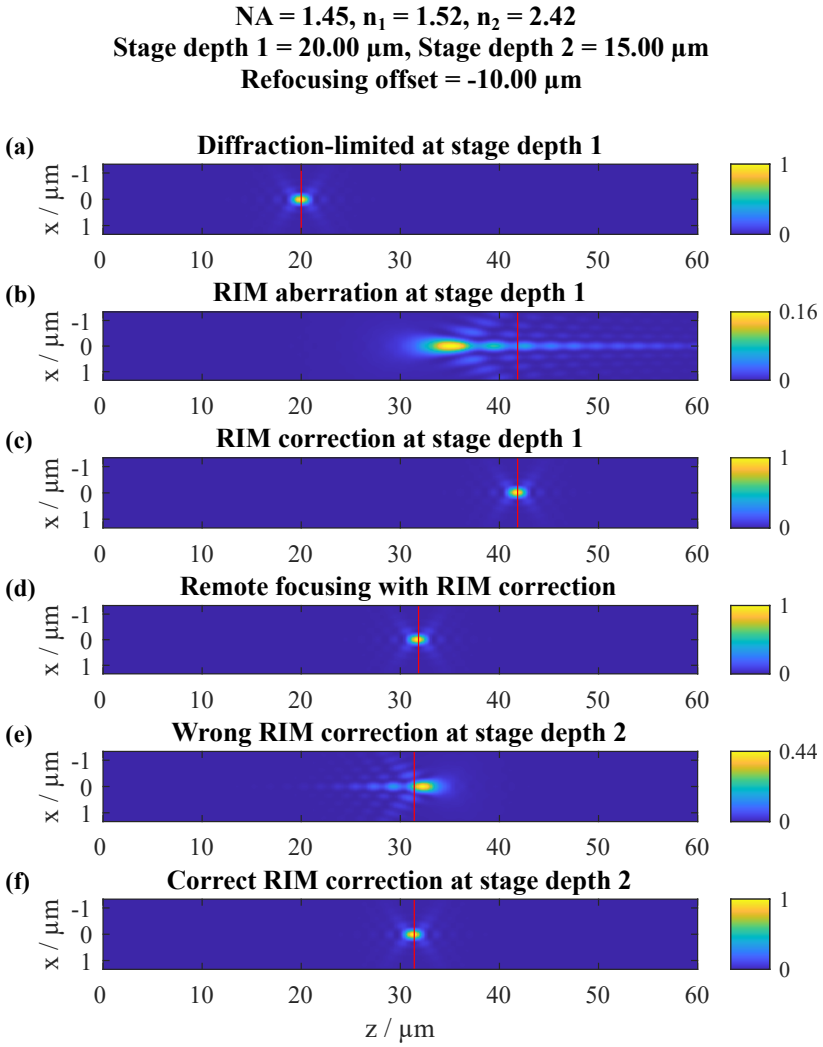


Figure 9.4: Simulation results of the proposed control algorithm for independent remote focusing and RIM aberration correction focusing from oil ($n_1 = 1.52$) to diamond ($n_2 = 2.42$) using an oil immersion lens of NA = 1.45 with incident wavelength $\lambda = 790$ nm. Plots show focal intensity distributions in the cases of: (a) diffraction-limited in stratum 2; (b) RIM aberration induced at $h_1 = 20\,\mu$m; (c) independent RIM correction for $h_1 = 20\,\mu$m; (d) independent remote focusing by an offset of $\Delta = -10\,\mu$m; (e) RIM correction for $h_1 = 20\,\mu$m when at $h_2 = 15\,\mu$m without remote focusing; (f) correct RIM correction for $h_2 = 15\,\mu$m.

the remaining elements of $\mathbf{s}_h$. A diffraction-limited focal spot (SR = 1) is thus obtained at the original focus position [219]. Note that in the presence of severe spherical aberrations, this is different from the position of maximum intensity in Figure 9.4(b), which is determined by the innermost rays of the illumination cone [233]. To demonstrate independent remote focusing after

correction of the RIM aberration for stage depth $h_1 = 20\,\mu\text{m}$, a refocusing offset of $\Delta = -10\,\mu\text{m}$ is introduced in Figure 9.4(d) by assigning 10 to the second element of $\mathbf{s}_h$, as well as -20 to the third. As expected, this operation causes the focus to shift $10\,\mu\text{m}$ towards the negative z-axis without introducing additional aberrations. Next, we set the second element of $\mathbf{s}_h$ back to zero, and translate the sample stage axially by $5\,\mu\text{m}$ to a stage depth of $h_2 = 15\,\mu\text{m}$ without updating the RIM correction accordingly. Figure 9.4(e) demonstrates how failing to apply the correct RIM correction for each stage shift leads to non-optimal results. Finally, the diffraction-limited focal spot is restored by assigning -15 to the third element of $\mathbf{s}_h$, as shown in Figure 9.4(f).

Here, we see how the RIM aberration is only related to stage depth h, and not affected by the magnitude of Δ. As a result, adjustments made to the remote focusing term Φ_d alone cannot cancel the additional RIM aberration incurred by a stage shift, as Φ_d has no terms in $k_1 \cos\beta_1$. Therefore, every stage movement must be followed by appropriate compensation of the additional RIM aberration. This is a different concept to remote focusing, where only the adaptive device is used for refocusing such that Φ_d changes while Φ_i remains constant.

9.5.4 Minimal root-mean-square balancing for a desired focal depth

Axial refocusing in an adaptive optical microscope can normally be achieved in two ways, either by translating the sample stage (or objective lens), or remote focusing using an adaptive device. The former changes stage depth h, thus the amount of RIM aberration, while the latter changes refocusing offset Δ. The QR decomposition method discussed in previous sections allows these two operations to be performed independently. However, it does not consider the total demanded stroke of the adaptive device, which could be a limiting factor in the case of large RIM aberrations or desired refocusing offsets. As we always assume refocusing in the last stratum, the first and second terms in Eq. (9.12) have opposite signs. This raises the possibility of balancing the phase term required for correction of RIM aberration $-\Phi_i$, which is a function of stage depth h, with that for remote focusing $-\Phi_d$, which is a function of refocusing offset Δ. In many practical cases, one may only be concerned about the desired focal depth at which to perform imaging or direct laser writing, and are happy for the values of h and Δ to be adjusted accordingly.

In such a scenario, the desired focal depth, which we denote as τ, can be considered a fixed parameter in the relation $\tau = h + \Delta$, and a criterion can be established such that h and Δ are functions of τ. One such criterion is to balance h and Δ such that the RMS of the total phase Φ_t is minimised. This may be an important consideration, if using an adaptive device with limited stroke. Finally, aberration-free refocusing to the desired focal depth τ can be achieved by adjusting both the sample translation stage and adaptive device.

Taking advantage of Eq. (9.15) and the orthogonality of Zernike polynomials, the RMS of Φ_t can be expressed as

$$\begin{aligned} \mathrm{RMS}(\Phi_t)^2 &= |-k_1 h \mathbf{s}_{l1} + k_2(h+\Delta)\mathbf{s}_{l2}|^2 \\ &= |k_1\mathbf{s}_{l1} - k_2\mathbf{s}_{l2}|^2\tau^2 + 2(k_1k_2\mathbf{s}_{l1}^T\mathbf{s}_{l2} - |k_1\mathbf{s}_{l1}|^2)\tau\Delta + |k_1\mathbf{s}_{l1}|^2\Delta^2, \end{aligned} \tag{9.17}$$

which is a quadratic function if one of the two variables τ and Δ is fixed and the other is free. Compute the derivative of Eq. (9.17) with respect to Δ and assign a value of zero to yield

$$\Delta^*(\tau) = \underset{\Delta}{\mathrm{argmin}} \left[\mathrm{RMS}(\Phi_t)^2\right] = \left(1 - \frac{k_2\mathbf{s}_{l1}^T\mathbf{s}_{l2}}{k_1|\mathbf{s}_{l1}|^2}\right)\tau, \tag{9.18}$$

and

$$h^*(\tau) = \tau - \Delta^*(\tau) = \frac{k_2\mathbf{s}_{l1}^T\mathbf{s}_{l2}}{k_1|\mathbf{s}_{l1}|^2}\tau. \tag{9.19}$$

Note that the first element of $\mathbf{s}_{l1}$ and $\mathbf{s}_{l2}$, which correspond to Zernike piston, should be removed before calculation. Using the same high-NA modes as those obtained by QR decomposition of basis matrix $\mathbf{A}$ given in Eq. (9.16), the second element of $\mathbf{s}_h$ can be set to Δ^* for high-NA remote focusing, while h^* is used to shift the translation stage, as well as to set the third element of $\mathbf{s}_h$ to correct for RIM aberration at this stage depth. As a result, aberration-free focusing will be achieved at desired depth τ below the RIM interface with minimal RMS stroke demanded from the adaptive device.

We note that other criteria for optimisation may also be applied, dependent on the scenario. For example, when using an SLM one may want to minimise the maximum derivative of Φ_t for minimal phase-wrapping [219]; when using membrane DMs, one might need to minimise the maximum curvature of Φ_t. Alternatively, a different normalisation procedure can be applied to the Zernike polynomials to evaluate the peak-to-valley magnitude of the phase, if the absolute stroke of the adaptive device is limited.

9.5.5 Balanced remote focusing and RIM aberration correction

So far, we have treated Δ and h as two independent DoFs, i.e., both values need to be explicitly assigned to vector $\mathbf{s}_h$ for focus control. Alternatively, a simpler and more efficient strategy would be to consider τ as a single DoF. This can be accomplished by rewriting Eq. (9.15) as

$$\mathbf{s}_t = -k_1 h(\tau)\mathbf{s}_{l1} + k_2 \tau \mathbf{s}_{l2}, \tag{9.20}$$

and expressing $h(\tau)$ using Eq. (9.19), which leads to

$$\mathbf{s}_t = \left(-k_2 \frac{\mathbf{s}_{l1}^T \mathbf{s}_{l2}}{|\mathbf{s}_{l1}|^2}\mathbf{s}_{l1} + k_2 \mathbf{s}_{l2}\right)\tau. \tag{9.21}$$

QR decomposition can now be performed on basis matrix $\mathbf{A}$ after substituting the third column of Eq. (9.16) with the first component of Eq. (9.21), which represents the high-NA RIM spherical aberration that exhibits minimal demanded stroke for desired focal depth $\tau = 1\,\mu\text{m}$, such that

$$\mathbf{A} = \begin{bmatrix} 1 & k_2 d_0 & k_2 d_0 - k_2 \Omega \cdot c_0 & 0 \ldots 0 \\ 0 & k_2 d_2 & k_2 d_2 - k_2 \Omega \cdot c_2 & 0 \ldots 0 \\ 0 & k_2 d_4 & k_2 d_4 - k_2 \Omega \cdot c_4 & 0 \ldots 0 \\ 0 & k_2 d_6 & k_2 d_6 - k_2 \Omega \cdot c_6 & 1 \ldots 0 \\ \vdots & \vdots & \vdots & \vdots \ddots \vdots \\ 0 & k_2 d_{2K} & k_2 d_{2K} - k_2 \Omega \cdot c_{2K} & 0 \ldots 1 \end{bmatrix}, \tag{9.22}$$

where $\Omega = \sum_{p=1}^{K} c_{2p} \cdot d_{2p} / \sum_{p=1}^{K} c_{2p}^2$. An aberration-free focal spot can thus be obtained at τ after shifting the translation stage to h^*, assigning $-\tau$ to the third element of $\mathbf{s}_h$, and applying the vector of low-NA spherical coefficients $\mathbf{s}_l$ computed by Eq. (9.8) to the adaptive device. Note that the Zernike coefficients for high-NA defocus are retained in the second column of $\mathbf{A}$, such that fine remote focusing could still be achieved without shifting the sample stage.

Figure 9.5 demonstrates simulation results of the proposed minimal RMS balancing algorithm for a desired focal depth $\tau = 40\,\mu\text{m}$. Others parameters are similar to Figure 9.4. Calculations according to Eq. (9.19) indicate an optimum stage depth of $h^* = 18.94\,\mu\text{m}$ for minimal RMS stroke. Figure 9.5(a) first simulates a diffraction-limited focal spot at $h^* = 18.94\,\mu\text{m}$ below a conceptual interface between $n_1 = n_2 = 2.42$. Figure 9.5(b) illustrates the RIM aberration in the case of $n_1 = 1.52$ and $n_2 = 2.42$ when zero phase is applied to the adaptive device at the

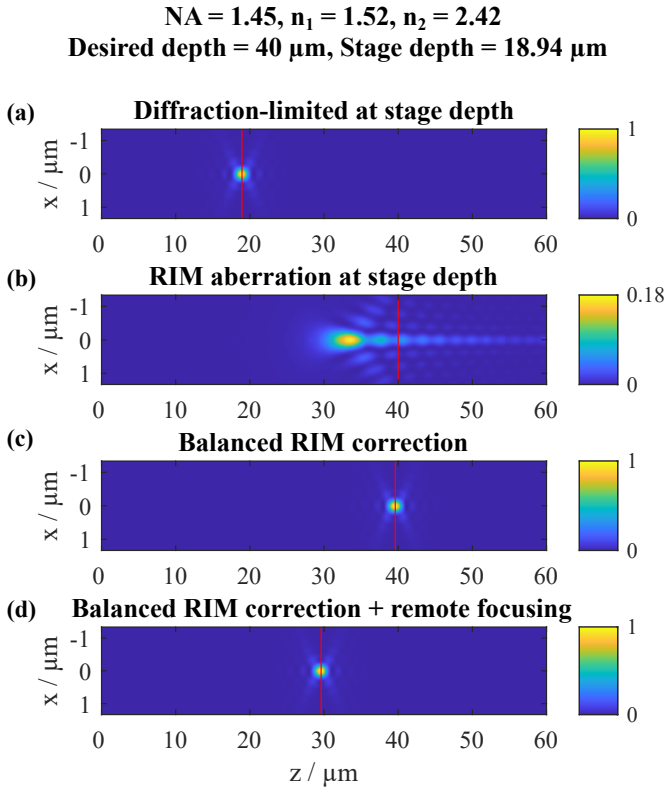


Figure 9.5: Simulation results of the proposed minimal RMS balancing algorithm for a desired focal depth $\tau = 40\,\mu\text{m}$. Others parameters are similar to Figure 9.4. Plots show focal intensity distributions in the cases of: (a) diffraction-limited in stratum 2; (b) RIM aberration induced at optimum stage depth $h^* = 18.94\,\mu\text{m}$; (c) minimal RMS balanced RIM correction for desired focal depth $\tau = 40\,\mu\text{m}$; (d) independent remote focusing by an offset of $\Delta = -10\,\mu\text{m}$.

same calculated stage depth. In Figure 9.5(c), we correct for this amount of RIM aberration and simultaneously remote focus to the desired depth $\tau = 40\,\mu\text{m}$ using the proposed minimal RMS balancing algorithm by assigning -40 to the third element and zero to the remaining elements of $\mathbf{s}_h$, successfully restoring a diffraction-limited focal spot (SR = 1). Finally, to demonstrate the retained remote focusing ability, an additional refocusing offset of $-10\,\mu\text{m}$ has been introduced in Figure 9.5(d) by assigning 10 to the second element of $\mathbf{s}_h$.

9.6 High-NA refocusing in stratified media with multiple interfaces

The two remote focusing and RIM correction strategies discussed above can be extended to scenarios with multiple interfaces. This section will first give the common example of focusing through a cover glass, before generalising the approach towards multiple interfaces.

9.6.1 Aberration-free refocusing through a cover glass

The geometry for deriving the phase contribution due to RIM when focusing through a cover glass of thickness d is given in Figure 9.6. Again, we always assume refocusing in the last stratum only, and h is the distance between the Gaussian focus O and the last RIM interface. Similar to the case of a single interface, the phase contribution due to RIM Φ_i can be obtained by computing the OPD between ray 1 and ray 2 as

$$\Phi_i = -k_1(d+h)\cos\beta_1 + k_2 d\cos\beta_2 + k_3 h\cos\beta_3, \tag{9.23}$$

and the phase contribution of high-NA defocus Φ_d at a refocusing offset Δ away from O is,

$$\Phi_d = k_3\Delta\cos\beta_3. \tag{9.24}$$

Using the relation $\cos\beta_i = \sqrt{1-(\rho\sin\alpha_i)^2} = \sum_{p=0}^{\infty} c_{2p,i}\cdot\mathcal{Z}_{2p}(\rho)$, where i denotes the i-th stratum, we can represent the total phase in terms of Zernike polynomials, such that

$$\begin{aligned}\Phi_t &= \Phi_i + \Phi_d \\ &= -k_1(d+h)\sum_{p=0}^{\infty} c_{2p,1}\cdot\mathcal{Z}_{2p}(\rho) + k_2 h\sum_{p=0}^{\infty} c_{2p,2}\cdot\mathcal{Z}_{2p}(\rho) + k_3(h+\Delta)\sum_{p=0}^{\infty} c_{2p,3}\cdot\mathcal{Z}_{2p}(\rho),\end{aligned} \tag{9.25}$$

and finally with a vector of low-NA spherical coefficients by,

$$\mathbf{s}_t = -k_1(d+h)\mathbf{s}_{l1} + k_2 d\mathbf{s}_{l2} + k_3(h+\Delta)\mathbf{s}_{l3}. \tag{9.26}$$

Thus $-\mathbf{s}_t$ can be applied to the adaptive device to refocus at an offset Δ away from O and simultaneously correct for the RIM aberration induced between the three strata.

Eq. (9.26) is a function of three distance parameters, d, h, and Δ. As we always assume refocusing in the last stratum, only two of these parameters, h and Δ, will be variables during

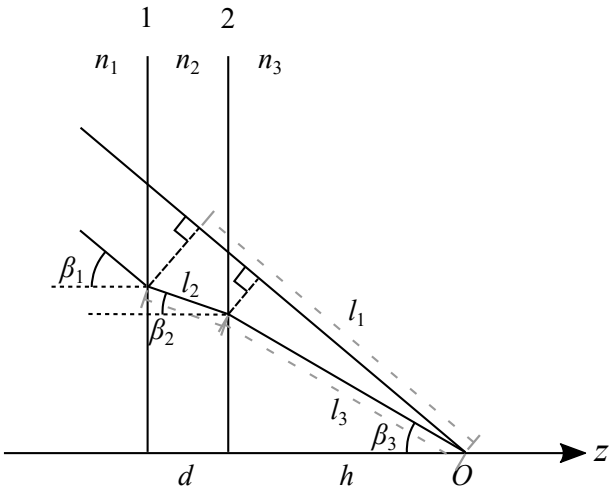


Figure 9.6: Geometry for deriving the phase contribution due to RIM when focusing through a cover glass. The refractive indices of the three strata are denoted by n_1, n_2 and n_3. The illustration shows the case where $n_1 < n_3 < n_2$.

experiments, whose phase contribution need to be continuously updated and corrected for by the adaptive device. On the other hand, the phase contribution of the cover glass,

$$\mathbf{s}_g = -k_1 d\mathbf{s}_{l1} + k_2 d\mathbf{s}_{l2}, \tag{9.27}$$

can be considered as a constant offset when updating the adaptive device. Therefore, to achieve independent remote focusing and RIM aberration correction, QR decomposition can be performed on a new basis matrix $\mathbf{A}$ that takes into account high-NA remote focusing in stratum 3 and RIM aberration between stratum 1 and stratum 3, such that

$$\mathbf{A} = \begin{bmatrix} 1 & k_3 c_{0,3} & k_3 c_{0,3} - k_1 c_{0,1} & 0 \ldots 0 \\ 0 & k_3 c_{2,3} & k_3 c_{2,3} - k_1 c_{2,1} & 0 \ldots 0 \\ 0 & k_3 c_{4,3} & k_3 c_{4,3} - k_1 c_{4,1} & 0 \ldots 0 \\ 0 & k_3 c_{6,3} & k_3 c_{6,3} - k_1 c_{6,1} & 1 \ldots 0 \\ \vdots & \vdots & \vdots & \vdots \ddots \vdots \\ 0 & k_3 c_{2K,3} & k_3 c_{2K,3} - k_1 c_{2K,1} & 0 \ldots 1 \end{bmatrix}. \tag{9.28}$$

When dealing with the phase contribution of the cover glass $\mathbf{s}_g$, two options are available. On the one hand, it may have been pre-corrected by an objective lens designed with a correction collar, in which case no further correction is needed. On the other hand, when the objective lens does not have a correction collar and/or the cover glass is not of the nominal thickness

and/or the refractive index of the objective lens immersion medium is not that of the nominal, $\mathbf{s}_g$ should be computed and added to the final vector of Zernike coefficients before updating the adaptive device. Failure to do so will lead to a partially corrected focal spot.

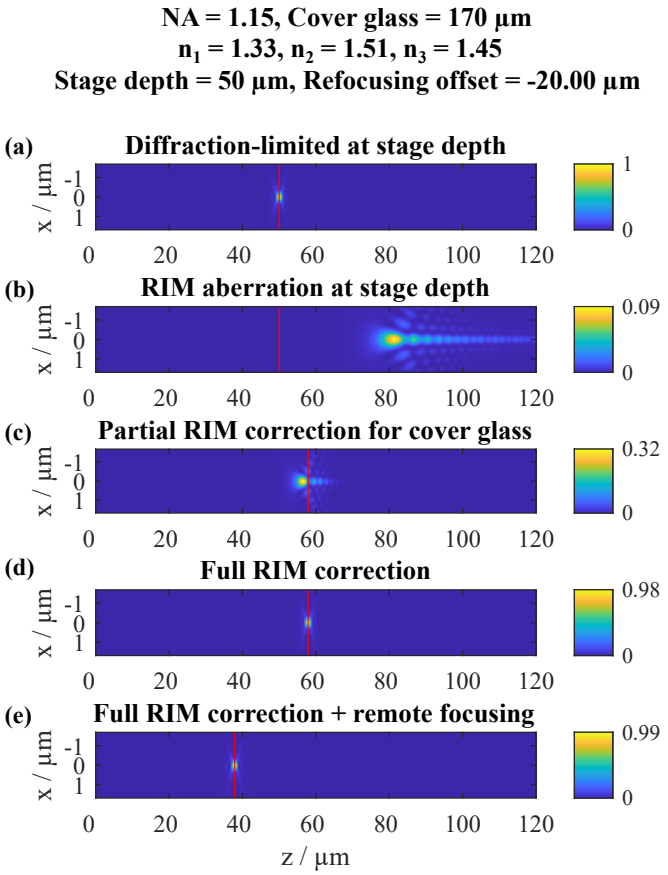


Figure 9.7: Simulation results of the proposed control algorithm for independent remote focusing and RIM aberration correction when focusing through a 170-µm thick cover glass ($n_2 = 1.51$) from $n_1 = 1.33$ to $n_3 = 1.45$ using a water immersion lens of NA = 1.15 with incident wavelength $\lambda = 790$ nm. Plots show focal intensity distributions in the cases of: (a) diffraction-limited in stratum 3; (b) RIM aberration induced at $h = 50\,\mu$m; (c) correction for constant RIM aberration of cover glass; (d) further correction for RIM aberration due to stage depth $h = 50\,\mu$m; (e) independent remote focusing by an offset of $\Delta = -20\,\mu$m.

Figure 9.7 demonstrates simulation results of the proposed control algorithm for independent remote focusing and RIM aberration correction when focusing through a 170-µm thick cover glass ($n_2 = 1.51$) from $n_1 = 1.33$ to $n_3 = 1.45$ using a water immersion lens of NA = 1.15 with incident wavelength $\lambda = 790$ nm. Figure 9.7(a) first simulates a diffraction-limited focal spot

at stage depth $h = 50\,\mu\text{m}$ below a conceptual interface between $n_1 = n_2 = n_3 = 1.45$ for an NA = 1.15 objective lens designed for perfect operation at this refractive index. Figure 9.7(b) illustrates RIM aberration in the case of $n_1 = 1.33$, $n_2 = 1.51$, and $n_3 = 1.45$ when zero phase is applied to the adaptive device at the same stage depth. In Figure 9.7(c), the constant RIM aberration due to the cover glass, as given in Eq. (9.27), is corrected for. Figure 9.7(d) further corrects for the RIM aberration due to stage depth h independently of its high-NA defocus component by assigning -50 to the third element and zero to the remaining elements of $\mathbf{s}_h$. A diffraction-limited focal spot (SR = 1) is thus obtained at the same focal depth as Figure 9.7(c). In order to demonstrate independent remote focusing after the RIM aberration for stage depth $h = 50\,\mu\text{m}$ and cover glass thickness $d = 170\,\mu\text{m}$ has been fully corrected, a refocusing offset of $\Delta = -20\,\mu\text{m}$ is introduced in Figure 9.7(e) by assigning 20 to the second element of $\mathbf{s}_h$, as well as -50 to the third.

We further derive expressions of the optimal refocusing offset Δ^* and stage depth h^* that minimises the total demanded stroke of the adaptive device for desired focal depth $\tau = h + \Delta$. h^* and Δ^* can be expressed as a function of τ (d is a constant) by performing the same RMS balancing method as that outlined in Section 9.5.5, which leads to

$$\Delta^*(\tau) = (1 - \frac{k_2 \mathbf{s}_{l1}^T \mathbf{s}_{l2}}{k_1 |\mathbf{s}_{l1}|^2})d + (1 - \frac{k_3 \mathbf{s}_{l1}^T \mathbf{s}_{l3}}{k_1 |\mathbf{s}_{l1}|^2})\tau, \tag{9.29}$$

and

$$h^*(\tau) = \tau - \Delta^* = \frac{k_3 \mathbf{s}_{l1}^T \mathbf{s}_{l3}}{k_1 |\mathbf{s}_{l1}|^2}\tau - (1 - \frac{k_2 \mathbf{s}_{l1}^T \mathbf{s}_{l2}}{k_1 |\mathbf{s}_{l1}|^2})d. \tag{9.30}$$

By substituting Eq. (9.29) and Eq. (9.30) into Eq. (9.26), we now obtain the minimal RMS phase at desired depth τ,

$$\mathbf{s}_t(\tau) = (-k_3 \frac{\mathbf{s}_{l1}^T \mathbf{s}_{l3}}{|\mathbf{s}_{l1}|^2} \mathbf{s}_{l1} + k_3 \mathbf{s}_{l3})\tau + (-k_2 \frac{\mathbf{s}_{l1}^T \mathbf{s}_{l2}}{|\mathbf{s}_{l1}|^2} \mathbf{s}_{l1} + k_2 \mathbf{s}_{l2})d. \tag{9.31}$$

By analogy to the procedure outlined in Section 9.5.5 for a single RIM interface, there are now two ways to obtain a diffraction-limited focal spot at desired depth τ with minimal RMS phase applied to the adaptive device. The first is to set the second and third elements of vector $\mathbf{s}_h$ to $-\Delta^*$ and $-h^*$, respectively, so that $\mathbf{s}_h$ can be used with the high-NA modes associated with basis matrix $\mathbf{A}$ defined in Eq. (9.28) to achieve independent remote focusing and RIM

aberration correction. Alternatively, the basis matrix $\mathbf{A}$ defined in Eq. (9.22) can be updated with the refractive index of stratum 3 and the coefficients associated with the first term of Eq. (9.31) to achieve balanced remote focusing and RIM aberration correction for a desired focal depth τ, so that $\mathbf{A}$ takes the form of

$$\mathbf{A} = \begin{bmatrix} 1 & k_3 c_{0,3} & k_3 c_{0,3} - k_3 \Omega c_{0,1} & 0 \ \dots \ 0 \\ 0 & k_3 c_{2,3} & k_3 c_{2,3} - k_3 \Omega c_{2,1} & 0 \ \dots \ 0 \\ 0 & k_3 c_{4,3} & k_3 c_{4,3} - k_3 \Omega c_{4,1} & 0 \ \dots \ 0 \\ 0 & k_3 c_{6,3} & k_3 c_{6,3} - k_3 \Omega c_{6,1} & 1 \ \dots \ 0 \\ \vdots & \vdots & \vdots & \vdots \ \ddots \ \vdots \\ 0 & k_3 c_{2K,3} & k_3 c_{2K,3} - k_3 \Omega c_{2K,1} & 0 \ \dots \ 1 \end{bmatrix}, \tag{9.32}$$

where $\Omega = \sum_{p=1}^{K} c_{2p,1} \cdot c_{2p,3} / \sum_{p=1}^{K} c_{2p,1}^2$.

Figure 9.8 demonstrates simulation results of the proposed minimal RMS balancing algorithm for desired focal depth $\tau = 100\,\mu\text{m}$. Others parameters are similar to Figure 9.7. Calculations according to Eq. (9.30) indicate an optimum stage depth of $h^* = 54.31\,\mu\text{m}$ for minimal RMS stroke. Figure 9.8(a) first simulates a diffraction-limited focal spot at $h^* = 54.31\,\mu\text{m}$ below the second conceptual interface between $n_1 = n_2 = n_3 = 1.45$. Figure 9.8(b) illustrates the RIM aberration in the case of $n_1 = 1.33$, $n_2 = 1.51$, and $n_3 = 1.45$ when zero phase is applied to the adaptive device at the same calculated stage depth. In Figure 9.8(c), we correct for the minimal RMS component of RIM aberration due to the cover glass, i.e., the second term of Eq. (9.31). In Figure 9.8(d), we further correct for the minimal RMS component of RIM aberration induced at the desired focal depth $\tau = 100\,\mu\text{m}$, i.e., the first term of Eq. (9.31), using the proposed minimal RMS balancing algorithm by assigning -100 to the third element and zero to the remaining elements of $\mathbf{s}_h$. Finally, to demonstrate the retained remote focusing ability, an additional refocusing offset of $-20\,\mu\text{m}$ has been introduced in Figure 9.8(e) by assigning 20 to the second element of $\mathbf{s}_h$.

9.6.2 Generalisation towards multiple interfaces

Through the discussions above, we can now obtain similar expressions for the general case of a stratified media with N strata. In doing so, we always assume refocusing in the last stratum

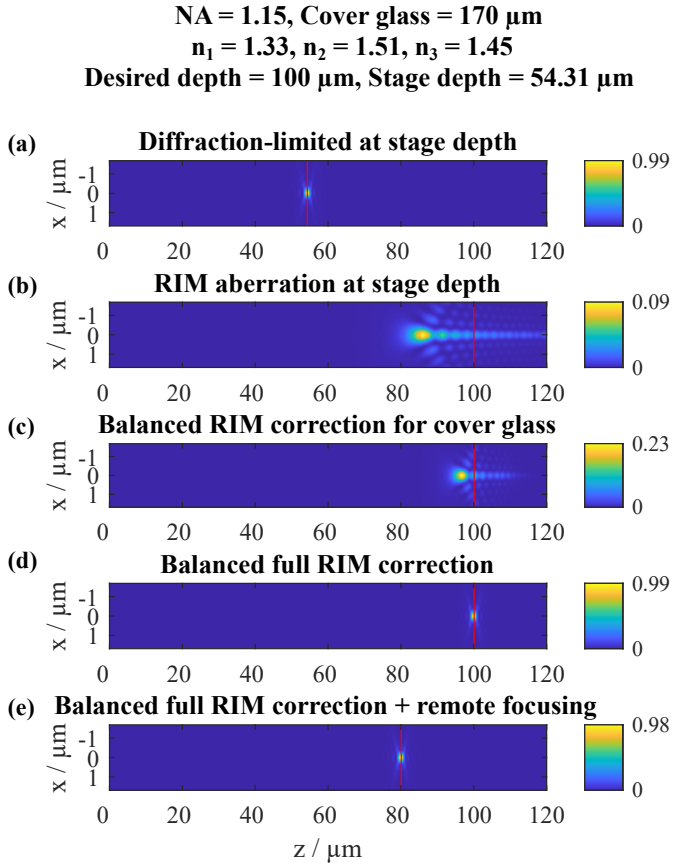


Figure 9.8: Simulation results of the proposed minimal RMS balancing algorithm focusing for desired focal depth $\tau = 100\,\mu\text{m}$. Others parameters are similar to Figure 9.7. Plots show focal intensity distributions in the cases of: (a) diffraction-limited in stratum 3; (b) RIM aberration induced at optimum stage depth $h^* = 54.31\,\mu\text{m}$; (c) correction for minimal RMS component of RIM aberration due to cover glass; (d) further correction for minimal RMS component of RIM aberration induced at the desired focal depth $\tau = 100\,\mu\text{m}$; (e) independent remote focusing by an offset of $\Delta = -20\,\mu\text{m}$.

only, such that stage depth h and refocusing offset Δ are variables, while the thickness d_i of strata $2, 3, ..., N-1$ is a constant. The effective NA is also effectively limited by the lowest RI of all strata. Thus we obtain the phase contribution due to RIM aberration,

$$\Phi_i = -k_1\Big(\sum_{i=2}^{N-1} d_i + h\Big)\cos\beta_1 + \sum_{i=2}^{N-1} k_i d_i \cos\beta_i + k_N h \cos\beta_N, \tag{9.33}$$

the phase contribution of high-NA defocus Φ_d at a refocusing offset Δ away from the Gaussian focus in the last stratum,

$$\Phi_d = k_N \Delta \cos\beta_N, \tag{9.34}$$

and the total phase contribution of both the RIM aberration and high-NA defocus,

$$\Phi_t = -k_1(\sum_{i=2}^{N-1} d_i + h)\cos\beta_1 + \sum_{i=2}^{N-1} k_i d_i \cos\beta_i + k_N(h+\Delta)\cos\beta_N. \tag{9.35}$$

Thus the total phase represented by a vector of low-NA spherical coefficients is

$$\mathbf{s}_t = -k_1(\sum_{i=2}^{N-1} d_i + h)\mathbf{s}_{l1} + \sum_{i=2}^{N-1} k_i d_i \mathbf{s}_{li} + k_N(h+\Delta)\mathbf{s}_{lN}. \tag{9.36}$$

The optimum refocusing offset Δ^* can be further derived as,

$$\Delta^*(\tau) = \sum_{i=2}^{N-1}(1 - \frac{k_i \mathbf{s}_{l1}^T \mathbf{s}_{li}}{k_1|\mathbf{s}_{l1}|^2})d_i + (1 - \frac{k_N \mathbf{s}_{l1}^T \mathbf{s}_{lN}}{k_1|\mathbf{s}_{l1}|^2})\tau, \tag{9.37}$$

the corresponding optimal stage depth h^*,

$$h^*(\tau) = \frac{k_N \mathbf{s}_{l1}^T \mathbf{s}_{lN}}{k_1|\mathbf{s}_{l1}|^2}\tau - \sum_{i=2}^{N-1}(1 - \frac{k_i \mathbf{s}_{l1}^T \mathbf{s}_{li}}{k_1|\mathbf{s}_{l1}|^2})d_i, \tag{9.38}$$

and the final representation of the minimal RMS phase at the desired focal depth τ,

$$\mathbf{s}_t(\tau) = \sum_{i=2}^{N-1}(\frac{\mathbf{s}_{l1}^T \mathbf{s}_{li}}{|\mathbf{s}_{l1}|^2}\mathbf{s}_{l1} - \mathbf{s}_{li})k_i d_i + (\frac{\mathbf{s}_{l1}^T \mathbf{s}_{lN}}{|\mathbf{s}_{l1}|^2}\mathbf{s}_{l1} - \mathbf{s}_{lN})k_N\tau. \tag{9.39}$$

In all cases, the phase components corresponding to intermediate strata are assumed to be constant and removed without applying the QR composition process, as was illustrated in Figure 9.7(c) and Figure 9.8(c).

9.7 Modified control matrix for adaptive device

In general, an adaptive device is configured to create not only radially symmetric but also non-radially symmetric Zernike modes. In this section, we discuss how in practice the control matrix of common adaptive devices can be updated to account for the newly derived radially symmetric high-NA modes without affecting its previous functionalities.

Let $\mathbf{a}$ represent a vector of Zernike coefficients commonly used for device control, and $\mathbf{e}_{\#i}$ the i-th standard unit vector, i.e., a vector whose elements are all zero except for the i-th element which is set to one. We define a permutation matrix $\mathbf{P}_f$ as

$$\mathbf{P}_f = \begin{bmatrix} \mathbf{e}_{\#1} & \mathbf{e}_{\#4} & \mathbf{e}_{\#11} & \dots & \mathbf{e}_{\#J} & \mathbf{e}_{\#2} & \mathbf{e}_{\#3} & \mathbf{e}_{\#5} & \dots \end{bmatrix}^{\mathrm{T}}, \tag{9.40}$$

where the first part corresponds to the indices of radially symmetric Zernike modes under the single index notation. Then define a new vector of coefficients $\mathbf{a}^{'}$ which replaces the radially symmetric Zernike coefficients in $\mathbf{a}$ with the new high-NA spherical coefficients. $\mathbf{P}_f$ can then be used to permute vector $\mathbf{a}^{'}$ by

$$\begin{bmatrix} \mathbf{s}_h \\ \mathbf{s}_o \end{bmatrix} = \mathbf{P}_f \cdot \mathbf{a}^{'}, \tag{9.41}$$

where $\mathbf{s}_h$ is the vector of high-NA spherical coefficients discussed above, and $\mathbf{s}_o$ is a vector of all non-radially symmetric Zernike coefficients. According to Eq. (9.8), we have

$$\begin{bmatrix} \mathbf{s}_l \\ \mathbf{s}_o \end{bmatrix} = \begin{bmatrix} \mathbf{T}_{l\leftarrow h} & \mathbf{0} \\ \mathbf{0} & \mathbf{I} \end{bmatrix} \begin{bmatrix} \mathbf{s}_h \\ \mathbf{s}_o \end{bmatrix}, \tag{9.42}$$

which is now a vector of pure Zernike coefficients. Finally, we take into account the constant RIM phase contribution of intermediate strata for sake of generality, the Zernike coefficient vector of which we denote as $\mathbf{s}_c$, and all coefficients are permuted back to their original order as defined in [126, 127], which results in

$$\mathbf{a} = \mathbf{P}_f^{\mathrm{T}} \begin{bmatrix} \mathbf{s}_l + \mathbf{s}_c \\ \mathbf{s}_o \end{bmatrix}. \tag{9.43}$$

For the case of using an SLM, no further modifications are required assuming a linear relationship between drive signal and phase. For a membrane DM that uses a control matrix $\mathbf{C}_z$ to calculate the desired actuator control signals $\mathbf{c}_z$ from Zernike coefficients $\mathbf{a}$ according to Eq. (3.23),

$$\mathbf{c}_z = \mathbf{C}_z \mathbf{a}, \tag{9.44}$$

a new control matrix $\mathbf{C}_z^{'}$ that relates between $\mathbf{a}^{'}$ and $\mathbf{c}_z$ can be given by

$$\mathbf{C}_z^{'} = \mathbf{C}_z \mathbf{P}_f^{\mathrm{T}} \begin{bmatrix} \mathbf{T}_{l\leftarrow h} & \mathbf{0} \\ \mathbf{0} & \mathbf{I} \end{bmatrix} \mathbf{P}_f \tag{9.45}$$

Thus the only modification to the experimental DM control program is to replace $\mathbf{C}_z$ with $\mathbf{C}_z^{'}$, and the new high-NA modes discussed in previous sections can be used without further changes.

9.8 Discussion and conclusion

This chapter presented a generalised method by means of QR decomposition for common adaptive devices (DM or SLM) to perform predictive remote focusing with simultaneous RIM aberra-

tion correction when imaging using high-NA lenses. Modified models of the conventional Zernike defocus and Zernike spherical modes were derived, and were referred to as high-NA modes. Numerical simulations validated that the high-NA modes successfully decoupled remote focusing and RIM aberration correction for both a single-interface stratified media and a cover glass, and the modified control matrix for common adaptive devices was also provided.

In particular, it was shown that when focusing in stratified media, both the adaptive device and translation stage should be operated simultaneously to achieve optimal refocusing. This implies in the first instance that each axial stage movement should be followed by a subsequent adjustment of the adaptive device. Secondly, one can focus at a desired depth below the RIM interface with minimal RMS stroke by balancing the phase required for correction of RIM aberration with that for remote focusing. An important distinction should thus be made between focusing in a homogeneous and stratified medium. In the former case, the position of the translation stage is irrelevant, and one can use a single strategy to control the adaptive device for aberration-free refocusing, as outlined in Section 9.4. In the latter case, the current state of the translation stage must be considered to maintain an aberration-free focus. Thus two distinct control strategies were thoroughly discussed. The first for independent remote focusing and RIM aberration correction, where adjustment of the axial focus position does not inherently induce aberrations, and the correction of RIM aberration does not affect the focus position. This strategy was outlined in Section 9.5.3 and the first part of Section 9.6.1, and can be further employed for closed-loop adaptive optics control [145]. The second strategy described in Section 9.5.5 and the latter part of Section 9.6.1 allows the user to precisely park an aberration-free focus at a desired depth below the RIM interface with minimal demanded stroke of the adaptive device. Both strategies may prove useful in practice.

It should be reiterated that derivations made in this chapter consider a stratified media with planar interfaces orthogonal to the optical axis and uniform RI between each interface. In the real world, this would be useful for a number of applications. First is laser fabrication where often the material surface is flat and polished, and the bulk beneath is homogeneous with a known RI. Second is for imaging in semiconductor devices that typically consist of many layers of planar material exhibiting different RI. For biomedical imaging, however, the specimen of

interest often does not have an obvious layered structure or a uniform RI within each layer. In the former case, if the RI variation is small, the theory in this chapter may still be applicable by using the average RI over the full imaging depth. In the latter case, the average RI within each layer may be used. Finally, if the specimen surface is curved or unflat, RIM correction should only be performed within a small region about the optical axis.

Possible directions for future work include focusing on not only the position and quality of the focal spot in the object space, but also how this would affect the imaging process [234] in the detection space with careful consideration of the microscope configuration, e.g., epi-/trans-illumination, the number of beam-passes on the adaptive device between the light source and detector, the type of image detector used, the effect of aberrations in the conjugate space between the adaptive device and objective lens [235], as well as how the design of different objective lenses behaves internally for rays passing through various lens elements when the model is not considered ideal. It would also be interesting to examine off-axis points in the sample and expand the approach towards non-telecentric systems.

Chapter 10

Multi-conjugate adaptive optics in a multi-purpose adaptive optical microscope

10.1 Overview

The previous chapters focused on performing adaptive optics (AO) at the conjugate pupil plane using a single adaptive device. In particular, it was demonstrated how depth-dependent aberrations could be better compensated to achieve aberration-free remote focusing with either a low-NA or high-NA objective lens. This has valuable clinical implications to extend the depth range for fast aberration-free axial scanning. In terms of 3D imaging, however, the lateral field of view (FOV) is equally important, and pupil-conjugate AO is only sufficient for correcting spatially-invariant aberrations over a limited FOV, as was discussed in Section 3.6. To increase the imaging FOV, unique correction patterns should be applied to different regions of the sample. In this chapter, preliminary research into a multi-conjugate adaptive optics (MCAO) method is presented. Due to complications in making hardware advancements for this work on a readily-developed system, experiments were not carried out on the compact and contactless reflectance confocal microscope intensively discussed in previous chapters. Instead, a multi-purpose adaptive optical microscope (MPAOM) was developed to incorporate different imaging and AO modalities besides the ability to perform MCAO, for the convenience of carrying out different tasks both independently and simultaneously on the same microscope.

In the following sections, a full description of the MPAOM development is first presented, including its capabilities, system layout, modular functional units, and practical design considerations. The system's imaging performance is further evaluated using both non-biological and biological samples. Then, the experimental design of performing MCAO in microscopy is described before presenting the preliminary results of MCAO acquired using HeLa cells.

10.2 Development of a multi-purpose adaptive optical microscope

The MPAOM was developed with consideration of incorporating the following capabilities:

- To function in fluorescence confocal (FC), reflectance confocal (RC), and two-photon excitation (2PE) mode;
- To choose whether or not to bypass the AO module;
- To demonstrate both sensor-based and sensorless AO;
- To choose whether or not to remove the interferometer module used for the calibration step of sensorless AO;
- To perform MCAO by placing a transmissive AO element at the conjugate sample plane and a deformable mirror (DM) at the conjugate pupil plane;
- To switch between two readily identified objectives.

Both theoretical and practical issues were considered in the design and implementation process, and various changes were made to improve the system functionality even after construction.

10.2.1 System layout and modular functional units

A schematic diagram of the MPAOM is illustrated in Figure 10.1. The MPAOM consists of 11 modular functional units indicated in dashed boxes, 10 of which are incorporated within a large enclosure box. According to their purpose they can be grouped to perform the following tasks:

- Near-infrared (NIR) confocal and 2PE imaging, which includes the NIR illumination module, the NIR reflectance detection module, and the 2PE detection module;
- Dual-channel visible light confocal imaging;

- Optional sensor-based and sensorless AO, which includes the common AO module, the Shack-Hartmann module, and the interferometer module;
- MCAO using a transmissive AO element;
- Raster scan in two dimensions;
- Reflective and transmissive widefield imaging.

Details of how the setup was designed to perform each task are thoroughly discussed below.

Near-infrared confocal and 2PE imaging

The NIR illumination module works jointly with the NIR reflectance detection module to enable RC imaging in the NIR regime, and with the 2PE detection module to perform 2PE microscopy. A mode-locked Ti:Sapphire laser (Mai Tai eHP DeepSee, Spectra-Physics) was used as illumination source for both imaging modes to generate an output pulse train of 70 fs pulse width at a 80 MHz repetition rate. The wavelength is tunable between 690∼1040 nm and the average power at 800 nm over a 1.1 mm diameter beam is 2.9 W. To flexibly adjust the laser power going into the system, polarisation control was implemented by combining a half-wave plate (1/2 WP, AHWP05M-980, Thorlabs) and a polarising beam-splitter (PBS1, CCM1-PBS252, Thorlabs) such that the horizontally-polarised laser output could be attenuated by rotating the half-wave plate. A silicon avalanche photodiode (APD, APD430A/M, Thorlabs) was chosen for detection of back-scattered light and a GaAsP photo-multiplier tube (PMT3, PMT2101/M, Thorlabs) was used to detect fluorescence signal when working in 2PE mode. The APD gives best performance between 400∼1000 nm and maximum responsivity is achieved at 800 nm. Response range for the PMT is 300∼720 nm and peak wavelength is 580 nm. For RC imaging, a 50 µm pinhole was placed before the APD to obstruct out-of-focus light, and a polarising plate beam-splitter (PBS2, PBSW-808, Thorlabs) was used in combination with a quarter-wave plate (1/4 WP, WPQ05M-830, Thorlabs) to block severe back reflections originating from multiple glass surfaces in a similar way to that described in Section 4.3.2.

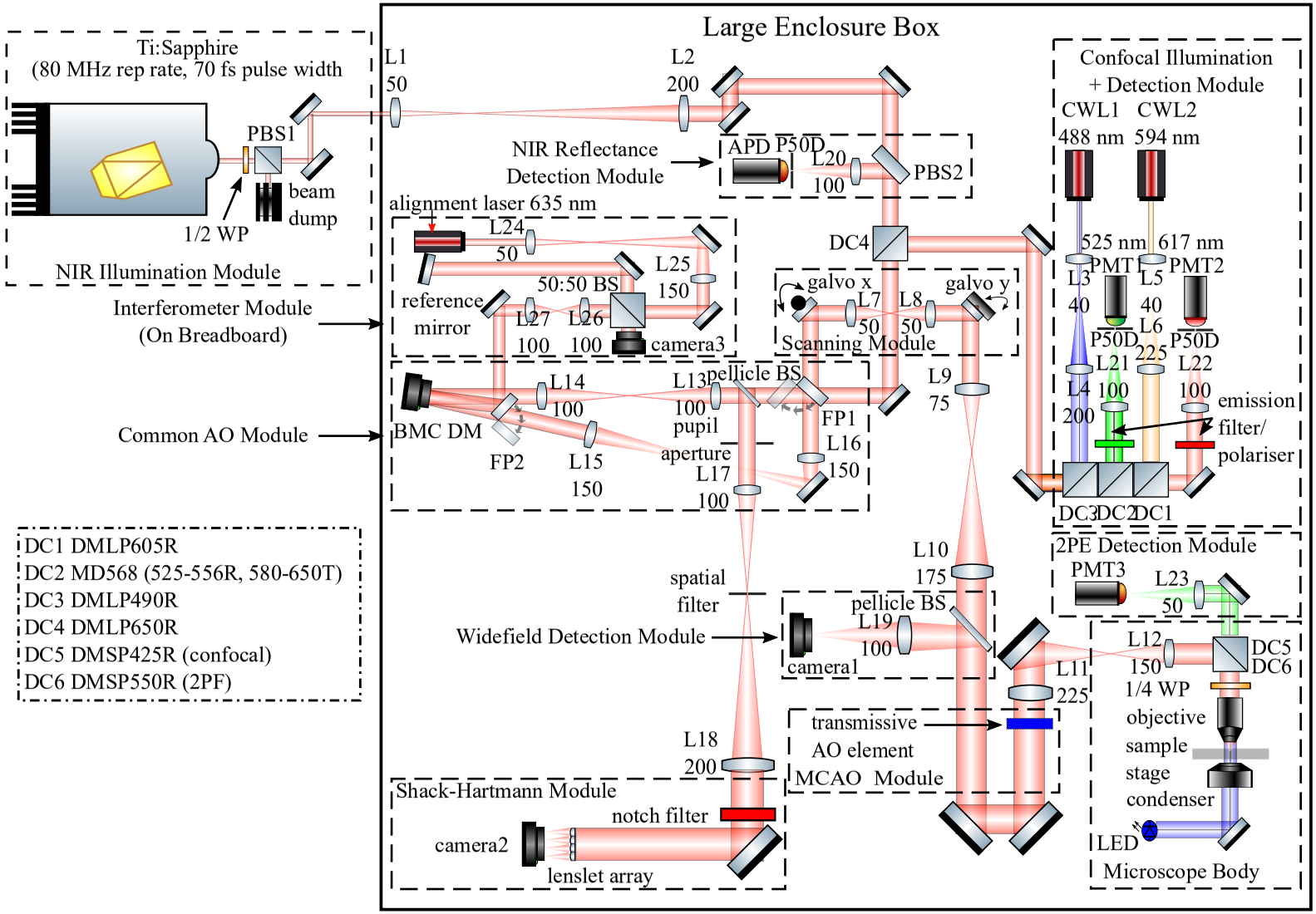


Figure 10.1: Schematic diagram of multi-purpose adaptive optical microscope. Modular functional units are indicated in dashed boxes for clarity. Side view is used for microscope body and top view is used for all other parts of the system.

Dual-channel visible light confocal imaging

The confocal illumination and detection module was designed to perform reflectance and fluorescence imaging with two colour channels in the visible light spectra. Two continuous wave (CW) lasers (CWL1, OBIS 488LX, Coherent; CWL2, OBIS 594LS, Coherent) were incorporated to work with fluorescent markers Alexa Fluor 488 and Alexa Fluor 594. The power of both lasers are tunable using their commercial software and peak powers reach 50 mW and 60 mW over a 0.8 mm and 0.7 mm output beam size, respectively. Both detection paths incorporate a 50 µm pinhole, and use a PMT as detector. For FC mode imaging, long-pass emission filters were placed in the collimated detection beam to transmit fluorescence signal; while they were replaced by linear polarisers for RC mode imaging. The order in which the two illumination and detection paths were arranged was carefully considered so that dichroic mirrors (DC1-DC3) could be selected to divert corresponding wavelengths in the correct direction.

Optional sensor-based and sensorless adaptive optics

The system was designed with the option to perform both sensor-based and sensorless AO (Section 1.3), and to bypass corresponding components when normal imaging is desired. The two AO modes share the same adaptive device, a 140-actuator electrostatic DM (Figure 10.2(a), BMC DM, Multi-3.5, Boston Micromachines), within the common AO module. It has 3.5 µm stroke, 400 µm pitch and a clear aperture of 4.4 mm. The option to bypass the BMC DM was made possible by a flip mirror (FP1). When FP1 is incorporated in the beam path, it diverts the illumination beam towards the objective lens before reaching the common AO module; whereas with FP1 flipped away, the illumination beam enters the common AO module and reflects off the BMC DM before being diverted to the objective lens. To maintain a quasi-circular beam profile on the BMC DM, effort was made to minimise the angle between incident and reflected light taking into account the size and spatial arrangement of opto-mechanical component, leading to 15° with an beam aspect ratio of 1.008 on the DM membrane.

In order to perform sensor-based AO, a custom Shack-Hartmann wavefront sensor (SHWS) was built to work jointly with the common AO module. It consists of an electron multiplying

charge coupled device (EMCCD, camera2, iXon 887, Andor) with 56 fps frame rate, 512×512 pixels, 16 µm pixel size, and a lenslet array with 500 µm pitch and 46.70 mm focal length (15-816, Edmund Optics). The beam was diverted by a 45:55 (R:T) pellicle beam-splitter from a collimated de-scanned position after the BMC DM so that the BMC DM and SHWS could work in a closed-loop configuration (Section 3.4.3). For fluorescence imaging, a notch filter was positioned before the SHWS to reject back reflections in the incident wavelength without losing signal light. In addition, a spatial filter was implemented for optical sectioning and a pupil aperture was used to adjust the beam size.

An interferometer module was built on a separate breadboard to calibrate the BMC DM before performing sensorless AO, and could be removed during the wavefront correction process. A 635 nm laser diode (CPS635R, Thorlabs) with 2.9 mm output beam diameter was used for alignment and calibration purposes, and interference patterns were recorded using a high speed camera (camera3, MQ042MG-CM, Ximea) with a sensor diameter of 11.2 mm. During calibration, the laser beam was first expanded to fill camera3 before being split by a 50:50 beam-splitter into a reference beam and a calibration beam. The former reflects off a tilted mirror before entering camera3, and the latter reflects off flip mirror FP2 before overfilling the BMC DM to fully analyse the membrane surface. Normal incidence was used for this process, and FP2 could be flipped away after DM calibration. The reflected beam then coincides with the reference beam at camera3. The DM calibration procedure for sensorless AO is given in [236].

MCAO using a transmissive AO element

The MCAO module incorporated a 37-element electrostatic fluidic transmissive adaptive element (Figure 10.2(b), custom made, Albert-Ludwigs University of Freiburg) with a clear aperture of 10.2 mm×12 mm, which was used in combination with the BMC DM to achieve AO correction over multiple field points. The actuators were arranged hexagonally and the fluidic chamber between substrate and membrane was filled with optical liquid so as to allow for flexible deformation of the membrane through electrostatic actuation. Fluidic ports were sealed with plugs after the filling process. During experiments, this device was first placed in the pupil plane for

functionality characterisations before being moved to a plane conjugate to a layer of dominant phase variation in the sample, as was illustrated in Figure 3.7(c).

Raster scan in two dimensions

Raster scan was performed in two dimensions using galvanometer scanners (galvo x, galvo y, 8315KM40B, Cambridge Technology). The scanner driver box was custom made by choosing the appropriate power supply and heatsink to match electrical specifications of the driver board (MicroMax 671 Series, Cambridge Technology). Two 10 A 24 V DC power supplies (705-9835, RS) were identified and reversely connected to act as a ±24 V power supply for the driver board, which required a voltage range between ±18 ∼ ±30 V for optimal performance. The current was slightly higher than the RMS current required to drive both the scanner head and driver board. The choice of heatsink took into account the full operational power, the heat dissipated in the scanner, and the maximum rise of temperature allowed in the amplifier junction. Required thermal resistance was then calculated as the selection criteria. To allow for operation under high ambient temperatures, a heatsink with 0.4 K/W thermal resistance was chosen, and a fan was used for more effective heat dissipation. Finally, a power entry module and BNC connectors for signal input and output were chosen, and all components were wired together after designing an optimum mechanical layout. The completed scanner box is shown in Figure 10.2(c).

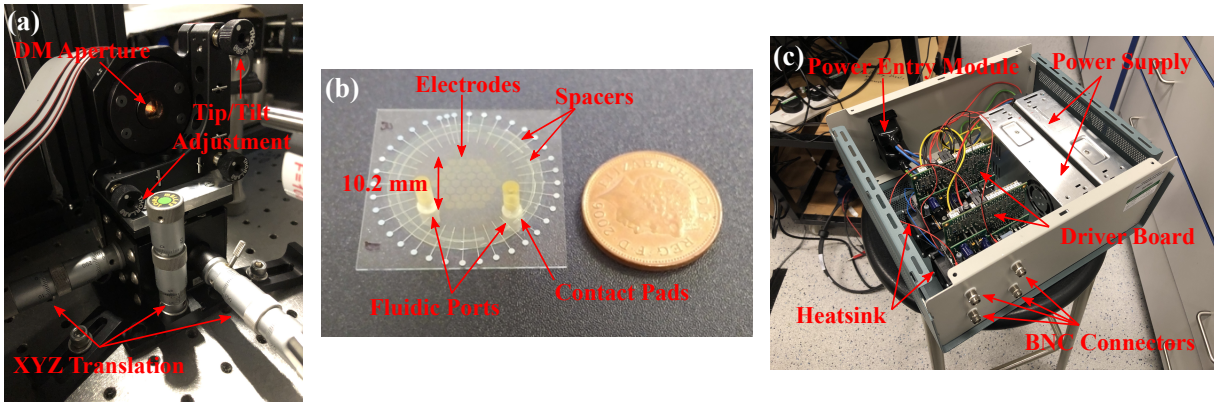


Figure 10.2: Main system devices. (a) Boston Micromachines deformable mirror. (b) Transmissive AO element custom made from Albert-Ludwigs University of Freiburg. (c) Completed scanner driver box. Labels indicate main components.

Reflective and transmissive widefield imaging

The microscope body allows both reflective imaging for confocal and 2PE channels discussed above, and transmissive widefield imaging when used jointly with a widefield detection module. The microscope body incorporates most importantly the objective and piezo scanner (not drawn, P-725.4CD, PI). Two objectives were identified (OBJ1, MPLFLN40X, Olympus; OBJ2, UAPON40XW340, Olympus) for different purposes. OBJ1 is an air immersion semi-apochromat with 40× magnification, 0.75 NA, and 0.63 mm working distance. OBJ2 is a water immersion apochromat with 40× magnification, 1.15 NA, and 0.25 mm working distance, identified for preliminary demonstrations of MCAO, which will be discussed in Section 10.3. OBJ2 works with a cover glass thickness of 0.13∼0.25 mm, and incorporates a correction collar to compensate for spherical aberration introduced by the refractive index mismatch. The sample stage is transmissive directly below the objective. A white LED (LED, MCWHL5, Thorlabs), condenser lens, and widefield detection module together form a flood illumination imaging module to locate the region of interest (ROI) in transparent samples.

10.2.2 Practical considerations for the system design

Many practical factors were taken into account during the optical and mechanical design process to allow optimum imaging performance both with and without the incorporation of AO.

First of all, the beam size at various locations of the system was of prime concern in the design stage for its influence on important system performance parameters such as resolution, FOV and aberration level. It can be restricted by the output laser beam, the clear aperture of the BMC DM and transmissive AO element, the size of galvanometer scanners, and most importantly the back aperture (OBA) of the two objective lenses, which can be calculated by,

$$\mathrm{OBA} = 2 \cdot f_{\mathrm{obj}} \cdot \mathrm{NA} = 2 \cdot f_{\mathrm{tube}} / M_{\mathrm{obj}} \cdot \mathrm{NA}, \tag{10.1}$$

where f_{obj} is the objective lens focal length, f_{tube} is the nominal tube lens focal length (200 mm for Nikon, Leica, and Mitutoyo; 180 mm for Olympus; and 165 mm for Zeiss), and M_{obj} is the objective lens magnification. Tube lenses are normally designed for use with infinity-corrected objectives to minimise the amount of aberrations compared to achromatic lenses. As mentioned

in Section 2.6.1, the objective lens NA determines the theoretical spatial resolution for a fixed illumination wavelength. For this reason, the OBA is usually overfilled to approach maximum resolution. As adaptive devices only affect the illumination beam size in a 2PE microscope, but affects both the illumination and detection beam sizes in a confocal microscope (Section 1.3), the system design needs to take this into account for optimum AO correction in both imaging modes. It is ideal for the beam to be smaller than the DM clear aperture by around half an actuator on each side so that there is enough freedom to correct for aberrations at the beam edge, while maintaining maximum capability to correct for high order aberrations. One must bear in mind that when the objective lens is overfilled, the detection beam diameter at the OBA may be smaller than that of the illumination, in which case considerations should be made for the detection beam to arrive at the adaptive element with an optimum diameter. Imaging FOV is dependent upon the maximum mechanical scan angle (MSA) of the galvanometer scanners and the system magnification. It is also limited by the diameter and focal length of lenses in between, as well as the magnitude of aberrations introduced when passing through these lenses at peripheral locations. A trade-off should be made between using lenses of short focal lengths to better restrict rays towards the central region and long focal lengths for comparably smaller aberrations introduced at the lens edge. Imaging FOV is therefore calculated as,

$$\mathrm{FOV} = 2 \cdot \tan 2\theta_{mech} \cdot f \cdot M, \tag{10.2}$$

where θ_{mech} is the semi-mechanical scan angle of the galvanometer scanners, f is the focal length of the lens immediately after the galvanometer scanners, and M is the magnification factor between this lens and the sample plane. Modelling results in Zemax showed that the largest MSA without vignetting was $\pm 1.5°$, leading to an FOV of 300 µm.

Second, the image update rate is an important parameter for practical imaging. This can be affected by various factors such as the scanner scan speed, image signal level, detector sensitivity, data acquisition speed, computer processing speed, etc. Compared to standard galvanometer scanners, MEMS or resonant scanners can provide much faster beam control for real-time imaging. However, as discussed in Chapter 7, the scanner movement is then non-uniform and thus requires substantial image post-processing to remove image artefacts. For the work in this chap-

ter, imaging speed was not of significant importance, which was why standard galvanometer scanners were used. The image signal level depends on the fluorophore brightness, distribution, and uptake, which fundamentally determines the beam dwell time, and the data acquisition speed limits the pixel resolution for a desired imaging FOV.

Third, the choice of detector plays a crucial role in enhancing image quality. APDs and PMTs are both commonly used for confocal and 2PE microscopy but it is important to understand their differences. Generally, PMTs have higher gain and broader dynamic range, but sensitivity in the red and near-infrared spectral regions are limited; whereas for APDs, sensitivity and resolution in these regions are much higher [237]. In addition, compared to PMTs, APDs have higher quantum efficiency but lower internal gain. With appropriate amplification the APD can give an SNR comparable to that of PMTs in the 500∼650 nm range and improved response in the 650∼850 nm range. In the 650∼1000 nm spectral range, performance of the PMT is quite poor. For the above reasons, PMTs were chosen in the system for detection of visible light whereas an APD was identified for the NIR reflectance detection path.

Finally, as there were two adaptive devices with different numbers of actuators in the system, a compromise was made when designing the SHWS, such that the relationship described in Eq. (6.1) was satisfied to the extent of achieving reasonable performance for both devices. 15 lenslets were used to sample all 6 actuators across the transmissive AO element and the central 8 for the BMC DM.

It should be mentioned that a lens-based imaging system involving multiple wavelengths may be prone to chromatic aberration, especially when the Stokes shift between excitation and detection wavelengths is large. This could ideally be circumvented using pure reflective optics, but at the expense of building a much larger system.

10.2.3 Demonstration of system imaging performance

To test the system imaging performance, preliminary results were obtained for RC and FC modes, the former via a stage micrometer (AGL4202, Agar Scientific) with 1 µm lines and 2 µm spacing, and the latter via pollen grain and mouse kidney cells labelled with Alexa Fluor 568.

The 594 nm CW laser was used as the illumination source, and the common AO module was bypassed throughout these experiments. Results are demonstrated in Figure 10.3, showing high resolution (∼300 nm effective system intensity point spread function as calculated using the method given in Section 4.3.4) and clear structural details.

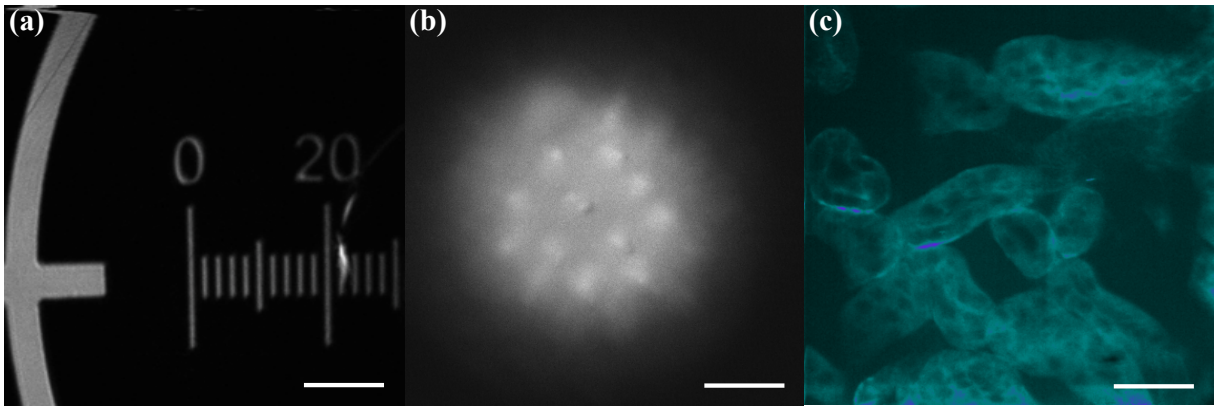


Figure 10.3: Demonstration of system imaging performance. (a) Reflectance imaging of stage micrometer. (b) Fluorescence imaging of pollen grain. (c) Fluorescence imaging of kidney cells. Scale bar: 10 µm.

10.3 Closed-loop multi-conjugate adaptive optics for microscopy

As was previously mentioned in Section 3.6.3, although MCAO has been thoroughly investigated in astronomy [238] and vision science [151], practical implementations are yet to be explored in microscopy [152]. Here, a transmissive AO element was used in combination with a BMC DM for preliminary demonstrations. In following sections, the closed-loop MCAO control algorithm is first introduced before presenting experimental results obtained in HeLa cells.

10.3.1 Closed-loop multi-conjugate adaptive optics control

The MCAO control workflow using direct slopes correction (Section 3.4.2) for one adaptive device is illustrated in Figure 10.4. The imaging FOV was first divided into 9 fields (three in each direction), as determined by the size of the full FOV (300 µm) and that of the isoplanatic patch (∼100 µm). Each field corresponded to a unique SH spot pattern produced by an approximate

point within the specimen, the raw slope values of which were collected into one column slope vector $\mathbf{S}_n$. Column slope vectors acquired from all fields were then concatenated into one full multi-conjugate slope vector $\mathbf{S}_{\mathrm{MC}}$.

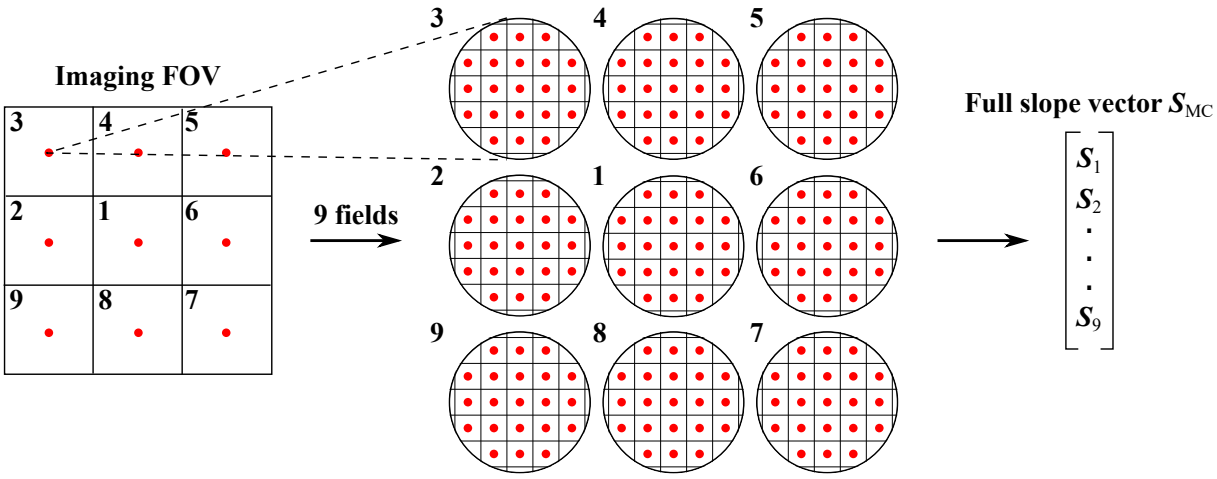


Figure 10.4: MCAO control workflow using direct slopes correction for one adaptive device. The imaging FOV was first divided into 9 fields, and each field corresponded to a unique SH spot pattern, the raw slope values of which were collected into one column slope vector $\mathbf{S}_n$. Column slope vectors acquired from all fields were then concatenated into one full multi-conjugate slope vector $\mathbf{S}_{\mathrm{MC}}$.

Acquisition of the influence function (IF) matrix for both adaptive devices over one field was similar to that outlined in Section 3.4.2, and the IF matrices obtained for all 9 fields were column-wise concatenated to obtain $\mathbf{I}_{\mathrm{MC}}$. After $\mathbf{I}_{\mathrm{MC}}$ was acquired for both devices, they were row-wise concatenated to generate a full IF matrix $\mathbf{I}_{\mathrm{MC_full}}$. Pseudo-inverse was then performed on $\mathbf{I}_{\mathrm{MC_full}}$ to acquire the full control matrix (CM) $\mathbf{C}_{\mathrm{MC_full}}$ that incorporated the CM of both devices. Thus for device 1 comprising of $N_{\mathrm{A},1}$ actuators, device 2 comprising of $N_{\mathrm{A},2}$ actuators, and an SHWS comprising of N_{L} lenslets, in order to correct for N_{F} fields, $\mathbf{C}_{\mathrm{MC_full}}$ would be a matrix of size $(N_{\mathrm{A},1} + N_{\mathrm{A},2}) \times (2N_{\mathrm{L}} \cdot N_{\mathrm{F}})$. It relates raw slope values detected within each field to the control voltages that should be applied to each adaptive device computed by,

$$\begin{bmatrix} \mathbf{c}_1 \\ \mathbf{c}_2 \end{bmatrix} = \mathbf{C}_{\mathrm{MC_full}} \mathbf{S}_{\mathrm{MC}}, \tag{10.3}$$

where $\mathbf{c}_1$ and $\mathbf{c}_2$ represent the control voltages of device 1 and device 2, respectively. Closed-loop MCAO control was then performed separately for each field by setting elements in $\mathbf{S}_{\mathrm{MC}}$

that corresponded to other fields to zero and updating the control loop in a similar way as that described in Section 3.4.3.

10.3.2 Multi-conjugate adaptive optics in HeLa cells

During experiments, as the transmissive AO element was severely limited in stroke, it was only possible to correct for field-dependent aberrations, and hence was placed close to a conjugate sample plane where the beam scanned across the device aperture, as shown in Figure 3.7 and Figure 10.1; while the BMC DM was placed at a conjugate pupil plane to correct for spatially-invariant aberrations. The 594 nm CW laser was used for illumination, and experiments were performed over a full imaging FOV of 300 µm on a single layer of HeLa cells (C127 cell line, Alexa Fluor 594) to induce minimum sample aberration. This was important for validation of the algorithm's effectiveness and stability in correcting field-dependent aberrations only.

After obtaining the MCAO CM for AO correction in all 9 fields using the procedure outlined in Section 10.3.1, correction was separately validated for the central field (Field 1) and a peripheral field (Field 2). Within each field, both adaptive devices were first set to their mid-stroke with a biased control voltage of 0.7 V (max. 1 V) applied to each actuator (stroke $\sim$ voltage^2, Section 3.4.1). The best possible SH spot profile was then obtained by adjusting the lateral position of the sample stage and axial location of the objective lens until spots on the SHWS were bright, round, and evenly distributed. HeLa cell images acquired at this position were used as reference and the biased control voltages were used as the goal for convergence during closed-loop MCAO control. Aberrations were then introduced by applying random voltages to both adaptive devices. Finally, closed-loop MCAO was performed to compensate for these aberrations with a loop gain of $g = 0.3$ until convergence of the control voltages.

Figure 10.4 demonstrates pseudo-coloured images obtained for the central field (Field 1, Figure 10.4(a)) and peripheral field (Field 2, Figure 10.4(b)) when applying biased voltages, random voltages, and voltages after closed-loop MCAO correction on both adaptive devices. A magnified view of the same cell is shown in each case for comparison of the image quality, and a profile plot of the same structure along the white line is given to better appreciate the

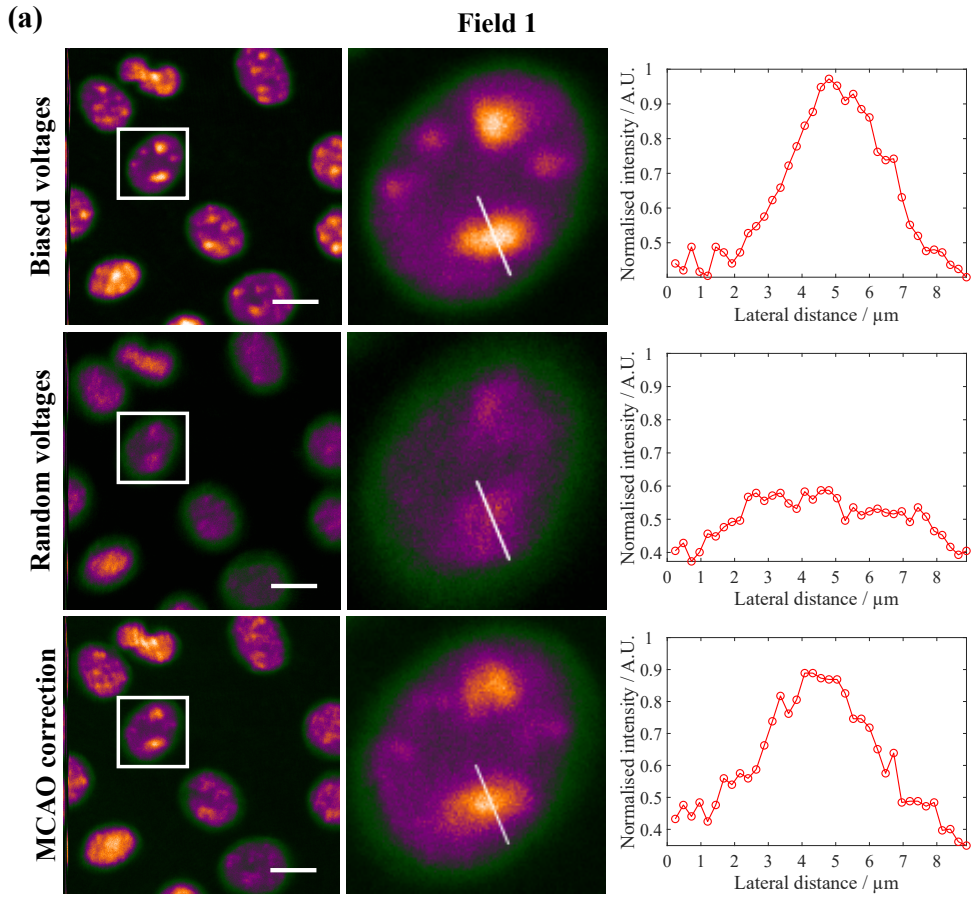


Figure 10.4: Preliminary results for demonstration of MCAO using HeLa cells labelled with Alexa Fluor 594. (a) Correction results for the central field (Field 1). Images obtained with both adaptive devices set at their biased control voltages indicate the goal for convergence during a closed-loop MCAO correction process. Aberrations were then introduced by applying random voltages to both adaptive elements. Finally, closed-loop MCAO was performed to compensate for these aberrations until convergence of the control voltages. A magnified view of the same cell and a profile plot of the same structure along the white line is given for comparison. Plots are normalised to the maximum intensity of the original biased image. Scale bar: 20 µm.

improvement in contrast before and after closed-loop MCAO correction. Plots are normalised to the maximum intensity of the original biased image for fair comparison and parameters for each profile plot is presented in Table 10.1. The MCAO control software in this work was written by Dr. Karen Hampson, and software parameters for this experiment are given in Table 10.2.

We can see from correction of Field 1 and Field 2 in Figure 10.4 and Table 10.1 that with both adaptive devices at their biased positions, cell borders were more defined and fine structures could be visualised within, of which the line profile plot saw a higher maximum normalised

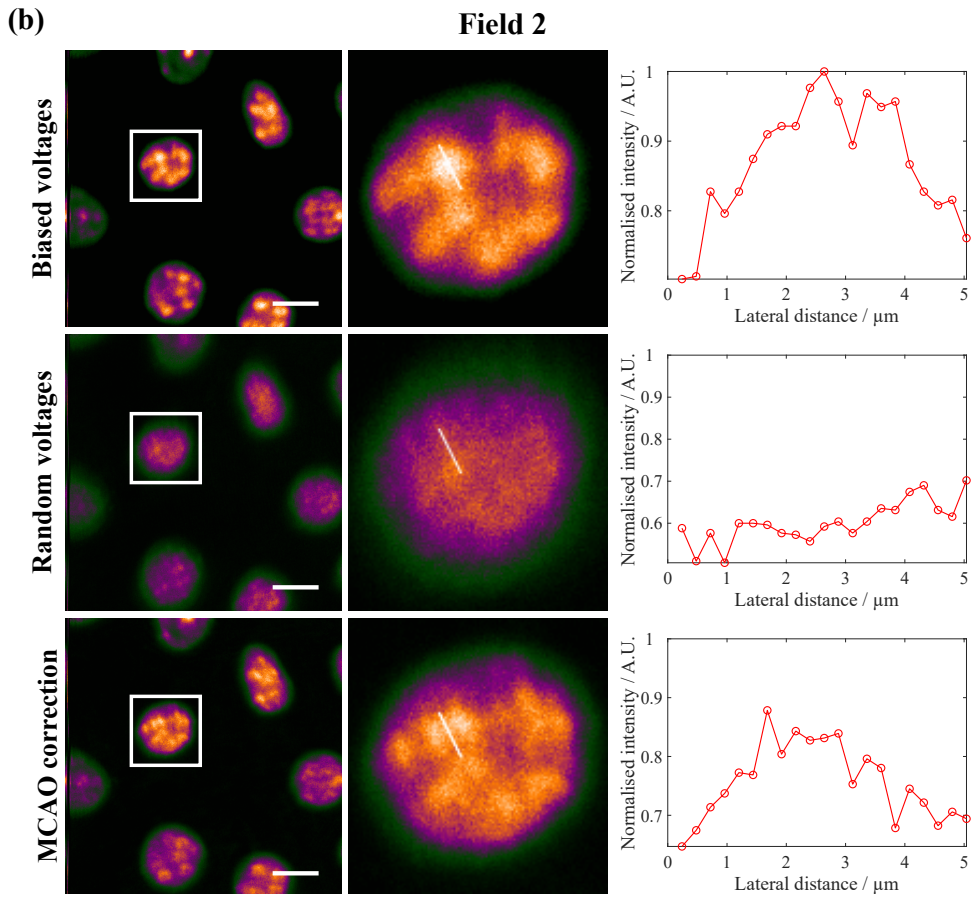


Figure 10.4: Preliminary results for demonstration of MCAO using HeLa cells labelled with Alexa Fluor 594. (b) Correction results for a peripheral field (Field 2). Similar description in (a) applies.

Table 10.1: Comparison of intensity parameters for each line profile plot.

Parameters	Field 1			Field 2		
	Biased	Random voltages	Corrected	Biased	Random voltages	Corrected
Max. Norm. Int.	1.00	0.59	0.89	1.00	0.70	0.88
FWHM (µm)	1.2	3.4	1.5	1.4	2.6	1.3

Table 10.2: Software parameters for closed-loop correction using MCAO

Parameters	Values
Exposure time (s)	0.3
No. of iterations	100
Loop gain	0.3
No. of spots across SHWS	15
No. system modes for BMC DM	40

intensity (Max. Norm. Int.) and a narrower full width half maximum (FWHM). After applying random voltages, these structures disappeared completely and cell borders were badly blurred into the background. Ideally, control voltages should stabilise around their bias after correction if all aberrations introduced had been effectively corrected for. In these initial results, after a 100-loop correction, control voltages were brought much closer towards the bias, but did not perfectly match. This was why images after correction did not exactly reach the quality when biased voltages were applied. Max. Norm. Int. was lower and FWHM was broader in Field 1; where as in Field 2, although Max. Norm. Int. was also lower, but FWHM was slightly narrower than when biased. This was due to the introduction of an artefact during the correction process causing the structure to be split into two parts.

10.4 Discussion and conclusion

This chapter described the design and development of a multi-purpose adaptive optical microscope incorporating three imaging modalities: reflectance confocal, fluorescence confocal, and 2PE microscopy; as well as three AO control modes: pupil-conjugate sensor-based AO, pupil-conjugate sensorless AO, and multi-conjugate sensor-based AO. Options were available to bypass the AO module, and to remove the interferometer after calibration of the BMC DM for sensorless AO correction. Preliminary validation experiments of a closed-loop MCAO control scheme within HeLa cells demonstrated the algorithm's effectiveness in correcting aberrations introduced by applying random voltages at both the central and peripheral imaging fields, showing great potential for the technique to permit AO correction over large FOVs.

The MPAOM can be used in the future as a generalised microscope to assist the development of new AO algorithms and promote research into multi-channel imaging, such as multimodal reflectance and fluorescence confocal microscopy for clinical purposes [29, 31]. Future work into the MCAO project should place major focus on the development and optimisation of the control algorithm in order to improve its effectiveness for different sample types. Ideally, an adaptive device with a larger stroke should be placed at the conjugate pupil plane to compensate for large amplitudes of global low-order modes such as astigmatism and spherical aberration.

The adaptive element at the conjugate sample plane should also have more actuators to allow correction of high frequency aberrations. Although the availability of suitable devices was limited during the course of this development, it should be considered for the future.

In addition, thick specimens should also be used to demonstrate the full potential of MCAO in correcting for field-dependent aberrations through multiple layers of biological tissue, which would be especially beneficial for clinical purposes. In the work described above, only a single layer of thin cells was used for demonstration, and aberration was generated by applying random patterns to the adaptive device. Although this forms an initial feasibility study, the design entails some inherent limitations. First, it does not consider a 3D biological specimen where aberrations can originate at multiple planes within the full imaging depth. Second, it cannot be guaranteed that the random pattern is within the correction ability of the adaptive device, i.e., the frequency may be too high. Therefore, a more realistic validation would be to prepare a phantom sample that embeds fluorescent beads beneath a layer of biological tissue, i.e., brain tissue. In this way, one could not only test the MCAO algorithm in its real context, but also be confident that the aberration variation is within the device's capability.

Chapter 11

Overall summary and outlook

This thesis focused on the development of novel microscopic devices for surgical imaging, and investigations of using adaptive optics methods to address outstanding problems in clinical settings. These include the provision of compact, high-resolution, and label-free imaging devices that cause minimal interruption for surgical guidance; the integration of rapid aberration-free axial focus control; the capability of providing stabilised high-quality image acquisition in the presence of axial sample motion; the extension of a larger aberration-free field of view for high-resolution imaging; and the introduction of a predictive control algorithm for high-NA refocusing in stratified media. An open-source adaptive optics control software has also been made publicly available to make the technology more easily accessible to the wider community. Comprehensive work was undertaken that covered all aspects of system hardware design, control software development, neural network training, and numerical simulations.

It is interesting at this point to look beyond this thesis and at its implications for future directions. First, in terms of high-resolution surgical imaging devices, the adaptive compact and contactless reflectance confocal microscope discussed in Chapters 4, 6, 7, and 8 would greatly benefit from the additional functionalities of visualising internal sites and overhanging margins to expand the device's applicability towards different scopes. By incorporating a rigid endoscope, a dual-imaging-mode device would be introduced to provide contactless high-resolution microscopic imaging for the main surgical site and endoscopic observation for internal and hard-to-reach locations. This dual-mode capability is expected to provide additional flexibility for

surgeons to access the entire surgical site. It is also anticipated that future devices would benefit from extracting a broader spectrum of information by the integration of polarisation techniques to better understand the structural differences between healthy and diseased tissue. Snap-shot methods rather than time-sequenced techniques should be adopted so as to update information in real time [239]. Finally, the unique sensitivity of optical coherent tomography may provide a deeper penetration depth for contactless imaging and should be exploited to better find the depth-wise tumour margin.

Second, adaptive optics can make substantial contributions to the ongoing pursuit of rapid, precise and minimally-invasive surgery, by improving not only the imaging, but also the sensing and therapeutic precision of surgical interventions. For example, in addition to observing diseased cells alone, information of their relative spatial distribution is also important for creating a decisive and holistic treatment plan. Position sensing/monitoring can be well achieved using Fibre-Bragg gratings [240], which are small periodic reflectors written in the core of an optical fibre that reflect particular wavelengths of light according to the grating period. Positional information can then be obtained through variations in the grating periodicity induced during laser fabrication. High-precision therapeutics can also be achieved by removing tumorous cells and lesions at identified positions through laser ablation with a thin optical probe [241], which is minimally-invasive and much safer than traditional manual surgery. Even without adaptive optics, these optical techniques already promise much higher precision and much less trauma than current methods used in the operating theatre. It is anticipated that this precision will be enhanced even further by the introduction of adaptive optics, which helps to improve the fabrication accuracy and quality of periodic structures in Fibre-Bragg gratings, the ability to focus light through these sensors for improved measurement accuracy, as well as the precision in targeting individual diseased cells during laser ablation. By integrating these techniques into a single medical device, data from different sources can be selected and fused using artificial intelligence to assist the decision-making process and take a substantial step towards developing high-precision instrumentation and intelligent surgical intervention systems. It should be remarked, however, that surgeons are end-users of the technology. Different to many other applications, their diagnostic decisions affect lives in a most direct way. Therefore, special

considerations should be given to adapting these complex optical techniques developed in engineering labs to their diagnostic habits and procedural workflows. Potential challenges, risks, and complexities should also be identified so as to reach consensus on a clear plan for smooth clinical translation of regulation-compliant instrumentation. Examples of these may include the device not being fully compliant with medical regulations of sterilisation, laser safety, and easy manoeuvring; the software not being as friendly as expected for surgeons; the imaging process not being as smooth as expected due to unforeseen complications in the surgical workflow, etc.

Finally, the lack of openly available software packages often prevents the wide application of certain technologies. It is envisaged that the open-source adaptive optics control software described in Chapter 5 will serve as a good platform for the dissemination of adaptive optics and its incorporation in more advanced and integrated control workflows. An example would be to investigate the effects of combined remote focusing (Chapter 9) and multi-conjugate adaptive optics (Chapter 10) for fast and high-resolution imaging with expanded fields of view. This will contribute to the areas of neuroimaging and cell biology where it is much desirable to capture dynamic processes over large volumes with sub-cellular resolution. Another example is to exploit the potential of hybrid adaptive optics by taking advantage of both the speed of sensor-based adaptive optics for imaging dynamic processes as well as the reliability of sensorless adaptive optics for deep-tissue imaging. This will have special implications to extend the depth at which calcium signals can be clearly visualised.

In conclusion, the work in this thesis is a small step towards introducing adaptive optics to the operating theatre. It also advocates the distribution of open-source software and the translation of advanced technology to the clinic in a socially-responsible way. I hope this thesis will find itself useful for future researchers in the long run.

Appendix A

Zernike expansion of $\cos\beta$ *and calculation of* c_{2p}

The closed-form expression for the expansion of $\cos\beta$ terms into a series of Zernike polynomials was given in [230]. The main result consists in evaluating the integral

$$\int_0^1 \sqrt{1-(\rho\sin\alpha)^2}\cdot R_{2p}^0(\rho)\,\rho\mathrm{d}\rho, \tag{A.1}$$

where ρ is the radial coordinate in the normalised pupil disk, α is the maximum semi-aperture angle, and $R_{2p}^0(\rho)$ is the radial polynomial of order $n=2p$ and azimuthal order $m=0$ (subsequently dropped for brevity), see [126, 127]. This expression can be rewritten as

$$\frac{\sin\alpha}{4\sqrt{2}}\int_{-1}^1\sqrt{\left(\frac{2}{(\sin\alpha)^2}-1\right)-x}\cdot P_k(x)\,\mathrm{d}x, \tag{A.2}$$

where $P_k(x)$ are Legendre polynomials of the first kind. The authors in [230] defined a function $K_k(\alpha)$ for the integral in Eq. (A.2) and showed that

$$\begin{aligned} K_k(\alpha) =& \int_{-1}^1\sqrt{\gamma-x}\cdot P_k(x)\,\mathrm{d}x \\ =& \frac{-\sqrt{2}}{(2p-1)(2p+1)}\frac{1}{(\gamma+\sqrt{\gamma^2-1})^{k-1/2}}\left[1-\frac{2p-1}{2p+3}\frac{1}{(\gamma+\sqrt{\gamma^2-1})^2}\right], \end{aligned} \tag{A.3}$$

where $\gamma = 2/(\sin\alpha)^2-1$. Using the results above, one can compute the Zernike analysis of a high-NA phase term. The direct formula to compute the Zernike coefficient is found to be

$$\begin{aligned} c_{2p} &= \frac{1}{\pi}\int_0^{2\pi}\int_0^1\sqrt{1-(\rho\sin\alpha)^2}\cdot\mathcal{Z}_{2p}(\rho,\theta)\,\rho\mathrm{d}\rho\,\mathrm{d}\theta \\ &= 2\int_0^1\sqrt{1-(\rho\sin\alpha)^2}\cdot\sqrt{2p+1}R_{2p}(\rho)\,\rho\mathrm{d}\rho \\ &= \left[\frac{2p-1}{2p+3}\tan^4\left(\frac{\alpha}{2}\right)-1\right]\frac{\sin(\alpha)\tan^{2p-1}(\alpha/2)}{2(2p-1)\sqrt{2p+1}}. \end{aligned} \tag{A.4}$$

A high-NA phase term $\Phi_d = k\Delta\sqrt{1-(\rho\sin\alpha)^2}$ can therefore be expanded as

$$\Phi_d = k\Delta \cdot \sum_{p=0}^{\infty} c_{2p} \cdot \sqrt{2p+1} R_{2p}(\rho). \tag{A.5}$$

Bibliography

[1] Z. Qin, C. Chen, S. He, et al., "Adaptive optics two-photon endomicroscopy enables deep-brain imaging at synaptic resolution over large volumes", Science Advances **6**, eabc6521 (2020).

[2] L. Streich, J. C. Boffi, L. Wang, et al., "High-resolution structural and functional deep brain imaging using adaptive optics three-photon microscopy", Nature Methods **18**, 1253–1258 (2021).

[3] N. Ji, J. Freeman, and S. L. Smith, "Technologies for imaging neural activity in large volumes", Nature Neuroscience **19**, 1154 (2016).

[4] Z. Zhang, L. E. Russell, A. M. Packer, et al., "Closed-loop all-optical interrogation of neural circuits in vivo", Nature Methods **15**, 1037–1040 (2018).

[5] R. Lu, W. Sun, Y. Liang, et al., "Video-rate volumetric functional imaging of the brain at synaptic resolution", Nature Neuroscience **20**, 620 (2017).

[6] D. R. Beaulieu, I. G. Davison, K. Kılıç, et al., "Simultaneous multiplane imaging with reverberation two-photon microscopy", Nature Methods, `10.1038/s41592-019-0728-9` (2020).

[7] S. Foersch, A. Heimann, A. Ayyad, et al., "Confocal laser endomicroscopy for diagnosis and histomorphologic imaging of brain tumors in vivo", PloS one **7**, e41760–e41760 (2012).

[8] G. Thomas, J. van Voskuilen, H. C. Gerritsen, et al., "Advances and challenges in label-free nonlinear optical imaging using two-photon excitation fluorescence and second har-

monic generation for cancer research", Journal of Photochemistry and Photobiology B: Biology **141**, 128–138 (2014).

[9] R. H. Wilson, K. Vishwanath, and M.-A. Mycek, "Optical methods for quantitative and label-free sensing in living human tissues: principles, techniques, and applications", Advances in Physics: X **1**, 523–543 (2016).

[10] N. L. Martirosyan, J. Georges, J. M. Eschbacher, et al., "Confocal scanning microscopy provides rapid, detailed intraoperative histological assessment of brain neoplasms: experience with 106 cases", Clinical Neurology and Neurosurgery **169**, 21–28 (2018).

[11] A. Madabhushi and G. Lee, "Image analysis and machine learning in digital pathology: challenges and opportunities", Medical Image Analysis **33**, 170–175 (2016).

[12] M. K. K. Niazi, A. V. Parwani, and M. N. Gurcan, "Digital pathology and artificial intelligence", The Lancet Oncology **20**, e253–e261 (2019).

[13] K. Sirinukunwattana, A. Aberdeen, H. Theissen, et al., "Artificial intelligence–based morphological fingerprinting of megakaryocytes: a new tool for assessing disease in mpn patients", Blood Advances **4**, 3284–3294 (2020).

[14] Z. Bian, C. Guo, S. Jiang, et al., "Autofocusing technologies for whole slide imaging and automated microscopy", Journal of Biophotonics **13**, e202000227 (2020).

[15] Y. Luo, L. Huang, Y. Rivenson, et al., "Single-shot autofocusing of microscopy images using deep learning", ACS Photonics **8**, 625–638 (2021).

[16] L. Ma and B. Fei, "Comprehensive review of surgical microscopes: technology development and medical applications", Journal of Biomedical Optics **26**, 010901 (2021).

[17] J. M. Eschbacher, J. F. Georges, E. Belykh, et al., "Immediate label-free ex vivo evaluation of human brain tumor biopsies with confocal reflectance microscopy", Journal of Neuropathology & Experimental Neurology **76**, 1008–1022 (2017).

[18] E. Belykh, A. A. Patel, E. J. Miller, et al., "Probe-based three-dimensional confocal laser endomicroscopy of brain tumors: technical note", Cancer management and research **10**, 3109–3123 (2018).

[19] P. Charalampaki, M. Nakamura, D. Athanasopoulos, et al., "Confocal-assisted multispectral fluorescent microscopy for brain tumor surgery", Frontiers in Oncology **9**, 10.3389/fonc.2019.00583 (2019).

[20] N. Lakomkin and C. G. Hadjipanayis, "The use of spectroscopy handheld tools in brain tumor surgery: current evidence and techniques", Frontiers in surgery **6**, 30–30 (2019).

[21] E. Jennifer, L. M. Nikolay, N. Peter, et al., "In vivo intraoperative confocal microscopy for real-time histopathological imaging of brain tumors", Journal of Neurosurgery JNS **116**, 854–860 (2012).

[22] S. R. Kantelhardt, D. Kalasauskas, K. König, et al., "In vivo multiphoton tomography and fluorescence lifetime imaging of human brain tumor tissue", Journal of Neuro-Oncology **127**, 473–482 (2016).

[23] T. Wilson and C. Sheppard, *Theory and practice of scanning optical microscopy*, Vol. 180 (Academic Press London, 1984).

[24] M. Minsky, "Memoir on inventing the confocal scanning microscope", Scanning **10**, 128–138 (1988).

[25] P. Davidovits and M. D. Egger, "Scanning laser microscope", Nature **223**, 831–831 (1969).

[26] W. B. Amos and J. G. White, "How the confocal laser scanning microscope entered biological research", Biology of the Cell **95**, 335–342 (2003).

[27] J. Pawley, *Handbook of biological confocal microscopy* (Springer Science & Business Media, 2010).

[28] J. G. White, W. B. Amos, and M. Fordham, "An evaluation of confocal versus conventional imaging of biological structures by fluorescence light microscopy", Journal of Cell Biology **105**, 41–48 (1987).

[29] D. J. Wirth, A. N. Yaroslavsky, M. Snuderl, et al., "Identifying brain neoplasms using dye-enhanced multimodal confocal imaging", Journal of Biomedical Optics **17**, 8 (2012).

[30] M. Peyre, E. Clermont-Taranchon, A. Stemmer-Rachamimov, et al., "Miniaturized handheld confocal microscopy identifies focal brain invasion in a mouse model of aggressive meningioma", Brain Pathology **23**, 371–377 (2013).

[31] M. Snuderl, D. Wirth, S. A. Sheth, et al., "Dye-enhanced multimodal confocal imaging as a novel approach to intraoperative diagnosis of brain tumors", Brain Pathology **23**, 73–81 (2013).

[32] D. J. Wirth, M. Snuderl, W. Curry, et al., "Comparative evaluation of methylene blue and demeclocycline for enhancing optical contrast of gliomas in optical images", Journal of Biomedical Optics **19**, 3 (2014).

[33] L. M. Nikolay, G. Joseph, M. E. Jennifer, et al., "Potential application of a handheld confocal endomicroscope imaging system using a variety of fluorophores in experimental gliomas and normal brain", Neurosurgical Focus FOC **36**, E16 (2014).

[34] F. Forest, E. Cinotti, V. Yvorel, et al., "Ex vivo confocal microscopy imaging to identify tumor tissue on freshly removed brain sample", Journal of Neuro-Oncology **124**, 157–164 (2015).

[35] W. Stummer, U. Pichlmeier, T. Meinel, et al., "Fluorescence-guided surgery with 5-aminolevulinic acid for resection of malignant glioma: a randomised controlled multicentre phase III trial", The Lancet Oncology **7**, 392–401 (2006).

[36] T. Sankar, P. M. Delaney, R. W. Ryan, et al., "Miniaturized handheld confocal microscopy for neurosurgeryresults in an experimental glioblastoma model", Neurosurgery **66**, 410–418 (2010).

[37] L. M. Nikolay, D. C. Daniel, M. E. Jennifer, et al., "Use of in vivo near-infrared laser confocal endomicroscopy with indocyanine green to detect the boundary of infiltrative tumor", Journal of Neurosurgery JNS **115**, 1131–1138 (2011).

[38] K. Erkmen, K. Bekelis, N. E. Simmons, et al., "5-aminolevulinic acid-induced protoporphyrin ix fluorescence in meningioma: qualitative and quantitative measurements in vivo", Operative Neurosurgery **10**, 74–83 (2013).

[39] A. V. Pablo, J. Valerie, T. H. Brent, et al., "Quantitative fluorescence using 5-aminolevulinic acid-induced protoporphyrin ix biomarker as a surgical adjunct in low-grade glioma surgery", Journal of Neurosurgery JNS **123**, 771–780 (2015).

[40] H. Stepp and W. Stummer, "5-ALA in the management of malignant glioma", Lasers in Surgery and Medicine **50**, 399–419 (2018).

[41] A. Alfonso-Garcia, J. Bec, S. S. Weaver, et al., "Real-time augmented reality for delineation of surgical margins during neurosurgery using autofluorescence lifetime contrast", Journal of Biophotonics **13**, `10.1002/jbio.201900108` (2020).

[42] A. J. Schain, R. A. Hill, and J. Grutzendler, "Label-free in vivo imaging of myelinated axons in health and disease with spectral confocal reflectance microscopy", Nature Medicine **20**, 443 (2014).

[43] F. Xia, C. Wu, D. Sinefeld, et al., "In vivo label-free confocal imaging of the deep mouse brain with long-wavelength illumination", Biomedical Optics Express **9**, 6545–6555 (2018).

[44] W. Denk, J. H. Strickler, and W. W. Webb, "Two-photon laser scanning fluorescence microscopy", Science **248**, 73 (1990).

[45] M. Oheim, E. Beaurepaire, E. Chaigneau, et al., "Two-photon microscopy in brain tissue: parameters influencing the imaging depth", Journal of Neuroscience Methods **111**, 29–37 (2001).

[46] K. Svoboda and R. Yasuda, "Principles of two-photon excitation microscopy and its applications to neuroscience", Neuron **50**, 823–839 (2006).

[47] K. Wang, W. Sun, C. T. Richie, et al., "Direct wavefront sensing for high-resolution in vivo imaging in scattering tissue", Nature Communications **6**, 7276 (2015).

[48] N. Petkus, S. Schlaffer, E. Reusche, et al., "Multiphoton excitation of autofluorescence for microscopy of glioma tissue", Neurosurgery **58**, 759–767 (2006).

[49] S. R. Kantelhardt, H. Diddens, J. Leppert, et al., "Multiphoton excitation fluorescence microscopy of 5-aminolevulinic acid induced fluorescence in experimental gliomas", Lasers in Surgery and Medicine **40**, 273–281 (2008).

[50] I. Riemann, R. Le Harzic, K. Mpoukouvalas, et al., "Sub-cellular tumor identification and markerless differentiation in the rat brain in vivo by multiphoton microscopy", Lasers in Surgery and Medicine **44**, 719–725 (2012).

[51] S. Wang, X. Chen, W. Wu, et al., "Rapid, label-free identification of cerebellar structures using multiphoton microscopy", Journal of Biophotonics **10**, 1617–1626 (2017).

[52] L. Jiang, X. Wang, Z. Wu, et al., "Label-free imaging of brain and brain tumor specimens with combined two-photon excited fluorescence and second harmonic generation microscopy", Laser Physics Letters **14**, 105401 (2017).

[53] D. Reichert, M. T. Erkkilä, G. Holst, et al., "Towards real-time wide-field fluorescence lifetime imaging of 5-ALA labeled brain tumors with multi-tap CMOS cameras", Biomedical Optics Express **11**, 1598–1616 (2020).

[54] A. F. Fercher, W. Drexler, C. K. Hitzenberger, et al., "Optical coherence tomography - principles and applications", Reports on Progress in Physics **66**, 239–303 (2003).

[55] C. K. Hitzenberger, "Optical measurement of the axial eye length by laser doppler interferometry", Investigative Ophthalmology & Visual Science **32**, 616–624 (1991).

[56] D. Huang, A. Swanson Eric, P. Lin Charles, et al., "Optical coherence tomography", Science **254**, 1178–1181 (1991).

[57] J. F. de Boer, R. Leitgeb, and M. Wojtkowski, "Twenty-five years of optical coherence tomography: the paradigm shift in sensitivity and speed provided by fourier domain oct [invited]", Biomedical Optics Express **8**, 3248–3280 (2017).

[58] J. Ben Arous, J. Binding, J.-F. Leger, et al., "Single myelin fiber imaging in living rodents without labeling by deep optical coherence microscopy", Journal of Biomedical Optics **16**, 116012 (2011).

[59] C. W. Merkle, S. P. Chong, A. M. Kho, et al., "Visible light optical coherence microscopy of the brain with isotropic femtoliter resolution in vivo", Optics Letters **43**, 198–201 (2018).

[60] E. Min, J. Lee, A. Vavilin, et al., "Wide-field optical coherence microscopy of the mouse brain slice", Optics Letters **40**, 4420–4423 (2015).

[61] V. J. Srinivasan, H. Radhakrishnan, J. Y. Jiang, et al., "Optical coherence microscopy for deep tissue imaging of the cerebral cortex with intrinsic contrast", Optics Express **20**, 2220–2239 (2012).

[62] C. Leahy, H. Radhakrishnan, and V. J. Srinivasan, "Volumetric imaging and quantification of cytoarchitecture and myeloarchitecture with intrinsic scattering contrast", Biomedical Optics Express **4**, 1978–1990 (2013).

[63] O. Assayag, K. Grieve, B. Devaux, et al., "Imaging of non-tumorous and tumorous human brain tissues with full-field optical coherence tomography", NeuroImage: Clinical **2**, 549–557 (2013).

[64] S. L. Jacques, "Optical properties of biological tissues: a review", Physics in Medicine & Biology **58**, R37–R61 (2013).

[65] M. Wang, C. Wu, D. Sinefeld, et al., "Comparing the effective attenuation lengths for long wavelength in vivo imaging of the mouse brain", Biomedical Optics Express **9**, 3534–3543 (2018).

[66] S. Nori, F. Rius-Díaz, J. Cuevas, et al., "Sensitivity and specificity of reflectance-mode confocal microscopy for in vivo diagnosis of basal cell carcinoma: a multicenter study", Journal of the American Academy of Dermatology **51**, 923–930 (2004).

[67] A. Scope, U. Mahmood, D. S. Gareau, et al., "In vivo reflectance confocal microscopy of shave biopsy wounds: feasibility of intraoperative mapping of cancer margins", British Journal of Dermatology **163**, 1218–1228 (2010).

[68] S. K. T. Que, N. Fraga-Braghiroli, J. M. Grant-Kels, et al., "Through the looking glass: basics and principles of reflectance confocal microscopy", Journal of the American Academy of Dermatology **73**, 276–284 (2015).

[69] C. Kielbassa, L. Roza, and B. Epe, "Wavelength dependence of oxidative dna damage induced by uv and visible light", Carcinogenesis **18**, 811–816 (1997).

[70] A. K. Dunn, C. Smithpeter, A. J. Welch, et al., "Sources of contrast in confocal reflectance imaging", Applied Optics **35**, 3441–3446 (1996).

[71] R. Ebrecht, C. Don Paul, and F. S. Wouters, "Fluorescence lifetime imaging microscopy in the medical sciences", Protoplasma **251**, 293–305 (2014).

[72] J. R. Mourant, J. P. Freyer, A. H. Hielscher, et al., "Mechanisms of light scattering from biological cells relevant to noninvasive optical-tissue diagnostics", Applied Optics **37**, 3586–3593 (1998).

[73] O. C. Marina, C. K. Sanders, and J. R. Mourant, "Correlating light scattering with internal cellular structures", Biomedical Optics Express **3**, 296–312 (2012).

[74] Y. N. Sulai, D. Scoles, Z. Harvey, et al., "Visualization of retinal vascular structure and perfusion with a nonconfocal adaptive optics scanning light ophthalmoscope", Journal of the Optical Society of America A **31**, 569–579 (2014).

[75] D. Scoles, Y. N. Sulai, C. S. Langlo, et al., "In vivo imaging of human cone photoreceptor inner segmentsin vivo imaging of photoreceptor inner segments", Investigative Ophthalmology & Visual Science **55**, 4244–4251 (2014).

[76] J. Becker, R. Förster, and R. Heintzmann, *Better than a lens - a novel concept to break the snr-limit, given by fermat's principle*, Electronic Article, 2018.

[77] J. M. Dela Cruz, J. D. McMullen, R. M. Williams, et al., "Feasibility of using multiphoton excited tissue autofluorescence for in vivo human histopathology", Biomedical Optics Express **1**, 1320–1330 (2010).

[78] N. Ji, "The practical and fundamental limits of optical imaging in mammalian brains", Neuron **83**, 1242–1245 (2014).

[79] K. König, P. T. C. So, W. W. Mantulin, et al., "Cellular response to near-infrared femtosecond laser pulses in two-photon microscopes", Optics Letters **22**, 135–136 (1997).

[80] K König, "Intracellular nanosurgery with near infrared femtosecond laser pulses k. könig ", i. riemann, p. fischer and k.-j. halbhuber", Cellular and molecular biology **45**, 195–201 (1999).

[81] F. F. Fischer, B. Volkmer, S. Puschmann, et al., *Risk estimation of skin damage due to ultrashort pulsed, focused near-infrared laser irradiation at 800 nm*, Vol. 13, 4 (2008), p. 041320.

[82] L.-C. Chen, W. Lloyd, S. Kuo, et al., "The potential of label-free nonlinear optical molecular microscopy to non-invasively characterize the viability of engineered human tissue constructs", Biomaterials **35**, 6667–6676 (2014).

[83] E. Belykh, N. L. Martirosyan, K. Yagmurlu, et al., "Intraoperative fluorescence imaging for personalized brain tumor resection: current state and future directions", Frontiers in surgery **3**, 55–55 (2016).

[84] R. K. Tyson, *Principles of adaptive optics* (CRC press, 2015).

[85] J. M. Beckers, "Adaptive optics for astronomy: principles, performance, and applications", Annual review of astronomy and astrophysics **31**, 13–62 (1993).

[86] J. W. Hardy, *Adaptive optics for astronomical telescopes*, Vol. 16 (Oxford University Press, 1998).

[87] J. Porter, H. Queener, J. Lin, et al., *Adaptive optics for vision science: principles, practices, design, and applications*, Vol. 171 (John Wiley & Sons, 2006).

[88] P. Godara, A. M. Dubis, A. Roorda, et al., "Adaptive optics retinal imaging: emerging clinical applications", Optometry and vision science : official publication of the American Academy of Optometry **87**, 930–941 (2010).

[89] J. Booth Martin, "Adaptive optics in microscopy", Philosophical Transactions of the Royal Society A: Mathematical, Physical and Engineering Sciences **365**, 2829–2843 (2007).

[90] J. M. Girkin, S. Poland, and A. J. Wright, "Adaptive optics for deeper imaging of biological samples", Current Opinion in Biotechnology **20**, 106–110 (2009).

[91] N. Ji, "Adaptive optical fluorescence microscopy", Nature Methods **14**, 374 (2017).

[92] P. S. Salter and M. J. Booth, "Adaptive optics in laser processing", Light: Science & Applications **8**, 110 (2019).

[93] M. J. Booth, M. A. A. Neil, R. Juškaitis, et al., "Adaptive aberration correction in a confocal microscope", Proceedings of the National Academy of Sciences **99**, 5788 (2002).

[94] L. Sherman, J. Y. Ye, O. Albert, et al., "Adaptive correction of depth-induced aberrations in multiphoton scanning microscopy using a deformable mirror", Journal of Microscopy **206**, 65–71 (2002).

[95] B. C. Platt and R. Shack, "History and principles of shack-hartmann wavefront sensing", Journal of Refractive Surgery **17**, S573–S577 (2001).

[96] A. Roorda, F. Romero-Borja, W. J. Donnelly Iii, et al., "Adaptive optics scanning laser ophthalmoscopy", Optics Express **10**, 405–412 (2002).

[97] M. J. Booth, "Adaptive optical microscopy: the ongoing quest for a perfect image", Light: Science & Applications **3**, e165 (2014).

[98] C. Rodríguez and N. Ji, "Adaptive optical microscopy for neurobiology", Current Opinion in Neurobiology **50**, 83–91 (2018).

[99] W. Göbel, B. M. Kampa, and F. Helmchen, "Imaging cellular network dynamics in three dimensions using fast 3d laser scanning", Nature Methods **4**, 73–79 (2007).

[100] G. Katona, A. Kaszás, G. F. Turi, et al., "Roller coaster scanning reveals spontaneous triggering of dendritic spikes in ca1 interneurons", Proceedings of the National Academy of Sciences **108**, 2148 (2011).

[101] B. F. Grewe, F. F. Voigt, M. van 't Hoff, et al., "Fast two-layer two-photon imaging of neuronal cell populations using an electrically tunable lens", Biomedical Optics Express **2**, 2035–2046 (2011).

[102] G. D. Reddy, K. Kelleher, R. Fink, et al., "Three-dimensional random access multiphoton microscopy for functional imaging of neuronal activity", Nature Neuroscience **11**, 713–720 (2008).

[103] B. F. Grewe, D. Langer, H. Kasper, et al., "High-speed in vivo calcium imaging reveals neuronal network activity with near-millisecond precision", Nature Methods **7**, 399–405 (2010).

[104] M. Dal Maschio, A. M. De Stasi, F. Benfenati, et al., "Three-dimensional in vivo scanning microscopy with inertia-free focus control", Optics Letters **36**, 3503–3505 (2011).

[105] E. J. Botcherby, R. Juskaitis, M. J. Booth, et al., "Aberration-free optical refocusing in high numerical aperture microscopy", Optics Letters **32**, 2007–2009 (2007).

[106] E. J. Botcherby, R. Juškaitis, M. J. Booth, et al., "An optical technique for remote focusing in microscopy", Optics Communications **281**, 880–887 (2008).

[107] E. J. Botcherby, C. W. Smith, M. M. Kohl, et al., "Aberration-free three-dimensional multiphoton imaging of neuronal activity at khz rates", Proceedings of the National Academy of Sciences **109**, 2919 (2012).

[108] S. Mohanan and A. D. Corbett, "Sensitivity of remote focusing microscopes to magnification mismatch", Journal of Microscopy, `10.1111/jmi.12991` (2020).

[109] A. Peinado, E. Bendek, S. Yokoyama, et al., "Deformable mirror-based axial scanning for two-photon mammalian brain imaging", Neurophotonics **8**, 015003 (2021).

[110] M. Žurauskas, O. Barnstedt, M. Frade-Rodriguez, et al., "Rapid adaptive remote focusing microscope for sensing of volumetric neural activity", Biomedical Optics Express **8**, 4369–4379 (2017).

[111] R. Liu, N. Ball, J. Brockill, et al., "Aberration-free multi-plane imaging of neural activity from the mammalian brain using a fast-switching liquid crystal spatial light modulator", Biomedical Optics Express **10**, 5059–5080 (2019).

[112] H. Jiang, C. Wang, B. Wei, et al., "Long-range remote focusing by image-plane aberration correction", Optics Express **28**, 34008–34014 (2020).

[113] Y. Yang, W. Chen, J. L. Fan, et al., "Adaptive optics enables aberration-free single-objective remote focusing for two-photon fluorescence microscopy", Biomedical Optics Express **12**, 354–366 (2021).

[114] P. Török, P. Varga, Z. Laczik, et al., "Electromagnetic diffraction of light focused through a planar interface between materials of mismatched refractive indices: an integral representation", Journal of the Optical Society of America A **12**, 325–332 (1995).

[115] M. Born and E. Wolf, *Principles of optics: electromagnetic theory of propagation, interference and diffraction of light* (Elsevier, 2013).

[116] J. W. Goodman, *Introduction to fourier optics. 3rd* (Roberts and Company Publishers, 2005).

[117] M. Gu, *Principles of three dimensional imaging in confocal microscopes* (World Scientific, 1996).

[118] W. Yang and R. Yuste, "In vivo imaging of neural activity", Nature Methods **14**, 349 (2017).

[119] S. A. Rahman, "Direct wavefront sensing in adaptive microscopy", Master of Science by Research (2012).

[120] C. Glazowski and M. Rajadhyaksha, "Optimal detection pinhole for lowering speckle noise while maintaining adequate optical sectioning in confocal reflectance microscopes", Journal of Biomedical Optics **17**, 085001 (2012).

[121] M. R. Foreman and P. Török, "Computational methods in vectorial imaging", Journal of Modern Optics **58**, 339–364 (2011).

[122] S. Hell, G. Reiner, C. Cremer, et al., "Aberrations in confocal fluorescence microscopy induced by mismatches in refractive index", Journal of Microscopy **169**, 391–405 (1993).

[123] H. Jacobsen, P. HÄNninen, E. Soini, et al., "Refractive-index-induced aberrations in two-photon confocal fluorescence microscopy", Journal of Microscopy **176**, 226–230 (1994).

[124] C. J. de Grauw, J. M. Vroom, H. T. M. van der Voort, et al., "Imaging properties in two-photon excitation microscopy and effects of refractive-index mismatch in thick specimens", Applied Optics **38**, 5995–6003 (1999).

[125] F. Zernike, "Diffraction theory of the knife-edge test and its improved form, the phase-contrast method", Monthly Notices of the Royal Astronomical Society **94**, 377–384 (1934).

[126] R. J. Noll, "Zernike polynomials and atmospheric turbulence", Journal of the Optical Society of America **66**, 207–211 (1976).

[127] V. N. Mahajan, "Zernike circle polynomials and optical aberrations of systems with circular pupils", Applied optics **33**, 8121–8124 (1994).

[128] L. N. Thibos, R. A. Applegate, J. T. Schwiegerling, et al., "Standards for reporting the optical aberrations of eyes", in Vision science and its applications (2000).

[129] V. N. Mahajan, "Strehl ratio for primary aberrations: some analytical results for circular and annular pupils", JOSA **72**, 1258–1266 (1982).

[130] V. Sacek, *Amateur telescope optics*, 2019.

[131] S. Thomas, T. Fusco, A. Tokovinin, et al., "Comparison of centroid computation algorithms in a shack–hartmann sensor", Monthly Notices of the Royal Astronomical Society **371**, 323–336 (2006).

[132] X. Tao, B. Fernandez, O. Azucena, et al., "Adaptive optics confocal microscopy using direct wavefront sensing", Optics Letters **36**, 1062–1064 (2011).

[133] X. Tao, O. Azucena, M. Fu, et al., "Adaptive optics microscopy with direct wavefront sensing using fluorescent protein guide stars", Optics Letters **36**, 3389–3391 (2011).

[134] J.-W. Cha, J. Ballesta, and P. T. So, "Shack-hartmann wavefront-sensor-based adaptive optics system for multiphoton microscopy", Journal of Biomedical Optics **15**, 046022 (2010).

[135] M. Shaw, K. O'Holleran, and C. Paterson, "Investigation of the confocal wavefront sensor and its application to biological microscopy", Optics Express **21**, 19353–19362 (2013).

[136] X. Tao, A. Norton, M. Kissel, et al., "Adaptive optical two-photon microscopy using autofluorescent guide stars", Optics Letters **38**, 5075–5078 (2013).

[137] R. Aviles-Espinosa, J. Andilla, R. Porcar-Guezenec, et al., "Measurement and correction of in vivo sample aberrations employing a nonlinear guide-star in two-photon excited fluorescence microscopy", Biomedical Optics Express **2**, 3135–3149 (2011).

[138] L. K. Young, T. J. Morris, C. D. Saunter, et al., "Compact, modular and in-plane aoslo for high-resolution retinal imaging", Biomedical Optics Express **9**, 4275–4293 (2018).

[139] R. Horstmeyer, H. Ruan, and C. Yang, "Guidestar-assisted wavefront-shaping methods for focusing light into biological tissue", Nature Photonics **9**, 563–571 (2015).

[140] D. J. Schroeder, "Chapter 16 - adaptive optics: an introduction", in *Astronomical optics (second edition)*, edited by D. J. Schroeder (Academic Press, San Diego, 2000), pp. 409–424.

[141] K. Bush, D. German, B. Klemme, et al., "Electrostatic membrane deformable mirror wavefront control systems: design and analysis", in Optical science and technology, the spie 49th annual meeting, Vol. 5553 (2004).

[142] U. Bitenc, N. A. Bharmal, T. J. Morris, et al., "Assessing the stability of an alpao deformable mirror for feed-forward operation", Optics Express **22**, 12438–12451 (2014).

[143] A. Kellerer, F. Vidal, E. Gendron, et al., "Deformable mirrors for open-loop adaptive optics", in Spie astronomical telescopes + instrumentation, Vol. 8447 (2012).

[144] J. Antonello, T. van Werkhoven, M. Verhaegen, et al., "Optimization-based wavefront sensorless adaptive optics for multiphoton microscopy", Journal of the Optical Society of America A **31**, 1337–1347 (2014).

[145] E. J. Fernández, I. Iglesias, and P. Artal, "Closed-loop adaptive optics in the human eye", Optics Letters **26**, 746–748 (2001).

[146] P. Artal, S. Marcos, R. Navarro, et al., "Odd aberrations and double-pass measurements of retinal image quality", Journal of the Optical Society of America A **12**, 195–201 (1995).

[147] J. Mertz, H. Paudel, and T. G. Bifano, "Field of view advantage of conjugate adaptive optics in microscopy applications", Applied Optics **54**, 3498–3506 (2015).

[148] H. P. Paudel, J. Taranto, J. Mertz, et al., "Axial range of conjugate adaptive optics in two-photon microscopy", Optics Express **23**, 20849–20857 (2015).

[149] J. Li, D. R. Beaulieu, H. Paudel, et al., "Conjugate adaptive optics in widefield microscopy with an extended-source wavefront sensor", Optica **2**, 682–688 (2015).

[150] J.-H. Park, W. Sun, and M. Cui, "High-resolution in vivo imaging of mouse brain through the intact skull", Proceedings of the National Academy of Sciences **112**, 9236 (2015).

[151] Z. Popovic, J. Thaung, P. Knutsson, et al., "Dual conjugate adaptive optics prototype for wide field high resolution retinal imaging", in *Adaptive optics progress* (IntechOpen, 2012).

[152] R. D. Simmonds and M. J. Booth, "Modelling of multi-conjugate adaptive optics for spatially variant aberrations in microscopy", Journal of Optics **15**, 094010 (2013).

[153] R. H. Dicke, "Phase-contrast detection of telescope seeing errors and their correction", The Astrophysical Journal **198**, 605–615 (1975).

[154] J. M. Beckers, "Detailed compensation of atmospheric seeing using multiconjugate adaptive optics", in Active telescope systems, Vol. 1114 (1989), pp. 215–219.

[155] N. V. Kuzmin, P. Wesseling, P. C. d. W. Hamer, et al., "Third harmonic generation imaging for fast, label-free pathology of human brain tumors", Biomedical Optics Express **7**, 1889–1904 (2016).

[156] K. S. Yashin, E. B. Kiseleva, A. A. Moiseev, et al., "Quantitative nontumorous and tumorous human brain tissue assessment using microstructural co- and cross-polarized optical coherence tomography", Scientific Reports **9**, 2024 (2019).

[157] J. Cha, A. Broch, S. Mudge, et al., "Real-time, label-free, intraoperative visualization of peripheral nerves and micro-vasculatures using multimodal optical imaging techniques", Biomedical Optics Express **9**, 1097–1110 (2018).

[158] N. L. Martirosyan, J. M. Eschbacher, M. Y. S. Kalani, et al., "Prospective evaluation of the utility of intraoperative confocal laser endomicroscopy in patients with brain neoplasms using fluorescein sodium: experience with 74 cases", Neurosurgical Focus **40**, 10.3171/2016.1.Focus15559 (2016).

[159] J.-C. Tonn and W. Stummer, "Fluorescence-guided resection of malignant gliomas using 5-aminolevulinic acid: practical use, risks, and pitfalls", Clinical Neurosurgery **55**, 20–26 (2008).

[160] A. Rodriguez, B. S. Tatter, and W. Debinski, "Neurosurgical techniques for disruption of the blood–brain barrier for glioblastoma treatment", Pharmaceutics **7**, 10.3390/pharmaceutics7030175 (2015).

[161] D. Y. Zhang, S. Singhal, and J. Y. K. Lee, "Optical principles of fluorescence-guided brain tumor surgery: a practical primer for the neurosurgeon", Neurosurgery **85**, 312–324 (2018).

[162] A. L. Vahrmeijer, M. Hutteman, J. R. van der Vorst, et al., "Image-guided cancer surgery using near-infrared fluorescence", Nature Reviews Clinical Oncology **10**, 507 (2013).

[163] N. Primerov, J. Dahdah, S. Gloor, et al., "A compact red-green-blue superluminescent diode module: a novel light source for ar microdisplays", in Spie digital optical technologies, Vol. 11062 (2019).

[164] R. Turcotte, Y. Liang, and N. Ji, "Adaptive optical versus spherical aberration corrections for in vivo brain imaging", Biomedical Optics Express **8**, 3891–3902 (2017).

[165] A. Grosche, J. Grosche, M. Tackenberg, et al., "Versatile and simple approach to determine astrocyte territories in mouse neocortex and hippocampus", PLoS One **8**, e69143 (2013).

[166] R. Benavides-Piccione, M. Regalado-Reyes, I. Fernaud-Espinosa, et al., "Differential structure of hippocampal CA1 pyramidal neurons in the human and mouse", Cerebral Cortex **30**, 730–752 (2019).

[167] R. Turcotte, C. Alt, L. J. Mortensen, et al., "Characterization of multiphoton microscopy in the bone marrow following intravital laser osteotomy", Biomedical Optics Express **5**, 3578–3588 (2014).

[168] K. Suto, K. Urabe, K. Naruse, et al., "Repeated freeze-thaw cycles reduce the survival rate of osteocytes in bone-tendon constructs without affecting the mechanical properties of tendons", Cell and tissue banking **13**, 71–80 (2012).

[169] A. L. Allegra Mascaro, I. Costantini, E. Margoni, et al., "Label-free near-infrared reflectance microscopy as a complimentary tool for two-photon fluorescence brain imaging", Biomedical optics express **6**, 4483–4492 (2015).

[170] C. Cheyuo, W. Grand, and L. L. Balos, "Near-infrared confocal laser reflectance cytoarchitectural imaging of the substantia nigra and cerebellum in the fresh human cadaver", World Neurosurgery **97**, 465–470 (2017).

[171] Y. Ohno, "Spectral design considerations for white LED color rendering", Optical Engineering **44**, 111302 (2005).

[172] J. Zhu, S. P. Chong, W. Zhou, et al., "Noninvasive, in vivo rodent brain optical coherence tomography at 2.1 microns", Optics Letters **44**, 4147–4150 (2019).

[173] T. DuBose, D. Nankivil, F. LaRocca, et al., "Handheld adaptive optics scanning laser ophthalmoscope", Optica **5**, 1027–1036 (2018).

[174] A. Rishpon, N. Kim, A. Scope, et al., "Reflectance confocal microscopy criteria for squamous cell carcinomas and actinic keratoses", Archives of Dermatology **145**, 766–772 (2009).

[175] C. Akladios, V. De Ruijter, S. Perretta, et al., "Feasibility and reliability of pancreatic cancer staging using a new confocal non-fluorescent microscopy probe: a double-blind study in rats", Surgical Endoscopy **31**, 995–1003 (2017).

[176] V. Campo-Ruiz, G. Y. Lauwers, R. R. Anderson, et al., "In vivo and ex vivo virtual biopsy of the liver with near-infrared, reflectance confocal microscopy", Modern Pathology **18**, 290–300 (2005).

[177] T. Y. C. So, Y.-L. Lam, and K.-L. Mak, "Computer-assisted navigation in bone tumor surgery: seamless workflow model and evolution of technique", Clinical Orthopaedics and Related Research **468**, 2985–2991 (2010).

[178] T. Keck, V. Campo-Ruiz, A. L. Warshaw, et al., "Evaluation of morphology and microcirculation of the pancreas by ex vivo and in vivo reflectance confocal microscopy", Pancreatology **1**, 48–57 (2001).

[179] E. Cinotti, L. Gergelé, J. L. Perrot, et al., "Quantification of capillary blood cell flow using reflectance confocal microscopy", Skin Research and Technology **20**, 373–378 (2014).

[180] M. Carbillet, C. Vérinaud, B. Femenía, et al., "Modelling astronomical adaptive optics - i. the software package caos", Monthly Notices of the Royal Astronomical Society **356**, 1263–1275 (2005).

[181] R. Conan and C. Correia, "Object-oriented matlab adaptive optics toolbox", in Spie astronomical telescopes + instrumentation, Vol. 9148 (2014).

[182] A. Ahmadia and B. Ellerbroek, "A software framework for fast adaptive optics control with atmospheric tomography", in Adaptive optics: analysis and methods/computational optical sensing and imaging/information photonics/signal recovery and synthesis topical meetings on cd-rom, Technical Digest (2005), AThB4.

[183] O. Guyon, A. Sevin, D. Gratadour, et al., "The compute and control for adaptive optics (cacao) real-time control software package", in Spie astronomical telescopes + instrumentation, Vol. 10703 (2018).

[184] M. J. Townson, O. J. D. Farley, G. Orban de Xivry, et al., "Aotools: a python package for adaptive optics modelling and analysis", Optics Express **27**, 31316–31329 (2019).

[185] N. Hall, J. Titlow, M. J. Booth, et al., "Microscope-aotools: a generalised adaptive optics implementation", Optics Express **28**, 28987–29003 (2020).

[186] U. Bitenc, "Software compensation method for achieving high stability of alpao deformable mirrors", Optics Express **25**, 4368–4381 (2017).

[187] B. Dong and M. J. Booth, "Wavefront control in adaptive microscopy using shack-hartmann sensors with arbitrarily shaped pupils", Optics Express **26**, 1655–1669 (2018).

[188] J. Ye, W. Wang, Z. Gao, et al., "Modal wavefront estimation from its slopes by numerical orthogonal transformation method over general shaped aperture", Optics Express **23**, 26208–26220 (2015).

[189] J. Cui, B. Dong, and M. J. Booth, *Shack-hartmann sensing with arbitrarily shaped pupil* (2020).

[190] B. W. Papież, B. Markelc, G. Brown, et al., "Image-based artefact removal in laser scanning microscopy", IEEE Transactions on Biomedical Engineering **67**, 79–87 (2020).

[191] P. Alfeld, "A trivariate clough—tocher scheme for tetrahedral data", Computer Aided Geometric Design **1**, 169–181 (1984).

[192] C. J. R. Sheppard, "Aberrations in high aperture conventional and confocal imaging systems", Applied Optics **27**, 4782–4786 (1988).

[193] T. Wilson and A. R. Carlini, "The effect of aberrations on the axial response of confocal imaging systems", Journal of Microscopy **154**, 243–256 (1989).

[194] M. Montalto, R. McKay, and R. Filkins, "Autofocus methods of whole slide imaging systems and the introduction of a second-generation independent dual sensor scanning method", Journal of Pathology Informatics **2**, 44–44 (2011).

[195] P. Langehanenberg, G. von Bally, and B. Kemper, "Autofocusing in digital holographic microscopy", 3D Research **2**, 4 (2011).

[196] R. Redondo, G. Cristóbal, G. B. Garcia, et al., "Autofocus evaluation for brightfield microscopy pathology", Journal of Biomedical Optics **17**, 036008 (2012).

[197] S. Yazdanfar, K. B. Kenny, K. Tasimi, et al., "Simple and robust image-based autofocusing for digital microscopy", Optics Express **16**, 8670–8677 (2008).

[198] J. Liao, L. Bian, Z. Bian, et al., "Single-frame rapid autofocusing for brightfield and fluorescence whole slide imaging", Biomedical Optics Express **7**, 4763–4768 (2016).

[199] J. Liao, Z. Wang, Z. Zhang, et al., "Dual light-emitting diode-based multichannel microscopy for whole-slide multiplane, multispectral and phase imaging", Journal of Biophotonics **11**, e201700075 (2018).

[200] J. Xu, X. Tian, X. Meng, et al., "Wavefront-sensing-based autofocusing in microscopy", Journal of Biomedical Optics **22**, 086012 (2017).

[201] J. Xu, Y. Kong, Z. Jiang, et al., "Accelerating wavefront-sensing-based autofocusing using pixel reduction in spatial and frequency domains", Applied Optics **58**, 3003–3012 (2019).

[202] Y. Wu, Y. Rivenson, Y. Zhang, et al., "Extended depth-of-field in holographic imaging using deep-learning-based autofocusing and phase recovery", Optica **5**, 704–710 (2018).

[203] Z. Ren, Z. Xu, and E. Y. Lam, "Learning-based nonparametric autofocusing for digital holography", Optica **5**, 337–344 (2018).

[204] L. Wei and E. Roberts, "Neural network control of focal position during time-lapse microscopy of cells", Scientific Reports **8**, 7313 (2018).

[205] S. Jiang, J. Liao, Z. Bian, et al., "Transform- and multi-domain deep learning for single-frame rapid autofocusing in whole slide imaging", Biomedical Optics Express **9**, 1601–1612 (2018).

[206] Y. Wu, Y. Rivenson, H. Wang, et al., "Three-dimensional virtual refocusing of fluorescence microscopy images using deep learning", Nature Methods **16**, 1323–1331 (2019).

[207] H. Pinkard, Z. Phillips, A. Babakhani, et al., "Deep learning for single-shot autofocus microscopy", Optica **6**, 794–797 (2019).

[208] Q. Li, X. Liu, J. Jiang, et al., "Rapid whole slide imaging via dual-shot deep autofocusing", IEEE Transactions on Computational Imaging **7**, 124–136 (2021).

[209] C. Belthangady and L. A. Royer, "Applications, promises, and pitfalls of deep learning for fluorescence image reconstruction", Nature Methods **16**, 1215–1225 (2019).

[210] S. Hochreiter and J. Schmidhuber, "Long short-term memory", Neural Computation **9**, 1735–1780 (1997).

[211] M. Schuster and K. K. Paliwal, "Bidirectional recurrent neural networks", IEEE Transactions on Signal Processing **45**, 2673–2681 (1997).

[212] D. P. Kingma and J. Ba, "Adam: a method for stochastic optimization", arXiv preprint arXiv:1412.6980 (2014).

[213] D. S. Moore and S. Kirkland, *The basic practice of statistics*, Vol. 2 (WH Freeman, 2007).

[214] L. Silvestri, M. C. Müllenbroich, I. Costantini, et al., "Universal autofocus for quantitative volumetric microscopy of whole mouse brains", Nature Methods **18**, 953–958 (2021).

[215] D. L. Fried, "Anisoplanatism in adaptive optics", Journal of the Optical Society of America **72**, 52–61 (1982).

[216] C. J. R. Sheppard, M. Gu, K. Brain, et al., "Influence of spherical aberration on axial imaging of confocal reflection microscopy", Applied Optics **33**, 616–624 (1994).

[217] E. E. Diel, J. W. Lichtman, and D. S. Richardson, "Tutorial: avoiding and correcting sample-induced spherical aberration artifacts in 3d fluorescence microscopy", Nature Protocols **15**, 2773–2784 (2020).

[218] N. Huot, R. Stoian, A. Mermillod-Blondin, et al., "Analysis of the effects of spherical aberration on ultrafast laser-induced refractive index variation in glass", Optics Express **15**, 12395–12408 (2007).

[219] P. S. Salter, M. Baum, I. Alexeev, et al., "Exploring the depth range for three-dimensional laser machining with aberration correction", Optics Express **22**, 17644–17656 (2014).

[220] M. J. Booth, M. A. A. Neil, and T. Wilson, "Aberration correction for confocal imaging in refractive-index-mismatched media", Journal of Microscopy **192**, 90–98 (1998).

[221] M. A. A. Neil, R. Juškaitis, M. J. Booth, et al., "Adaptive aberration correction in a two-photon microscope", Journal of Microscopy **200**, 105–108 (2000).

[222] N. Matsumoto, T. Inoue, A. Matsumoto, et al., "Correction of depth-induced spherical aberration for deep observation using two-photon excitation fluorescence microscopy with spatial light modulator", Biomedical Optics Express **6**, 2575–2587 (2015).

[223] D. P. Ryan, E. A. Gould, G. J. Seedorf, et al., "Automatic and adaptive heterogeneous refractive index compensation for light-sheet microscopy", Nature Communications **8**, 612 (2017).

[224] Y.-C. Chen, B. Griffiths, L. Weng, et al., "Laser writing of individual nitrogen-vacancy defects in diamond with near-unity yield", Optica **6**, 662–667 (2019).

[225] D. S. Richardson and J. W. Lichtman, "Clarifying tissue clearing", Cell **162**, 246–257 (2015).

[226] M. J. Booth, M. Schwertner, T. Wilson, et al., "Predictive aberration correction for multilayer optical data storage", Applied Physics Letters **88**, 031109 (2006).

[227] A. Jesacher and M. J. Booth, "Parallel direct laser writing in three dimensions with spatially dependent aberration correction", Optics Express **18**, 21090–21099 (2010).

[228] A. Jesacher, G. D. Marshall, T. Wilson, et al., "Adaptive optics for direct laser writing with plasma emission aberration sensing", Optics Express **18**, 656–661 (2010).

[229] B. P. Cumming, M. D. Turner, G. E. Schröder-Turk, et al., "Adaptive optics enhanced direct laser writing of high refractive index gyroid photonic crystals in chalcogenide glass", Optics Express **22**, 689–698 (2014).

[230] P. Török, P. Varga, and G. Németh, "Analytical solution of the diffraction integrals and interpretation of wave-front distortion when light is focused through a planar interface between materials of mismatched refractive indices", Journal of the Optical Society of America A **12**, 2660–2671 (1995).

[231] F. Huang, G. Sirinakis, E. S. Allgeyer, et al., "Ultra-high resolution 3d imaging of whole cells", Cell **166**, 1028–1040 (2016).

[232] G. Golub and C. Van Loan, *Matrix computations* (Johns Hopkins University Press, Baltimore, 2013).

[233] K. Carlsson, "The influence of specimen refractive index, detector signal integration, and non-uniform scan speed on the imaging properties in confocal microscopy", Journal of Microscopy **163**, 167–178 (1991).

[234] J. Sasian, "Interpretation of pupil aberrations in imaging systems", Proc. SPIE **6342**, 634208 (2006).

[235] J. A. Strother, "Reduction of spherical and chromatic aberration in axial-scanning optical systems with tunable lenses", Biomedical Optics Express **12**, 3530–3552 (2021).

[236] J. Antonello, J. Wang, C. He, et al., *Interferometric calibration of a deformable mirror* (2020).

[237] W. G. Lawrence, G. Varadi, G. Entine, et al., "A comparison of avalanche photodiode and photomultiplier tube detectors for flow cytometry", in Spie bios, Vol. 6859 (2008).

[238] F. Rigaut and B. Neichel, "Multiconjugate adaptive optics for astronomy", Annual Review of Astronomy and Astrophysics **56**, 277–314 (2018).

[239] C. He, H. He, J. Chang, et al., "Polarisation optics for biomedical and clinical applications: a review", Light: Science & Applications **10**, 194 (2021).

[240] D. Tosi, "Review of chirped fiber bragg grating (cfbg) fiber-optic sensors and their applications", Sensors **18**, 10.3390/s18072147 (2018).

[241] A. A. Alattar, J. Bartek, V. L. Chiang, et al., "Stereotactic laser ablation as treatment of brain metastases recurring after stereotactic radiosurgery: a systematic literature review", World Neurosurgery **128**, 134–142 (2019).

Publications arising from this work

1. **Cui J.**, Antonello J., Kirkpatrick A.R., et al., "Generalised Adaptive Optics Method for High-NA Aberration-Free Refocusing in Refractive-Index-Mismatched Media," *Optics Express*, 30(7), 11809, 2022. doi: 10.1364/OE.454912. **Chapter 9 was based predominantly on this work.**

2. **Cui J.**, Hampson K.M., Wincott M., et al., "SenAOReFoc: A Closed-Loop Sensorbased Adaptive Optics and Remote Focusing Control Software," *Journal of Open Source Software*, 7(71), 4075, 2022. doi: 10.21105/joss.04075. **Chapters 5 and 6 were based predominantly on this work.**

3. **Cui J.**, Turcotte R., Emptage N.J., et al., "Extended Range and Aberration-Free Autofocusing via Remote Focusing and Sequence-Dependent Learning," *Optics Express*, 29(22), 36660, 2021. doi: 10.1364/OE.442025. **Chapter 8 was based predominantly on this work.**

4. **Cui J.**, Turcotte R., Hampson K.M., et al., "Remote-Focussing for Volumetric Imaging in a Contactless and Label-Free Neurosurgical Microscope," *Biophotonics Congress 2021: Optics in the Life Sciences*, OSA Technical Digest, paper DTh2A.2, 2021. doi: 10.1364/boda.2021.dth2a.2. **Chapter 6 was based predominantly on this work.**

5. **Cui J.**, Turcotte R., Hampson K.M., et al., "Compact and Contactless Reflectance Confocal Microscope for Neurosurgery," *Biomedical Optics Express*, 11(8), 4772, 2020. doi: 10.1364/BOE.397832. **Chapter 4 was based predominantly on this work.**

6. Hampson K.M., **Cui J.**, Wincott M., et al., "Closed-Loop Multiconjugate Adaptive Optics for Microscopy," *Proc. SPIE*, 11248, 2020. doi: 10.1117/12.2544391. **Chapter 10 was based predominantly on this work.**